ARISTOTLE UNIVERSITY OF THESSALONIKI
FACULTY OF SCIENCES
SCHOOL OF GEOLOGY

CHRISTOS DOMAKINIS
MSc Geologist

USE OF REMOTE SENSING AND GEOGRAPHIC INFORMATION SYSTEMS IN MAPPING FLOOD EXTENT AND ASSESSING FLOOD HAZARD. APPLICATION EXAMPLE: EVROS'S TRIBUTARY, ERYTHROPOTAMOS RIVER.

DISSERTATION THESIS

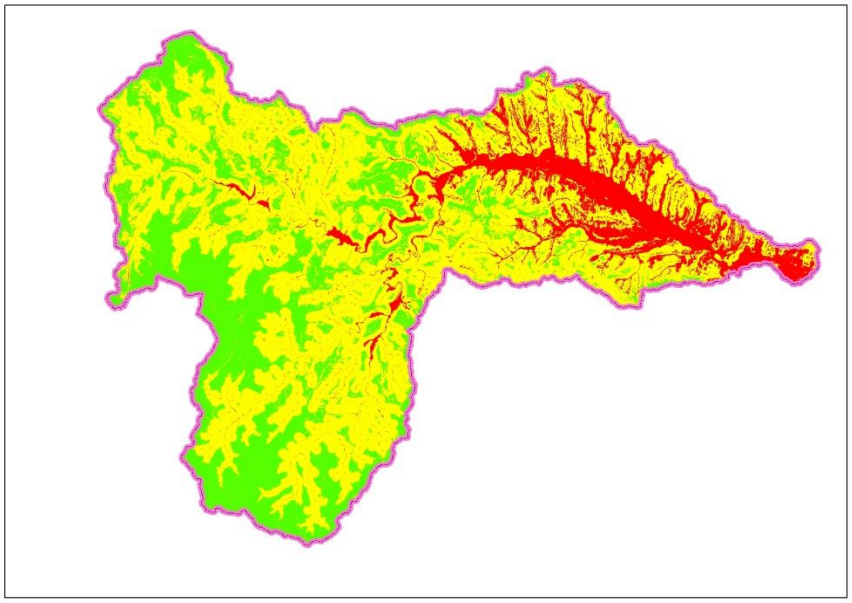

THESSALONIKI
2020

ΑΡΙΣΤΟΤΕΛΕΙΟ ΠΑΝΕΠΙΣΤΗΜΙΟ ΘΕΣΣΑΛΟΝΙΚΗΣ
ΣΧΟΛΗ ΘΕΤΙΚΩΝ ΕΠΙΣΤΗΜΩΝ
ΤΜΗΜΑ ΓΕΩΛΟΓΙΑΣ

ΧΡΗΣΤΟΣ ΔΟΜΑΚΙΝΗΣ
MSc Γεωλόγος

ΧΡΗΣΗ ΤΗΣ ΤΗΛΕΠΙΣΚΟΠΗΣΗΣ ΚΑΙ ΤΩΝ ΓΕΩΓΡΑΦΙΚΩΝ ΣΥΣΤΗΜΑΤΩΝ ΠΛΗΡΟΦΟΡΙΩΝ ΣΤΗΝ ΚΑΤΑΓΡΑΦΗ ΠΛΗΜΜΥΡΩΝ ΚΑΙ ΣΤΗΝ ΕΚΤΙΜΗΣΗ ΤΗΣ ΠΛΗΜΜΥΡΙΚΗΣ ΕΠΙΚΙΝΔΥΝΟΤΗΤΑΣ. ΠΑΡΑΔΕΙΓΜΑ ΕΦΑΡΜΟΓΗΣ ΑΠΌ ΤΟΝ ΕΡΥΘΡΟΠΌΤΑΜΟ ΕΒΡΟΥ

ΔΙΔΑΚΤΟΡΙΚΗ ΔΙΑΤΡΙΒΗ

ΘΕΣΣΑΛΟΝΙΚΗ
2020

"For apart from me you can do nothing"
(John 15:5)

«Χωρίς εμού ου δύνασθε ποιείν ουδέν»
(Ιω. 15:5)

CHRISTOS DOMAKINIS
MSc Geologist

USE OF REMOTE SENSING AND GEOGRAPHIC INFORMATION SYSTEMS IN MAPPING FLOOD EXTENT AND ASSESSING FLOOD HAZARD. APPLICATION EXAMPLE: EVROS'S TRIBUTARY, ERYTHROPOTAMOS RIVER.

Undertaken at the Department of Physical and Environmental Geography of the School of Geology A.U.TH.

Submitted at the School of Geology on

Oral examination date: 09/04/2020

Annex Number of Scientific Annals of the School of Geology N°:

Three-member Advisory Board

Professor Emeritus Theodore Astaras, Supervisor
Professor Konstantinos Voudouris
Assistant Professor Antonios Mouratidis

Examination Board

Professor Emeritus Theodore Astaras
Professor Konstantinos Voudouris
Assistant Professor Antonios Mouratidis
Associate Professor Dimitris Karpouzos
Associate Professor Konstantinos Vouvalidis
Associate Professor Giorgos Mallinis
Assistant Researcher Dimitrios Alexakis

USE OF REMOTE SENSING AND GEOGRAPHIC INFORMATION SYSTEMS IN MAPPING FLOOD EXTENT AND ASSESSING FLOOD HAZARD. APPLICATION EXAMPLE: EVROS'S TRIBUTARY, ERYTHROPOTAMOS RIVER. – *Dissertation Thesis*

ΧΡΗΣΗ ΤΗΣ ΤΗΛΕΠΙΣΚΟΠΗΣΗΣ ΚΑΙ ΤΩΝ ΓΕΩΓΡΑΦΙΚΩΝ ΣΥΣΤΗΜΑΤΩΝ ΠΛΗΡΟΦΟΡΙΩΝ ΣΤΗΝ ΚΑΤΑΓΡΑΦΗ ΠΛΗΜΜΥΡΩΝ ΚΑΙ ΣΤΗΝ ΕΚΤΙΜΗΣΗ ΤΗΣ ΠΛΗΜΜΥΡΙΚΗΣ ΕΠΙΚΙΝΔΥΝΟΤΗΤΑΣ. ΠΑΡΑΔΕΙΓΜΑ ΕΦΑΡΜΟΓΗΣ ΑΠΌ ΤΟΝ ΕΡΥΘΡΟΠΌΤΑΜΟ ΕΒΡΟΥ – *Διδακτορική Διατριβή*

Citation:
Domakinis C., 2020. – Use of Remote Sensing and Geographic Information Systems in mapping flood extent and assessing flood hazard. Application example: Evros's tributary, Erythropotamos river. Doctoral Thesis, School of Geology, Aristotle University of Thessaloniki, Annex Number of Scientific Annals of the School of Geology No___, 216 pp.
Δομακίνης Χ., 2020. – Χρήση της Τηλεπισκόπησης και των Γεωγραφικών Συστημάτων Πληροφοριών στην καταγραφή πλημμύρων και στην εκτίμηση της πλημμυρικής επικινδυνότητας. Παράδειγμα εφαρμογής από τον Ερυθροπόταμο Έβρου. Διδακτορική Διατριβή, Τμήμα Γεωλογίας Α.Π.Θ., Αριθμός Παραρτήματος Επιστημονικής Επετηρίδας Τμ. Γεωλογίας Νο ___, 216 σελ.

Cover Figure: Flood susceptibility map of Erythropotamos' river basin

Table of Contents

List of figures

List of tables

ABSTRACT

Erythropotamos is a tributary of river Evros and during the last decade its drainage basin flooded many times, causing extensive damage on properties. In order to pave the path for effective flood risk management and compensate for the lack of studies in such a flood-prone area the flood hazard assessment procedures of inundation mapping, flood hazard and risk mapping, along with flood susceptibility mapping were employed. Inundation mapping was carried out with the aid of SAR (Synthetic Aperture Radar) imagery. Specifically, ENVISAT/ASAR and SENTINEL – 1 A/B imagery was utilized to delineate the inundated areas of flood events that occurred in 2010, 2017 and 2018. Flood hazard and risk mapping was implemented with the use of Geographic Information Systems (GIS) for both only the thalweg and the river reaches of the 5th stream order and higher, providing predictions of flood extents and the spatial distribution of water depths according to scenarios that were suggested by both the 2007/60/EC Directive and certain gauges of the station that is located on the bridge of Didymoteicho. Furthermore, flood susceptibility mapping was conducted for the study area by applying the Analytical Hierarchy Process (AHP). Topographical, hydrological and meteorological factors were used and each one of them was classified into three (3) flood susceptibility categories (low, medium and high). The importance of each factor over the others was determined with the aid of either the results of inundation or flood hazard mapping, thus dealing with the subjectivity that involves the determination of the hierarchy of factors in AHP. Subsequently, the resulting flood susceptibility maps were validated according to the inundated areas of the April 2017, March 2018 and, in the case where the hierarchy of factors was determined by the results of flood hazard mapping, February 2010 flood extent. The results of the aforementioned procedure indicated that large portions of the delineated areas intersected with each susceptibility map's high susceptibility zone. Finally, the results of each flood hazard assessment procedure were not only compared with the zone of potential high flood risk that is suggested by Ministry of Environment and Energy but also they were combined in a number of ways in order to determine whether it was feasible to achieve better outcomes.

ΠΕΡΙΛΗΨΗ

Ο Ερυθροπόταμος είναι παραπόταμος του ποταμού Έβρου και κατά τη διάρκεια της τελευταίας δεκαετίας η λεκάνη απορροής του πλημμύρησε αρκετές φορές, προκαλώντας εκτεταμένες ζημιές σε περιουσίες. Προκειμένου να προετοιμαστεί ο δρόμος για αποτελεσματική διαχείριση του πλημμυρικού κινδύνου και να αντισταθμιστεί η έλλειψη τέτοιων μελετών σε μια περιοχή που είναι τόσο επιρρεπής σε πλημμύρες, χρησιμοποιήθηκαν διαδικασίες εκτίμησης της επικινδυνότητας της πλημμύρας όπως η χαρτογράφηση κατακλυζόμενων περιοχών, η χαρτογράφηση της επικινδυνότητας και του κινδύνου της πλημμύρας, καθώς και η χαρτογράφηση της πλημμυρικής επιδεκτικότητας. Η χαρτογράφηση κατακλυζόμενων περιοχών διεξήχθη με τη βοήθεια εικόνων Ραντάρ Συνθετικού Ανοίγματος. Ειδικότερα, χρησιμοποιήθηκαν εικόνες ENVISAT/ASAR και SENTINEL – 1 A/B προκειμένου να οριοθετηθεί ο χώρος των κατακλυζόμενων περιοχών που συνέβησαν τις χρονιές 2010, 2017 και 2018. Η χαρτογράφηση της επικινδυνότητας και του κινδύνου της πλημμύρας υλοποιηθήκαν με τη βοήθεια των Γεωγραφικών Συστημάτων Πληροφοριών (Γ.Σ.Π.), όχι μόνο για την κύρια μισγάγγεια άλλα και για τους κλάδους του υδρογραφικού δικτύου άνω της 5ης τάξης, παρέχοντας προβλέψεις για την έκταση των πλημμυρών και για τη χωρική κατανομή του βάθους του νερού συμφώνα με τα σενάρια που προτείνονται από την Οδηγία 2007/60 του Ευρωπαϊκού Κοινοβουλίου, καθώς και για συγκεκριμένες μετρήσεις του σταθμού που είναι τοποθετημένος στη γέφυρα του Διδυμοτείχου. Επιπλέον, η χαρτογράφηση της πλημμυρικής επιδεκτικότητας διεξήχθη για την υπό μελέτη περιοχή εφαρμόζοντας τη Διαδικασία της Αναλυτικής Ιεραρχίας (Analytical Hierarchy Process/AHP). Χρησιμοποιήθηκαν τοπογραφικοί, υδρολογικοί και μετεωρολογικοί παράγοντες και ο καθένας από αυτούς ταξινομήθηκε σε τρεις (3) κατηγορίες επιδεκτικότητας (χαμηλή, μέτρια και υψηλή). Η σημαντικότητα του κάθε παράγοντα έναντι των υπολοίπων καθορίστηκε με τη βοήθεια είτε της χαρτογράφησης κατακλυζόμενων περιοχών ή της χαρτογράφησης της επικινδυνότητας της πλημμύρας, αντιμετωπίζοντας με αυτό τον τρόπο την υποκειμενικότητα που περιλαμβάνεται στον καθορισμό της ιεραρχίας των παραγόντων από τη Διαδικασία της Αναλυτικής Ιεραρχίας. Ακολούθως, οι παραγόμενοι χάρτες πλημμυρικής επιδεκτικότητας αξιολογήθηκαν σύμφωνα με τις κατακλυζόμενες

περιοχές των πλημμυρών του Απριλίου 2017, του Μαρτίου 2018 και, στην περίπτωση που η ιεραρχία των παραγόντων καθορίστηκε από τα αποτελέσματα της χαρτογράφησης της επικινδυνότητας, με τις κατακλυζόμενες περιοχές των πλημμυρών του Φεβρουαρίου 2010. Τα αποτελέσματα των ως άνω αναφερθέντων διαδικασιών υπέδειξαν ότι μεγάλα ποσοστά των οριοθετημένων περιοχών κατάκλυσης τέμνουν τις ζώνες υψηλής επιδεκτικότητας του κάθε χάρτη πλημμυρικής επιδεκτικότητας. Τελικά, τα αποτελέσματα κάθε διαδικασίας εκτίμησης της επικινδυνότητας της πλημμύρας δεν συγκρίθηκαν μόνο με τη Ζώνη Δυνητικά Υψηλού Κινδύνου Πλημμύρας που προτείνεται από το Υπουργείο Περιβάλλοντος και Ενέργειας αλλά και συνδυάστηκαν ποικιλοτρόπως προκειμένου να διερευνηθεί αν είναι εφικτό να επιτευχθούν καλύτερα αποτελέσματα.

ΕΚΤΕΤΑΜΕΝΗ ΠΕΡΙΛΗΨΗ

Στις μέρες μας δεν υπάρχει αμφιβολία για το πόσο καταστροφικά είναι τα φαινόμενα των πλημμυρών, τα οποία αποτελούν απειλή όχι μόνο για τις περιουσίες αλλά και για τις ζωές των ανθρώπων. Το Ευρωπαϊκό Κοινοβούλιο και το Συμβούλιο της Ευρωπαϊκής Ένωσης, έχοντας κατανοήσει ότι «οι πλημμύρες είναι φαινόμενα τα οποία είναι αδύνατο να προληφθούν» υιοθέτησε την Οδηγία 2007/60/ΕΚ προκειμένου να αμβλύνει τις δυσμενείς συνέπειες.

Στην εν λόγω Οδηγία εκτός από τον καθορισμό βασικών εννοιών, όπως για παράδειγμα της πλημμύρας (flood) και του κίνδυνου πλημμύρας (flood risk), παρατίθενται και οι περιγραφές για τα θεματικά επίπεδα που περιλαμβάνονται στους χάρτες επικινδυνότητας πλημμύρας (flood hazard maps) και στους χάρτες κινδύνου πλημμύρας (flood risk maps).

Το Κέντρο Έρευνας της Επιδημιολογίας των Καταστροφών (KEEK/CRED) θεωρεί ως καταστροφή τον φυσικό κίνδυνο που βλάπτει με οποιονδήποτε τρόπο τους ανθρώπους και έχει δημιουργήσει την παγκόσμια βάση δεδομένων για τις φυσικές καταστροφές (EM –DAT). Σύμφωνα με την τελευταία 7.255 καταγεγραμμένα γεγονότα από το 1998 έως το 2017, δείχνουν ότι πλημμύρες είναι οι πιο συχνές καταστροφές και επίσης εκείνες οι οποίες πλήττουν τους περισσότερους ανθρώπους.

Όσον αφορά τα στάδια που οδηγούν στην διαχείριση του κινδύνου πλημμύρας (flood risk management), η παρούσα διδακτορική διατριβή αφορά το κομμάτι της εκτίμησης ή ανάλυσης της επικινδυνότητας (hazard assessment or analysis). Συγκεκριμένα εξετάζει τις μεθοδολογίες: 1) της χαρτογράφησης πλημμύρας με τη βοήθεια εικόνων Ραντάρ Συνθετικού Ανοίγματος (ΡΣΑ/SAR), 2) της χαρτογράφησης της επικινδυνότητας και του κινδύνου πλημμύρας (flood hazard and risk mapping) και 3) της χαρτογράφησης της πλημμυρικής επιδεκτικότητας (flood susceptibility mapping).

Η περιοχή της λεκάνης απορροής του Ερυθροποτάμου επιλέχθηκε ως η περιοχή της εφαρμογής των προαναφερθέντων μεθοδολογιών. Η έκταση της εν λόγω περιοχής είναι 1,618.5 km^2 και το μεγαλύτερο τμήμα της ανήκει στην περιοχή της Θράκης στην Βόρεια Ελλάδα, ενώ το υπόλοιπο ανήκει στη Βουλγαρία. Από διοικητική άποψη το τμήμα της λεκάνης απορροής που βρίσκεται στον ελληνικό χώρο ανήκει στους νομούς Έβρου και

Ροδόπης. Από γεωτεκτονική άποψη η περιοχή έρευνας ανήκει στη μάζα της Ροδόπης και την Περιροδοπική ζώνη. ενώ στην περιοχή επικρατεί ένας γεωλογικός σχηματισμός που αποτελείται από οφθαλμογνεύσιους. Το Ψηφιακό Υψομετρικό Μοντέλο (ΨΥΜ) EU-DEM, με οριζόντια και κατακόρυφη διακριτική ικανότητα 25m και 3,6m αντίστοιχα, χρησιμοποιήθηκε στην ανάλυση του αναγλύφου. Σύμφωνα με την ταξινόμηση κατά Dikau (1989), στην περιοχή έρευνας επικρατεί το λοφώδες ανάγλυφο, ενώ σύμφωνα με την ταξινόμηση κατά Demek (1972), το μεγαλύτερο μέρος της λεκάνης απορροής καταλαμβάνει ισχυρά κεκλιμένο ανάγλυφο. Το υδρογραφικό δίκτυο του Ερυθροπόταμου είναι δενδριτικού τύπου και η μέγιστη τάξη κλάδου είναι η έβδομη. Επιπλέον, ο συντελεστής διακλάδωσης R_b έχει μέση τιμή 4,97, ενώ χαμηλές τιμές για αυτή τη μορφομετρική παράμετρο παρατηρούνται μεταξύ των κλάδων τάξης 4 και 5. Επιπρόσθετα, σύμφωνα με το υψομετρικό ολοκλήρωμα και την υψομετρική καμπύλη, η λεκάνη απορροής του Ερυθροπόταμου η περιοχή ανήκει στο στάδιο «γήρατος» του Κύκλου Διάβρωσης. Όσον αφορά την κάλυψη γης, σύμφωνα με τις χρήσεις γης κατά Corine Land Cover 2012, η περιοχή έρευνας αποτελείται κυρίως από δάση και ακολούθως από τις διάφορες κατηγορίες αρόσιμης γης. Τέλος, στην εν λόγω περιοχή χωροθετούνται οι Ειδικές Ζώνες Προστασίας (Special Protection Areas / SPA) του Δικτύου Natura 2000 της Κοιλάδας του Φιλιούρη (GR1130011) και της Κοιλάδας Ορείνου Έβρου – Δέρειου (GR1110010).

Στη λεκάνη απορροής του Ερυθροποτάμου έχουν συμβεί πολλά πλημμυρικά επεισόδια. Το σημαντικότερο ξεκίνησε στις 8/2/2010 και ολοκληρώθηκε στις 18/2/2010, σημειώνοντας μέγιστο ύψος στάθμης 7.42m και μέγιστη τιμή πλημμυρικής παροχής 1.255,05 m^3/s. Το εν λόγω φαινόμενο καταγράφηκε από το σταθμό που βρίσκεται τοποθετημένος στη γέφυρα του Διδυμοτείχου και παρέμεινε σε λειτουργία από το 2008 μέχρι και το 2010. Άλλα πλημμυρικά φαινόμενα τα οποία έπληξαν την ερευνούμενη περιοχή συνέβησαν κατά τα χρονικά διαστήματα 16/4/2017 – 20/4/2017 και 25/3/2018 – 1/4/2018 σύμφωνα με πληροφορίες από τη Διεύθυνση Πολιτικής Προστασίας του Έβρου.

Όσον αφορά τη χαρτογράφηση πλημμύρας με τη βοήθεια εικόνων SAR, και ειδικότερα εικόνων ENVISAT/ASAR, αρχικά εφαρμόστηκε μια απλοποιημένη

μεθοδολογία ανίχνευσης αλλαγών (change detection) σύμφωνα με την ESA (2008). Η μεθοδολογία αυτή στηρίζεται στη σύνθεση ψευδοέγχρωμης εικόνας RGB, όπου μια εικόνα που λήφθηκε έξω από το χρονικό διάστημα κατά το οποίο εξελίσσονταν το πλημμυρικό φαινόμενο αντιστοιχίζεται στην μπλε και πράσινη χρωματική έξοδο (εικόνα αρχείου / archive image), ενώ αντίστοιχα μια εικόνα που λήφθηκε κατά τη διάρκεια εξέλιξης του εν λόγω φαινομένου αντιστοιχίζεται στην κόκκινη χρωματική έξοδο (εικόνα καταστροφής / crisis image). Ακολούθως, στην ψευδοέγχρωμη εικόνα που προκύπτει εφαρμόζονται τιμές κατωφλίου (thresholding) που αφορούν τις τιμές εύρους (amplitude). Συγκεκριμένα, επιλέγονται τα εικονοστοιχεία με τιμές μεγαλύτερες του 900 για την εικόνα αρχείου και με τιμές μικρότερες του 800 για την εικόνα καταστροφής. Οι περιοχές που έχουν πλημμυρήσει απεικονίζονται με κυανό χρώμα. Για την εν λόγω μεθοδολογία επιλέχθηκε η εικόνα που λήφθηκε στις 16/2/2010 ως «εικόνα καταστροφής» και η εικόνα που λήφθηκε στις 23/12/2008 ως «εικόνα αρχείου».

Στη συνέχεια εφαρμόστηκε η μεθοδολογία των Cian et al. (2018), κατά την οποία χρησιμοποιήθηκαν 11 εικόνες ENVISAT/ASAR διακριτικής ικανότητας 30m και 27 εικόνες SENTIENL – 1 A/B διακριτικής ικανότητας 20m. Στη συνέχεια δημιουργήθηκαν στοίβες (stacks) και ειδικότερα η «στοίβα αναφοράς» (reference stack) που περιέχει μόνο τις εικόνες αναφοράς (reference images) και η «στοίβα εικόνων αναφοράς και πλημμύρας» (reference & flood images) που περιέχει τις εικόνες αναφοράς και την/τις εικόνες που λήφθηκαν κατά τη διάρκεια της πλημμύρας. Ακολούθως, εφαρμόστηκαν οι δείκτες NDFI & NDFVI σύμφωνα με τον υπολογισμό της ελάχιστης, μέγιστης και μέσης τιμής για κάθε εικονοστοιχείο (pixel) είτε της «στοίβας αναφοράς» ή της «στοίβας αναφοράς και πλημμύρας». Χαρακτηριστικό του δείκτη NDFI είναι οτι μπορεί να διαχωρίσει περιοχές που καλύπτονται μόνιμα από ύδατα και περιοχές που καλύπτονται πρόσκαιρα από ύδατα. Επιπλέον, η ανίχνευση ρηχού νερού (shallow water) που προέρχεται από πλημμύρες σε περιοχές χαμηλής βλάστησης (short vegetation) γίνεται με τη βοήθεια του δείκτη NDFVI. Τέλος, σύμφωνα με τους Cian et al. (2018) για τους προαναφερθέντες δείκτες εφαρμόζονται οι ακόλουθες τιμές κατωφλίου: 1) NDFI > 0,7 και 2) NDFVI > 0,75, ενώ στις τελικές υπολογιζόμενες περιοχές εξαιρούνται οι περιοχές

που είναι μικρότερες από 10 εικονοστοιχεία και εικονοστοιχεία για τα οποία ισχύει: 1) $\sigma_{o(μέση)} < 0,015$ και 1) $\sigma_{o(μέση)} > 0,03$.

Σύμφωνα με τη μεθοδολογία της ESA (2008) η έκταση των κατακλυζόμενων εκτάσεων για την πλημμύρα του 2010 βρέθηκε 15,75km^2. Από την εφαρμογή της μεθοδολογίας των Cian et al. (2018) προέκυψαν κατακλυζόμενες περιοχές με έκταση 6,84km^2, 18,23km^2 και 20,6km^2 για τις πλημμύρες του 2010, 2017 και 2018 αντίστοιχα.

Όσον αφορά τη μεθοδολογία της ESA (2008), επειδή είναι εμπειρική, δεν μπορεί να εφαρμοστεί σε άλλους αισθητήρες ραντάρ και επιπλέον δεν μπορεί να ανιχνεύσει κατακλυζόμενες περιοχές σε χαμηλή βλάστηση. Οι κατακλυζόμενες περιοχές των πλημμυρών του 2010, 2017 και 2018, που υπολογίστηκαν με τη βοήθεια της μεθοδολογίας των Cian et al. (2018), παρουσιάζουν διαφορές στην έκτασή τους οι οποίες μπορούν να αποδοθούν είτε στη διαφορά της περιόδου επαναφοράς (return periods) των φαινομένων ή στη χρονική λήψη της εικόνας σε σχέση με τη χρονική στιγμή της μέγιστης τιμής της πλημυρικής παροχής. Παρόλο που υπάρχουν αρκετές αβεβαιότητες (uncertainties) όσον αφορά την οριοθέτηση (delenaeation) των κατακλυζόμενων περιοχών με τη βοήθεια εικόνων ραντάρ, αυτές εξακολουθούν να χρησιμοποιούνται στην αξιολόγηση (validation) αποτελεσμάτων χαρτογράφησης επικινδυνότητας πλημμύρας & πλημμυρικής επιδεκτικότητας, χωρίς να υπάρχει κάποια ευρέως καθιερωμένη μεθοδολογία.

Η χαρτογράφηση της επικινδυνότητας πλημμύρας και του κινδύνου πλημμύρας είχε ως σκοπό τον υπολογισμό των εκτάσεων των κατακλυζόμενων περιοχών και της χωρικής κατανομής του ύψους στάθμης (water depth). Η διαδικασία αυτή περιλάμβανε αρχικά την προετοιμασία των γεωμετρικών στοιχείων (geometric data) με τη βοήθεια του HEC-GeoRAS και εφαρμόστηκε τόσο στην κύρια κοίτη, όσο και στους κλάδους 5ης τάξης και άνω του υδρογραφικού δικτύου. Τα γεωμετρικά στοιχεία που δημιουργήθηκαν με τη βοήθεια του HEC-GeoRAS ήταν: 1) η κεντρική γραμμή της κοίτης (stream centerline), 2) οι όχθες (banks), 3) οι δίοδοι ροής (flow paths), 4) οι διατομές (cut lines) και 5) η κάλυψη γης (land cover).

Ακολούθως, τα προαναφερθέντα στοιχεία εισήχθησαν στο λογισμικό HEC-RAS προκειμένου να διεξαχθεί υδραυλική ανάλυση σταθεράς ροής (steady flow). Η

πλημμυρική παροχή (flood discharge), που αποτελεί και το βασικό δεδομένο εισόδου (input), υπολογίστηκε με τη βοήθεια της λογικής μεθόδου (rational method). Τα σενάρια περιόδων επαναφοράς που εφαρμόστηκαν ήταν εκείνα της υψηλής, μέσης και χαμηλής πιθανότητας, σύμφωνα με την Οδηγία 2007/60/ΕΚ, καθώς και εκείνα που αντιστοιχούσαν στην τιμή παροχής κατά τη λήψη της εικόνας ENVISAT/ASAR στις 16/2/2010 και στη μέγιστη τιμή παροχής που μετρήθηκε για την πλημμύρα του 2010 σύμφωνα με τις μετρήσεις του σταθμού του Διδυμοτείχου.

Στη συνέχεια τα αποτελέσματα της υδραυλικής ανάλυσης κατόπιν επεξεργασίας με τη βοήθεια του λογισμικού HEC-GeoRAS παρήγαγαν τα επίπεδα πληροφορίας που αφορά τα όρια των κατακλυζόμενων περιοχών και τη χωρική κατανομή του ύψους στάθμης για τα προαναφερθέντα σενάρια. Έχοντας ολοκληρώσει με τον τρόπο αυτό τη χαρτογράφηση της επικινδυνότητας πλημμύρας, τα προαναφερθέντα επίπεδα υπερτέθηκαν σε αστικές και περοστατευόμενες περιοχές με τη βοήθεια των ΓΠΣ προκειμένου να υλοποιηθεί και κ χαρτογράφηση του κινδύνου πλημμύρας.Επειδή η χρήση όλου του υδρογραφικού δικτύου δεν είναι εφικτή γιατί τα λογισμικά HEC-RAS & HEC-GeoRAS δεν μπορούν να διαχειριστούν μεγάλο όγκο δεδομένων, η παρούσα διδακτορική διατριβή πρότεινε τη χρήση του λόγου διακλάδωσης σύμφωνα με την Das (2016) προκειμένου να ξεπεραστεί αυτή η δυσκολία, εντοπίζοντας το τμήμα του υδρογραφικού δικτύου που κινδυνεύει περισσότερο από πλημμύρες. Οι κατακλυζόμενες περιοχές που υπολογίστηκαν από τη γεωμετρία των κλάδων 5ης τάξης και άνω είναι περίπου κατά 10km^2 μεγαλύτερες από τις αντίστοιχες που προέκυψαν από τη γεωμετρία της κύριας κοίτης. Ομοίως, οι μέγιστες τιμές του ύψους στάθμης που υπολογίστηκαν από τη γεωμετρία των κλάδων 5ης τάξης και άνω είναι περίπου κατά 16-17m μεγαλύτερες από τις αντίστοιχες τιμές που προέκυψαν από τη γεωμετρία της κύριας κοίτης. Σχετικά με τους χάρτες κινδύνου πλημμύρας παρατηρήθηκε ότι οι προστατευόμενες περιοχές του δικτύου Natura 2000 πλήττονται περισσότερο από τις τεχνητές επιφάνειες.

Για τη χαρτογράφηση της πλημμυρικής επιδεκτικότητας χρησιμοποιήθηκαν τοπογραφικοί (υψόμετρο, γωνίες κλίσης, υδρογραφική πυκνότητα), υδρολογικοί (τοπογραφικός δείκτης υγρασίας, απόσταση από τα ρέματα, γεωλογία, κάλυψη γης) και μετεωρολογικοί (βροχόπτωση) δείκτες (indicators). Ακολούθως, προκειμένου να

εφαρμοστεί η Διαδικασία της Αναλυτικής Ιεραρχίας (Analytical Hierarchy Process/AHP), το επίπεδο πληροφορίας του κάθε δείκτη ταξινομήθηκε σε 3 τάξεις (χαμηλά επιδεκτικές, μέτρια επιδεκτικές, υψηλά επιδεκτικές) σύμφωνα με το πόσο επιδεκτική είναι η κάθε τάξη στις πλημμύρες. Όσον αφορά τον καθορισμό της σημαντικότητας μεταξύ των δεικτών αυτή καθορίστηκε με: α) τη βοήθεια των αποτελεσμάτων της χαρτογράφησης κατακλυζόμενων περιοχών και β) τη βοήθεια των αποτελεσμάτων της χαρτογράφησης της επικινδυνότητας πλημμύρας. Στην πρώτη περίπτωση, η παρούσα διδακτορική διατριβή καθόρισε την ιεράρχηση μεταξύ των δεικτών ανάλογα με το ποιος από αυτούς περιλάμβανε το μεγαλύτερο ποσοστό της έκτασης των κατακλυζόμενων περιοχών της πλημμύρας του 2010, όπως αυτή οριοθετήθηκε σύμφωνα με τους δείκτες NDFI και NDFVI, στις ζώνες του με την υψηλότερη διαβάθμιση. Ο χάρτης επιδεκτικότητας που προέκυψε αξιολογήθηκε, με τη βοήθεια των ΓΠΣ, σύμφωνα με το ποσοστό των κατακλυζόμενων περιοχών, που συνέβησαν τον Απρίλιο του 2017 και των Μάρτιο του 2018, το οποίο τέμνει τις περιοχές υψηλής επιδεκτικότητας του εν λόγω χάρτη. Στην δεύτερη περίπτωση, η παρούσα διδακτορική διατριβή καθόρισε την ιεράρχηση μεταξύ των δεικτών ανάλογα με το ποιος από αυτούς περιλάμβανε το μεγαλύτερο ποσοστό της έκτασης των κατακλυζόμενων περιοχών, που προβλέφθηκαν με τη βοήθεια της χαρτογράφησης επικινδυνότητας πλημμύρας, στις ζώνες του με την υψηλότερη διαβάθμιση. Για το σκοπό αυτό χρησιμοποιήθηκαν τα σενάρια της Οδηγίας 2007/60/ΕΚ. Ο χάρτης επιδεκτικότητας που προέκυψε σε αυτή την περίπτωση αξιολογήθηκε με τη βοήθεια των ΓΣΠ σύμφωνα με το ποσοστό των κατακλυζόμενων περιοχών, που συνέβησαν τον Φεβρουάριο του 2010, τον Απρίλιο του 2017 και τον Μάρτιο του 2018, το οποίο τέμνει τις περιοχές υψηλής επιδεκτικότητας του εν λόγω χάρτη.

Από την εφαρμογή της Διαδικασίας της Αναλυτικής Ιεραρχίας έδειξε ως πιο σημαντικό παράγοντα και στις δυο περιπτώσεις καθορισμού της ιεραρχίας των δεικτών το υψόμετρο, ενώ γενικά επικρατούν οι τοπογραφικοί παράγοντες. Όσον αφορά την αξιολόγηση των αποτελεσμάτων που προέκυψαν με τη βοήθεια της ιεράρχησης των δεικτών με τη χρήση των κατακλυζόμενων περιοχών που οριοθετήθηκαν από εικόνες SAR, το μεγαλύτερο ποσοστό των κατακλυζόμενων περιοχών των πλημμυρών του 2017

και του 2018 συνέπεσαν χωρικά με τις ζώνες υψηλής επιδεκτικότητας. Ομοίως, στην αξιολόγηση των αποτελεσμάτων που προέκυψαν με τη βοήθεια της ιεράρχησης των δεικτών με τη βοήθεια της επικινδυνότητας πλημμύρας, το μεγαλύτερο ποσοστό των κατακλυζόμενων περιοχών των πλημμυρών του 2017 και του 2018 συνέπεσαν χωρικά με τις ζώνες υψηλής επιδεκτικότητας.

Επιπρόσθετα, τα αποτελέσματα της χαρτογράφησης της επικινδυνότητας πλημμύρας, της επιδεκτικότητας πλημμύρας και των κατακλυζόμενων περιοχών που οριοθετήθηκαν με τη χρήση εικόνων SAR συγκρίθηκαν με τη Ζώνη Δυνητικά Υψηλού Κινδύνου Πλημμύρας (ΖΔΥΚΠ) που συμπεριλαμβάνεται στο Σχέδιο Διαχείρισης Κινδύνων Πλημμύρας της Λεκάνης Απορροής του π. Έβρου (Υπουργείο Περιβάλλοντος, Ενέργειας & Κλιματικής Αλλαγής 2014) που εκπονήθηκε σύμφωνα με την Οδηγία 2007/60/ΕΚ. Από την εν λόγω σύγκριση παρατηρήθηκε ισχυρός χωρικός συσχετισμός μεταξύ της ΖΔΥΚΠ και των ζωνών της υψηλής πλημμυρικής επιδεκτικότητας.

Επιπλέον, δοκιμάστηκαν διάφοροι συνδυασμοί μεταξύ των αποτελεσμάτων των διαφόρων μεθοδολογιών εκτίμησης της πλημμυρικής επικινδυνότητας που χρησιμοποιήθηκαν στην παρούσα διδακτορική διατριβή. Συγκεκριμένα έγινε: α) σύγκριση μεταξύ της χαρτογράφησης κατακλυζόμενων περιοχών με τη βοήθεια εικόνων SAR και της χαρτογράφησης της επικινδύνοτητας πλημμύρας, β) σύγκριση μεταξύ της χαρτογράφησης πλημμυρικής επικινδυνότητας και της χαρτογράφησης της επιδεκτικότητας πλημμύρας και γ) σύγκριση μεταξύ της χαρτογράφησης κατακλυζόμενων περιοχών με τη βοήθεια των εικόνων ραντάρ και του συνδυασμού των αποτελεσμάτων της πλημμυρικής επιδεκτικότητας και της επικινδυνότητας πλημμύρας. Από τις προαναφερθείσες δοκιμές, παρατηρήθηκε ότι περιοχές υψηλής πλημμυρικής επιδεκτικότητας, ανεξάρτητα με τη μεθοδολογία που ακολουθήθηκε για τον καθορισμό της σημαντικότητας των παραγόντων, παρουσίασαν ισχυρό χωρικό συσχετισμό με τα αποτελέσματα της χαρτογράφησης της επικινδυνότητας πλημμύρας.

1. Prologue

Floods can potentially cause the loss of human lives, destruction of properties and damage to the environment, thus severely compromising economic development and undermining the economic activities of every community that suffers the effects of these destructive environmental hazards (Bell 1999, Astaras et al. 2011, Mouratidis and Sarti 2013, Yésou et al. 2013, Birkholz et al. 2014, Patrikaki et al. 2018, Zhong et al. 2018). During the last decade, such phenomena have also plagued Greece, with their majority occurring in the eastern part of the region of Thrace (Mouratidis 2011, Mouratidis et al. 2011, Kazakis et al., 2015, Nikolaidou et al. 2015). Most such cases were attributed to the river Evros, which is the natural borderline between Greece and Turkey, and, along with its tributaries, has burst its banks on several occasions during the aforementioned time period. Erythropotamos is one of Evros' tributaries and although, in many occasions, flood phenomena have been observed within its river basin, there is a lack of flood risk management studies referring to this catchment. In fact, the only study that referred to the drainage basin of Erythropotamos was carried out by Bezes (1994) and it mostly dealt with the construction of the dam in Mikro Derio and how this infrastructure would affect the aquifer of the Valley of Erythropotamos River.

Flood occurrence in Erythropotamos' catchment is very frequent especially during the last decade. The heavy rainfall that took place from the 9th to the 18th of February 2010 posed a threat for entire villages and the town of Didymoteicho, which is located approximately 2 km away from the confluence between the rivers of Erythropotamos and Evros. More recently, from the 16th of April to the 20th of April in 2017 and from the 25th of March to the 1st of April in 2018, heavy precipitation caused again extensive flooding within the river basin of Erythropotamos. These recent flood events were verified by statements from members of the Department of Civil Protection of the region of Evros, who were tasked with the evaluation of damages that were caused by these floods (C. Papapostolou, personal communication, 2018). Moreover, except for the aforementioned major flood events, other lesser flood events occurred during the period from 2010 to 2018 in the same river basin that endangered many settlements and human

lives. These events not only established that flood hazard is very frequent in the area, but also that the need for effective flood risk management is of paramount importance.

Flood hazard assessment plays an important role when it comes to effective flood risk management. Furthermore, during the last few decades, advances in Remote Sensing (RS) and GIS (Geographic Information Systems) have helped to facilitate the application of flood hazard assessment procedures. Nowadays, there is a plethora of methodologies that help to monitor flood events and predict flood extents and these can surely help in order to mitigate the adverse effects of floods in the drainage basin of Erythropotamos River.

The aim of this dissertation thesis is to assess flood hazard in Erythropotamos' river basin, with the aid of Remote Sensing and GIS, thus paving the path for more effective flood risk management at local and regional level. To this end, ENVISAT/ASAR and SENTINEL-1 A/B images were used initially to conduct flood mapping for three major flood events that occurred in the study area during the period from 2010 to 2018. Also, flood hazard and risk mapping was carried out with the aid of GIS in order to predict flood extents and the spatial distribution of water depth according to probability scenarios that were established by the 2007/60/EC Directive as well as scenarios that corresponded to certain gauges of the station that is located on the bridge of Didymoteicho. Moreover, the susceptibility map for Erythropotamos' river basin was compiled and AHP (Analytical Hierarchy Process) was applied, in order to calculate the weight values for each factor. During this step of the procedure, the results of either inundation or flood hazard mapping were used to determine the importance of each factor during the stage of pairwise comparison. Additionally, the resulting susceptibility maps were validated according to the inundated areas of the April 2017, March 2018 and, in the case where the hierarchy of factors was determined by the results of flood hazard mapping, the February 2010 flood extent.

Finally, the results of each flood hazard assessment procedure were compared with the zone of potential high flood risk that is suggested by Ministry of Environment and Energy, while, in order to examine whether it was feasible to further improve the results of the

aforementioned flood hazard assessment procedures, this dissertation thesis tried to combine the aforementioned results.

Acknowledgements

I would like to express my sincere gratitude to the supervisor of this doctoral thesis Professor Emeritus of the School of Geology, Mr. Theodore Astaras, for his invaluable counseling and guidance throughout the completion of this research.

I would also like to thank:

Professor of the School of Geology, Mr. Konstantinos Voudouris, member of the Advisory Board, for his vitally important counselling on issues concerning hydrogeology that were raised during the completion of the present doctoral thesis and for initiating me to the basic concepts of flood hazard analysis.

Assistant Professor of the School of Geology, Mr. Antonios Mouratidis, member of the Advisory Board, for his priceless contribution on Synthetic Aperture Radar (SAR) imagery processing issues and for his invaluable counsels, which lead to the overall improvement of my doctoral thesis.

Ph.D. candidate of the School of Geology, Ms. Maria Chara Karypidou, for her indispensable contribution and counselling on issues that involved meteorology and climatology.

Assistant Professor of the Faculty of Agriculture, Mr. Thomas Alexandridis, for providing useful advice on issues that were raised during the completion of the my doctoral thesis and involved his field of scientific knowledge.

Associate Manager of the Department of Environmental Infrastructures of the Region of East Macedonia and Thrace, Ms. Maria Chamitidou, for providing the river gauges of the station that is located on Didymoteicho's bridge.

Survey engineer of the Department of Civil Protection of the Region of East Macedonia and Thrace, Mr. Christos Papapostolou, for providing useful information that involved his field of scientific knowledge.

The National Cadastre and Mapping Agency S.A. (NCMA), for providing the 5m spatial resolution Digital Elevation Model (DEM) for the part of the study area that is located in Greece.

Finally, I would like to express my deepest gratitude to my parents, Alexander and Kalliopi, without whose moral and material support this doctoral thesis would not have been completed.

2. Introduction

2.1 The 2007/60/EC Directive – basic definitions and concepts

Nowadays, there is little doubt about how catastrophic are the natural phenomena of floods. They pose a threat not only on properties but sometimes even on human lives. The European Parliament and the Council of the European Union, having understood that "floods are phenomena that cannot be prevented" (E.C. 2007), adopted the 2007/60/EC Directive in order to mitigate their adverse consequences.

The Directive initially established the definitions for "flood" and "flood risk". Consequently, "flood means the temporary covering by water of land not normally covered by water. This shall include floods from rivers, mountain torrents, Mediterranean ephemeral water courses, and floods from the sea in coastal areas, and may exclude floods from sewerage systems", whereas, "flood risk means the combination of the probability of a flood event and of the potential adverse consequences for human health, the environment, cultural heritage and economic activity associated with a flood event" (E.C. 2007).

Furthermore, the Directive urged the members of the European Union to conduct preliminary flood risk assessment for river basins and coastal areas lying within their territories. Additionally, in the case of international river basins, the Member States had to undertake a preliminary flood risk assessment for the portion of the catchment lying within their territory. All Member States had to complete this obligation until the 22nd of December 2011(E.C. 2007).

Moreover, when this part of the Directive was completed, the Member States had to proceed to the compilation of flood hazard and risk maps. At this point, in order to avoid the ambiguity of these terms, the European Parliament and the Council of the European Union provided definitions that indicated the contents of such maps (E.C. 2007).

Specifically, flood hazard maps ought to cover geographical areas that can potentially be flooded according to the following return period scenarios:

a) low or extreme probability floods
b) medium probability floods (return period ≥ 100 years)

c) high probability floods

Regarding the elements that will be included in each scenario of flood hazard maps, these are:

a) flood extent
b) water depths or water level
c) the flow velocity or the relevant water flow

On the other hand, flood risk maps show the potential adverse consequences that the aforementioned flood scenarios have upon:

a) the number of inhabitants that are potentially affected by a flood phenomenon
b) types of economic activity that can be potentially threatened
c) installations, in accordance with Annex I of the Council Directive 96/61/EC, which might accidentally, during floods, cause pollution and potentially threaten protected areas in compliance with Annex IV of Directive 2000/60/EC.
d) other areas that Member States consider important

The Member States ought to complete their flood hazard and risk mapping obligations by 22nd December 2013 and, on the basis of that material, to complete flood risk management plans by 22nd December 2015 (E.C. 2007).

Finally, the Directive encouraged Member States to constantly review and if necessary update the aforementioned processes in a six year interval. Specifically, preliminary flood risk assessment had to be reviewed and updated every six years, starting from 22nd December 2018, whereas flood hazard and risk maps had to be reviewed and updated in a six year interval, starting from 22nd December 2019. Additionally, flood risk management plans had to be reviewed and updated every six years, starting from 22nd December 2021 (E.C. 2007).

2.2 The characteristics of floods

2.2.1 Flood hazard in the context of fluvial geomorphology

Whenever a river bursts its banks and water inundates its adjacent floodplains, flooding occurs. This process is actually comprised of a combination of other discreet processes that operate at both local and watershed scales. Moreover, the floodplain can be

described as the relatively flat alluvial landform that is located adjacent to a river and is at varying degrees related to the modern flood regime (Wolman and Leopold 1957, Nanson and Croke 1992, Knighton 1998, Bridge 2003, Benito and Hudson 2010). The majority of floods are considered natural events, which are very important to either river and floodplain geomorphological (Leopold et al. 1964, Benito and Hudson 2010) or ecosystem processes (Hupp 1988, Junk et al. 1989, Thoms 2003, Benito and Hudson 2010). However, when floods affect in any way humans, then they become "natural disasters" (Benito and Hudson 2010).

Excessive rainfall that is created by a variety of atmospheric mechanisms causes flood phenomena in the majority of river catchments (Smith and Ward 1998, Slade and Patton 2002). In regions where cold-winter climate is prevalent, the melting of snow and/or ice, especially when combined with rainfall, can become the cause of large floods. Additionally, storm surge events cause such phenomena along coastal-draining rivers, while floods can also be attributed to catastrophic failure of artificial (reservoirs) and natural lakes. Finally, it is important to mention that the latter category also involves landslides, volcanic lava flows, glacial moraines and dams created by ice (Costa 1988). (Benito and Hudson 2010)

2.2.2 Flood disaster statistics in a global scale

The Centre for Research on the Epidemiology of Disasters (CRED) is regarded as the world's most prominent agency concerning the study of public health during the occurrence of mass emergencies, such as the structural and socio-economic impacts caused by not only natural and technological disasters but also from human conflicts and the epidemiology of diseases. From 1900 until nowadays, data concerning the effects and occurrence of more than 23,000 technological and natural disasters has been used by CRED in order to compile the Emergency Events Database (EM-DAT). Moreover, since 2014, EM-DAT managed to combine geographical spatial values along with numeric data that concerned natural disasters, practically georeferencing and enabling more effective analysis for the latter. Also, it is important to clarify that CRED perceives as a disaster the natural hazard that results in people being hurt.

According to EM-DAT's data that covers a total of 7,255 recorded events from 1998 to 2017, in terms of occurrences, floods are the most frequent type of disaster, accounting for 43% of all recorded events (CRED and UNISDR 2018) (Figure 1). Additionally, in the same period, floods affected more than 2 billion people, which is more than any other natural disaster (CRED and UNISDR 2018) (Figure 2), while they were fourth in terms of fatalities, having killed 233,000 people (Figure 3). Furthermore, it is worth noting that flood-related deaths and homelessness are concentrated in the Least Developed Countries (LDCs), while industrialized countries, which invest heavily on in flood defense and emergency measures, suffer large economic losses (Smith and Petley 2009).

Finally, it is significant to mention that during the latest 20-year period the average amount of disasters per year was 329, which is almost double the average of 165 such events per year during the period from 1978 to 1997. However, this increase in the frequency of disasters can be attributed to the better reporting of disaster data in the latest decades (CRED and UNISDR 2018).

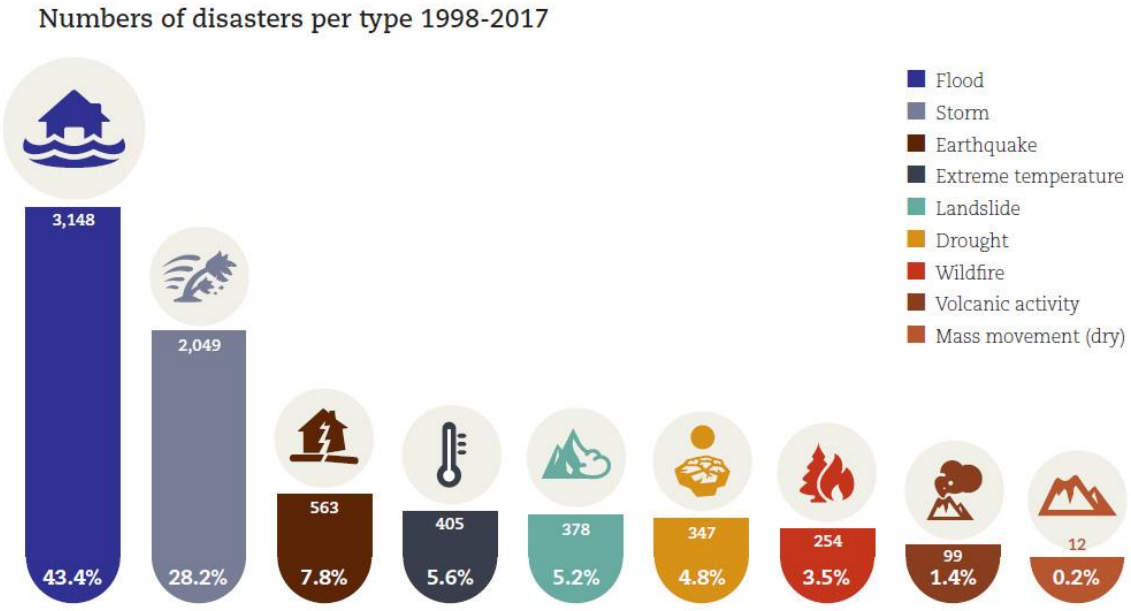

Figure 1: Total number of disasters, according to their type, during the period from 1998 to 2017 (CRED and UNISDR 2018).

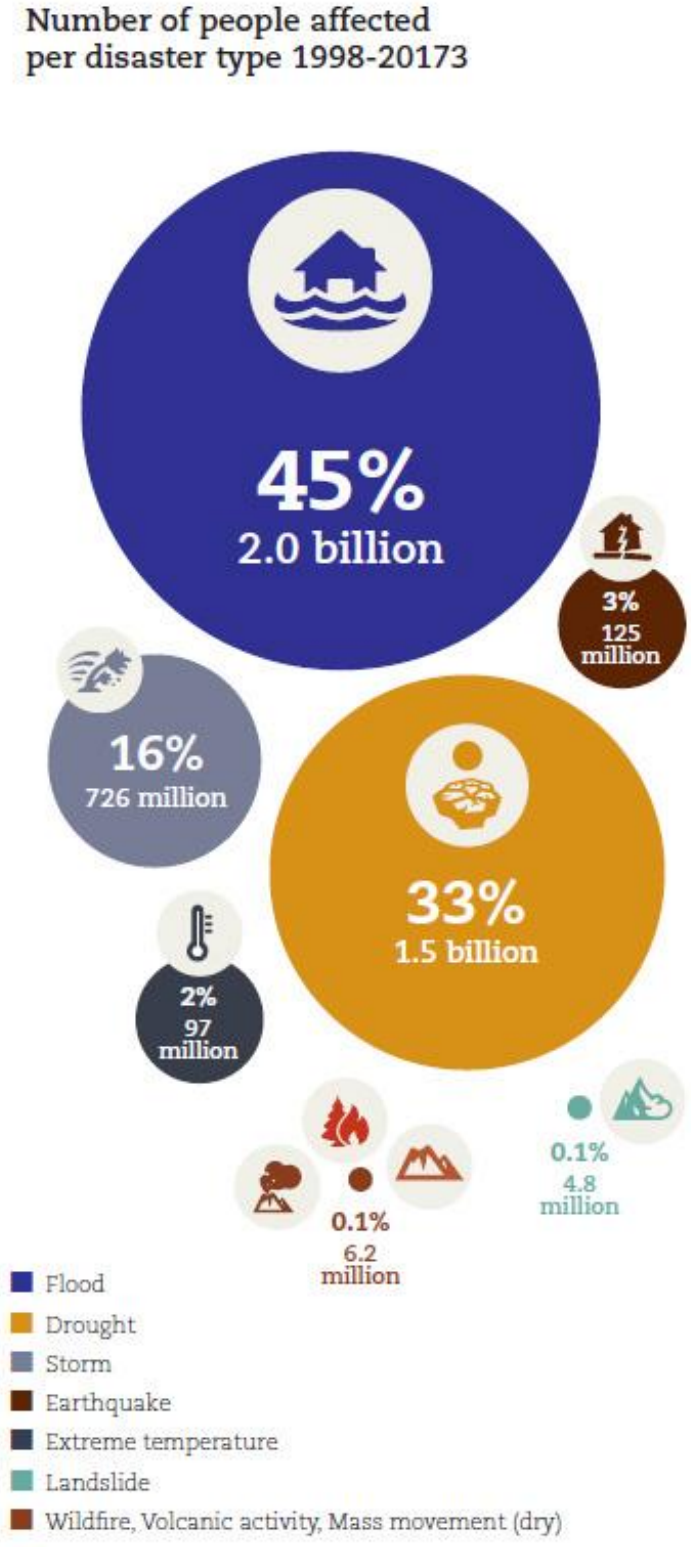

Figure 2: Total number of people that have been affected by each disaster type during the period from 1998 to 2017 (CRED and UNISDR 2018).

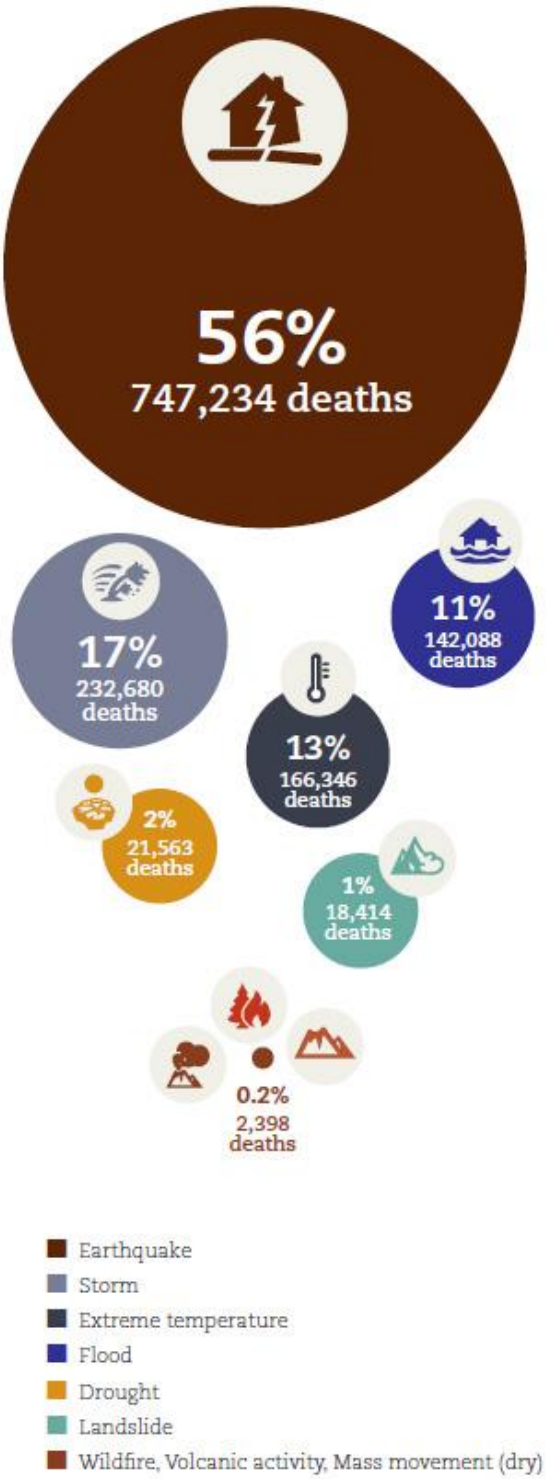

Figure 3: Total number of recorded deaths corresponding to each disaster type during the period from 1998 to 2017 (CRED and UNISDR 2018).

2.3 The stages that lead to effective risk management

Regarding risk management, nowadays it is considered to be the key to effective mitigation of damage that is caused by natural disasters such as floods, landslides, tsunamis, storms and drought. However, since the terms of ***hazard*** and ***risk*** are both involved when somebody refers to risk management, it is important to initially quote their definition in order to avoid confusion in their usage. Therefore, ***hazard*** is the probability of a damaging event and, expressed as such, has the implicit element of prediction and a requirement for exceedence of a notional damage threshold (Crozier and Glade 2010). On the other hand, ***risk*** is defined as the probability of harmful consequences, or expected losses (deaths, injuries, property, livelihoods, economic activity disrupted or environment damaged) resulting from interactions between natural or human-induced hazards and vulnerable conditions (UN-ISDR 2004).

According to Crozier and Glade (2010), there is a certain order of stages that must be followed and completed in order to reach the goal of successful risk management. The first stage involves risk analysis (Figure 4), which is the most complicated stage, because it involves a lot of sub-stages and steps that need to be fulfilled for its finalization. Initially, this stage requires the accurate identification of the hazard that is being faced. This step involves discerning the type of hazard and its approximate scale. For example, the hazard can be a landslide or a flood, while the scale can range from site specific to regional. The next step in risk analysis is risk estimation and requires the completion of consequence and hazard analysis in order to achieve risk calculation. The component of consequence analysis requires determination of the elements that will be threatened by the hazard, whether these are people, properties, roads or some other type of infrastructure. Likewise, the sub-stage of hazard analysis requires determination of the parameters of the hazard that will be studied and how these are spatially distributed. Usually, this step requires the compilation of thematic maps which depict the areas that will be affected by a hazard and in some cases they might also include the spatial distribution of values for other parameters. In the final step of the stage of risk analysis, the components of consequence and hazard analysis are combined in order to complete the sub-sage of risk calculation. This step utilizes the thematic maps of hazard analysis

along with data layers that usually contain information concerning the elements that are threatened by a hazard, therefore producing thematic maps that contain information for both the parameters of the hazard and the elements at risk.

During the stage of risk assessment (Figure 4), risk evaluation can be achieved by setting levels of tolerance or acceptable risk on the parameters of the hazard that are being studied. This procedure leads to the classification of values for the parameter of the hazard that is being studied according to regulations, priorities or other options. The resulting classification of a parameter can then be conveyed to the thematic maps of the previous stage, thus allowing visualization of the spatial distribution of parameter value ranges that can be perceived as dangerous.

The final stage of risk management (Figure 4) takes into consideration the results or products of the previous stage in order to formulate plans on how to mitigate the threats that will be posed by a hazard. Usually, this planning procedure leads to the implementation of certain measures or policies that could avoid the risk or reduce the likelihood or reduce the consequences of natural disasters.

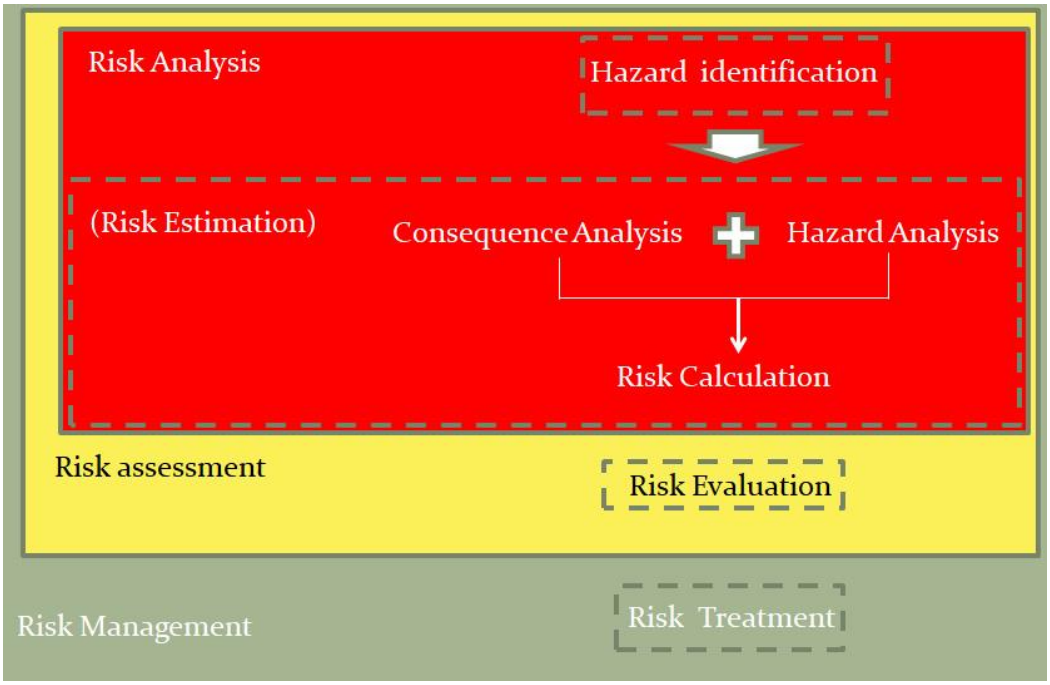

Figure 4: Modified flow chart from Crozier and Glade (2010) showing all the stages involved in risk management.

2.4 Flood hazard analysis or assessment

Bearing in mind the stages of risk management and that Crozier and Glade (2010) consider the terms of hazard assessment and hazard analysis as being the same, flood hazard assessment involves the compilation of maps that depict the spatial distribution of the hydraulic characteristics of floods. Flood extent, flow velocity, shear stress and stream power are a few examples of such characteristics and due to the advances in Remote Sensing (RS) and Geographic Information Systems (GIS) during the last few decades, these parameters can be converted into data layers that can be included in flood hazard assessment maps. Needless to say, nowadays there is a plethora of flood hazard assessment procedures that have been developed in order to enable both researchers and surveyors to conduct effective flood risk management.

The present dissertation thesis has applied flood hazard analysis procedures in the drainage basin of Erythropotamos River in order to compare their results and examine if they can be combined in order to improve their effectiveness regarding flood extent mapping. Specifically, the flood hazard analysis procedures that were employed were: 1) inundation mapping, 2) flood hazard and risk mapping and 3) flood susceptibility mapping.

2.4.1 Inundation mapping literature review

The earliest attempt to employ inundation mapping was by Lowry et al. (1981), who mapped the Manitoba flood that occurred in 1979, using side-looking airborne radar that operated at X- and L-bands (Pulvirenti et al. 2011a). The mapping of floods, especially those of large scale, was one of the objectives of satellite imagery analysis since the advent of the forest satellites during the 1960s. Initially, this effort involved Remote Sensing data from optical sensors such as Landsat – TM5, Landsat – ETM7, ASTER, MODIS and the AVHRR sensor of NOAA. Likewise, Synthetic Aperture Radar (SAR) sensors that were used for the same purpose, sometimes operating on global scale (Prigent et al. 2007), included satellite sensors of: 1) European origin such as ENVISAT, ERS-1 & 2, SENTINEL-1 A/B and the COSMO-SkyMed satellite constellation, 2) Japanese origin such as JERS-1 & 2 and 3) Canadian origin such as Radarsat-1 & 2 (Hess

et al. 1995, Wang et al. 1995, Horritt 1999, 2006, Bates and De Roo 2000, Jodouin et al. 2003, Bates 2004, Gan et al. 2012, Mouratidis and Sarti 2013, Yésou et al. 2013).

From the aforementioned remote sensing sensors, SAR systems proved to be especially effective regarding flood mapping due to the sensitivity of the microwave radiation to water, their synoptic view and also their capability to operate during both day-time and night-time regardless of weather conditions (Pierdicca et al. 2013). Thus, with the improvement of SAR satellite sensors throughout the years, many methodologies emerged that allowed flood detection and mapping. From ERS – 1 SAR imagery that was used to map inundation with the aid of interferometric coherence change detection (Nico et al. 2000) or by utilizing the active contour model (Horritt et al. 2001), to more contemporary approaches that detect floods with the use of probabilistic change detection on ENVISAT imagery (Schlaffer et al. 2017) or by employing multi-temporal statistics and thresholding on SENTINEL - 1 imagery (Cian et al. 2018).

According to Clement et al. (2018), the literature describes many methods that have been used in order to delineate water with the aid of SAR data, either as a singular process or in combination. Such processes involve: 1) region growing (Matgen et al. 2011, Mason et al. 2012, Martinis et al. 2015, Twele et al. 2016, Chapman et al. 2015), 2) fuzzy classification (Martinis et al. 2015, Twele et al. 2016), 3) texture analysis (Pradhan et al. 2014) and 4) histogram thresholding (Brivio et al. 2002, Henry et al. 2006, Brown et al. 2016, Zoka et al. 2018, Tsyganskaya et al. 2018). Dissimilar to the above methodologies, which employ a single SAR image, change detection locates temporal changes via the comparison between an image that was taken during the flood and an image that depicts the same area during dry conditions (Giustarini et al. 2013, Schlaffer et al. 2015, Li et al. 2018, Psomiadis 2016). The detected differences between the images can be further processed with the use of other image segmentation methodologies so as to identify areas that produce unusually low backscatter responses, therefore enhancing the reliability of the flood delineation in contradistinction to the single image methodologies (Matgen et al. 2011).

2.4.2 Flood hazard and risk mapping literature review

Flood hazard mapping involves the construction of data layers that show the spatial distribution of fundamental hydraulic information such as flood extent, flood depth and velocity with the aid of hydraulic models. Hydraulic models (also termed hydrodynamic models or flood models) are computerized algorithms that simulate and predict a simplification of the dynamic process of water flow based on the shallow water equations (Schumann et al. 2015).

The latter attempt to simulate the flooding process by not only routing the flood wave over time through a large number of cross-sections that are usually obtained by ground surveying, but also by reproducing the propagation of water throughout the floodplain with the use of specific flow equations. The solution, by utilizing both implicit or explicit schemes, of St Venant equations of continuity and momentum may be discretized in space and time over 1D cross-sectional data, regular 2D grids or irregular 2D and 3D mesh structures. There are various ways not only to solve the aforementioned equations, but also to simplify them in order to speed up the calculation processes without sacrificing accuracy or proper physics that govern the various types of flows (Bates et al., 2010). It is beyond doubt that external forces such as surface friction or roughness, which are usually expressed by Manning's n coefficient, apply resistance to flow thus affecting the propagation of water. It also should be emphasized that there are uncertainties regarding the incorporation of the effect of external forces on flow, the calculation of discharge and the precision of topographic and bathymetric data. However, these do not subtract from how invaluable hydraulic models are in effective flood risk management, in forecasting or reanalysis of flood events and in the compilation of flood risk maps for specific flow return periods. (Schumann et al. 2015)

At the present time, there are numerous 1D, hybrid 1D-2D, or 2D hydraulic models that are used in predicting and simulating floodplain flow and river dynamics, flood depth, inundated area and flow velocity. Regarding 1D models, such as HEC-RAS (Hydrologic Engineering Center – River Analysis System) (Appendix F), ther main characteristics are: 1) simplification of the floodplain inundation process with the use of storage cell approaches or a DEM fill process and 2) the solution of in-channel flow

physics only at river cross-sections. Concerning hybrid 1D-2D models, they reproduce the 2D flow processes that is operating in the floodplain, while, on the other hand, the 2D models are able to simulate the flow processes in 2D everywhere by combining a floodplain DEM with 2D channel bathymetric data. All hydraulic models depend their performance heavily on the accuracy of the floodplain and channel topography, because they are used as inputs. This is of outmost significance when hydraulic modeling is carried out at large scales and in regions that lack high quality and high resolution LiDAR (Light Detection and Ranging) elevation data. A DEM is essential for the simulation of the flow process by hydraulic models. Moreover, apart from elevation data, hydraulic models, in order to operate properly, require additional input such as flow data and the setting of upstream or downstream boundary conditions. (Schumann et al. 2015)

The idea of integrating hydraulic modeling with Remote Sensing imagery was introduced by Bates et al. (1997) and although this work is now more than 20 years old, this concept is still quite unexplored. In a recent approach, Giustarini et al. (2015a) carried out flood hazard mapping by combining multi-annual Remote Sensing data and hydrodynamic modelling in a part of Severn River's (UK) drainage basin. The aforementioned process combined the results that were produced by a large number of ENVISAT/ASAR imagery, along with a global inundation model that was compiled by the European Centre for Medium-range Weather Forecasts. Moreover, Hardesty et al. (2018) currently introduced the concept of using atmospheric reanalysis driven hydrologic and hydraulic simulations to produce long-term flow data based flood frequency analysis, in order to examine the impact of dam operation at a site of interest in the Naugatuck River under varying flood return periods.

Apart from combining hydraulic modeling with Remote Sensing imagery, the literature in the field of hydraulic modelling also involves: 1) comparisons between 1D and 2D hydraulic models (Colby et al. 2000, Horritt and Bates 2002), 2) improvements on the performance of hydraulic models (Pappenberger et al. 2007, Cook and Merwade 2009) and 3) applications of hydraulic models (Baky et al. 2012, Khalfallah and Saidi 2018). Furthermore, it is worth noting that the vast majority of the study areas that were

chosen for the application of hydraulic modelling involved river reaches rather than drainage basins.

2.4.3 Flood susceptibility mapping literature review

The procedure of flood susceptibility mapping involves the assignment of weights upon certain data layers, which represent factors that affect flood occurrence. These layers are then processed with the aid of GIS softwares in order to produce a map which indicates the spatial distribution of flood-prone areas and thus potential flood extent. Concerning flood susceptibility, according to the current literature, there are three main approaches that are used for its assessment. Hong et al. (2018) state in their research that these are: 1) non-linear machine learning algorithms such as random forest (Wang et al. 2015), support vector machine (SVM) (Tehrany et al. 2015a), artificial neural network (ANN) (Kia et al. 2012), k-nearest neighbour (KNN) (Liu et al. 2016) and decision tree (DT) (Tehrany et al. 2013), 2) hydrological models such as Wet Spa (Bahremand et al. 2007), SWAT (Oeurng et al. 2011) and HYDROTEL (Aissia et al. 2012) and 3) statistical and data-driven approaches such as fuzzy logic (FL) (Pulvirenti et al. 2011b), frequency ratio (FR) (Tehrany et al. 2015b), weights-of-evidence (WOE) (Tehrany et al. 2014), the analytical hierarchy process (AHP) (Stefanidis and Stathis 2013, Kazakis et al. 2015) and logistic regression (LR) (Ettinger et al. 2016, Nandi et al. 2016). All these methods have been used successfully in flood susceptibility assessments, but they also suffer from restrictions (Ward et al. 2015). However, among them, AHP is considered as the most widely used, mainly because its implementation becomes simple, with the aid of GIS computer softwares. Additionally, this methodology has proved many times that it can handle sparse or poor quality data and that it can operate efficiently in regional studies (Dewan et al. 2007, Chen et al. 2010, 2013, 2015, Wang et al. 2011).

Furthermore, the compilation of the susceptibility map depends heavily on the selection of criteria. The existing literature on flood susceptibility mapping reveals that a plethora of criteria has been used (Kazakis et al. 2015, Hong et al. 2018, Lyu et al 2018, Seejata et al. 2018, Tang et al. 2018, Xiao et al. 2018, Zhao et al. 2018). Their main characteristics being that they should be correlated with the physical process of the flood

generation mechanism, they can be quickly calculated or measured for the whole study area and that they ought to be easily interpreted (Papaioannou et al., 2015).

2.5 Description of the study area

2.5.1 Location of the study area

The study area involves the drainage basin of Erythropotamos River. The latter is a tributary of Evros River, which is the longest river that runs solely in the interior of the Balkans. Erythropotamos' watershed covers an extent of 1,618.5 km^2 and its largest part belongs to the geographic region of Thrace in Northern Greece, while the rest of its drainage basin belongs to Bulgaria (Figure 5).

Regarding administrative distribution within national borders, the Greek part of Erythropotamos' river basin belongs to the Prefectures of Evros and Rhodopi.

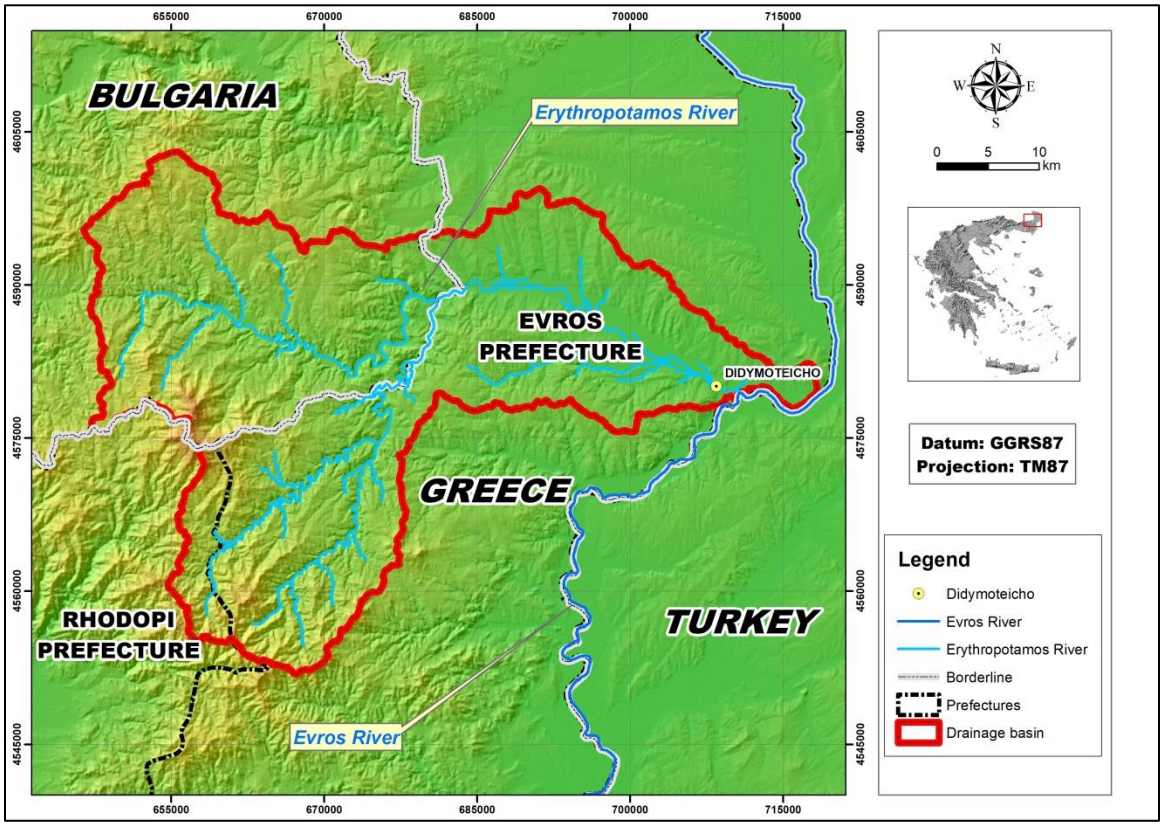

Figure 5: Location of the study area (drainage basin of Erythropotamos).

2.5.2 Geology of the study area

The drainage basin of Erythropotamos River belongs to both the Circum – Rhodope geotectonic zone and the Rhodope massif. According to the geologic maps of Bulgaria (CoG 1989) and Rhodope – Thrace (I.G.M.E. 2002), the geological formations that occur in the study area are the following (Figure 6):

Holocene

Holocene sediments and terraces (al)

Pleistocene

Pleistocene sediments and terraces (dl)

Oligocene

Granite (γρ)

Sandstone-marl clay phase (Ol.s,m,tf): The formation consists of sandstones, marls, clays and pyroclastics.

Rhyolites-Rhyodacites-Pyroclastics (ρ)

Monzonitic Diorite (μδ)

Eocene

Clay limestones (Ek2)

Volcano-sedimentary series (E.tf-m,c): It contains conglomerates, marls, clay limestones and pyroclasticss.

Mesozoic

Sandstones and conglomerates (K2): Sandstone-conglomerate formation with diorite bodies in SE Rhodopes.

Greenschists (Sch1)

Mafic rocks (O2): The formation contains gabbros, gabbrodiorite, diabase and pillow lavas.

Sandstones and siltstones (J3-K1)

Rhodope Massif

Pegmatites, marbles and amphibolites (πγ-αμγν-μγ): It consists of pegmatites, marbles, amphibolites, gneisses and migmatites.

Augen gneiss (γν2): It involves augen gneisses and orthogneisses.

Orthogneiss (γνμ): The formation contains hypermylonitized, leucocratic orthogneisses.

Ophiolites (O1): The ophiolite series consists of meta-peridotites, meta-harzburgites, meta-dunites, meta-pyroxenites, meta-gabbros, meta-pegmatites and serpentinites that are related tectonically with the rocks that surround them.

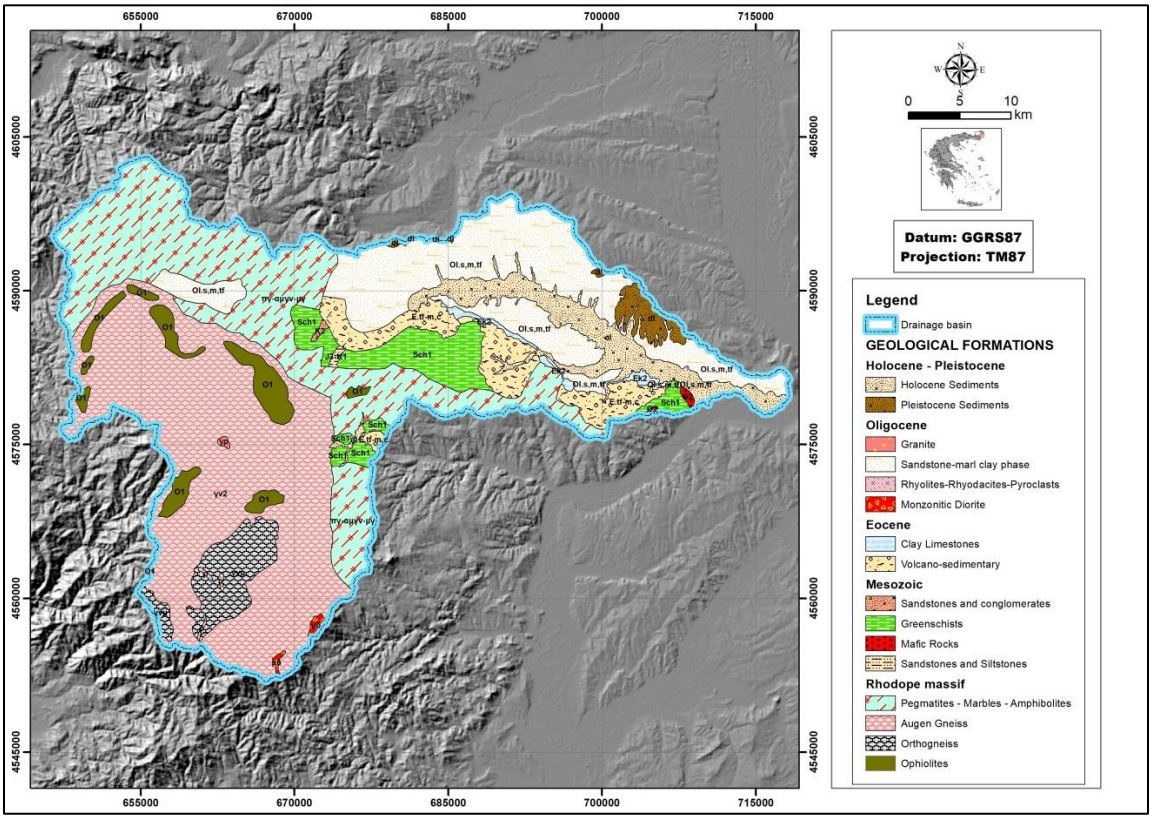

Figure 6: Spatial distribution of the geological formations within the drainage basin of Erythropotamos River (CoG 1989, I.G.M.E. 2002).

The geological formation that covers the largest part of the study area is augen gneisses (31.59%), followed by a formation that is comprised of pegmatites, marbles and amphibolites (24.13%) (Table 1). Furthermore, the former formation occupies most of the W and SW part of the study area, while the latter formation occurs mostly on the NW part of the watershed.

Table 1: Distribution of the geological formations within the drainage basin of Erythropotamos River.

Geological Formation	Area (km^2)	Percent (%)
Clay Limestone	9.40	0.58
Mafic Rocks	2.00	0.12
Granite	1.00	0.06
Volcano-sedimentary	89.20	5.51
Greenschists	88.70	5.48
Orthogneiss	62.50	3.86
Monzonitic Diorite	3.30	0.20
Holocene Sediments	96.00	5.93
Augen Gneiss	511.30	31.59
Ophiolites	54.80	3.39
Pegmatites - Marbles - Amphibolites	390.60	24.13
Pleistocene Sediments	24.70	1.53
Rhyolites - Rhyodacites - Pyroclasts	1.70	0.11
Sandstones & Siltstones	1.70	0.11
Sandstones & Conglomerates	1.30	0.08
Sandstone-marl clay phase	280.30	17.32
Total	1,618.50	100

2.5.3 Geomorphology of the study area

Information for the relief of the study area was provided by EU-DEM, which is the Digital Surface Model (DSM) of European Environment Agency (EEA) member and cooperating countries that represents the first surface as illuminated by the sensors. The aforementioned DSM is a hybrid product based on SRTM and ASTER GDEM data fused by a weighted averaging approach (E.E.A. 2017). Moreover, its horizontal spatial resolution is 1 arc second (approximately 25 m), while its absolute and relative vertical accuracy are 3.6 m and 5.3 m, respectively (Mouratidis and Ampatzidis 2019).

Therefore, elevation in the drainage basin of Erythropotamos River ranges from 16m to about 1,258m above mean sea level (M.S.L.), while the length of the thalweg (maximum watercourse) is 104.17km and mean elevation is 328.22m, which can be further ascertained by the hypsographic curve (Figure 7). Furthermore, approximately 60% of the study area can be described as hilly according to Dikau's classification (Dikau 1989) (Figure 8 and Table 2). Additionally, the spatial distribution of slope angle values within the study area, indicates that most of its terrain belongs to the strongly inclined category (5° – 15°) according to Demek's classification of slope angles (Demek 1972) (Figure 9 and Table 3).

Table 2: Distribution of elevation into categories according to Dikau's classification (Dikau 1989).

Elevation	Description	Area (km^2)	Percent (%)
<150	Lowland	429.60	26.54
150-600	Hilly	969.10	59.88
600-900	Semi-mountainous	197.30	12.19
900>	Mountainous	22.50	1.39
Total		1,618.50	100

Table 3: Slope angle categorization within the study area according to Demek's classification (Demek 1972).

Slope Angle (°)	Description	Area (km^2)	Percent (%)
0 - 2	Plain to slightly sloping	147.50	9.11
2 - 5	Gently inclined	390.30	24.11
5 - 15	Strongly inclined	864.90	53.44
15 - 35	Steep	215.70	13.33
>35	Precipitous	0.10	0.01
Total		1,618.50	100

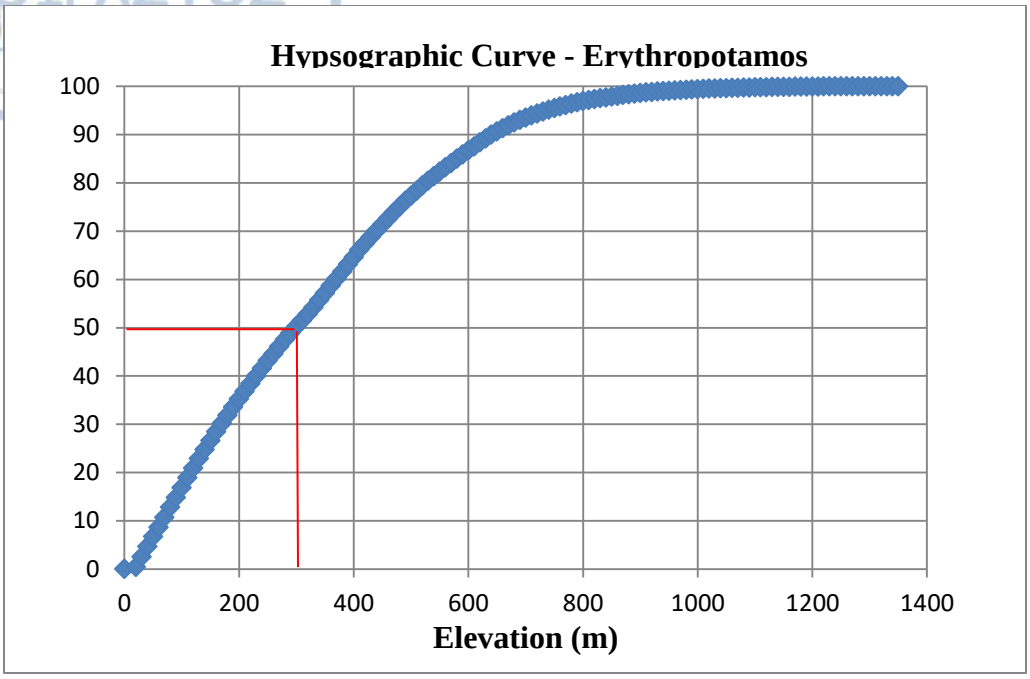

Figure 7: The hypsographic curve of Erythropotamos' drainage basin.

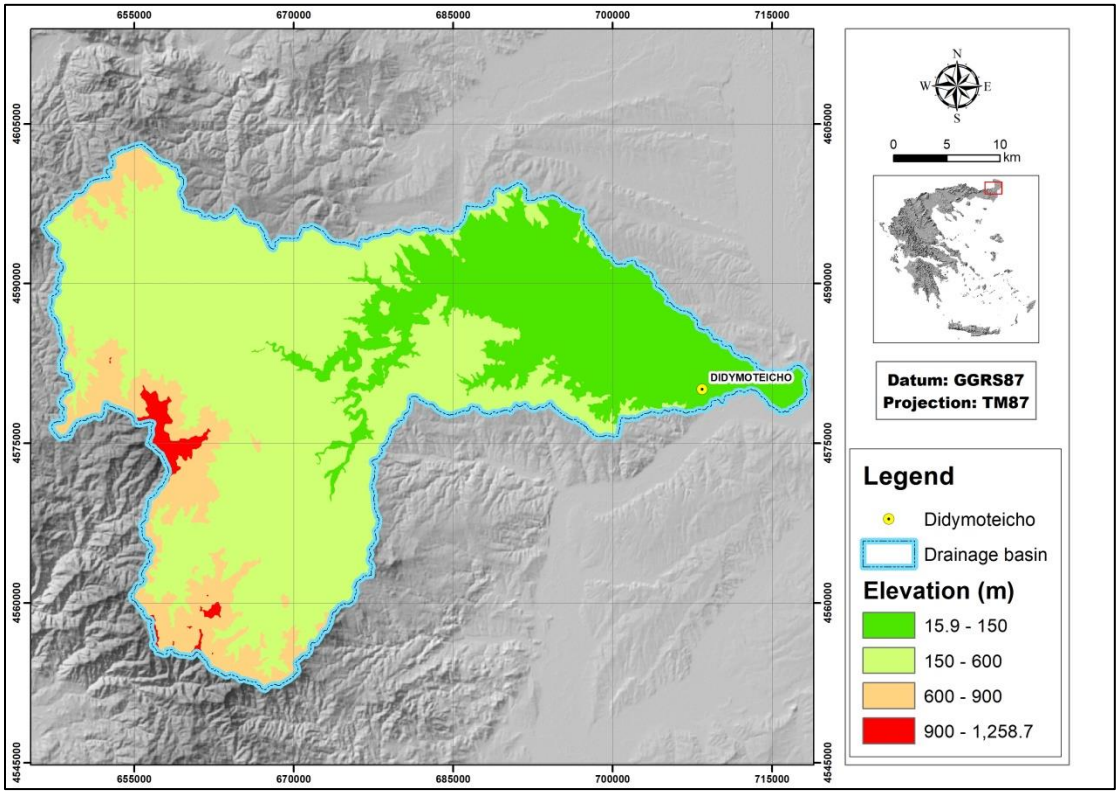

Figure 8: Spatial distribution of elevation within the catchment of Erythropotamos river (E.E.A. 2017)

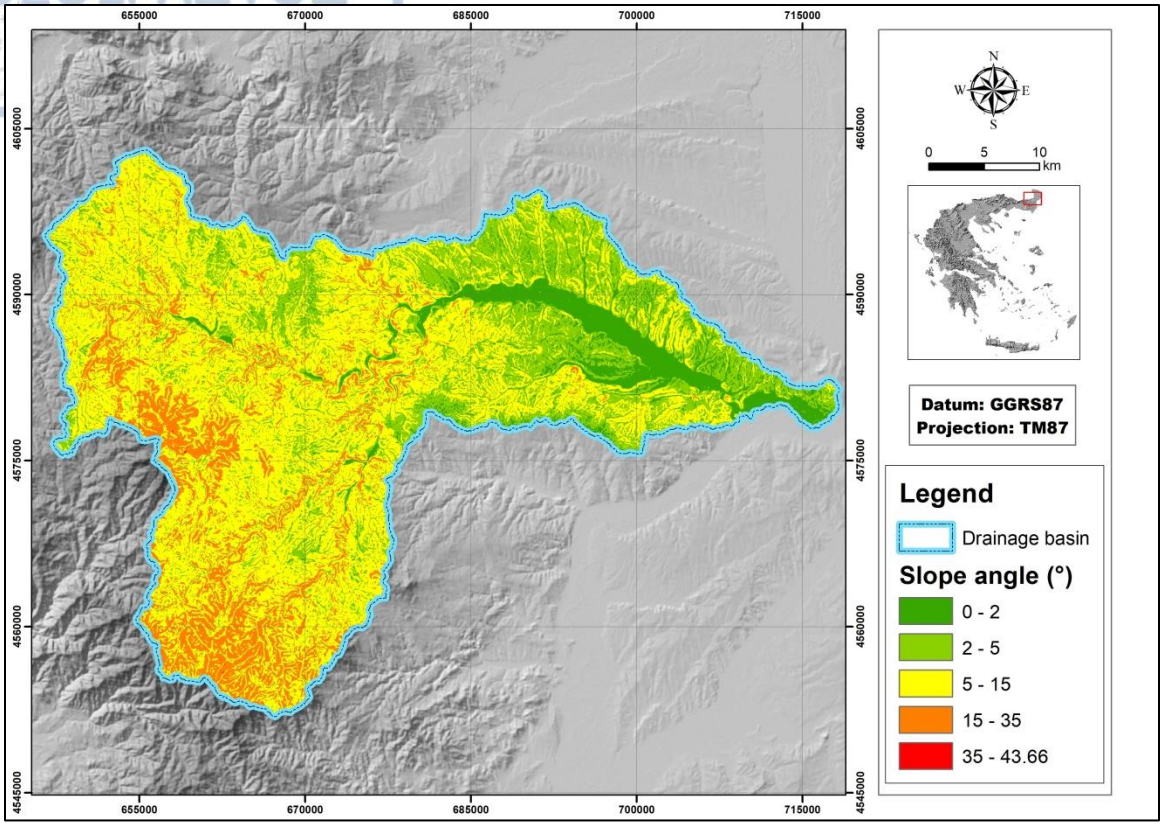

Figure 9: Spatial distribution of slope angle values within the drainage basin of Erythropotamos River.

The drainage network of Erythropotamos' river basin was produced with the aid of EU-DEM, the DEM of National Cadastre and Mapping Agency S.A. (NCMA) with a 5m spatial resolution and the topographic maps of the Hellenic Military Geographical Service (H.M.G.S.) at a 1:50,000 scale. Regarding the topographic maps, the sheets of Aisymi, Khardhamos, Sapai, Mega Dherion, Souflion, Ormenion, Rizia, Didymoteichon, Vyrsini, Metaxades, Pythion and Orestias (H.M.G.S. 1970a, 1970b, 1970c, 1970d, 1970e, 1970f, 1970g, 1970h, 1970i, 1970j, 1969a, 1969b) were used for that purpose.

Regarding the drainage pattern of the study area's drainage network, it can be described as dendritic. Furthermore, according to Strahler's stream ordering (Strahler 1952, 1957), the drainage basin of Erythropotamos is of the seventh order. (Figure 10)

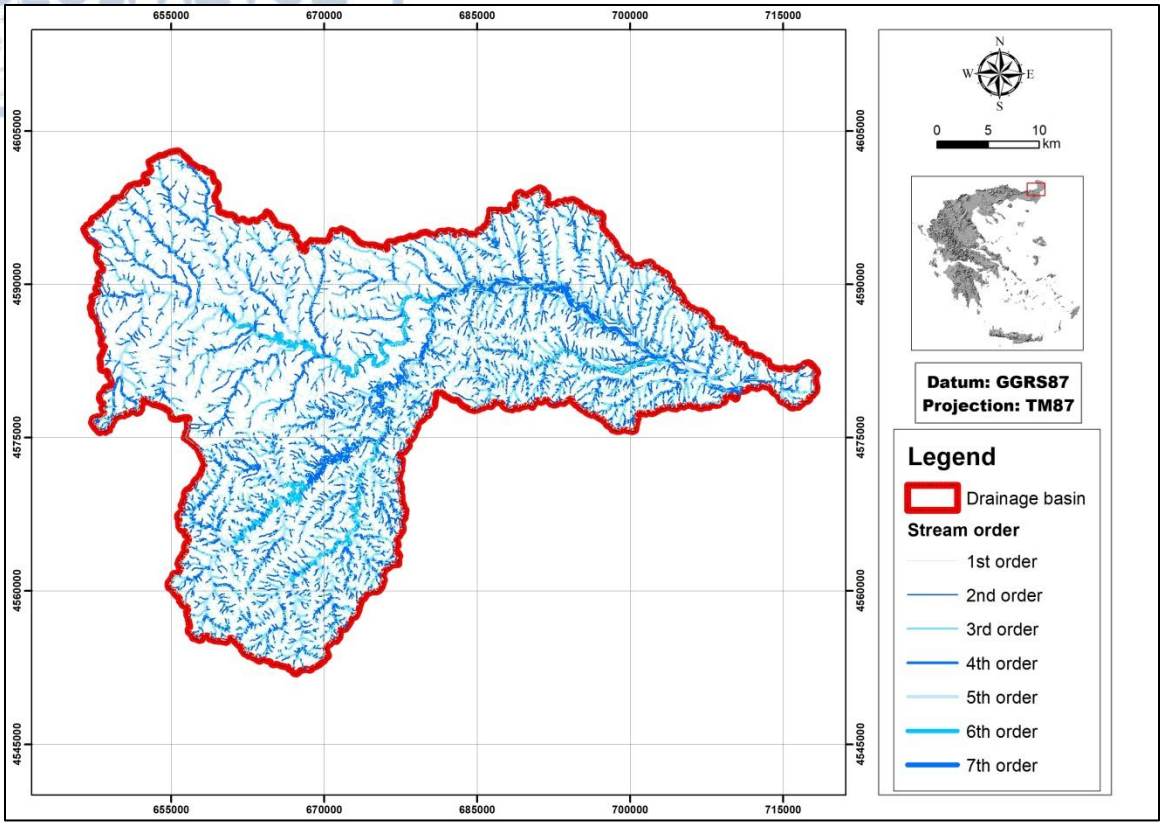

Figure 10: The drainage network of Erythropotamos River.

2.5.4 Quantitative geomorphological analysis of the study area

2.5.4.1 Bifurcation ratio (Rb)

The bifurcation ratio (Rb), as described in equation (1), is the ratio of the number of the stream segments of any order N_u divided by the number of streams of the next higher order $N_{(u+1)}$ (Schumm 1956).

$$Rb = \frac{N_u}{N_{(u+1)}} \quad (1)$$

It is a dimensionless number with values ranging usually from 3 to 5, which indicate drainage networks that have evolved naturally. According to Das (2016), low bifurcation

ratio values indicate high chances of flooding. The mean bifurcation ratio for the drainage basin of Erythropotamos River is 4.97 (Table 4).

Table 4: Bifurcation ratio values for the drainage basin of Erythropotamos River.

Stream Order (u)	Number of Streams (N_u)	Rb
1	13,524	4.61
2	2931	4.76
3	616	4.81
4	128	3.66
5	35	5
6	7	7
7	1	
Total	17,242	Mean (Rb): 4.97

2.5.4.2 Length, Mean Length and Length Ratio of Streams

The total length (L_u) and the mean stream length of the streams of a certain order u ($L_{(u)m}$), along with the stream length ratio (R_L), were calculated for the study area with the aid of ArcGIS™. The mean stream length ($L_{(u)m}$) was obtained by dividing the total length of the streams that belong to a certain order u (L_u) by the total number of stream segments that belong to the same order u (L_u). Regarding the stream length ratio (R_L), according to Horton (1945), as shown in equation (2), it can be obtained by dividing the cumulative mean length of a certain stream order ($\Sigma L_{(u)m}$) by the cumulative mean length of the previous stream order u-1 ($\Sigma L_{(u-1)m}$).

$$R_L = \frac{\Sigma L_{(u)m}}{\Sigma L_{(u-1)m}} \quad (2)$$

Furthermore, the mean stream lengths of stream segments of each of the successive orders of a watershed tend to approximate a direct geometric sequence in which the first term (stream length) is the average length of segments of the first order (Horton 1945). Table 5 shows the values of the aforementioned morphometric parameters for the drainage basin of Erythropotamos River.

Table 5: Results of the calculation of the morphometric parameters of stream length, mean stream length and stream length ratio for the drainage basin of Erythropotamos River.

Stream Order (u)	Stream Length (L_u)	Number of Streams (N_u)	Mean Stream Length ($L_{(u)m}$)	Cumulative Mean Stream Length ($\Sigma L_{(u)m}$)	RL
1	3,692.51	13,524	0.27	0.27	
2	1,833.36	2,931	0.63	0.90	3.29
3	859.32	616	1.40	2.29	2.55
4	496.46	128	3.88	6.17	2.69
5	256.44	35	7.33	13.50	2.19
6	129.35	7	18.48	31.98	2.37
7	84.01	1	84.01	115.99	3.63
Total	7,351.45	17,242	-	-	-

2.5.4.3 Stream frequency and drainage density

The term stream frequency (Fs) was introduced by Horton (1932). According to mathematic formula (3), stream frequency is the ratio of the total number of streams (ΣN_u) in a drainage basin to the area of the same basin (A).

$$Fs = \frac{\Sigma N_u}{A} \quad (3)$$

This morphometric parameter is measured in km^{-2} and for the drainage basin of Erythropotamos River its value is 10.65 km^{-2}, which indicates high stream frequency.

On the other hand, drainage density (Dd) is the stream length per unit area in the region of the watershed (Horton 1945, Strahler 1952, Melton, 1958). According to equation (4), stream frequency is the ratio of the total length of streams (ΣL_u) in a drainage basin to the area of the same basin (A).

$$Dd = \frac{\Sigma L_u}{A} \quad (4)$$

This morphometric parameter is measured in km^{-1} and for the drainage basin of Erythropotamos River its value equals 4.54 km^{-1}, which indicates low drainage density.

2.5.4.4 Hypsometric curve and hypsometric integral

The hypsometric curve describes the distribution of elevations within an area of land, covering an extent that ranges from one catchment to the whole of the planet. The resulting plot involves the proportion of total basin height (h/H = relative height) against the proportion of total basin area (a/A = relative area). The parameter of total height (H) stands for the relief that lies within the basin (the maximum elevation minus the minimum elevation), while, on the other hand, the parameter of the total surface area of the basin (A) involves the sum of the areas between each pair of adjacent contour lines. Moreover, area (a) is the surface area lying within the basin above a given contour of elevation (h). The value of relative area always ranges from 1 at the lowest point within the basin to 0 at the highest point in the basin. (Keller and Pinter 2002)

Concerning any drainage basin, the hypsometric integral (H_i) can be used in order to characterize the shape of the hypsometric curve, which is the area under the hypsometric curve. The hypsometric integral can be calculated according to equation (5) (Pike and Wilson 1971, Mayer 1990).

$$H_i = \frac{mean\ elevation - minimum\ elevation}{maximum\ elevation - minimum\ elevation} \quad (5)$$

High values of H_i show that the greatest part of the topography of a certain area is high in comparison with the mean value of elevation of the same area. For example, a flat upland surface that is interrupted by deeply incised streams. Additionally, intermediate to low values of H_i can be related with more evenly dissected drainage basins (Keller and Pinter 2002).

Moreover, the stage of a landscape in the Cycle of Erosion can be determined with the aid of the relationship between the degree of dissection and the hypsometric integral. Consequently, high H_i values are indicative of youthful topography. Furthermore,

intermediate H_i values combined with a sigmoidal-shaped hypsometric curve show a mature stage of development. (Keller and Pinter 2002)

Regarding the catchment of Erythropotamos River, the value of the hypsometric integral, which equals to 0.25, along with the shape of the hypsometric curve, as shown on Figure 11, were both produced with the aid of EU-DEM. These morphometric indices indicate that the drainage basin of the study area belongs to the "old age" stage of the Erosion Cycle. This result is further maintained by the fact that, as shown in Figure 8, the landscape of the study area is near base level with very subdued relief.

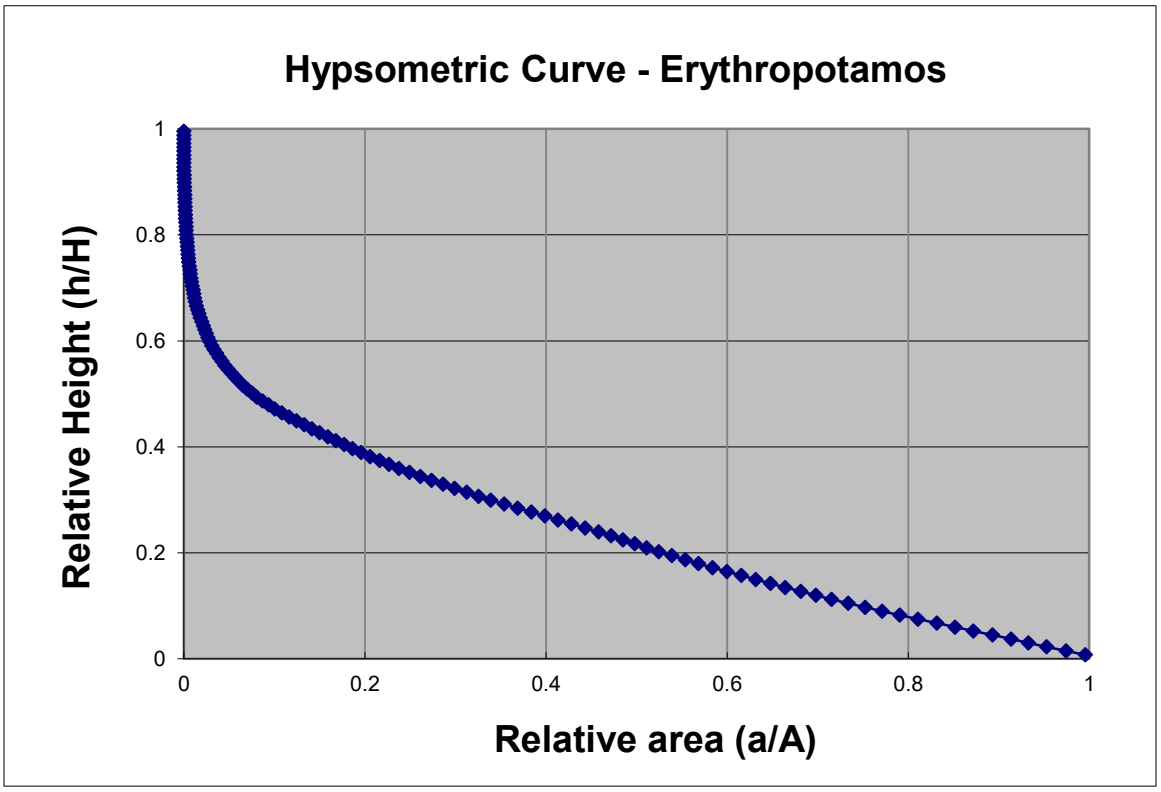

Figure 11: The Hypsometric curve of Erythropotamos' drainage basin.

2.5.5 Spatial distribution of land cover in the study area

Based on the data layer of Corine Land Cover 2012 (Copernicus 2017), the catchment of Erythropotamos River is dominated by forests and semi natural areas (Figure 12). They cover more than 60% of the study area, occupying the NW, W and SW parts of the

drainage basin. Agricultural areas occupy mostly the NE part of the watershed, covering more than 35% of the study area (Table 6).

Table 6: Distribution of Land Cover within the river basin of Erythropotamos according to Corine Land Cover 2012.

Land Cover	Area (km^2)	Percent (%)
Artificial surfaces	18.40	1.14
Agricultural areas	586.20	36.22
Forest and semi natural areas	1007.90	62.27
Wetlands	0.10	0.01
Water bodies	5.90	0.37
Total	1,618.50	100

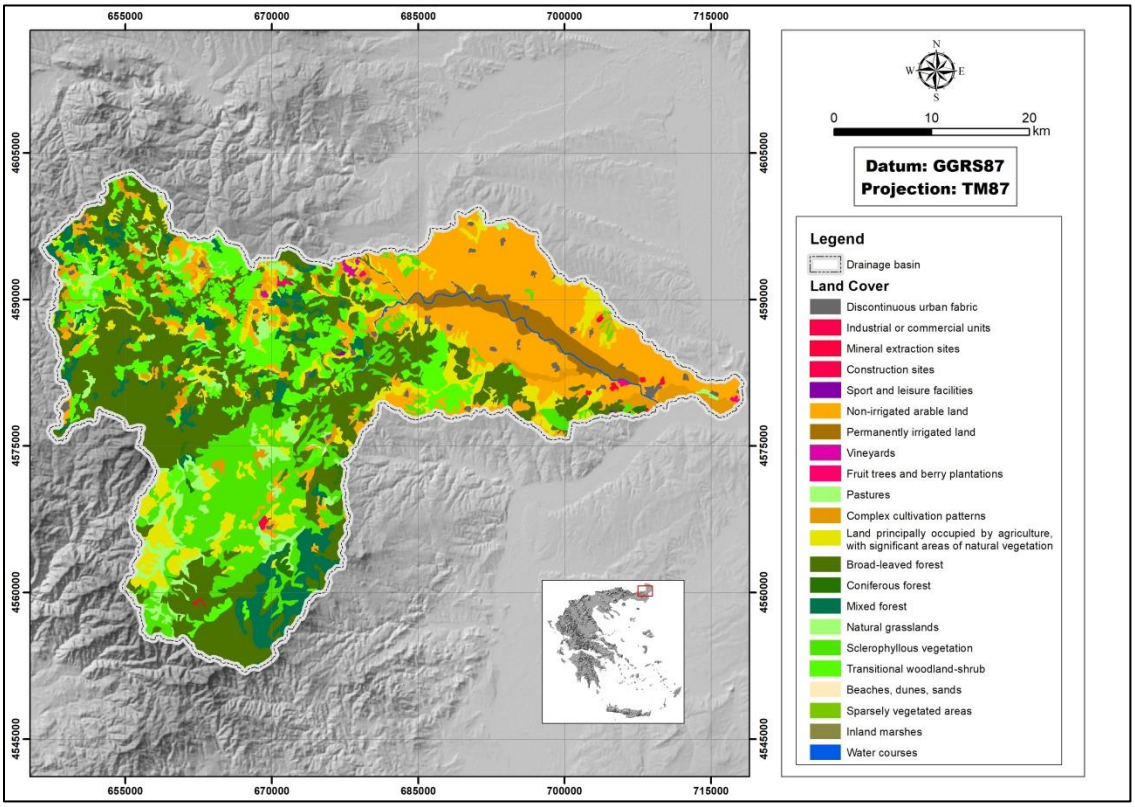

Figure 12: Spatial distribution of land cover in the catchment of Erythropotamos river (Copernicus 2017).

2.5.6 Protected areas

The drainage basin of Erythropotamos River intersects with the boundaries of Special Protection Areas (SPA) that belong to the Natura 2000 network. Namely these are Filiouri Valley (GR1130011) and Oreinos Evros – Dereio Valley (GR1110010) (Figure 13). Specifically, Erythropotamos' catchment intersects with only the eastern part the former and includes the major part of the later.

Regarding Filiouri Valley, the site consists of the Filiouri River watershed and the south-east part of Mount Rodopi, along with the wildlife refuge named Poas – Dichalas Dimou Sosti. Grazed oak forest and scrub comprise the majority of the vegetation cover, while land-use is non-intensive and traditional. Moreover, this site is also important because it is used for passage and breeding by raptors and species that inhabit areas of scrub and forest. Significant species include: *Aquila chrysaetos, Aquila heliacal, Aegypius monachus, Neophron percnopterus, Circaetus gallicus, Gyps fulvus, Emberiza hortulana, Dendrocopos medius, Falco naumanni, Lanius collurio, Ficedula semitorquata, Dendrocopos syriacus*. (Filotis, 2019)

The protected area Oreinos Evros – Dereio Valley lies at the western part of Evros prefecture, and includes the wildlife refuges named Kallithea - Treis Vryses (Government Gazette No 712B of 19 August 1997) and Poulia (Government Gazette No 343B of 20 June 1987). Beech forests with small clumps of pine trees and oak comprises the majority of the vegetation cover of the aforementioned protected area. Furthermore, the site includes partly forested areas, comprised mostly of dispersed mature oak trees, which are used for traditional non-intensive livestock grazing. Additionally, Diavolorema River is crossing the protected area, thus creating sites of riparian vegetation and small rocky gorges. (Filotis, 2019)

It is also worth mentioning that Oreinos Evros – Dereio Valley is significant because it is mainly used by breeding raptors, species that inhabit in mountainous wooded areas and as feeding ground for the Black Vulture population that breeds at Dadia forest. Significant species include: *Aegypius monachus, Aquila pomarina, Hieraaetus pennatus, Ciconia nigra, Circaetus gallicus, Neophron percnopterus and Aquila chrysaetos.*

Finally, the site is important for rare breeding passerines such as *Sylvia nisoria* and *Ficedula semitorquata*. (Filotis, 2019)

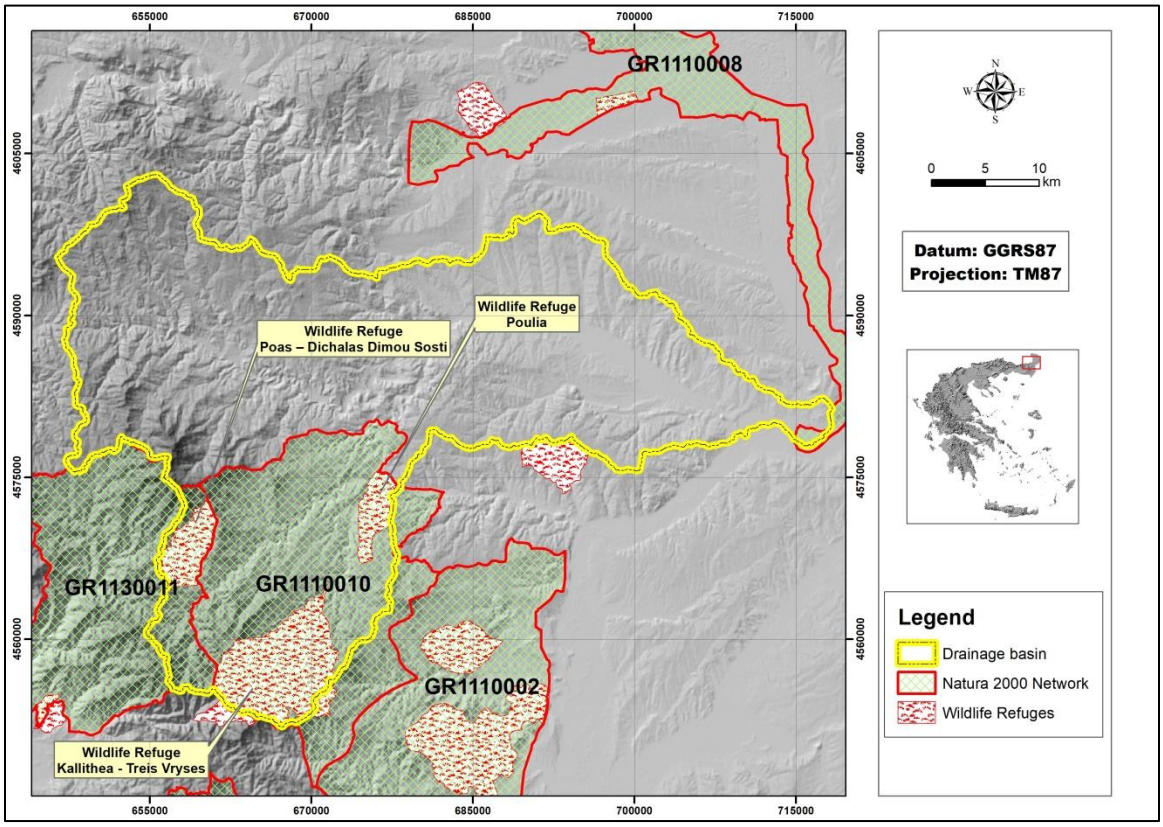

Figure 13: Thematic map showing the sites of Special Protection Areas (SPA) that belong to the Natura 2000 Network and wildlife refuges, which are located within the study area.

2.5.7 Climatic and bioclimatic characteristics of the study area

Measurements, dating from 2008 to 2010, of the gauging station (Appendix A) on Didymoteicho's bridge (Longtitude: 708,600, Latitude: 4,580,000 and at an elevation of approximately 32.09m), which was installed by the Department of Civil Protection of the region of Evros, were used in order to determine the climatic and bioclimatic characteristics of the drainage basin of Erythropotamos River.

Furthermore, according to the Bioclimatic Map of the Greek Ministry of Agriculture (1978), the study area can be categorized as belonging to the attenuated Sub-Mediterranean category (Figure 14).

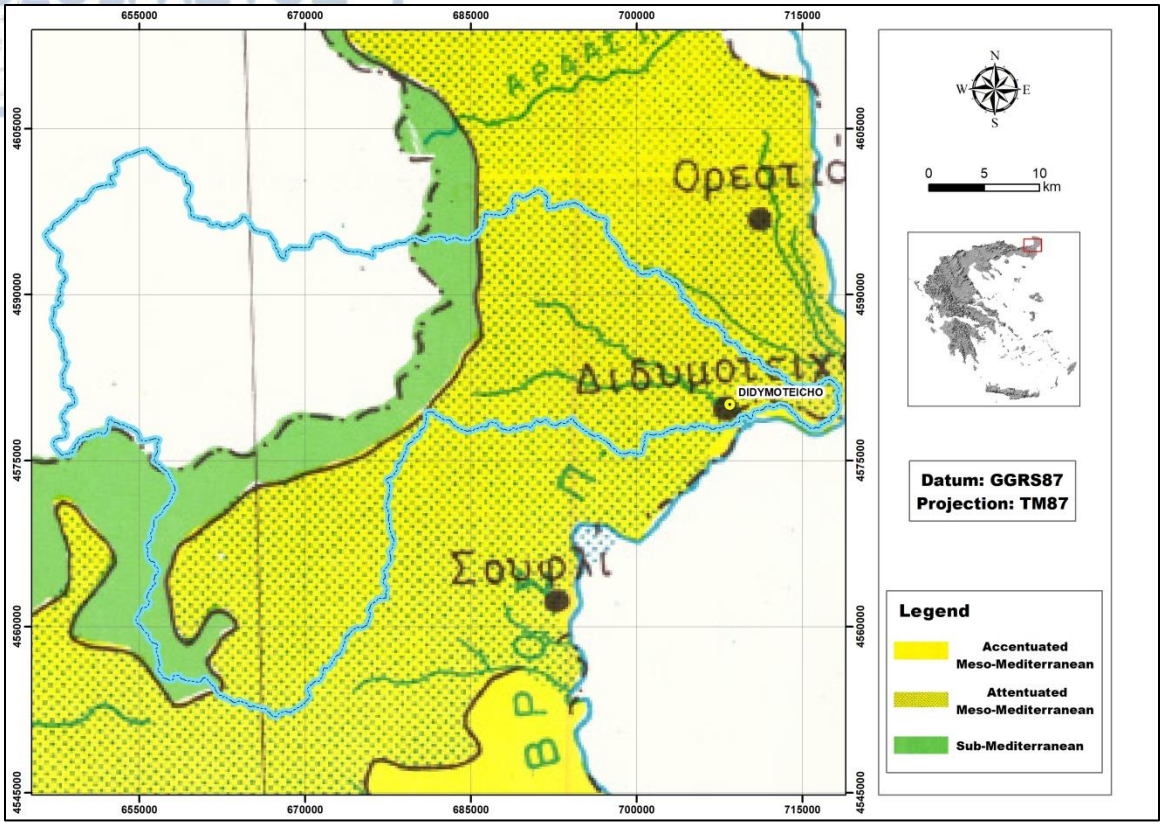

Figure 14: Superimposition of the Erythropotamos' drainage basin upon the Bioclimatic Map of the Greek Ministry of Agriculture. (Adapted from the Bioclimatic Map of the Greek Ministry of Agriculture that was compiled in 1978)

2.5.7.1 Temperature

According to measurements from the gauging station on Didymoteicho's bridge, the mean annual temperature of the study area is equal to 13.81 °C. The hottest month is August with a mean temperature of 24.76 °C, while January is the coldest month with a mean temperature of 2.23 °C (Table 7).

2.5.7.2 Rainfall

Gauges from the station that is located on Didymoteicho's bridge indicate that, with a monthly mean total rainfall of 123.5 mm, February is considered as the rainiest month. On the other hand, the least rainy month is August with a monthly mean total rainfall of 22 mm (Table 8).

Table 7: Temperature characteristics according to measurements from the gauging station on Didymoteicho's bridge.

Month	Mean Temperature (°C)	Mean Maximum Temperature (°C)	Mean Minimum Temperature (°C)
January	2.23	5.57	-0.90
February	5.40	9.24	2.02
March	7.14	11.56	3.06
April	12.03	18.13	6.54
May	19.74	24.69	11.50
June	22.01	29.02	15.14
July	23.67	30.46	16.80
August	24.76	32.28	17.62
September	18.50	24.82	12.77
October	14.22	19.96	9.42
November	9.25	14.48	4.83
December	6.74	10.29	3.54
Average value	**13.81**	**19.21**	**8.53**

Table 8: Monthly mean total rainfall according to measurements from the gauging station on Didymoteicho's bridge.

Month	Mean total rainfall (mm)	Maximum total rainfall (mm)	Minimum total rainfall (mm)
January	81.00	89	75
February	123.50	187	121
March	86.00	89	84
April	30.50	37	26
May	29.00	35	23
June	27.00	31	20
July	25.00	28	18
August	22.00	24	15
September	65.50	75	54
October	72.00	83	63
November	43.50	50	37
December	82.50	91	72
Annual	**687.50**	**819.00**	**608.00**

2.5.7.3 Wind

Data provided by the station that is located on Didymoteicho's bridge show that the average wind direction is 211.07° (SSW) and average wind speed is 1.92 m/s (Table 9).

Table 9: Wind characteristics according to measurements from the gauging station on Didymoteicho's bridge.

Month	Wind direction (°)	Wind speed (m/s)
January	241.39	2.46
February	216.84	2.38
March	217.78	2.39
April	194.08	1.76
May	189.03	1.54
June	195.53	1.49
July	197.46	1.80
August	189.98	1.80
September	235.04	1.56
October	213.89	1.86
November	212.25	1.72
December	229.56	2.28
Average	**211.07**	**1.92**

2.5.7.4 Climatic and bioclimatic characteristics

Precipitation and temperature are the main climate factors influencing vegetation and the configuration of vegetation zones in a certain region.

Based on Koppen's climate classification, the drainage basin of Erythropotamos' River belongs to the Hot-summer Mediterranean climate (Csa) category in accordance with precipitation and temperature data provided by the gauging station on Didymoteicho's bridge. These indicate that the coldest month (January) averages above 0 °C, at least one month's average temperature is above 22 °C (June, July and August) and at least four months are averaging above 10 °C (Table 7). Furthermore, precipitation gauges show at least three times as much precipitation in the wettest month of winter (February) as in the driest month of summer (August) and the driest month of summer receives less than 30 mm (Table 8)

The pluviothermic quotient (Q) was created by Luis Emberger in 1939 and it has been designed in order to classify the Mediterranean climate into four types: arid, semi-arid,

humid and sub-humid. Therefore, regarding Mediterranean regions, the aforementioned quotient can be estimated with aid of the following formula (6):

$$Q = \frac{1000 \times P}{\frac{(M+m)}{2} \times (M-m)} \quad (6)$$

Where P stands for annual rainfall, M stands for the average temperature of the maximums of the hottest month and m stands for the average temperature of the minimums of the coldest month. Additionally, P is measured in mm, while M and m are measured in Kelvin degrees (°K). Moreover, in formula (6) the term (M+m)/2 is used in order to indicate the range of temperature values in which plants can grow, while the term (M-m) indirectly refers to evaporation, which is considered as an expression of the continental "characteristics" of a climate.

The measurements for precipitation and temperature from Didymoteicho's gauging station were used in order to estimate the pluviothermic quotient for the study area. Therefore, according to Tables 7 and 8, P = 687.5mm, M = 273.15 + 32.28 = 305.43 °K and m = 273.15 – 0.9 = 272.25 °K, which means that Q = 71.74.

In order to complete the determination of the Mediterranean climate type, to which the study area belongs, it is necessary to employ Emberger's two-dimensional climate diagram, which uses the average minimum temperature, in Celsius degrees, of the coldest month in its X axis and values of the pluviothermic quotient (Q) in its Y axis. Furthermore, the diagram's area is separated into zones that are related to the arid, semi-arid, humid and sub-humid Mediterranean climate characteristic, while lines perpendicular to the X axis determine the Mediterranean climate subtype in relation to the values of m according to the following categorization:

- m > 7°C (hot winter)
- 3°C < m < 7°C (mild winter)
- 0°C < m < 3°C (cold winter)
- m < 0°C (severe winter)

Mavromatis (1980) plotted on Emberger's climatic diagram the meteorological stations of Greece according to their Q and m values. Likewise, by plotting the values of Q and m that were calculated for the gauging station on Didymoteicho's bridge the Mediterranean climate type of the study area was determined to be sub-humid with severe winter (Figure 15).

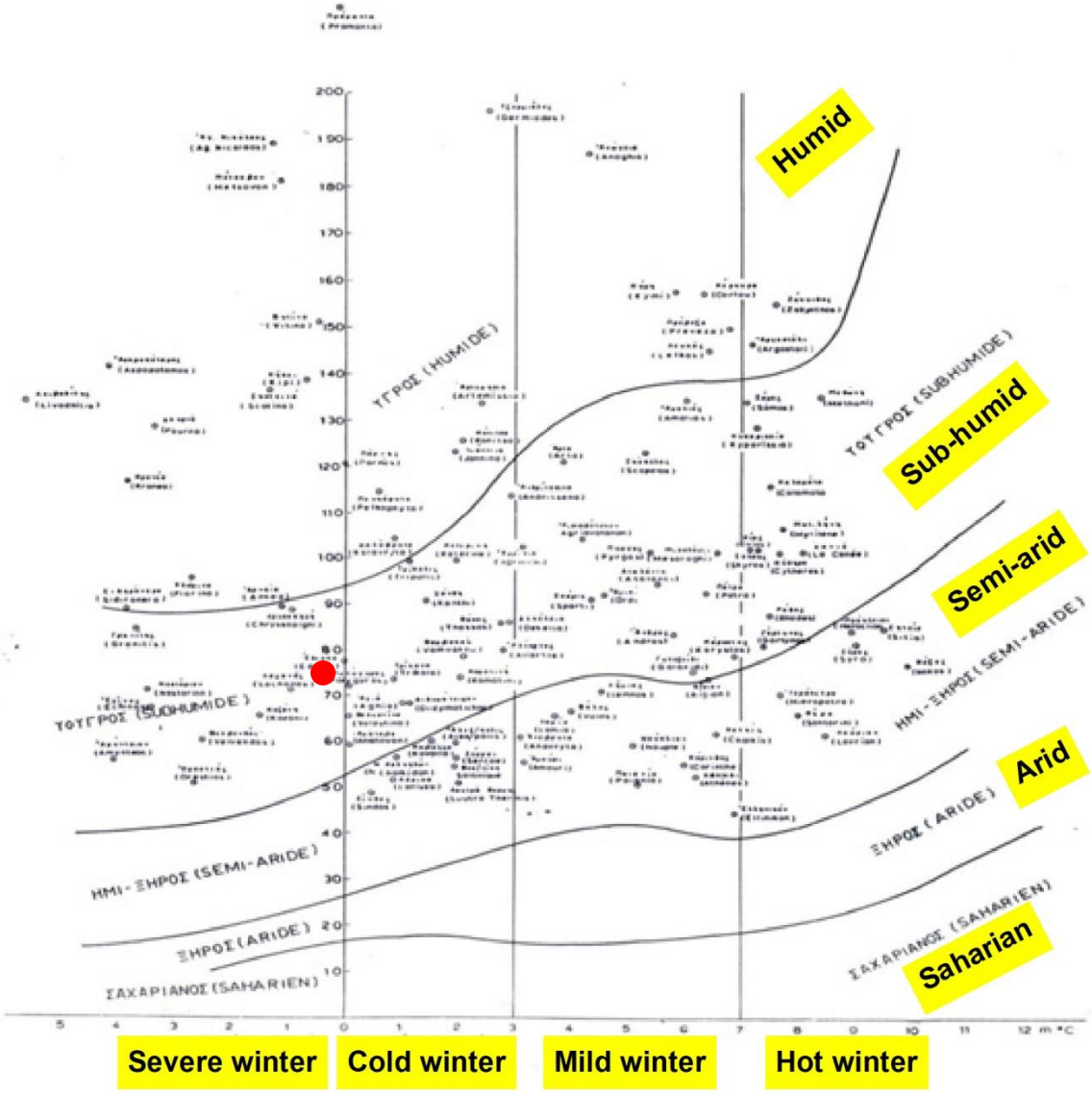

Figure 15: Modified Emberger' s climate diagram (adapted from Mavromatis 1980).

2.5.7.5 Bagnouls – Gaussen ombrothermic diagram

The ombrothermic diagram that was introduced by Bagnouls and Gaussen (1957) depicts the monthly progression of the of mean monthly temperature and precipitation values, which are measured in Celsius degrees and millimeters respectively. Additionally, regarding the aforementioned diagram, the scale of the temperature axis is higher than the scale of precipitation axis so that P (mm) = 2T (°C).

A month is considered dry if its mean precipitation value is equal or lower than two times its mean temperature value (P (mm) ≤ 2T (°C)) (Bagnouls and Gaussen 1957) and the total amount of days that comply with this condition are defined as "dry season". Regarding the drainage basin of Erythropotamos River, the Bagnouls – Gaussen ombrothermic diagram that was compiled according to measurements provided by the gauging station on Didymoteicho's bridge (Table 10) indicated that the study area's "dry season" begins during mid-April and ends during mid-August (Figure 16).

Table 10: Temperature and precipitation data from Didymoteicho's gauging station that were used in order to construct the Bagnouls – Gaussen ombrothermic diagram for the study area.

Month	Mean Temperature (°C)	Mean total precipitation (mm)
January	2.23	81.00
February	5.40	123.50
March	7.14	86.00
April	12.03	30.50
May	19.74	29.00
June	22.01	27.00
July	23.67	25.00
August	24.76	22.00
September	18.50	65.50
October	14.22	72.00
November	9.25	43.50
December	6.74	82.50

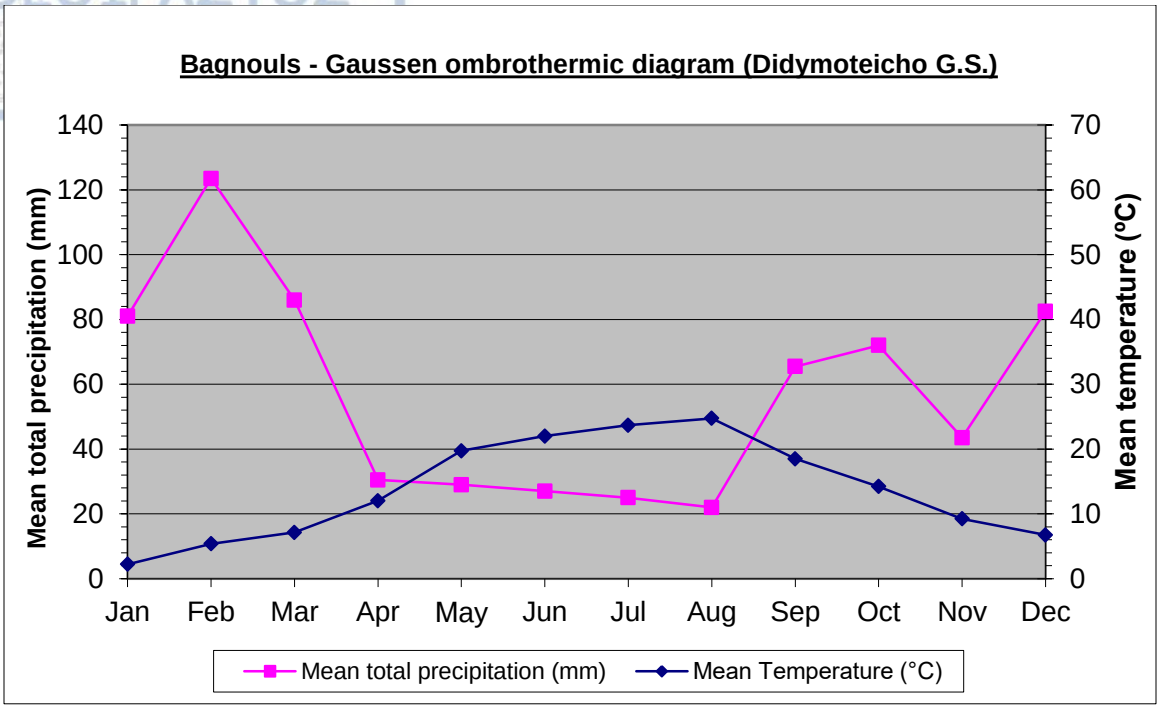

Figure 16: The Bagnouls – Gaussen ombrothermic diagram of Didymoteicho's gauging station.

2.5.8 Notable flood events

The catchment of Erythropotamos River contains cities and villages, which are frequently plagued by flood phenomena that threaten both human lives and properties. Initially, the sole source of information for such phenomena was observations made from eye-witnesses. This condition changed in 2008 with the installation of a gauging station on the bridge of Didymoteicho, which is located approximately 2 km from the confluence between the rivers of Erythropotamos and Evros, that enabled the measurements of meteorological and hydraulic characteristics (discharge, water depth, rainfall etc.) during flood occurrences. Unfortunately, by the end of June in 2010 the gauging station went out of order.

Data regarding measurements of discharge and water depth were used in constructing the discharge versus stage curve for the gauging station of Didymoteicho (Figure 17). Specifically, the x axis involved values of measured discharge (Q) and y axis contained values of water depth (h). The trend line that connects these parameters can be described by the following equation (7), while the value of the coefficient of correlation is 0.82 (R=0.82):

$$h = 0.604 \ln(Q) + 1.852 \quad (7)$$

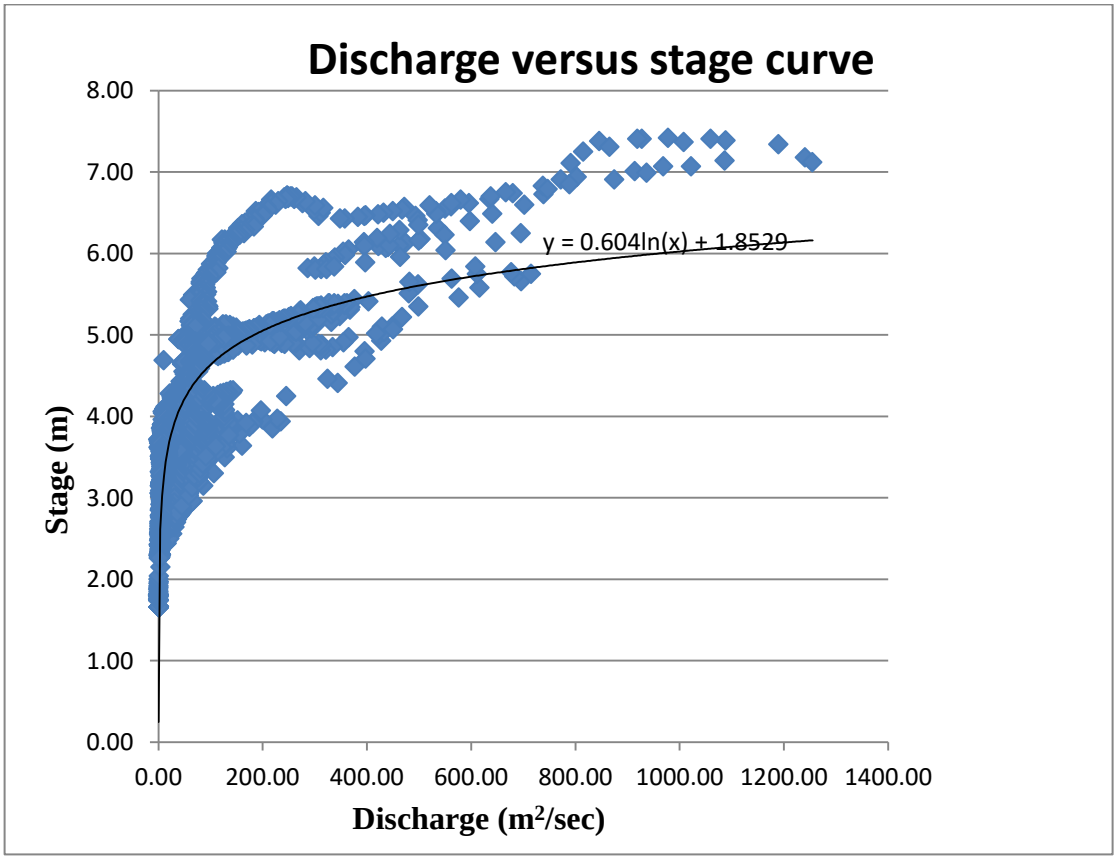

Figure 17: The discharge versus stage curve for the gauging station of Didymoteicho

Furthermore, the most notable flood event that has been recorded by the aforementioned gauging station has taken place from the 8th to the 18th of February in 2010 (Figure 18). Specifically, intense rainfall on the 7th of February, which reached the amount of 48mm within 24 hours, lead to discharge values that exceeded 200 m^3/s on the 8th of February that signified the onset of the flood event.

Figure 18: Photos of the February 2010 flood depicting inundated areas in Didymoteicho's Farm location, which is on Egnatia Motorway. (R.E.M.TH. 2018)

During the flood, discharge peaked three times (Figure 19) by reaching the values of: 1) 1,189.46 m^3/s at 1:00 a.m. on the 12th of February, 2) 1,086.53 m^3/s at 7:00 p.m. on the 13th of February and 3) 1,255.05 m^3/s at 7:00 p.m. on the 15th of February. Correspondingly, water depth also peaked three times (Figure 20) reaching: 1) 7.42 m at 5:00 a.m. on the 12th of February, 2) 7.14 m at 7:00 p.m. on the 13th of February and 3) 7.18 m at 5:00 a.m. on the 15th of February. The flood event was attributed to heavy rainfall that started on the 6th of February at 5:00 p.m. and reached the value of 48mm by the end of 7th of February. Rain continued pouring until the end of the 17th of February and by that time a total of 151mm of rainfall have been measured by the Didymoteicho station, which corresponds to approximately 80% of the total rainfall that was gauged for the whole of February in 2010. Fortunately, although the damage on properties was extensive, no lives were claimed during the disaster.

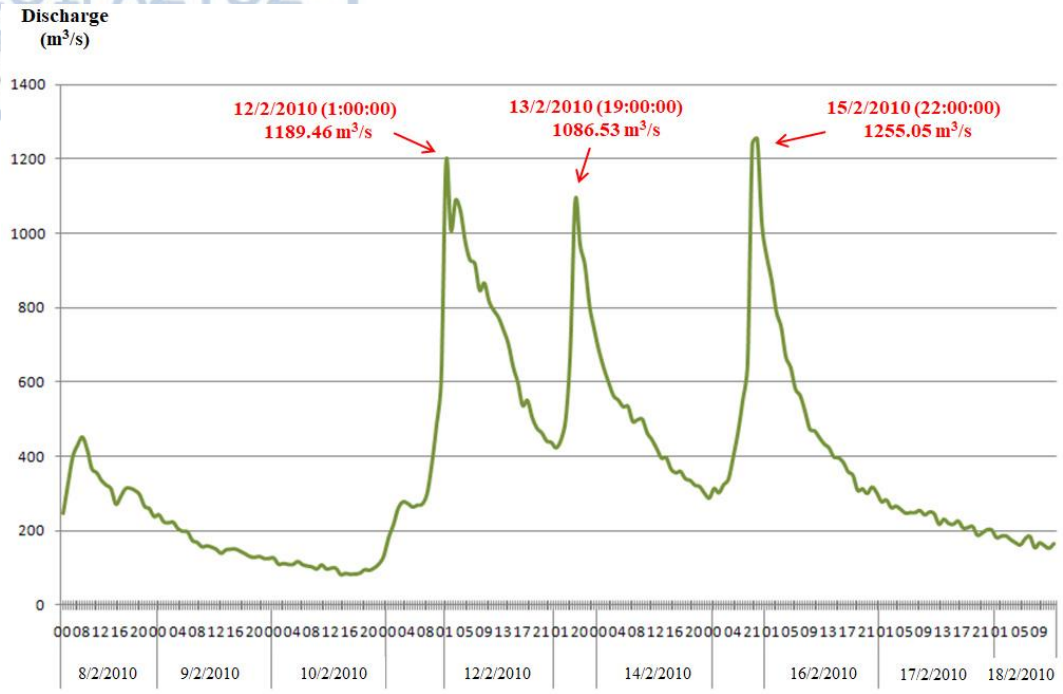

Figure 19: The plot shows the fluctuation of discharge values according to Didymoteicho station measurements from 8/2/2010 to 18/2/2010.

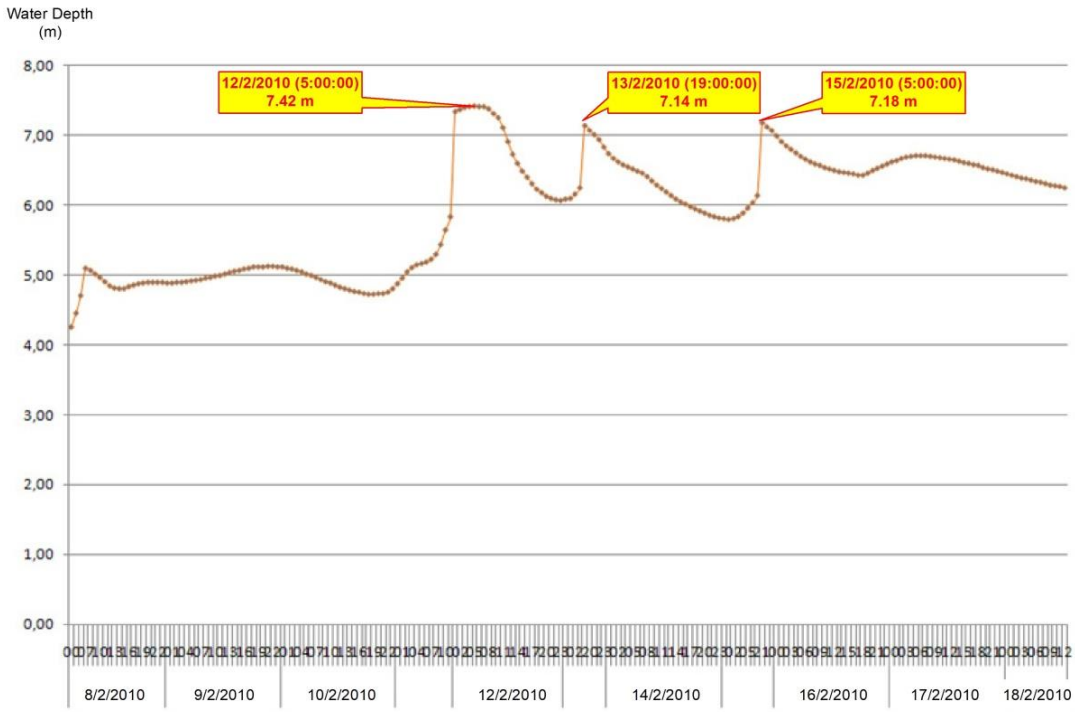

Figure 20: The plot shows the fluctuation of water depth according to Didymoteicho station measurements from 8/2/2010 to 18/2/2010.

Except for the aforementioned major flood event, other lesser flood events occurred during the period from 2010 to 2018 in the study area. Since exact measurements are no longer available, in order to obtain a more detailed description of the phenomena, information gathering relies solely on eye-witness testimonies and images published by local news. More recently, from the 16th of April to the 20th of April in 2017 and from the 25th of March to the 1st of April in 2018, heavy precipitation caused again extensive flooding within the river basin of Erythropotamos (Figures 21 & 22). Information regarding these recent flood events was provided by statements from members of the Department of Civil Protection of the region of Evros, who were tasked with the evaluation of damages that were caused by these floods (C. Papapostolou, personal communication, 2018).

Figure 21: Photo taken from the April 2017 flood that affected Didymoteicho. (Inevros.gr 2017)

Figure 22: Photo taken from the March 2018 flood that affected Didymoteicho. (E-evros.gr 2017)

3. Methodology

3.1 Inundation mapping

Regarding the detection of inundated areas in the drainage basin of Erythropotamos River, an initial approach involved the application of a simplified change detection methodology with the aid of SAR data that was proposed by ESA (2008). The main objective of the suggested procedure was to create RGB images that enable the distinction between areas that are flooded and permanent water bodies. This could be achieved by using one SAR image that was acquired during the flood event (crisis image) and another image (archive image) that was acquired outside the disaster period. By placing the "crisis image" in the Red channel and the "archive image" in both the Green and Blue channels, inundated areas appear dark-colored in the red channel and bright-colored in the Green and Blue channels. Therefore, regarding the resulting false color RBG image, the flooded pixels should appear in bright cyan colors. Moreover, permanent water bodies are depicted as dark in all channels and all other areas appear in various tones of grey as the backscatter intensity should be the same (ESA, 2008).

In the case of Erythropotamos' catchment, this procedure was applied to the February 2010 flood. To this end, ENVISAT/ASAR (Appendix B) images of VV (Vertical transmit – Vertical receive) polarization (Table 11), which were taken from the year 2002 up to the year 2010, were utilized. These images, which were acquired through the submission of a CAT-1 proposal to ESA (European Space Agency) for the completion of the present dissertation thesis, were initially pre-processed with the aid of ESA's NEST (Next ESA SAR Toolbox) (Appendix C) satellite image analysis software (Mouratidis, 2011). The images were firstly despeckled using a 3×3 Gamma map filter and after that step they were co-registerd and terrain-corrected with the use of SRTM DEM (Shuttle Radar Topography Mission Digital Elevation Model) whose horizontal spatial resolution is 3 arc second (approximately 90 m). Specifically, the image that was acquired on 16/2/2010 (Figure 23) was chosen as the "crisis image" and the ENVISAT/ASAR image that was acquired on 23/12/08 (Figure 24) was chosen as the "archive image". The selection of the "archive image" was based on the weather conditions during the time that

the image was taken and information on that matter were provided by Didymoteicho's gauging station. First of all, the "archive image" was taken during winter, which is the same season in which the "crisis image" was taken. Furthermore, according to Marti-Cardona et al. (2010), when deep bare soil areas are flooded, their backscattering is highly dependent on the wind-induced surface roughness at steep incidence angles with wind speed exceeding the value of 1.5 m/s. Therefore, according to measurements from the gauging station of the study area, during the date and time that both images were acquired, wind speed did not exceed 1.5 m/s, so the water surface of the river could be considered as calm. Finally, ESA (2008) suggests that good amplitude threshold values (in Digital Number/DN) for flooded areas (on SAR images) could be those less than 800 for the "crisis image" and those more than 900 for the "archive image". So, in the case of the 2010 flood event, these thresholds were applied on the resulting RGB image.

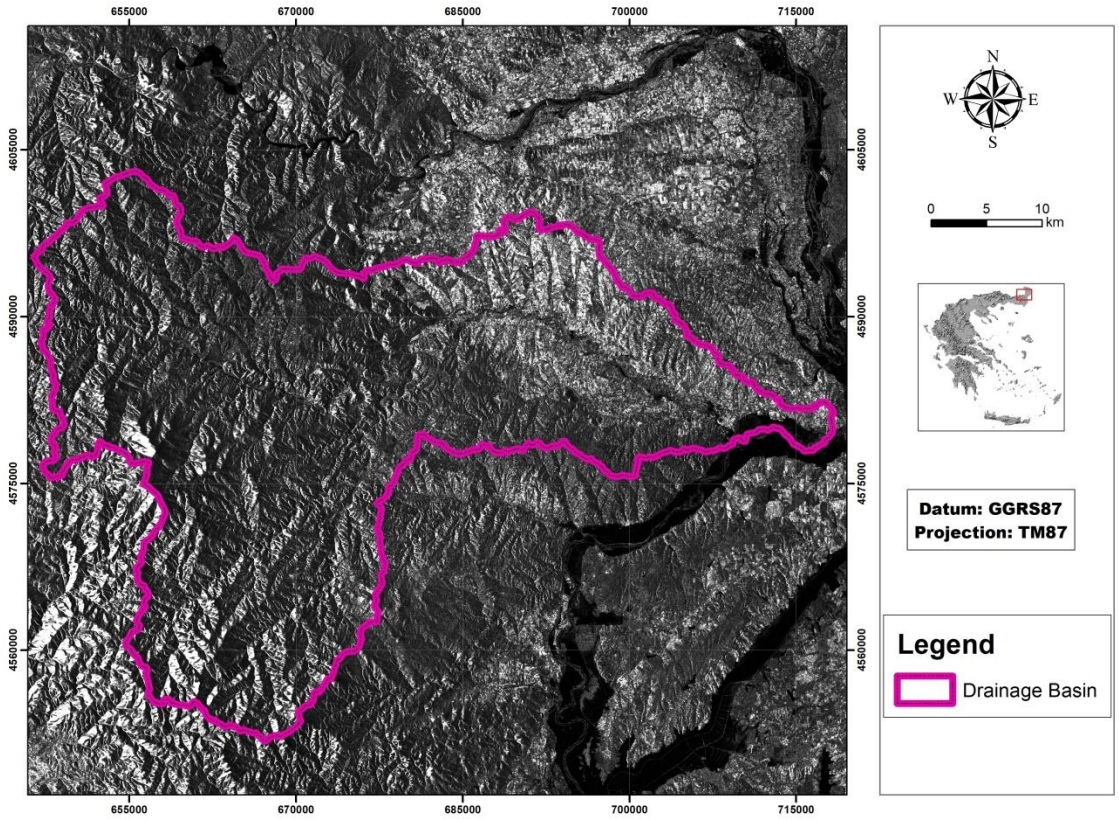

Figure 23: ENVISAT/ASAR image that was taken on 16/2/2010 (crisis image).

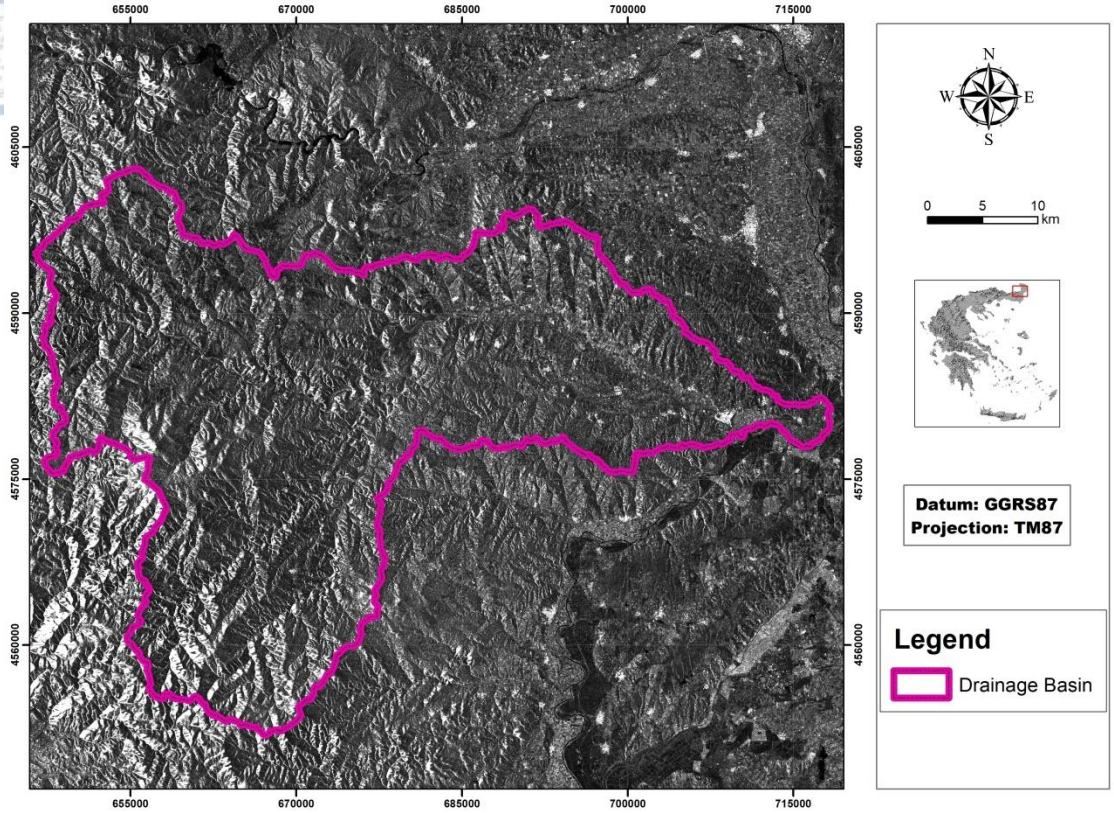

Figure 24: ENVISAT/ASAR image that was taken on 23/12/2008 (archive image).

Table 11: Product information of ENVISAT/ASAR imagery that was used for the application of ESA's (2008) methodology in the study area.

Satellite	**ENVISAT**
Dates	Flood image: 16/2/2010 (1) Reference images: 5/8/2008 to 27/4/2010 (10)
Spatial Resolution	30 m × 30 m
Pass	Ascending
Mode	IMP
Type	GRD
Level	1
Polarization	VV
Relative Orbit	14

On another approach that was employed to perform inundation mapping in the study area, eleven ENVISAT/ASAR and twenty seven SENTINEL – 1 A/B (Appendix D)

images of VV (Vertical transmit – Vertical receive) polarization were used to map the flood extents of the February 2010, April 2017 and March 2018 flood events. Their detailed product characteristics appear on table 12. Generally, for flood mapping with the use of SAR imagery, co-polarization images are preferred over cross-polarization images (Gan et al. 2012). Although HH (Horizontal transmit – Horizontal receive) polarization SAR images are generally preferable for flood mapping, VV- polarized data have been successfully used for flood mapping in many previous studies (Schumann et al. 2009, Matgen et al. 2011, Schlaffer et al. 2015, Giustarini et al. 2015b, Clement et al. 2018).

Table 12: Product information of ENVISAT/ASAR and SENTINEL - 1 A/B imagery that was used for the application of Cian's et al. (2018) methodology in the study area.

Satellite	**ENVISAT**	**SENTINEL - 1**
Dates	Flood image: 16/2/2010 (1) Reference images: 5/8/2008 to 27/4/2010 (10)	Flood images: 18/4/2017 & 26/3/2018 (2) Reference images: 8/10/2016 to 28/9/2018 (25)
Spatial Resolution	30 m × 30 m	20 m × 20 m
Pass	Ascending	Descending
Mode	IMP	IW
Type	GRD	GRD
Level	1	1
Polarization	VV	VV
Relative Orbit	14	109

The aforementioned SAR images were pre-processed with the aid of ESA's SAR satellite image analysis software SNAP (Sentinel Application Platform) (Appendix E). Initially, they were calibrated to σ° backscatter coefficient values and despeckled using a 3×3 Gamma map filter. Regarding the co-registration step, the SAR images were co-registered with the use of EU-DEM. Furthermore, during the co-registration step, SAR multi-temporal series were created according to the date that the floods occurred and according to the SAR sensors that managed to capture these events. Subsequently, for the 2010 flood event two stacks were created. The first stack, which will be henceforth called the 'reference stack', contained only the 10 reference images from ENVISAT/ASAR,

while the second stack, which will be henceforth called the 'reference and flood stack', contained both the reference and the images of the flood under investigation, for a total of 11 images. The same practice was followed for the 2017 and 2018 floods that were captured by SENTINEL -1 A/B and resulted in the creation of two more stacks. A 'reference stack' that included only the 25 reference images and a 'reference and flood stack', which contained both the reference and the flood images, for a total of 27 images.

Cian et al. (2018) proposed a Change Detection And Thresholding methodology (CDAT), based on the work of Long et al. (2014), that involves the calculation of the minimum, maximum and mean, for each pixel of both the 'reference stack' and 'reference and flood stack'. The calculated temporal statistics are used to compute the Normalized Difference Flood Index (NDFI) and the Normalized Difference Flood in short Vegetation Index (NDFVI) images.

NDFI was used for highlighting temporary open water bodies and is defined by the following equation (8):

$$NDFI = \frac{mean\ \sigma_{o}\ (reference\ stack) - min\ \sigma_{o}\ (reference + flood\ stack)}{mean\ \sigma_{o}\ (reference\ stack) + min\ \sigma_{o}\ (reference + flood\ stack)} \quad (8)$$

This index categorizes as flooded only areas that are temporarily covered by water, excluding non-water land cover types and permanent water bodies. The average behavior of the earthly surface is represented by each pixel's mean value (Figures 25 and 26). Moreover, the minimum value of each pixel in the 'reference and flood stack' was used in order to detect discontinuities within the time series, such as pixels that during the flood attain very low backscatter values (Figures 27 – 29). Specifically, the difference between the mean and the minimum backscatter pixel values identifies such discontinuities, which in turn indicate flooded areas. NDFI values range from 0 to 1 and this helps to set a threshold value that will aid in discerning flooded areas. Surface features that do not present significant change have NDFI index values that are close to 0 and can be easily detected. Such features, which do not change their backscatter

significantly, include permanent water bodies and non-water pixels with low backscattering such as smooth tarmac, dry bare soil and roads. (Cian et al. 2018)

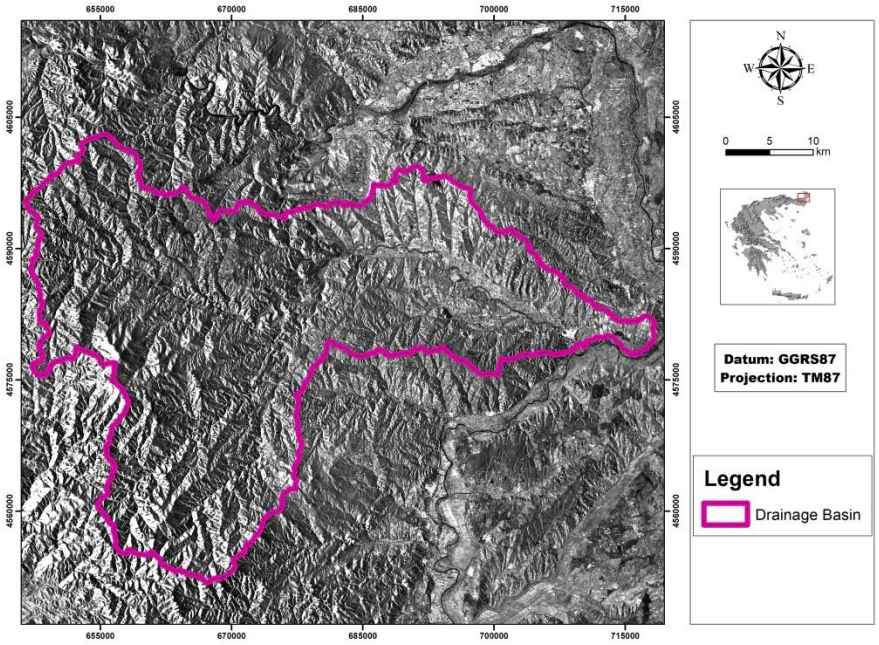

Figure 25: The mean σ_o value image that was derived from the 'reference stack' which contained ENVISAT/ASAR imagery.

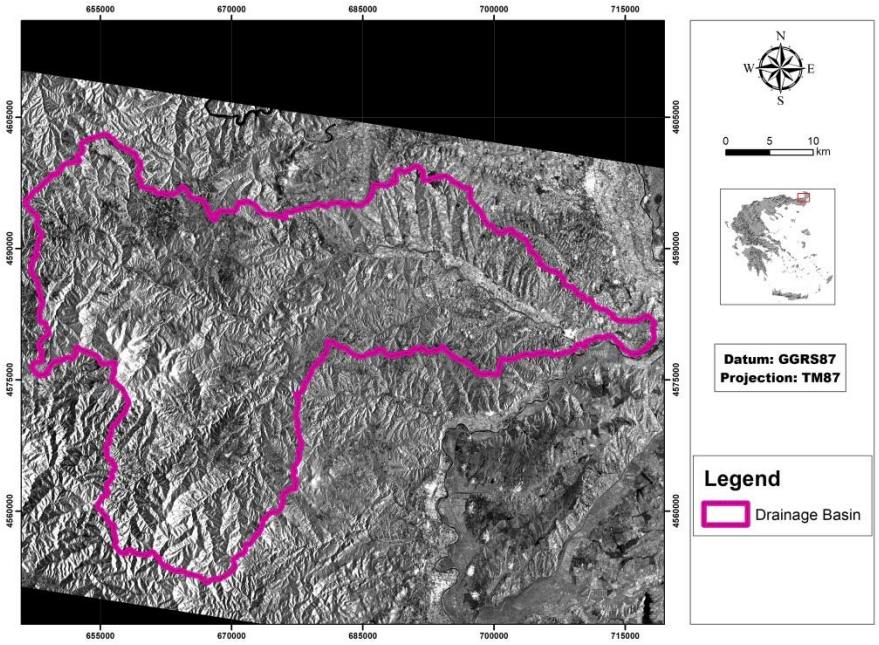

Figure 26: The mean σ_o value image that was derived from the 'reference stack' which contained SENTINEL – 1 A/B imagery.

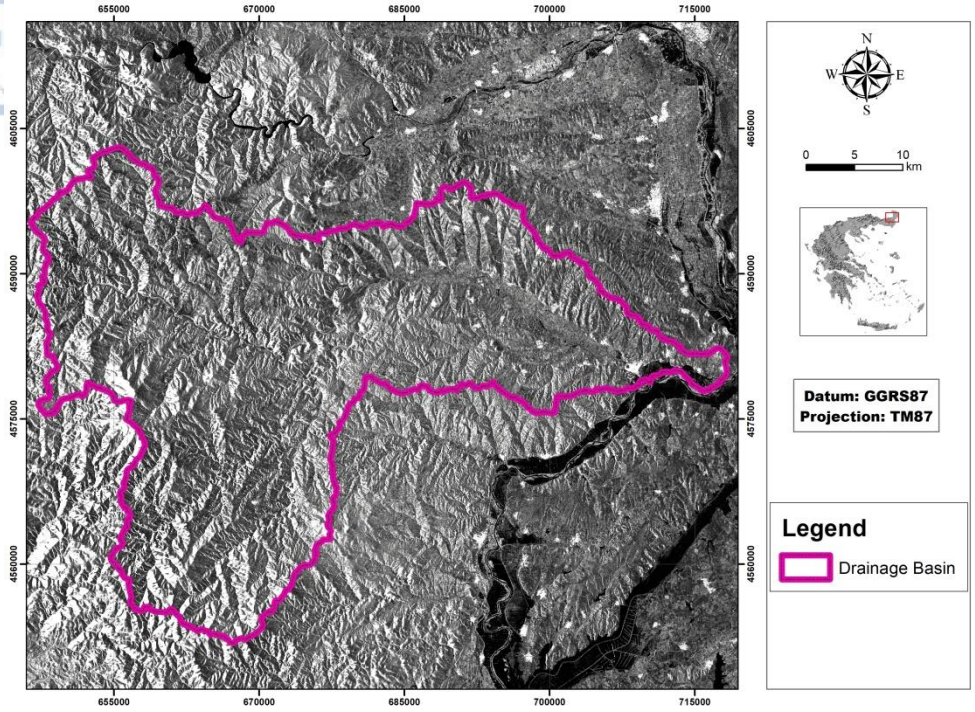

Figure 27: The minimum σ_o value image that was derived from the 'reference and flood stack' which contained ENVISAT/ASAR imagery.

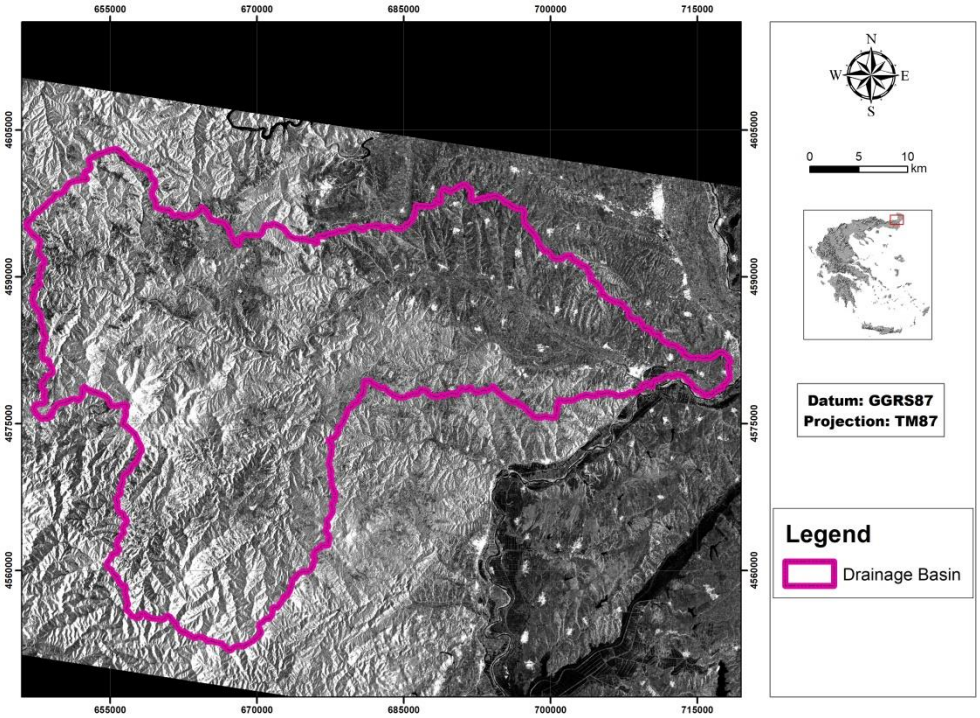

Figure 28: The minimum σ_o value image that was derived from the 'reference and flood stack' which contained the SENTINEL – 1 A/B image that was acquired on 18/4/2017.

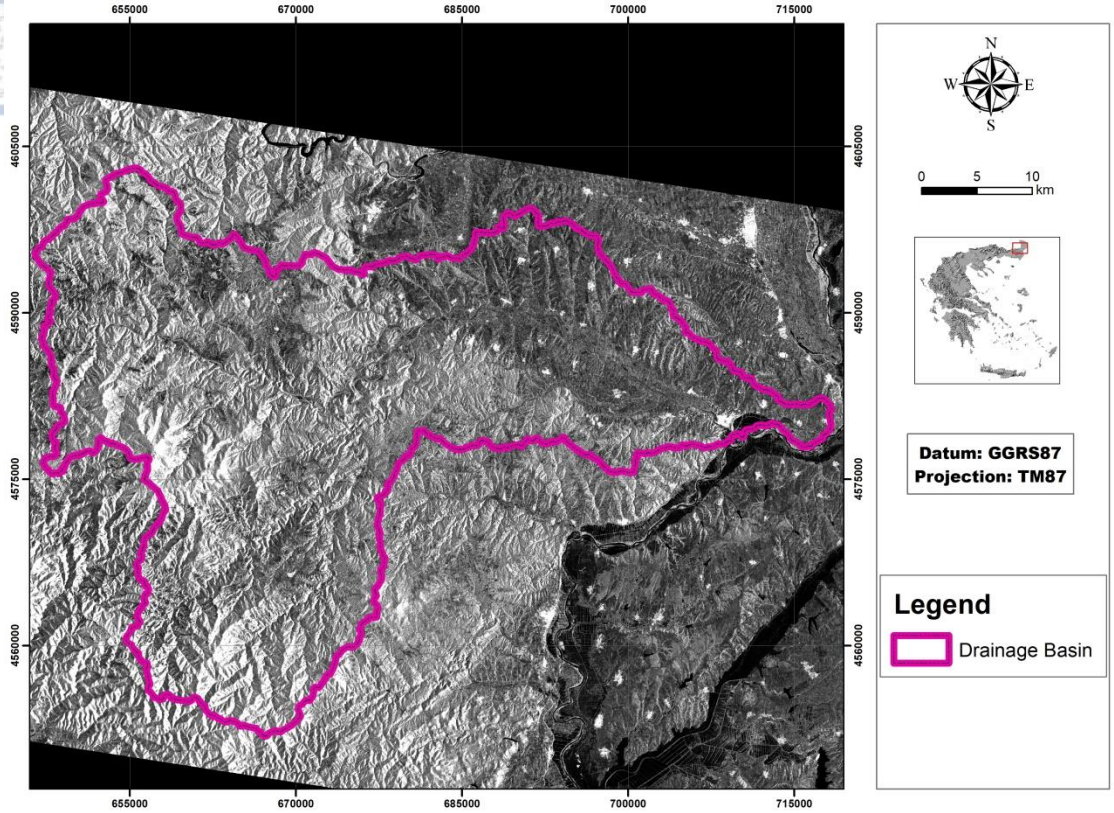

Figure 29: The minimum σ_o value image that was derived from the 'reference and flood stack' which contained the SENTINEL – 1 A/B image that was acquired on 26/3/2018.

In order to detect shallow water in short vegetation, the NDFVI index was used to detect the increase of backscatter that occurs in such circumstances. Using the statistics on the corresponding stacks NDFVI was computed according to the following formula (9):

$$NDFVI = \frac{max\ \sigma_o\ (reference\ +flood\ stack) - mean\ \sigma_o\ (reference\ stack)}{max\ \sigma_o\ (reference\ +flood\ stack) + mean\ \sigma_o\ (reference\ stack)} \quad (9)$$

Regarding the NDFVI index, the maximum value of the pixels highlights the discontinuity, which is caused by shallow water in short vegetation, in the time-series (Figures 30 – 32). Pixels that indicate a notable increase in their respective backscatter values can be detected via their difference with the mean backscatter pixel values. (Cian et al. 2018)

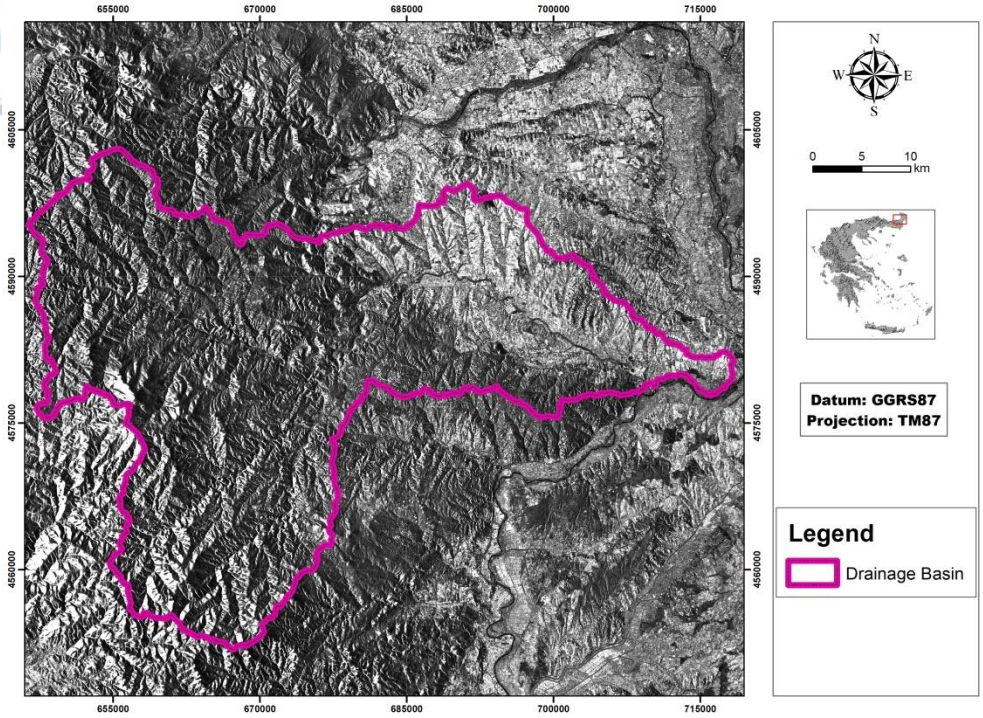

Figure 30: The maximum σ_o value image that was derived from the 'reference and flood stack' which contained ENVISAT/ASAR imagery.

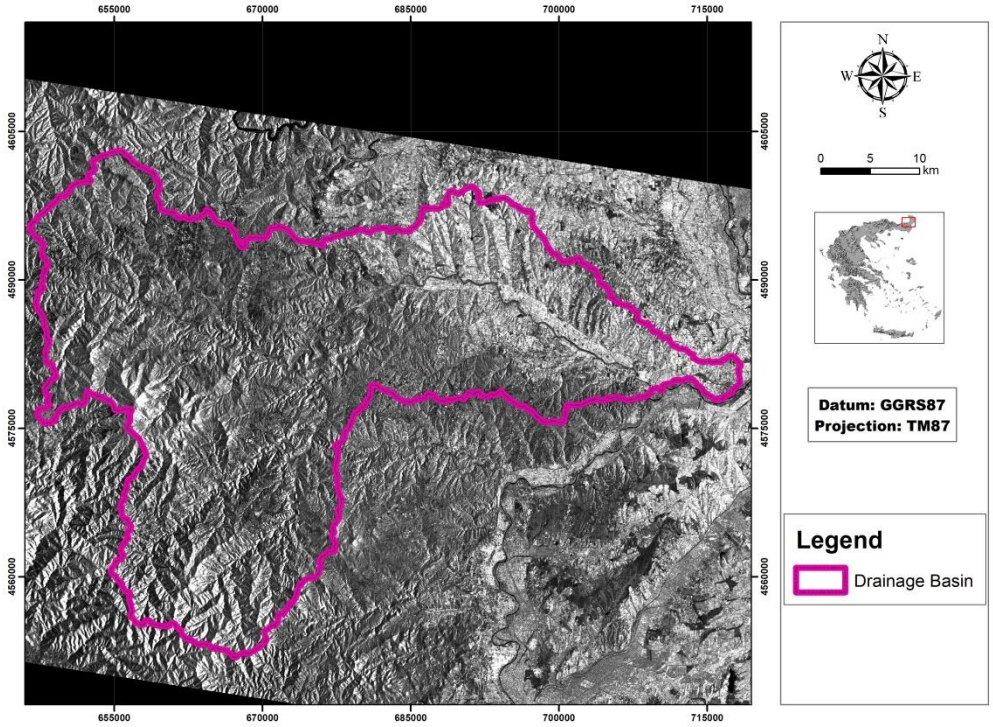

Figure 31: The maximum σ_o value image that was derived from the 'reference and flood stack' which contained the SENTINEL – 1 A/B image that was acquired on 18/4/2017.

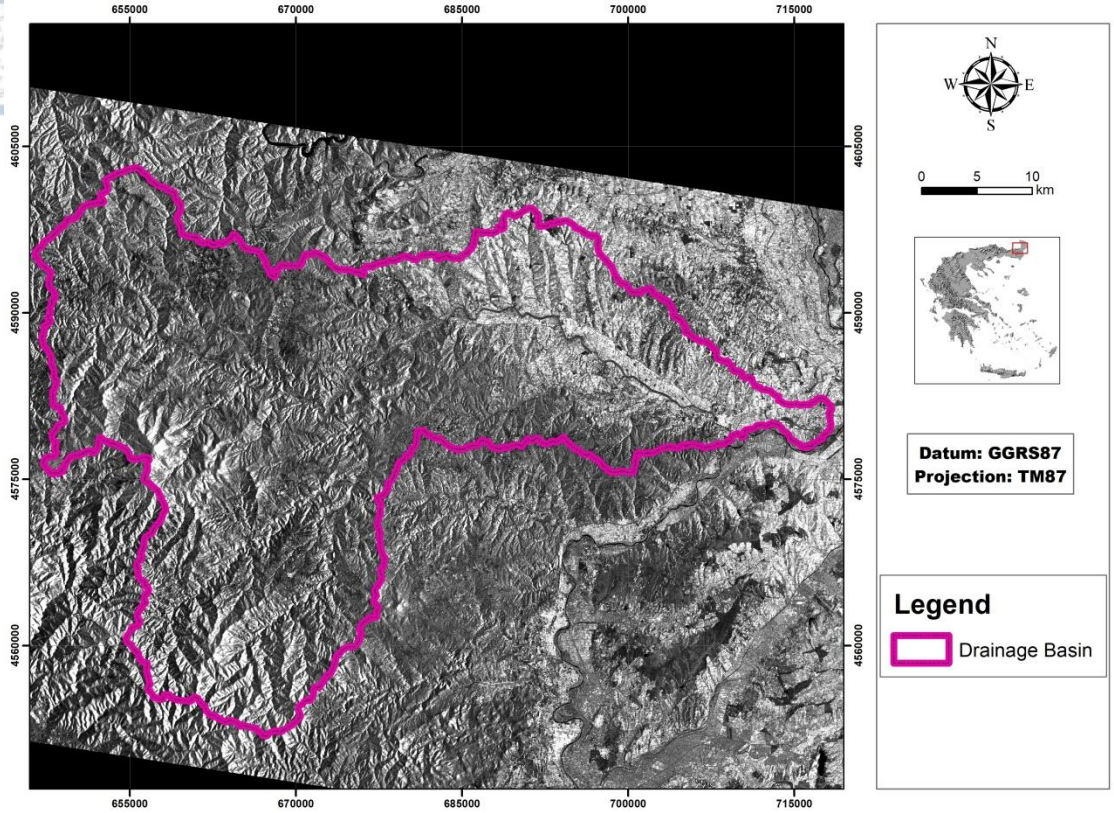

Figure 32: The maximum σ_o value image that was derived from the 'reference and flood stack' which contained the SENTINEL – 1 A/B image that was acquired on 26/3/2018.

According to Cian et al. (2018) NDFI values that are greater than 0.7 and NDFVI values that are greater than 0.75 can be used to delineate inundated areas in open land and in short vegetation respectively. However, the resulting flooded areas require further processing according to the following three criteria:

a) Flooded areas with extent smaller than the size of 10 pixels in NDFI and NDFVI images were excluded because they can be considered as spurious (Cian et al. 2018). Specifically, in the case of ENVISAT/ASAR imagery (2010 flood event) these areas have an extent of less than 1,231.2 m^2, while in the case of SENTINEL – 1 imagery (2018 and 2017 flood events) spuriously flooded areas might cover an extent of less than 788.5 m^2.

b) Pixels with $\sigma_{o(mean)}$ values less than 0.015 ($\sigma_{o(mean)} < 0.015$), which correspond to permanent water bodies, and pixels with $\sigma_{o(min)}$ values greater than 0.03 ($\sigma_{o(min)} >$

0.03) that represent pixels that consistently decrease their backscatter during the flood, indicating that something happened, but not enough to reach a $\sigma_{o(min)}$ value typical of water pixels, have to be filtered out from the resulting inundation maps (Cian et al. 2018).

Finally, the methodologies of ESA (2008) and Cian et al. (2018), regarding inundation mapping of the 2010 flood with the use of ENVISAT/ASAR imagery, were compared in order to find out if there are important differences in their corresponding flood extent areas. Moreover, the flood extents of the inundated areas that were produced by the application of Cian et al. (2018) methodology were compared in order to determine not only the common area that they covered, but also the total area that they covered when combined together.

3.2 Flood hazard and risk mapping

3.2.1 Preparation of geometric data with the aid of HEC-GeoRAS

The application of flood hazard mapping in the drainage basin of Erythropotamos River aimed at delineating the extents of inundated areas and depicting the spatial distribution of water depth for specific return periods. This procedure was applied to both the thalweg (Domakinis et al. 2015) and river reaches of the 5th order and higher, because according to Das (2016), low values of bifurcation ratio, such as the value of 3.66 between streams of the 4th and 5th order of the drainage network of Erythropotamos River (Table 4), indicate which part of the drainage basin is more likely to flood. To this end, the geometric data of the drainage network, such as the stream centerline, bank lines, flow paths, land cover and cross-sectional cut lines were created using ArcGIS's extension HEC-GeoRAS (Appendix G) (Figure 33). Moreover, EU-DEM and the DEM of NCMA were used in order to provide the elevation characteristic for the geometric data and convert them from 2D features to 3D features.

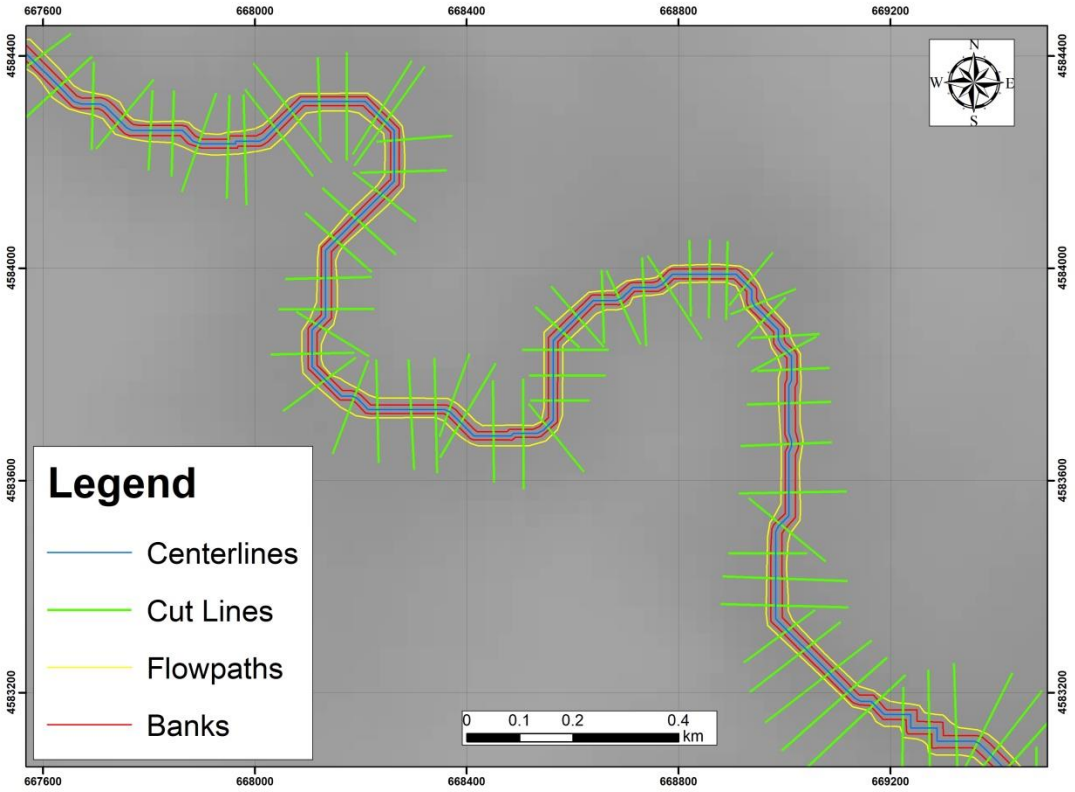

Figure 33: Erythropotamos' drainage network geometric data that were constructed with the use of the ArcGIS™ extension HEC-GeoRAS.

3.2.2 Steady flow hydraulic analysis with the aid of HEC-RAS

The next step involved importing all the aforementioned data to HEC-RAS software in order to conduct steady flow hydraulic analysis. Flood discharge was calculated with the aid of rational method (10) (Giandotti 1934, Soulios, 1996 and Voudouris 2013):

$$Q = 0.278 \times E \times P_i \times I_\sigma \quad (10)$$

Where Q stands for flood discharge measured in m^3/s, E stands for the area of the drainage basin measured in km^2 (1,618.5 km^2), P_i stands for critical rainfall intensity for a specific return period measured in mm/h and I_σ stands for the runoff coefficient, which is dimensionless.

The value of the runoff coefficient for the part of the drainage basin of Erythropotamos River that was used for conducting hydraulic analysis was calculated according to the guidelines proposed for road construction surveys by the Ministry of Environment and Energy. Specifically, the runoff coefficient is the sum of runoff coefficients regarding: 1) surface relief (C_r), 2) soil permeability (C_i), 3) vegetation cover (C_v) and 4) soil storage capability (C_s) according to the following formula (11) (Ministry of Environment and Energy 2002):

$$I_\sigma = C_r + C_i + C_v + C_s \quad (11)$$

The values for C_r, C_i, C_v and C_s were determined according to Table 13.

Therefore, by considering that C_r = 0.1, C_i = 0.1, C_v = 0.05 and C_s= 0.1, the value of I_σ has been calculated equal to 0.35. Furthermore, this value had to be multiplied by a modifier that depended on the return period according to table 14.

Consequently, the value of I_σ equaled to 0.42 for the 50 year return period and 0.4375 for the 100 year return period. However, since there were no multipliers suggested for return periods higher than 100 years, the multiplier of 1.25 was considered valid for such cases.

Critical rainfall intensity was initially calculated by the universal equation (12) (Giandotti 1934 and Soulios 1996):

$$P_i = (30 \times logT + 15)t_c^{-0.6} \quad (12)$$

Where T stands for the return period measured in years and t_c stands for concentration time measured in hours.

Table 13: Runoff coeffient values for drainage basins which are located in non-developed areas. (Ministry of Environment and Energy 2002)

Runoff Coefficient	Extreme values	High values	Common values	Low values
Surface relief (C_r)	0.28 – 0.35 Rough surfaces with mean slope angle values >30%	0.20 – 0.28 Hilly surfaces with mean slope angle values 10-30%	0.14 – 0.20 Wavy-shaped surfaces with mean slope angle values 5-10%	0.08 – 0.14 Generally flat surfaces with mean slope angle values 0-5%
Soil permeability (C_i)	0.12 – 0.16 Soil cover is either rocky or fine-grained along with insignificant permeability	0.08 – 0.12 Clays or shallow soils of low permeability or low drainage capability	0.06 – 0.08 Well – drained soils of normal permeability. Soils composed of sand or silt.	0.04 – 0.06 Deep sand of high permeability or soils that absorb water. Well-drained soils
Vegetation cover (C_v)	0.12 – 0.16 Bare soils or sparse vegetation cover	0.08 – 0.12 Poor to average vegetation cover. Non-vegetated agricultural areas or poorly naturally vegetated areas. Less than 20% of the drainage area is sufficiently covered with vegetation	0.06 – 0.08 Average to good vegetation cover. Approximately 50% of the surface is composed of topsoil or forests. Less than 50% of the surface contains agricultural areas.	0.04 – 0.06 Good to excellent vegetation cover. Approximately 90% of the drainage area contains topsoil or forests.
Soil storage capability (C_s)	0.10 – 0.12 Insignificant number of troughs. Shallow floodways. No swamps.	0.08 – 0.10 Low soil storage capability. Well-defined floodways. No lakes or swamps.	0.06 – 0.08 Normal soil storage capability. Significant number of troughs. No lakes or swamps.	0.04 – 0.06 High soil storage capability. Not well-defined floodways. Large amount of lakes and inundated areas.

Table 14: Multipliers of the runoff coefficient according to the return period. (Ministry of Environment and Energy 2002)

Return period (years)	25	50	100
Multiplier	1.1	1.2	1.25

However, the formula (13) suggested by the Ministry of Environment and Energy (2016) based on a survey that was conducted by Koutsogiannis et al. (2010) was also taken under cosidaration:

$$P_i = \frac{\lambda(T^{\kappa} - \psi)}{(1 + \frac{t_c}{\theta})^{\nu}} \quad (13)$$

Where κ is the shape parameter, λ is the parameter of scale, ψ is the parameter of the position of the distribution function, while θ and ν are parameters of the duration function. The parameters of this equation (13) were calculated for each rainfall gauging station across Greece. The rainfall gauging stations that could be located within the drainage basin of Erythropotamos River were those of Mega Dereio, Mikro Dereio, Metaxades and Didymoteicho and the parameters for each station are shown in table 15.

Table 15: The parameters of formula (13) for each rainfall gauging station which is located within the drainage basin of Erythropotamos River. (Ministry of Environment and Energy 2016)

Name	Elevation (m)	κ	λ	ψ	θ	ν
Mega Dereio	381.6	0.04	1108.9	0.87	0.082	0.708
Mikro Dereio	116.2	0.04	981.2	0.891	0.082	0.708
Metaxades	138.7	0.04	982.6	0.886	0.082	0.708
Didymoteicho	24.7	0.093	499.1	0.839	0.082	0.708

For both equations (12) and (13), concentration time was calculated with the use of Giandotti's formula (14) (Giandotti 1934, Soulios, 1996 and Voudouris 2013):

$$t_c = \frac{4 \times \sqrt{E} + 1.5 \times L}{0.8 \times \sqrt{z}} \quad (14)$$

Where E stands for the area of the drainage basin measured in km^2 (1,618.5 km^2), L stands for the length of the longest flowpath measured in km (104,17 km) and z stands for the difference between the values of mean basin elevation and basin outlet elevation measured in m (328.22m – 15.9m = 312.32m). Consequently, the value of concentration time for the catchment of Erythropotamos River was found equal to 22.43 h.

Additionally, regarding formula (13), rainfall intensity-duration-frequency curves for the rainfall gauging stations of Mega Dereio, Mikro Dereio, Metaxades and Didymoteicho were compiled in order to further aid in the calculation of rainfall intensity (Figures 34 – 37).

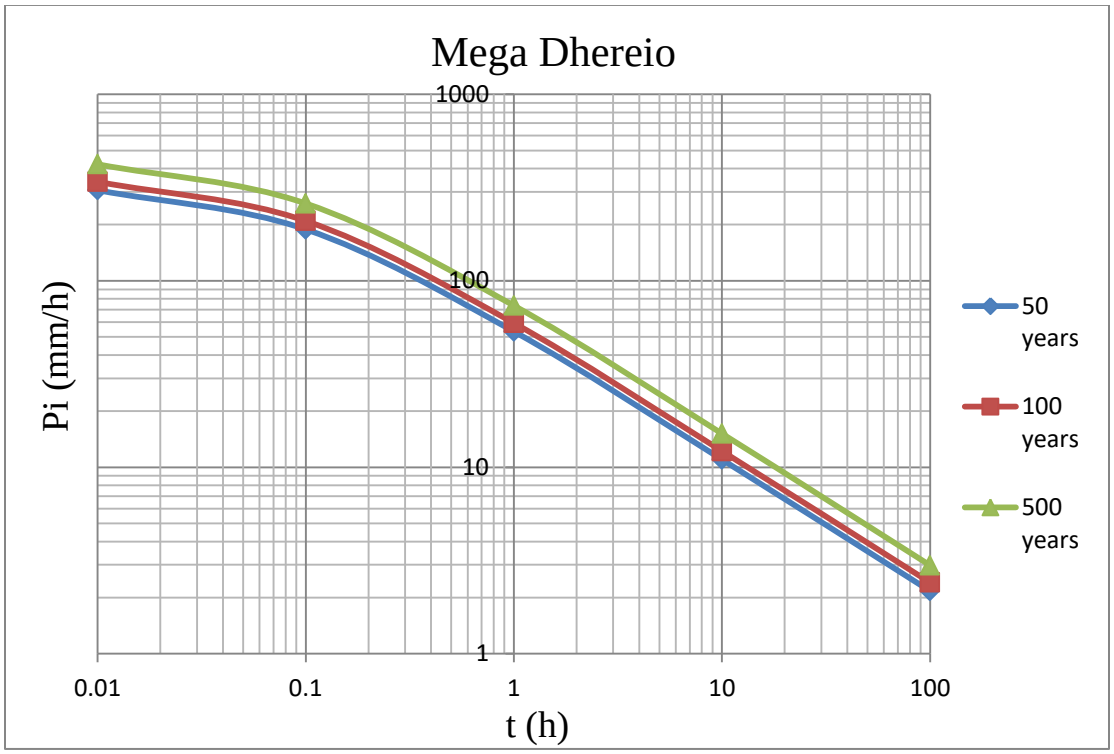

Figure 34: The Rainfall intensity-duration-frequency curve for the rainfall gauging station of Mega Dereio.

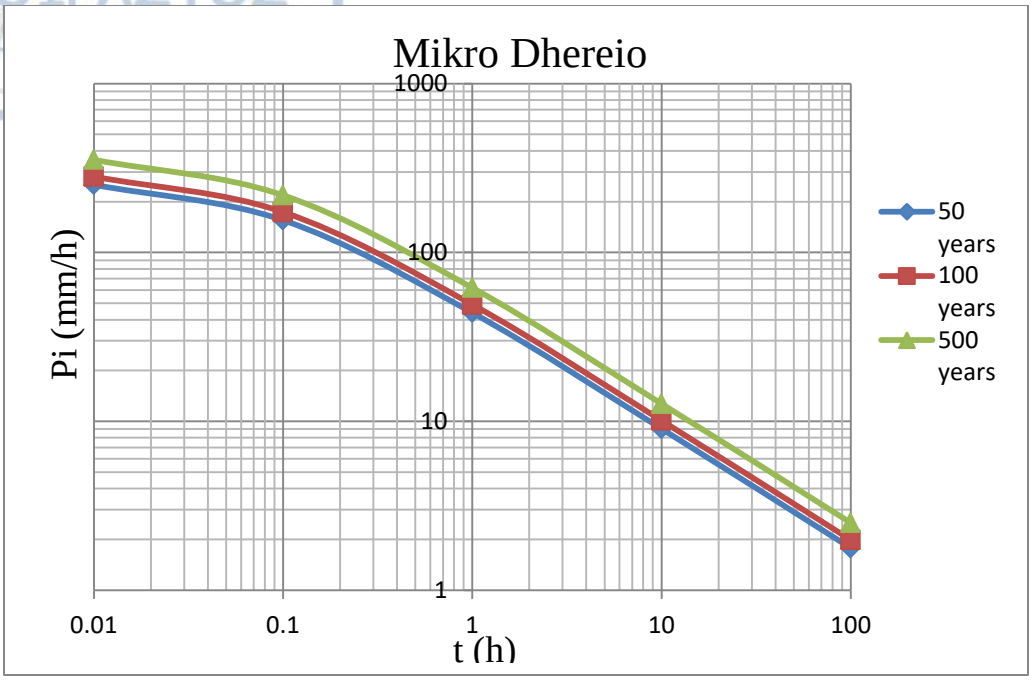

Figure 35: The Rainfall intensity-duration-frequency curve for the rainfall gauging station of Mikro Dereio.

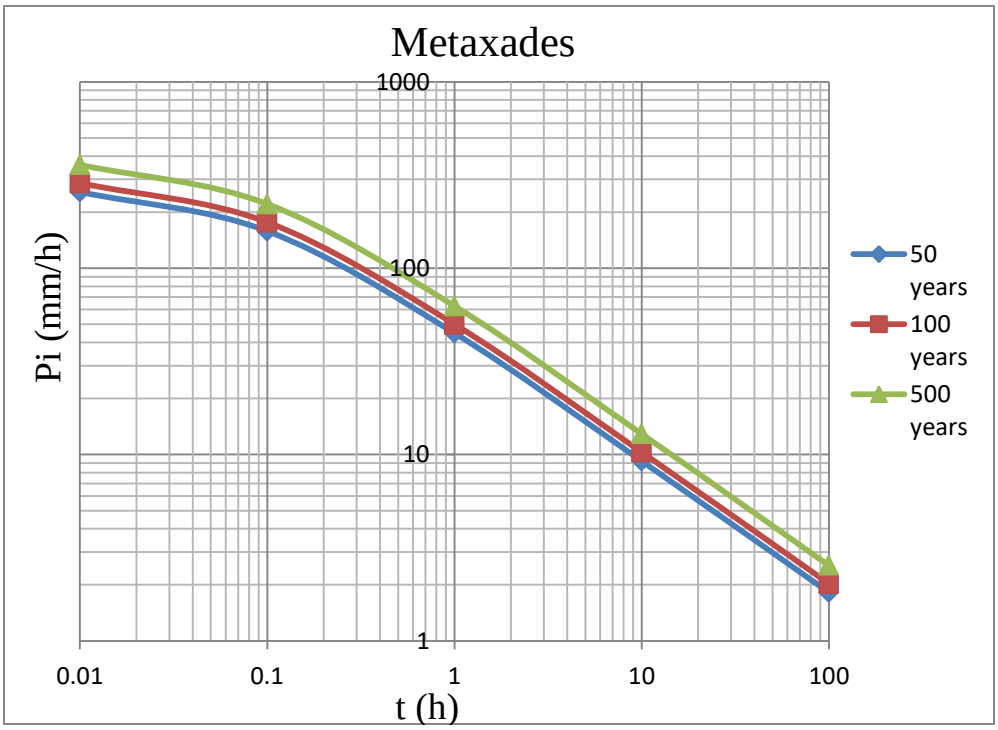

Figure 36: The Rainfall intensity-duration-frequency curve for the rainfall gauging station of Metaxades.

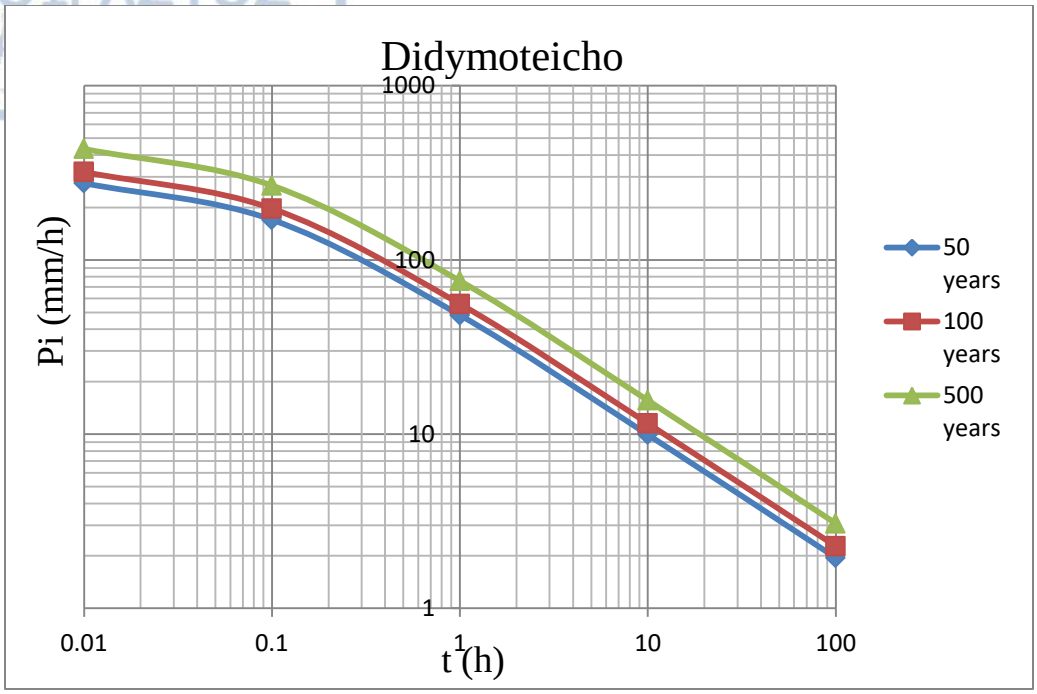

Figure 37: The Rainfall intensity-duration-frequency curve for the rainfall gauging station of Didymoteicho.

Rainfall intensity values were then calculated using formulas (12) and (13). Specifically, equation (13) used the corresponding parameters referring to the rainfall gauging stations of Mega Dereio, Mikro Dereio, Metaxades and Didymoteicho (Table 15). The return periods that were selected were: 1) 50 years, which is the return period value that corresponds to the high probability flood hazard scenario according to the 2007/60/EC Directive, 2) 100 years, which is the return period value that corresponds to the medium probability flood hazard scenario according to the 2007/60/EC Directive and 3) 500 years, which is the return period value that corresponds to the low or extreme probability flood hazard scenario according to the 2007/60/EC Directive. The calculated rainfall intensity values for each case are presented in table 16.

Having considered all the aforementioned cases regarding rainfall intensity calculation, the flood discharge values that were used in the steady flow analysis step in HEC-RAS were finally based on the rainfall intensity values of Mega Dereio (Table 17), since the elevation at which the rainfall gauging station is located (381.6 m) is closer to the mean elevation of the drainage basin of Erythropotamos River (328.22 m). Moreover,

the return periods that were used in the steady flow analysis were: 1) 0.5 years, which is the return period value that corresponds to the value of discharge that was measured by the Didymoteicho station during the time that the ENVISAT/ASAR image that was taken on 16/2/2010, 2) 50 years, which is the return period value that corresponds to the high probability flood hazard scenario according to the 2007/60/EC Directive, 3) 50.6 years, which is the return period value that corresponds to the maximum value of discharge that was measured by the Didymoteicho station during the time of the February 2010 flood event, 4) 100 years, which is the return period value that corresponds to the medium probability flood hazard scenario according to the 2007/60/EC Directive and 5) 500 years, which is the return period value that corresponds to the low or extreme probability flood hazard scenario according to the 2007/60/EC Directive (Figures 38 & 39)

Table 16: Rainfall intensity values that were calculated with the use of formulas (12) and (13).

Return period	Mega Dereio Equation (13)	Mikro Dereio Equation (13)	Metaxades Equation (13)	Didymoteicho Equation (13)	Equation (12)
50 years	6.23	5.12	5.23	5.62	10.23
100 years	6.91	5.73	5.83	6.52	11.63
500 years	8.58	7.2	7.31	8.84	14.88

Table 17: The values for flood discharge that were used for each scenario of the steady flow hydraulic analysis.

Return period	**Flood Discharge (m^3/sec)**
0.5 years	311.64
50 years	1177.35
50.6 years	1,255.05
100 years	1360.23
500 years	1,688.97

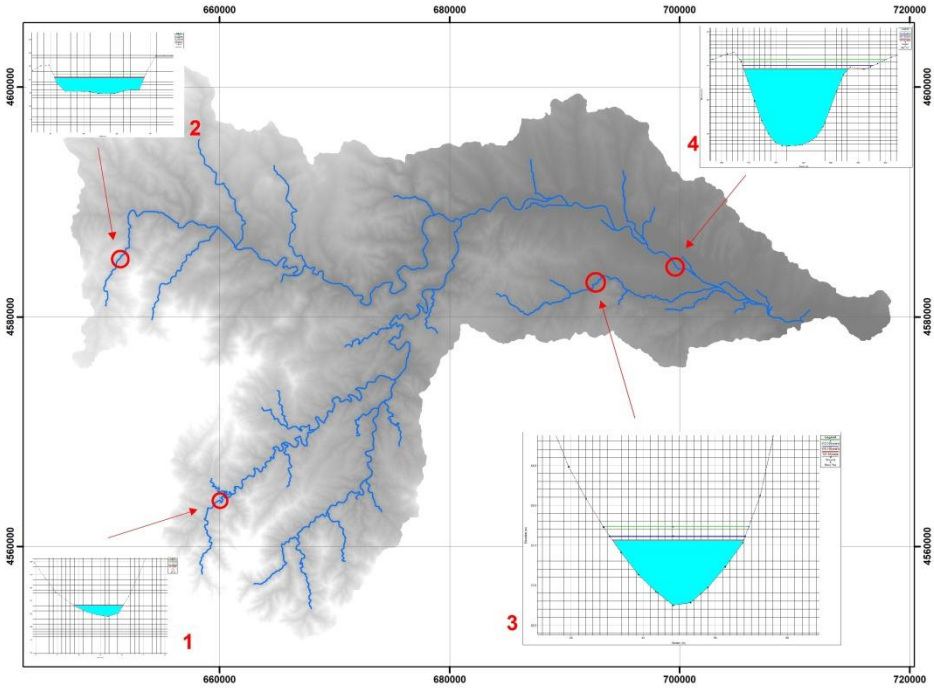

Figure 38: Locations of sample cross-sections that were utilized by HEC-RAS in order to perform steady flow hydraulic analysis.

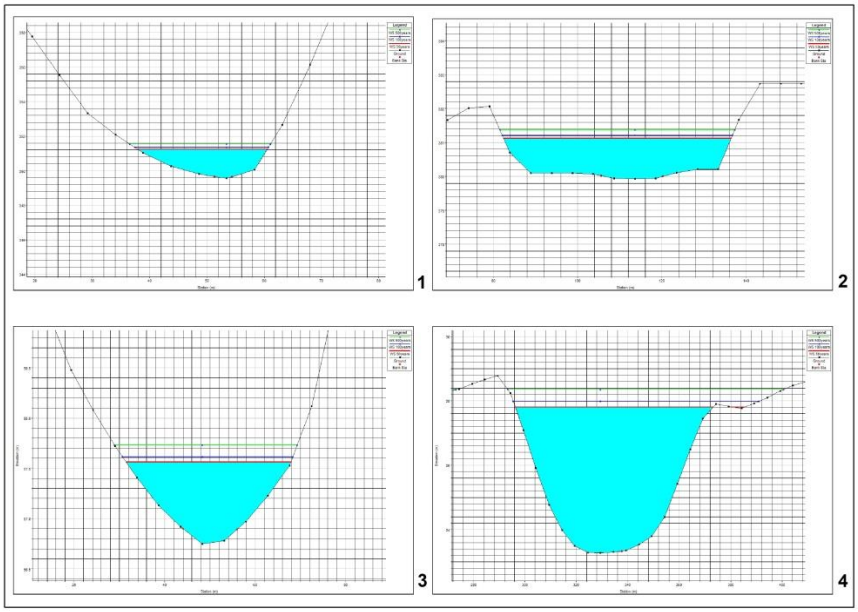

Figure 39: Sample Cross-sections that were utilized by HEC-RAS in order to perform steady flow hydraulic analysis. The water surfaces for the 50, 100 and 500 years return period scenarios are presented.

3.2.3 Flood hazard and risk mapping with the aid of HEC-GeoRAS

During the final step of the procedure, the results of the steady flow hydraulic analysis were imported back to the ArcGIS software and there, with the aid of the HEC-GeoRAS extension, the data layers that depicted the spatial distribution of flood extent and water depth for the corresponding return periods were produced. However, in order for the resulting flood hazard maps to have a more practical meaning and value, it was deemed appropriate to compile additional flood risk maps for each return period, which included data layers that contained information about elements that will be potentially threatened by floods such as urban and protected areas. From this procedure the scenarios that involved only the thalweg were excluded on the grounds of not representing "worst case" scenarios.

3.3 Flood susceptibility mapping

According to the analysis from Xiao et al. (2018) and Zhao et al. (2018), the factor's effect on the flood hazard and data availability in our study area, three types of indicators were utilized in the present dissertation thesis, i.e. hydrological, topographical and meteorological. Specifically, topographical indicators (Xiao et al. 2018) provide information of the flow or stagnating of the water on the ground due to the impact of the terrain. In the current thesis they consisted of elevation, slope angle and drainage density. On the other hand, hydrological indicators (Xiao et al. 2018) provide information of the accumulation, infiltration, and intercept of the water and the river network. For the drainage basin of Erythropotamos River these indicators consisted of Topographic Wetness Index (TWI), distance from streams, land cover and geology. Finally, the meteorological indicators (Zhao et al. 2018) provide information on the spatial distribution of precipitation in the study area and they were represented by the annual total rainfall.

3.3.1 Topographical Indicators

3.3.1.1 Elevation

Elevation is considered as an important factor for floods, because flood-prone areas tend to occupy drainage basin areas with low elevation values. The data layer of elevation was derived from EU-DEM.

3.3.1.2 Slope Angle

The slope angle data layer was produced by processing the EU-DEM data layer with the aid of ArcGIS's toolbox routines. Slope angle is also an important factor when it comes to discerning flood-prone areas, because areas in a river basin that occupy flat terrain surfaces tend to flood more easily than areas with more steep surface terrain.

3.3.1.3 Drainage Density

The drainage density is defined as the total stream length per unit area, which can be calculated according to the following equation (15) (Han et al. 2003; Zhou et al. 2014):

$$DD = \frac{1}{S} \times \Sigma_i L_i^S \quad (15)$$

Where DD stands for drainage density, while S indicates the area of the grid and L_i^S stands for the length of river i within the grid. Areas with high drainage density indicate high flood susceptibility.

3.3.2 Hydrological Indicators

3.3.2.1 Topographic Wetness Index (TWI)

This index is considered by Miliaresis (2011) to belong to the indices of soil erosion, since it is used to relate the effects of runoff with geomorphometry. It is used in order to assess soil moisture and it is defined by the Beven and Kirkby (1979) equation:

$$TWI = \ln\left(\frac{\alpha}{\tan(\beta)}\right) \quad (16)$$

In equation (16), α stands for the local upslope area draining through a certain point per unit contour length and tan(β) is the local slope in radians. High values of TWI indicate areas more susceptible to flooding.

3.3.2.2 Distance from streams

The drainage network of the drainage basin of Erythropotamos river has been produced by processing the EU-DEM data layer through ArcGIS's toolbox routines (Voudouris et al. 2007). Furthermore, the distance from the streams of the drainage network data layer was also compiled with the use of ArcGIS routines. This factor is crucial to flood susceptibility mapping, because areas that are closer to streams are more likely to be inundated during a flood event.

3.3.2.3 Geology

The synoptic geologic map of SE Rhodope – Thrace from the Institute of Geology and Mineral Exploration (IGME) of Greece, at a scale of 1:200,000 (I.G.M.E. 2002), was used in order to produce the part of the data layer that belongs to Greece. Accordingly, the geologic map of Bulgaria from the Department of Geophysical Prospecting and Geological Mapping of the Committee of Geology (CoG 1989), at a scale of 1:50,000, which was compiled on the base of the Geological map of Bulgaria at a scale of 1:100,000, was used in order to produce the part of the data layer that belongs to Bulgaria.

Geology is considered a significant factor in determining flood-prone areas, because impermeable geological formations favor surface runoff. On the other hand, permeable geological formations favor infiltration.

3.3.2.4 Land Cover

The data layer of Corine Land Cover 2012 (Copernicus 2017) was used to determine the land cover classes within the limits of the study area. Vieux (2004) correlated land cover classes with Manning's n roughness coefficient (Table 18), which participates in Manning's formula:

$$V = \frac{1}{n} \times A \times r^{\frac{2}{3}} \times S^{\frac{1}{2}} \quad (17)$$

Table 18: Manning's n rougness coefficients for certain land cover types according to Vieux (2004).

Land Cover	Manning's *n* coefficient
Artificial surfaces	0.015
Agricultural areas	0.035
Forest and semi natural areas	0.1
Wetlands	0.7
Water bodies	0.03

In equation (17), V stands for discharge/flow (m^3/s), n is Manning's roughness coefficient, A is the "wetted" cross-sectional area (m^2), r stands for the hydraulic radius and S is the slope of hydraulic grade or the linear head loss (m/m). Moreover, Manning's n roughness coefficient is inversely proportional to discharge, which means that low Manning's n values correspond to high discharge values. In that way, areas susceptible to floods can be related to low Manning's n values.

3.2.3 Meteorological Indicators

3.2.3.1 Rainfall

The annual total rainfall layer was derived using raw data that were retrieved from the WorldClim database (Fick and Hijmans 2017). The raw data involve monthly precipitation totals, which refer to the climatological period 1970 - 2000 and are available as an approximately 30 seconds by 30 seconds (approximately 824 by 824 m) grid (Fick

and Hijmans 2017). The total annual precipitation layer was constructed by summing all 12 monthly precipitation totals with the aid of ArcGIS™. Subsequently, the aforementioned rainfall layer was converted to a point shapefile, from which the final rainfall data layer, with a spatial resolution of 25 m, was derived. The downscaling of the original WorldClim layer (824 x 824 m grid resolution) to the layer that was eventually used in the current analysis (25 x 25 m grid resolution), was performed by employing the universal kriging spatial interpolation method (Li and Heap 2014). The interpolated values were the total annual precipitation values obtained at each point of the original WorldClim grid. The auxiliary variables used were elevation, slope, aspect and distance from the sea. The elevation data used was the EU-DEM obtained from the COPERNICUS Land Monitoring Services data portal (E.E.A.2017) and is provided on a 25 by 25 m grid. Slope and aspect were derived from the EU-DEM using the ArcGIS™ routines available. Distance from the sea was also computed by ArcGIS™ routines at a spatial resolution of 25 m. Areas with high annual precipitation sums were considered as more prone to flooding.

3.4 Analytical Hierarchy Process (AHP)

In order to determine the level of importance for each factor by assigning weights to each one of them, the Analytical Hierarchy Process introduced by Saaty (1980) was used, which due to its simplicity, continues to be popular even in recent works regarding susceptibility mapping (Lyu et al 2018, Seejata et al. 2018, Tang et al. 2018). Firstly, in order to apply the AHP methodology, the data layer of each factor was classified into three classes according to how prone each one of these classes was to flooding. Classes that are highly susceptible to flooding were assigned a rating of three (3), while those that are of medium susceptibility were assigned a rating of two (2) and those of low susceptibility were assigned a rating of one (1). The next step involved the determination of importance of one factor in comparison with the rest of the other factors, so that pairwise comparison could be performed. At this point, in order to deal with the subjectivity that often accompanies this step of AHP, the importance of each factor was

determined by utilizing either the results of inundation mapping or the results of flood hazard mapping.

3.4.1 Determination of the hierarchy of factors with the aid of inundation mapping

In this case the importance of each factor was determined according to the proportion of the inundated areas of the 2010 flood event (total area of 6.84 km^2 that was calculated with the aid of NDFI and NDFVI indices) that intersected with each factor's high susceptibility class (Figures 40 – 47 and Table 19) (Domakinis et al.: In press). This concept was based on the idea that a SAR image that is taken during a flood indicates the areas where flood water is concentrated. Moreover, the factors or indicators of flood susceptibility all coexist in these areas and it is known how each factor influences floods. For example it is known that, regarding e.g. slope angle, flat areas tend to flood more easily. Thus, the areas where flood water is concentrating are those where the most favourable conditions for most factors coexist, i.e. where the high susceptibility classes for most factors or indicators intersect. Subsequently, the more a high susceptibility class of a factor or indicator is encountered in inundated areas, the more influential this factor or indicator is in terms of flood susceptibility.

Table 19: Proportion of the total inundated area of the 2010 flood event that intersects with each factor's high susceptibility class.

Factor	Extent of inundated area (km^2)	Percent ratio (%)
Land Use / Cover	0.15	2.19
TWI	0.12	1.75
Geology	0.39	5.7
Distance from streams	3.44	50.29
Rainfall	0.01	0.15
Slope Angle	5.59	81.73
Drainage Density	0.99	14.47
Elevation	6.66	97.37

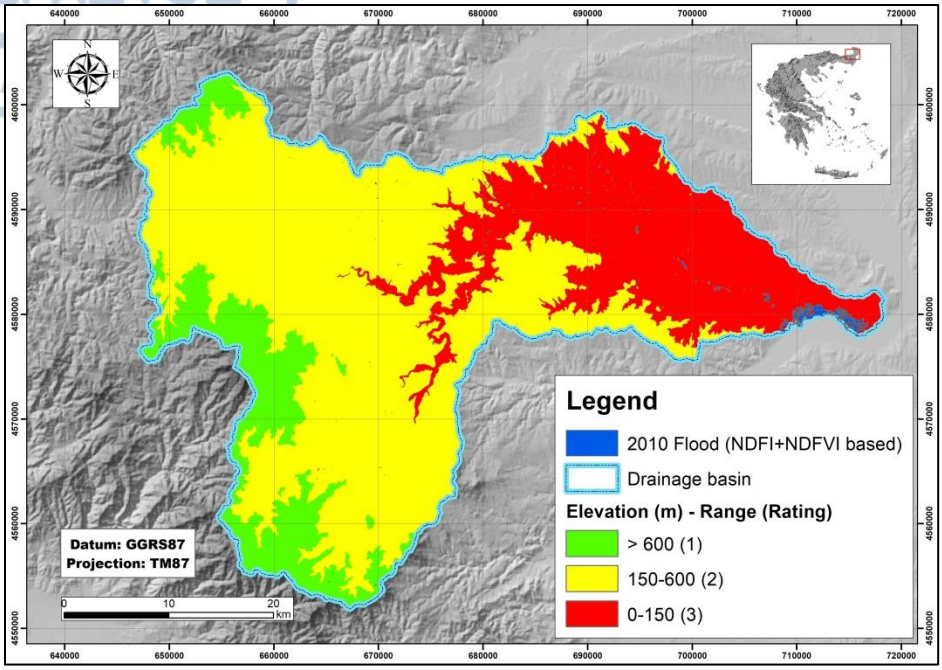

Figure 40: The data layer of the inundated areas of the 2010 flood event (calculated with the aid of NDFI and NDFVI indices) has been superimposed upon the flood susceptibility classes of the elevation data layer.

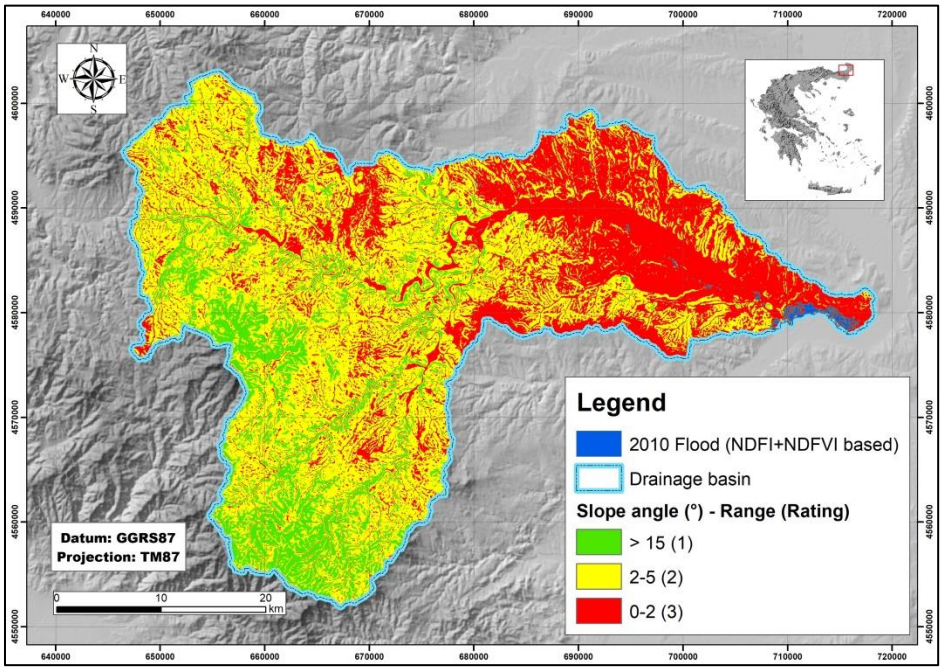

Figure 41: The data layer of the inundated areas of the 2010 flood event (calculated with the aid of NDFI and NDFVI indices) has been superimposed upon the flood susceptibility classes of the slope angle data layer.

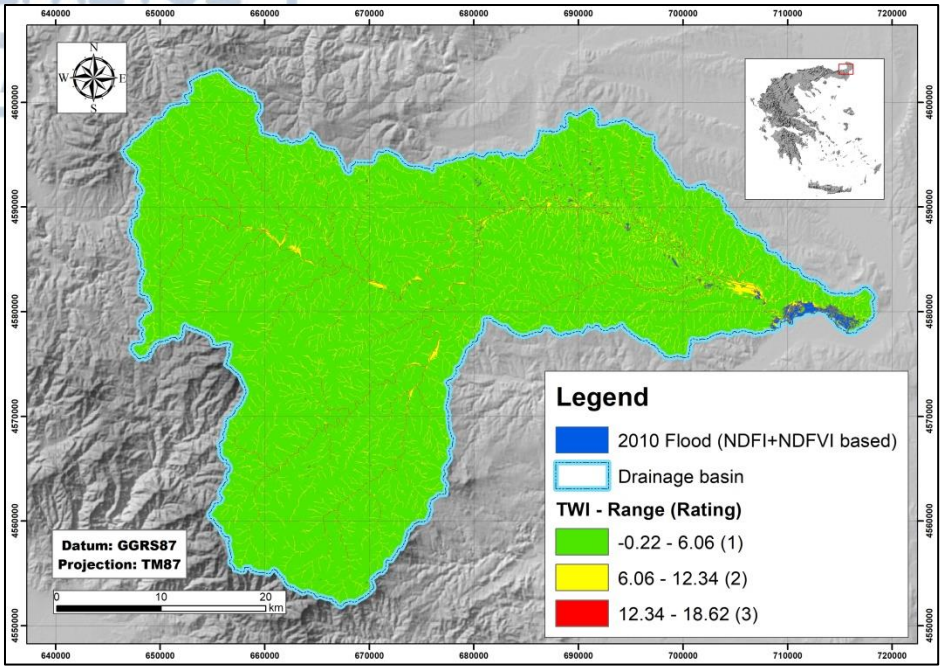

Figure 42: The data layer of the inundated areas of the 2010 flood event (calculated with the aid of NDFI and NDFVI indices) has been superimposed upon the flood susceptibility classes of the TWI data layer.

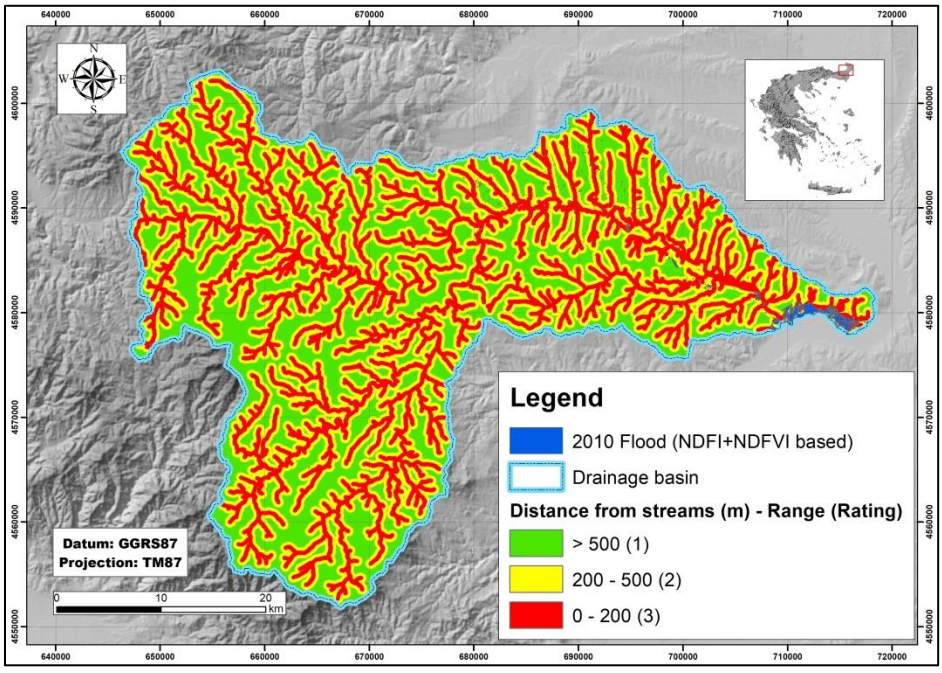

Figure 43: The data layer of the inundated areas of the 2010 flood event (calculated with the aid of NDFI and NDFVI indices) has been superimposed upon the flood susceptibility classes of the distance from streams data layer.

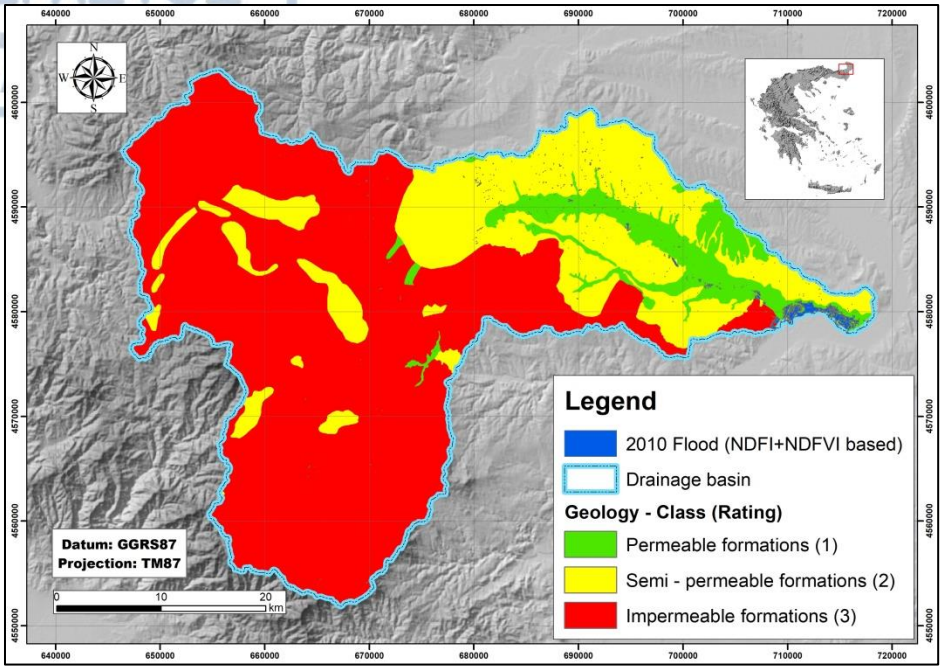

Figure 44: The data layer of the inundated areas of the 2010 flood event (calculated with the aid of NDFI and NDFVI indices) has been superimposed upon the flood susceptibility classes of the geology data layer.

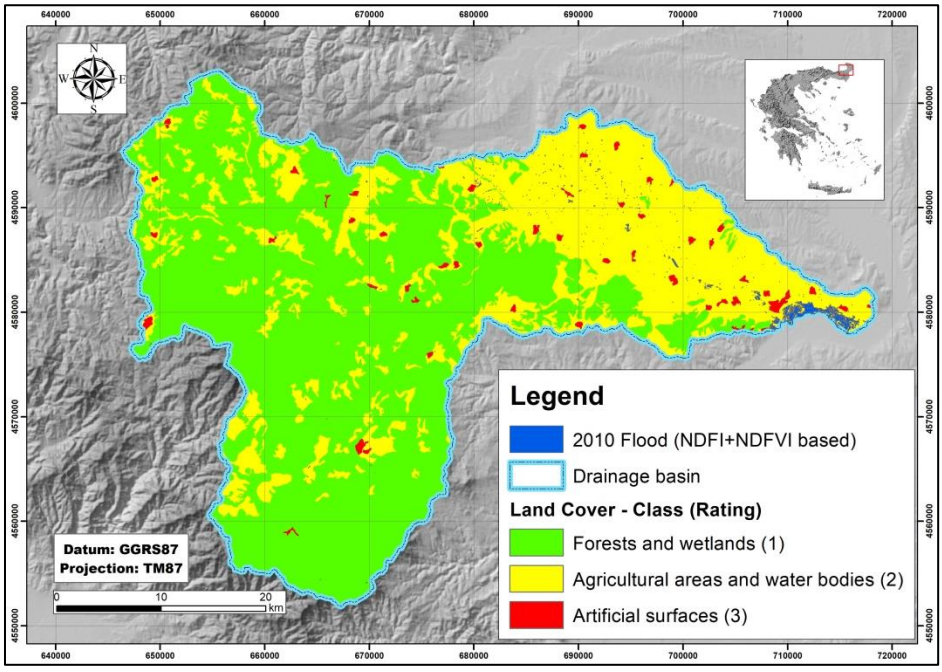

Figure 45: The data layer of the inundated areas of the 2010 flood event (calculated with the aid of NDFI and NDFVI indices) has been superimposed upon the flood susceptibility classes of the land cover data layer.

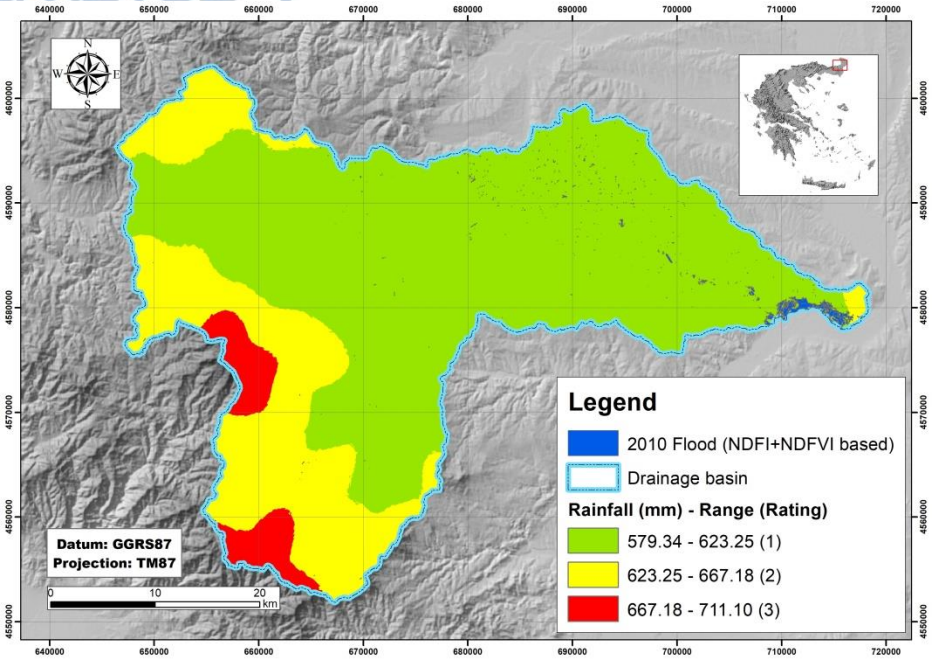

Figure 46: The data layer of the inundated areas of the 2010 flood event (calculated with the aid of NDFI and NDFVI indices) has been superimposed upon the flood susceptibility classes of the rainfall data layer.

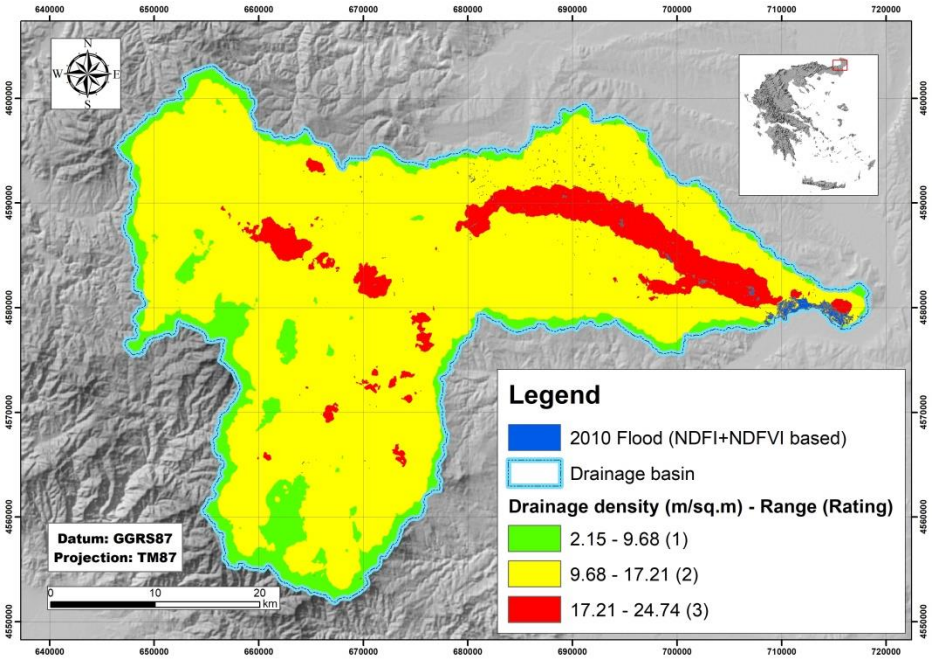

Figure 47: The data layer of the inundated areas of the 2010 flood event (calculated with the aid of NDFI and NDFVI indices) has been superimposed upon the flood susceptibility classes of the drainage density data layer.

The 2010 flood extent was chosen for that purpose, because the measurements from the gauging station on Didymoteicho's bridge confirmed that during the date and time that the ENVISAT/ASAR's flood image was taken on 16/2/2010, Erythropotamos indeed flooded. Additionally, ENVISAT/ASAR's imagery has lower spatial resolution when compared with SENTINEL-1 A/B imagery. Since the aforementioned gauging station went out of order in 2012, the only way to collect information for the 2017 and 2018 flood events was to rely on statements from members of the Department of Civil Protection of the region of Evros (C. Papapostolou, Department of Civil Protection of the region of Evros, personal communication, 2018).

Having completed the hierarchy of factors, the pairwise comparison of the factors that affect flood susceptibility was performed. The factors then formed pairs with each other and arithmetic values ranging from 1 to 8 were assigned to them according to their significance regarding the factor with which it formed the pair (Table 20) and in agreement with table 19. Concerning the arithmetic values of table 20, a value of 8 shows that a row factor is much more important than the corresponding column factor with which it has been paired. On the contrary, a value of 1 indicates that both of the paired factors are equally important. Moreover, table 21, which was used for the calculation of the weights for each factor, was constructed by applying the arithmetic mean method to the results of table 20.

To sum up, table 22 presents synoptically the factors, the classes of flood susceptibility into which they were classified, the rating that was assigned for each class and the weight that was calculated for each factor via the application of AHP methodology (Kazakis et al. 2015).

In order to check the consistency of the eigenvector matrix of AHP, the consistency ratio was calculated according to the following formula:

$$CR = \frac{CI}{RI} \quad (18)$$

Table 20: Pairwise comparison of the factors that affect flood susceptibility.

	Elevation	**Slope angle**	**Distance from streams**	**Drainage Density**	**Geology**	**Land Use/ Cover**	**TWI**	**Rainfall**
Elevation	1	2	3	4	5	6	7	8
Slope angle	1/2	1	2	3	4	5	6	7
Distance from streams	1/3	1/2	1	2	3	4	5	6
Drainage Density	1/4	1/3	1/2	1	2	3	4	5
Geology	1/5	1/4	1/3	1/2	1	2	3	4
Land Use / Cover	1/6	1/5	1/4	1/3	1/2	1	2	3
TWI	1/7	1/6	1/5	1/4	1/3	1/2	1	2
Rainfall	1/8	1/7	1/6	1/5	1/4	1/3	1/2	1
Total	2.718	4.593	7.5	11.28	16.08	21.83	28.5	36

In mathematic formula (18), CR stands for consistency ratio, CI stands for consistency index, and RI stands for random index. RI depends on the number of factors that are used to perform AHP and in our case, for an 8 by 8 matrix, RI= 1.41 (Table 23), while RI can be calculated by the following equation:

$$CI = \frac{\lambda_{max} - n}{n - 1} \quad (19)$$

In equation (19), λ_{max} is the maximum eigenvalue of the comparison matrix and n is the number of factors. In the current study, λ_{max} = 8.41 and n = 8, therefore CR=0.042. According to Saaty (1980), if CR is less than 0.1, then the weights' consistency is affirmed.

Table 21: Calculation of the factor weights with the use of the arithmetic mean method.

	Elevation	**Slope angle**	**Distance from streams**	**Drainage Density**	**Geology**	**Land Use/Cover**	**TWI**	**Rainfall**	**Mean**
Elevation	0.368	0.435	0.403	0.355	0.311	0.275	0.246	0.222	0.327 (32.7%)
Slope angle	0.184	0.218	0.268	0.266	0.249	0.229	0.211	0.194	0.227 (22.7 %)
Distance from streams	0.123	0.109	0.134	0.177	0.187	0.183	0.175	0.167	0.157 (15.7 %)
Drainage Density	0.092	0.073	0.067	0.089	0.124	0.137	0.14	0.139	0.108 (10.8 %)
Geology	0.074	0.054	0.045	0.044	0.062	0.092	0.105	0.111	0.073 (7.3 %)
Land Use/Cover	0.061	0.044	0.034	0.03	0.031	0.046	0.07	0.083	0.05 (5 %)
TWI	0.053	0.036	0.027	0.022	0.021	0.023	0.035	0.056	0.034 (3.4 %)
Rainfall	0.046	0.031	0.022	0.018	0.016	0.015	0.018	0.028	0.024 (2.4 %)
Total									1 (100%)

Finally, the data layers for each factor were added together in accordance with the following formula (20):

$$S = w_1X_1 + w_2X_2 + w_3X_3 + w_4X_4 + w_5X_5 + w_6X_6 + w_7X_7 + w_8X_8 \quad (20)$$

In formula (20), S is the value for each pixel of the final flood susceptibility map of the study area. Variables W_1, W_2, W_3, W_4, W_5, W_6, W_7 and W_8 are the weight values for each factor and variables X_1, X_2, X_3, X_4, X_5, X_6, X_7 and X_8 are the rating values for each pixel according to the factor to which it is referred.

Table 22: Synoptic table presenting the factors, their flood susceptibility classes, the rating that was assigned for each class and the weight for each factor that was assigned through AHP methodology.

Factor	Class	Rating	Weight
Elevation (m)	> 600	1	0.327
	150 - 600	2	
	0 - 150	3	
Slope angle (°)	> 15	1	0.227
	2 - 5	2	
	0 - 2	3	
Distance from streams (m)	> 500	1	0.157
	200 - 500	2	
	0 - 200	3	
Drainage density (m/m^2)	2.15 - 9.68	1	0.108
	9.68 - 17.21	2	
	17.21 - 24.74	3	
Geology	Permeable formations	1	0.073
	Semi - permeable formations	2	
	Impermeable formations	3	
Land Cover	Forests and wetlands	1	0.05
	Agricultural areas and water bodies	2	
	Artificial surfaces	3	
TWI	-0.22 - 6.06	1	0.034
	6.06 - 12.34	2	
	12.34 - 18.62	3	
Rainfall (mm)	579.34 - 623.25	1	0.024
	623.25 - 667.18	2	
	667.18 - 711.10	3	

Table 23: Random index (RI) used to calculate consistency ratios (CR) (Saaty 1980).

n	**1**	**2**	**3**	**4**	**5**	**6**	**7**	**8**	**9**	**10**
RI	0	0	0.58	0.90	1.12	1.24	1.32	1.41	1..45	1.49

The resulting susceptibility map was validated by calculating, with the aid of ArcGIS's geoprocessing routines, the proportion of the inundated areas of the April 2017 and March 2018 flood events that intersected with its high susceptibility areas.

3.4.2 Determination of the hierarchy of factors with the aid of flood hazard mapping

In this occasion the importance of each factor was determined according to the proportion of the inundated areas, predicted by flood hazard mapping, which intersected with each factor's high susceptibility class (Figures 48 – 71 and Table 24). To this end, the following flood hazard mapping return period scenarios were employed: 1) 50 years (total area of 44.27 km^2), 2) 100 years (total area of 45.16 km^2) and 3) 500 years (total area of 46.46 km^2). Additionally, the selection of the aforementioned flood hazard mapping scenarios also aimed in examining whether there is a correlation between the hierarchy of factors and the return period of a flood phenomenon.

Table 24: Proportion of the inundated area predicted by each scenario of flood hazard mapping that intersects with each factor's high susceptibility class.

Factor	**Extent of inundated area [km^2 (%)]**		
	50 year return period	**100 year return period**	**500 year return period**
Land Use / Cover	0.5 (1.13%)	0.51 (1.13%)	0.54 (1.16%)
TWI	2.98 (6.73%)	3.01 (6.67%)	3.05 (6.56%)
Geology	15.12 (1.13%)	15.39 (1.13%)	15.38 (1.13%)
Distance from streams	31.29 (34.15%)	31.87 (34.08%)	32.75 (33.1%)
Rainfall	0.03 (0.07%)	0.03 (0.07%)	0.03 (0.06%)
Slope Angle	24.4 (55.12%)	24.77 (54.85%)	25.27 (54.39%)
Drainage Density	24.8 (56.02%)	25.26 (55.93%)	25.88 (55.7%)
Elevation	33.36 (75.36%)	34.05 (75.4%)	35.04 (75.42%)

This concept was based on the idea that since flood hazard mapping indicates areas that are likely to become inundated, these areas are located where the most favourable conditions for most factors coexist. Thus, the more a high susceptibility class of a factor or indicator is encountered within the predicted areas of flood hazard mapping, the more influential this factor or indicator is in terms of flood susceptibility.

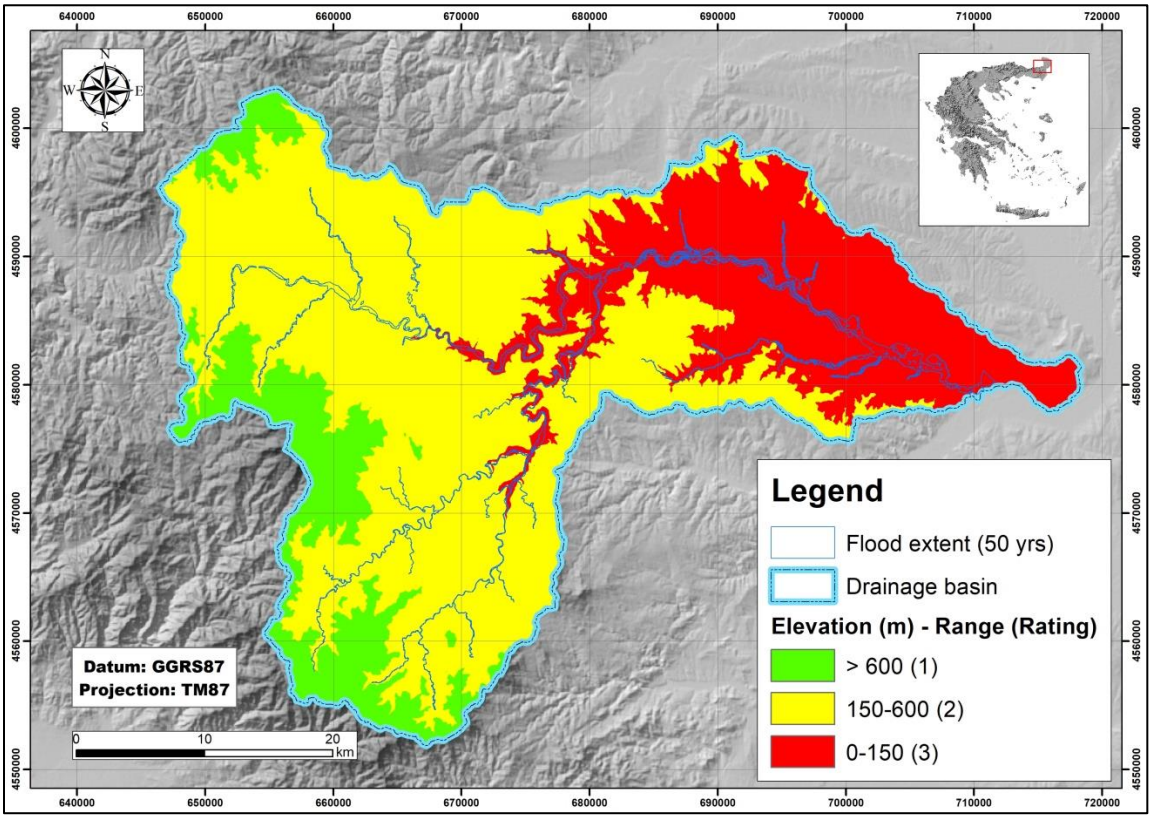

Figure 48: The data layer of the inundated areas that were predicted by flood hazard mapping (50-year return period scenario) has been superimposed upon the flood susceptibility classes of the elevation data layer.

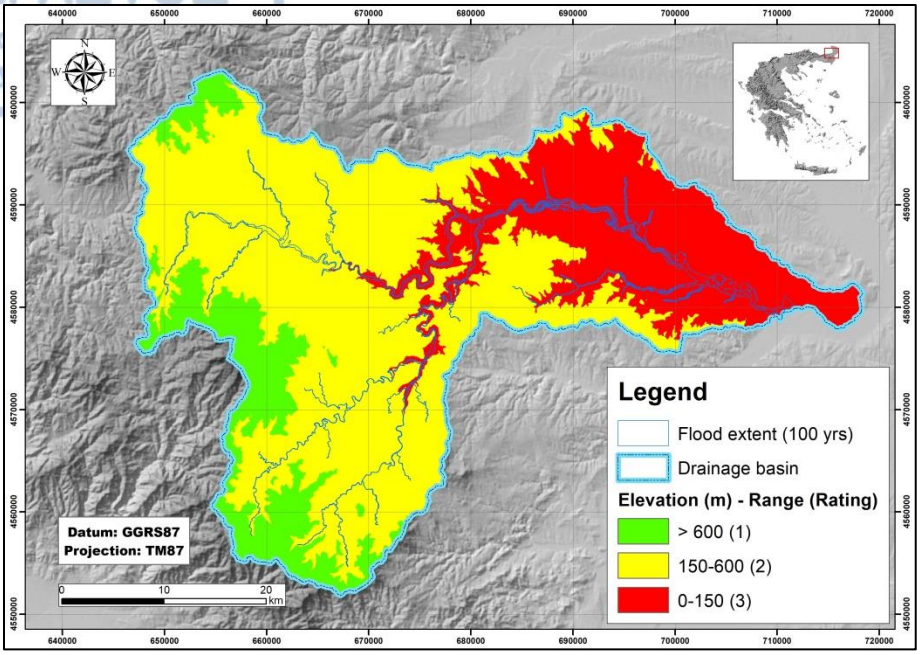

Figure 49: The data layer of the inundated areas that were predicted by flood hazard mapping (100-year return period scenario) has been superimposed upon the flood susceptibility classes of the elevation data layer.

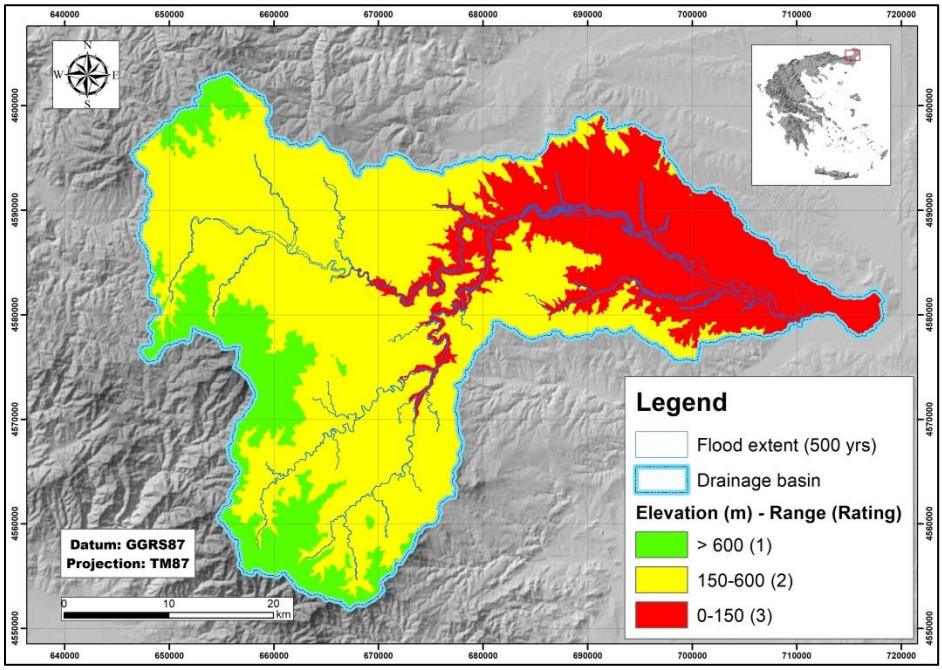

Figure 50: The data layer of the inundated areas that were predicted by flood hazard mapping (500-year return period scenario) has been superimposed upon the flood susceptibility classes of the elevation data layer.

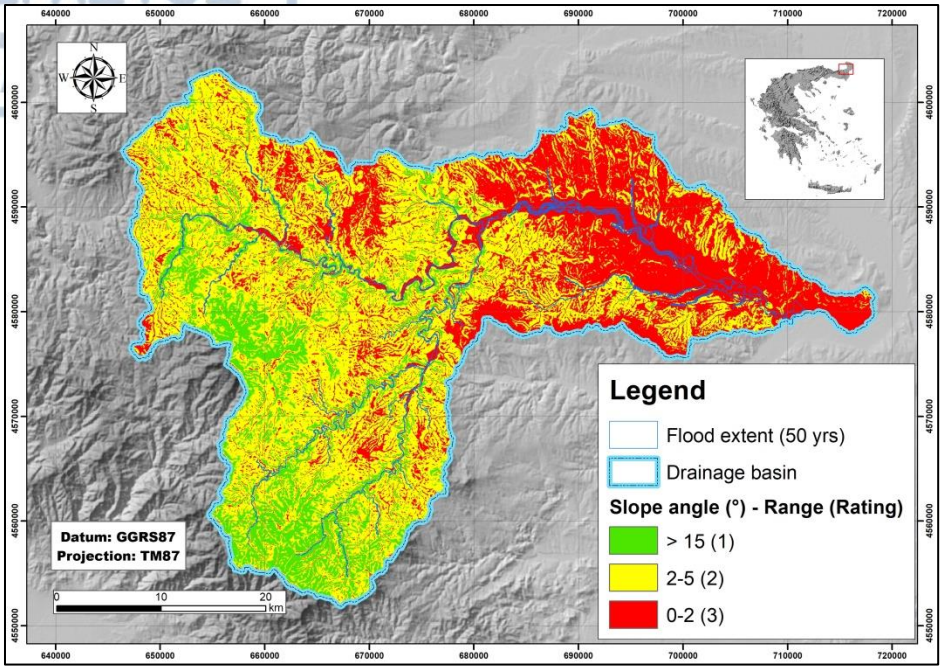

Figure 51: The data layer of the inundated areas that were predicted by flood hazard mapping (50-year return period scenario) has been superimposed upon the flood susceptibility classes of the slope angle data layer.

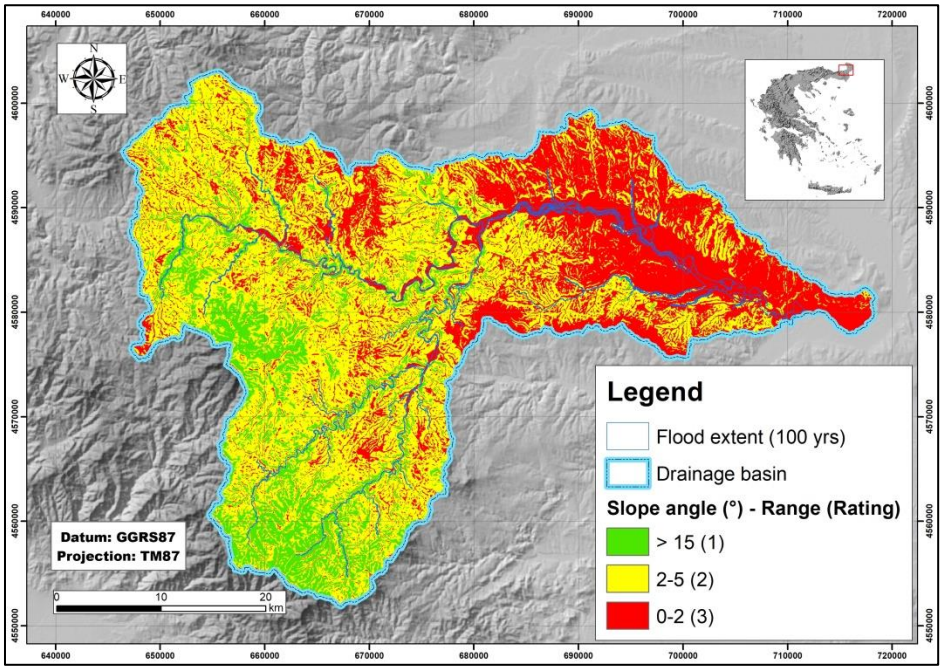

Figure 52: The data layer of the inundated areas that were predicted by flood hazard mapping (100-year return period scenario) has been superimposed upon the flood susceptibility classes of the slope angle data layer.

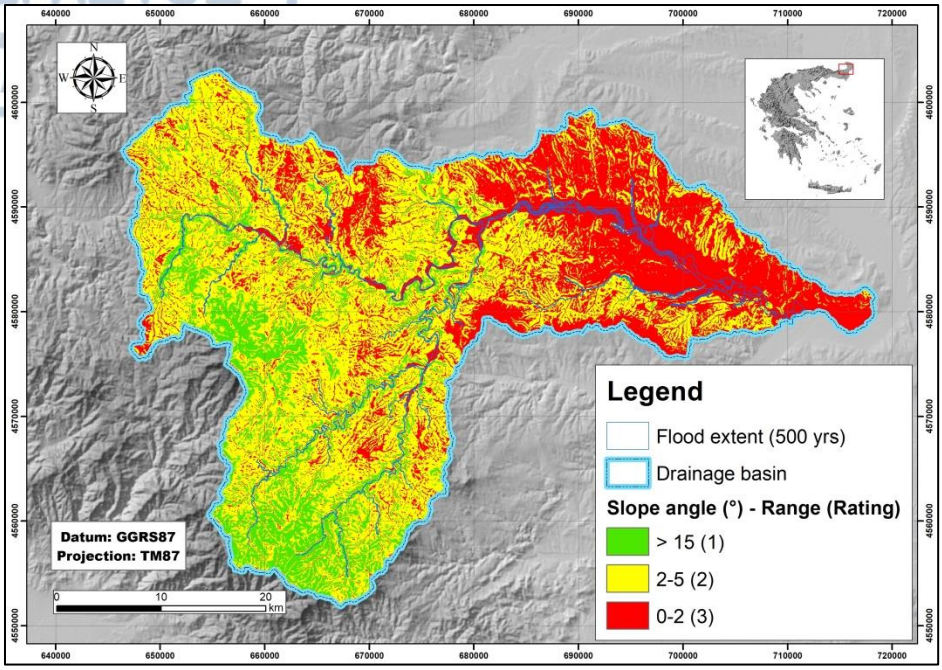

Figure 53: The data layer of the inundated areas that were predicted by flood hazard mapping (500-year return period scenario) has been superimposed upon the flood susceptibility classes of the slope angle data layer.

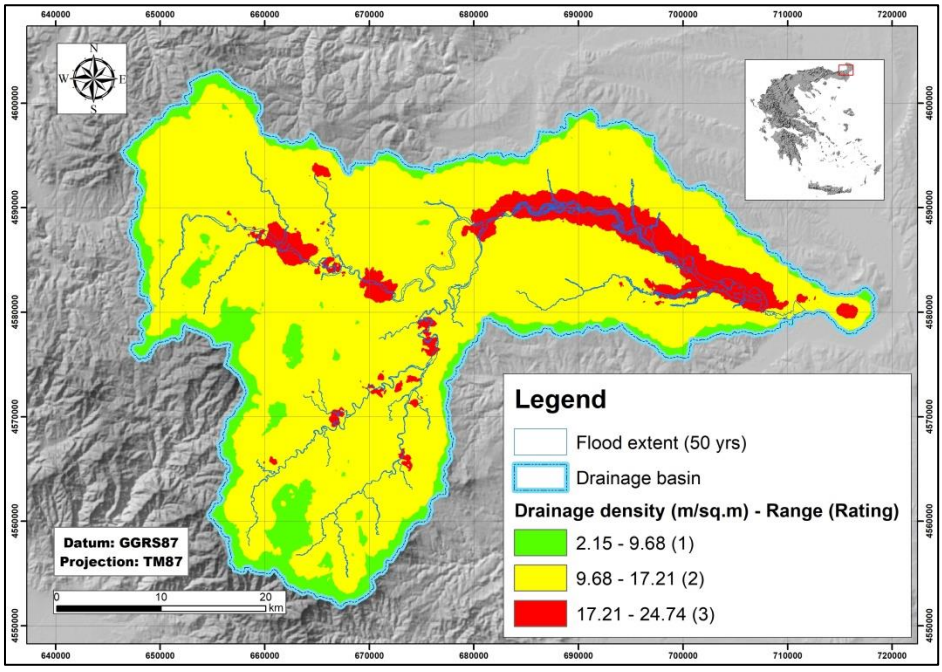

Figure 54: The data layer of the inundated areas that were predicted by flood hazard mapping (50-year return period scenario) has been superimposed upon the flood susceptibility classes of the drainage density data layer.

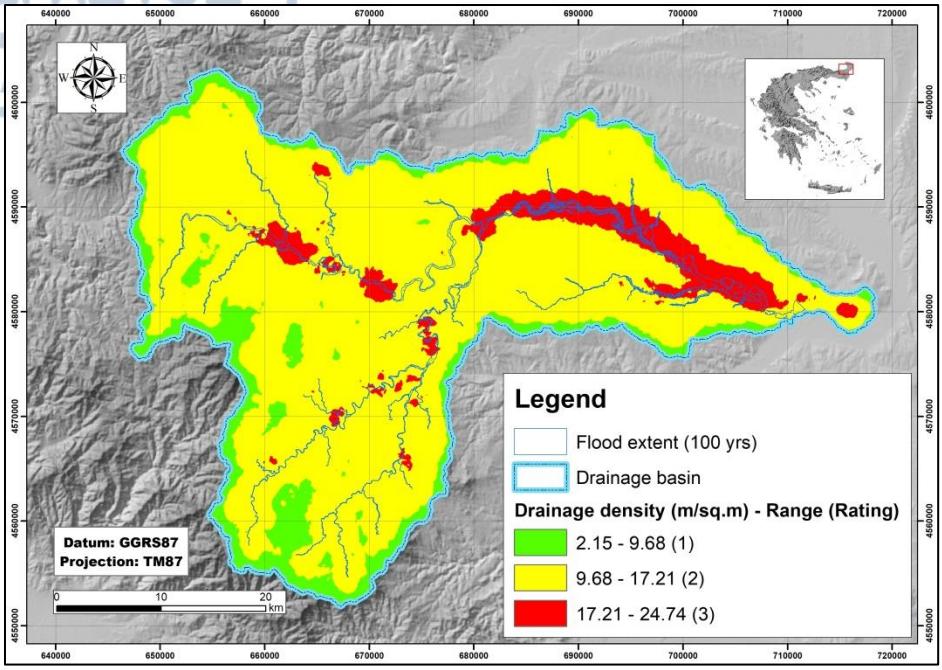

Figure 55: The data layer of the inundated areas that were predicted by flood hazard mapping (100-year return period scenario) has been superimposed upon the flood susceptibility classes of the drainage density data layer.

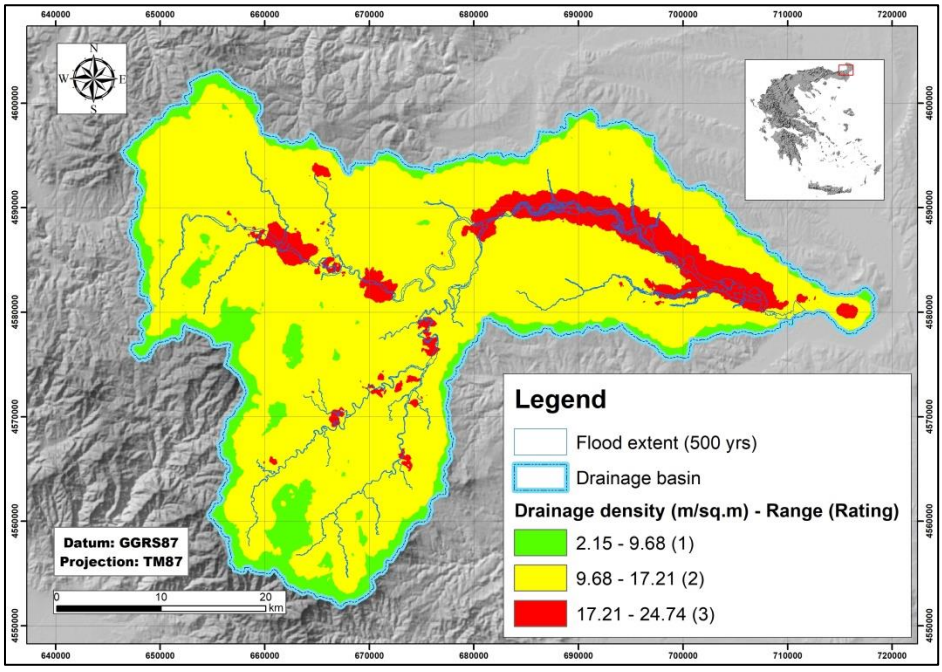

Figure 56: The data layer of the inundated areas that were predicted by flood hazard mapping (500-year return period scenario) has been superimposed upon the flood susceptibility classes of the drainage density data layer.

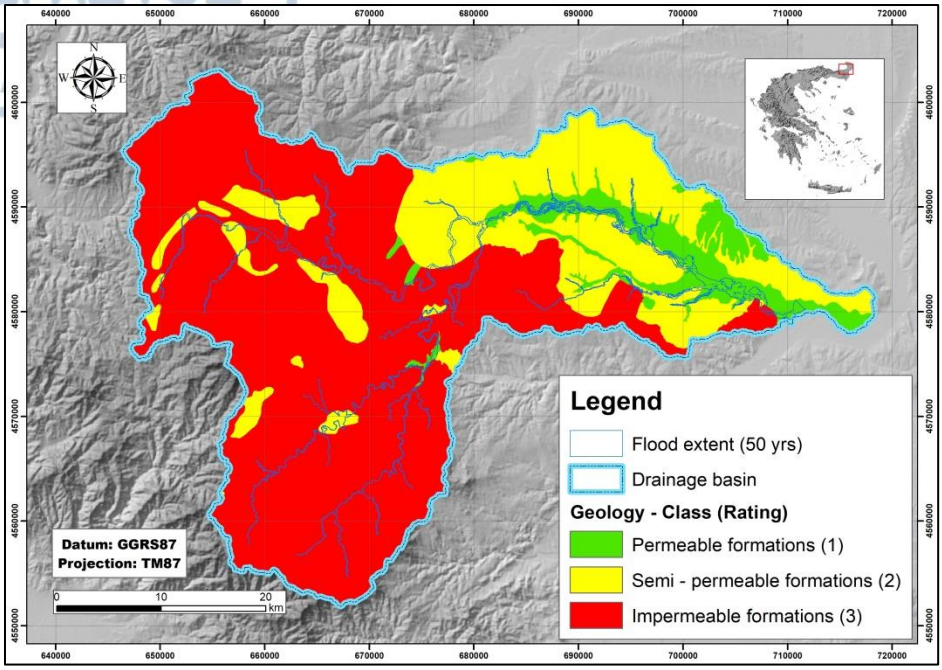

Figure 57: The data layer of the inundated areas that were predicted by flood hazard mapping (50-year return period scenario) has been superimposed upon the flood susceptibility classes of the geology data layer.

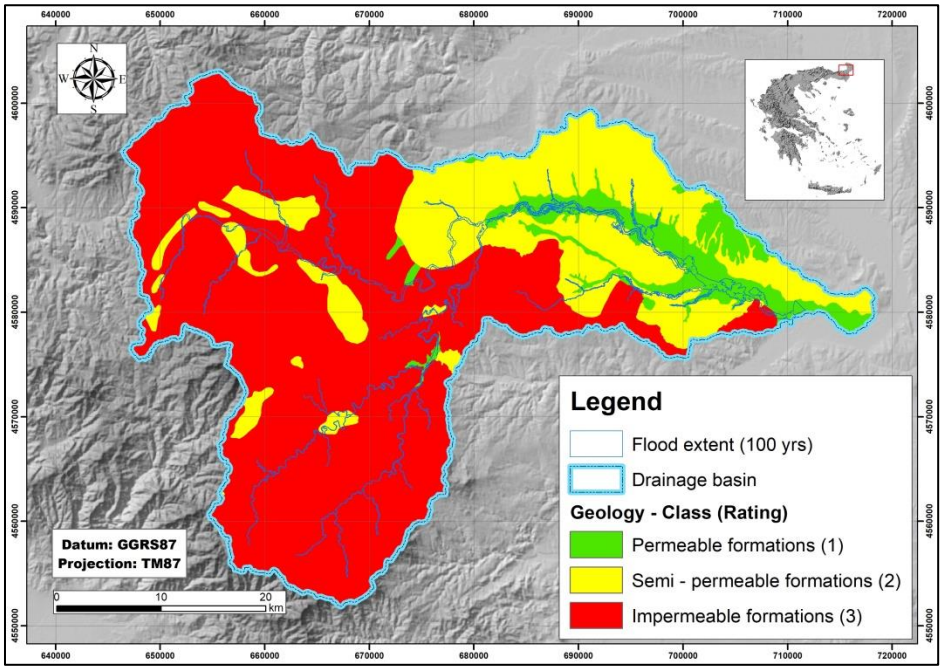

Figure 58: The data layer of the inundated areas that were predicted by flood hazard mapping (100-year return period scenario) has been superimposed upon the flood susceptibility classes of the geology data layer.

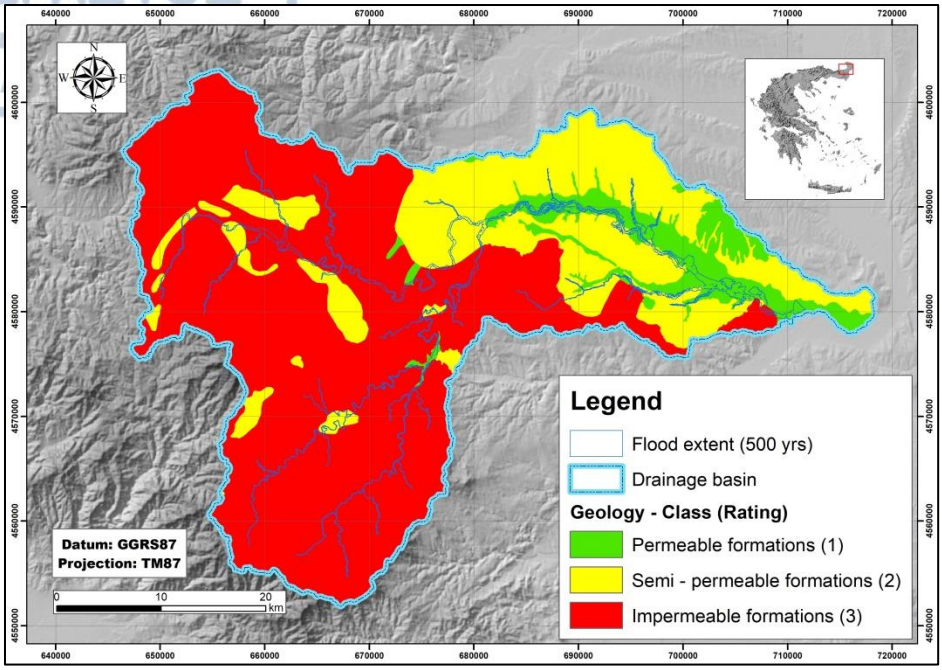

Figure 59: The data layer of the inundated areas that were predicted by flood hazard mapping (500-year return period scenario) has been superimposed upon the flood susceptibility classes of the geology data layer.

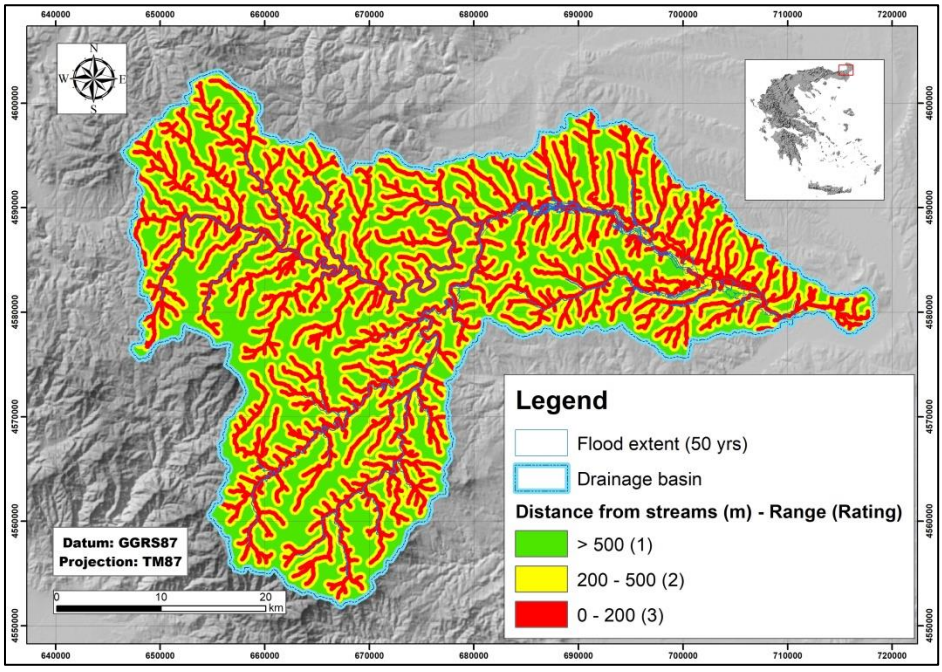

Figure 60: The data layer of the inundated areas that were predicted by flood hazard mapping (50-year return period scenario) has been superimposed upon the flood susceptibility classes of the distance from streams data layer.

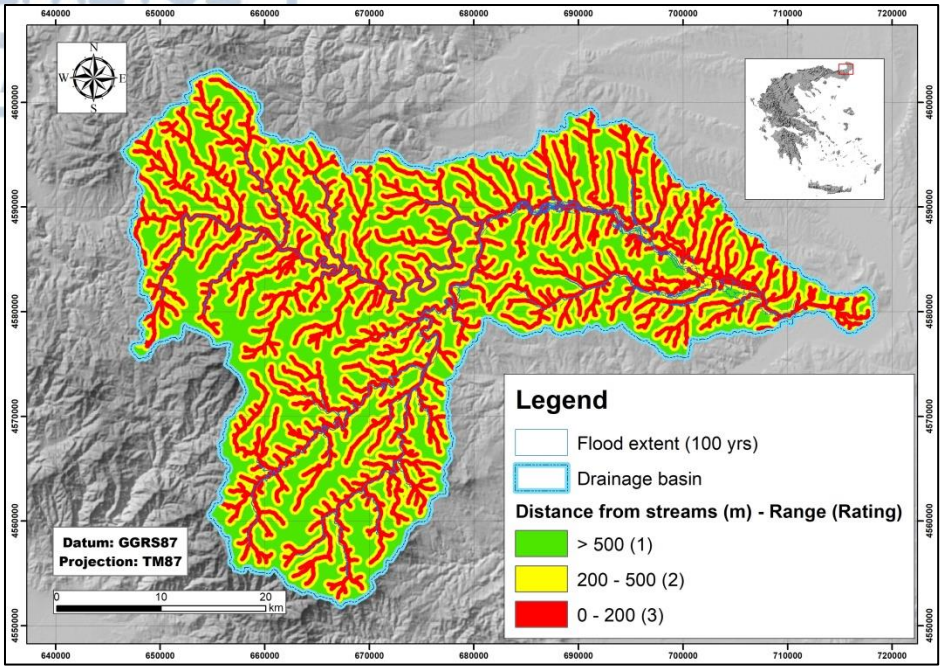

Figure 61: The data layer of the inundated areas that were predicted by flood hazard mapping (100-year return period scenario) has been superimposed upon the flood susceptibility classes of the distance from streams data layer.

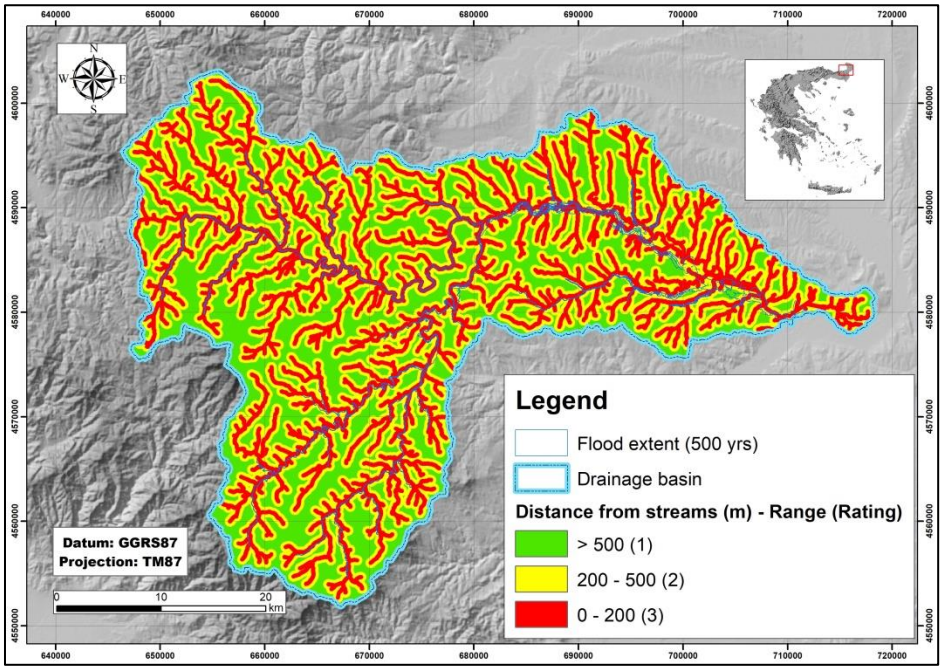

Figure 62: The data layer of the inundated areas that were predicted by flood hazard mapping (500-year return period scenario) has been superimposed upon the flood susceptibility classes of the distance from streams data layer.

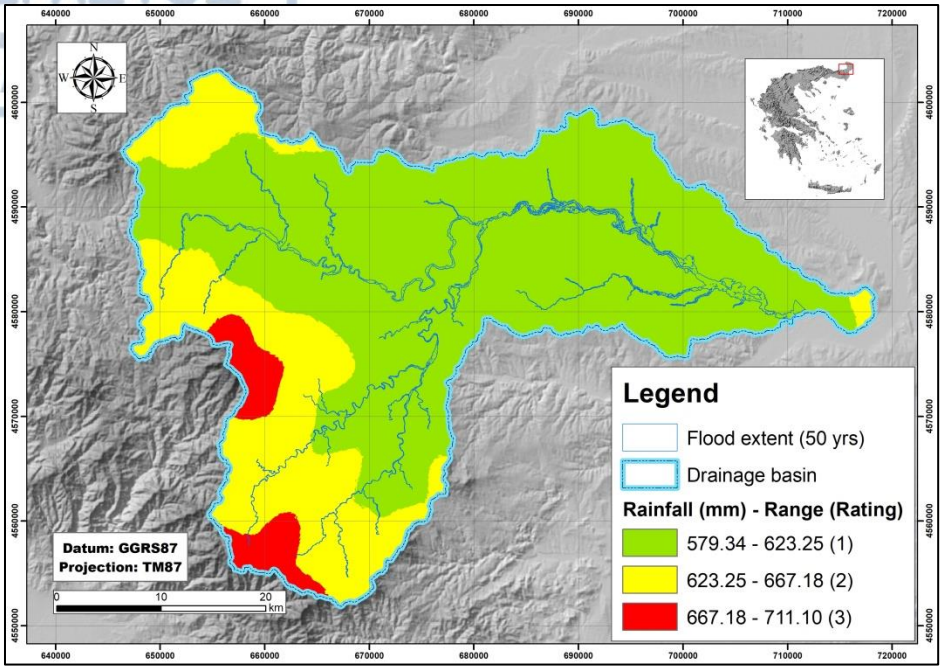

Figure 63: The data layer of the inundated areas that were predicted by flood hazard mapping (50-year return period scenario) has been superimposed upon the flood susceptibility classes of the rainfall data layer.

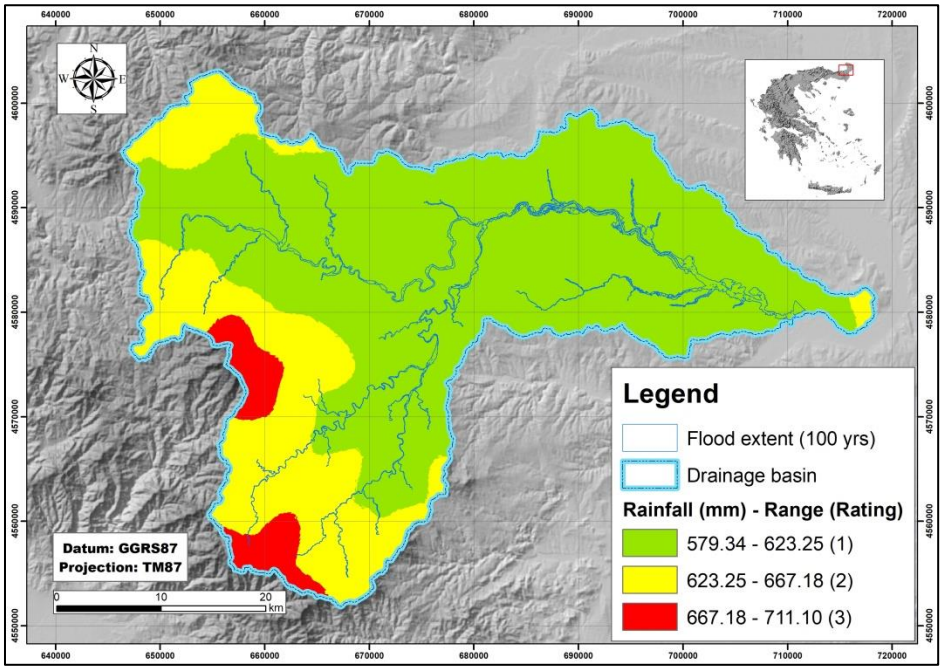

Figure 64: The data layer of the inundated areas that were predicted by flood hazard mapping (100-year return period scenario) has been superimposed upon the flood susceptibility classes of the rainfall data layer.

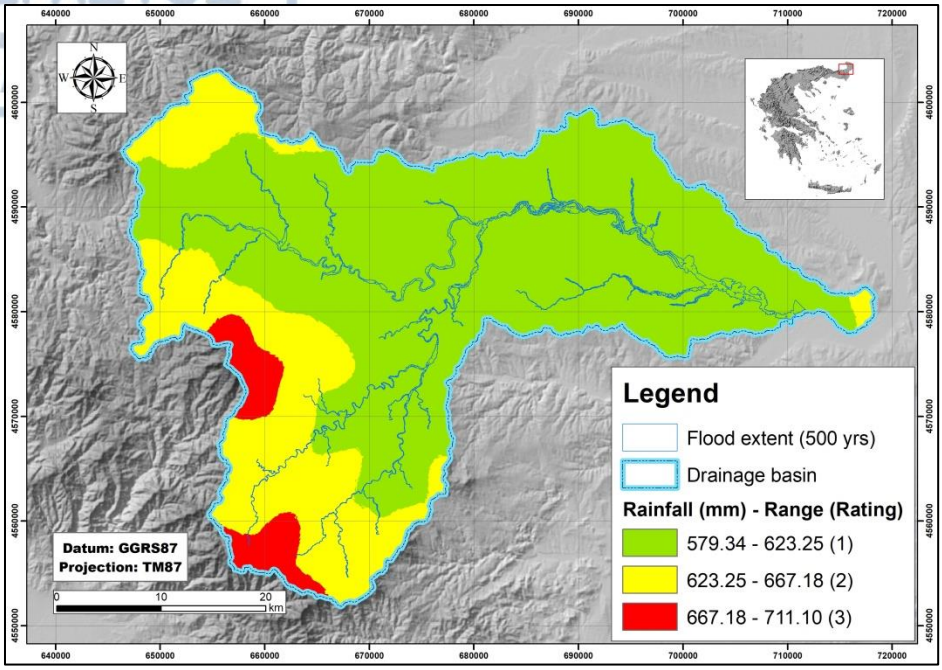

Figure 65: The data layer of the inundated areas that were predicted by flood hazard mapping (500-year return period scenario) has been superimposed upon the flood susceptibility classes of the rainfall data layer.

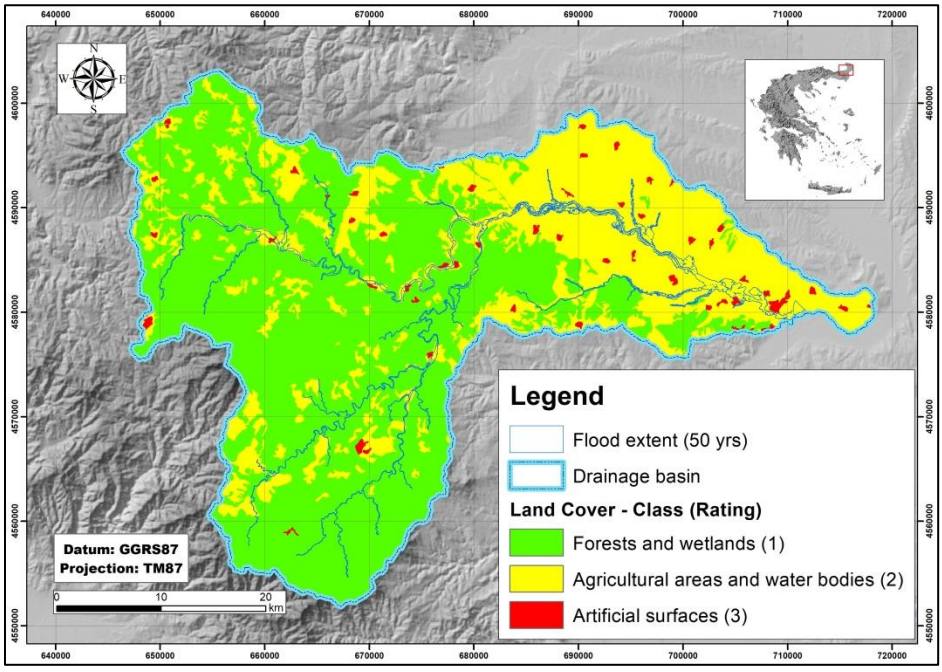

Figure 66: The data layer of the inundated areas that were predicted by flood hazard mapping (50-year return period scenario) has been superimposed upon the flood susceptibility classes of the land cover data layer.

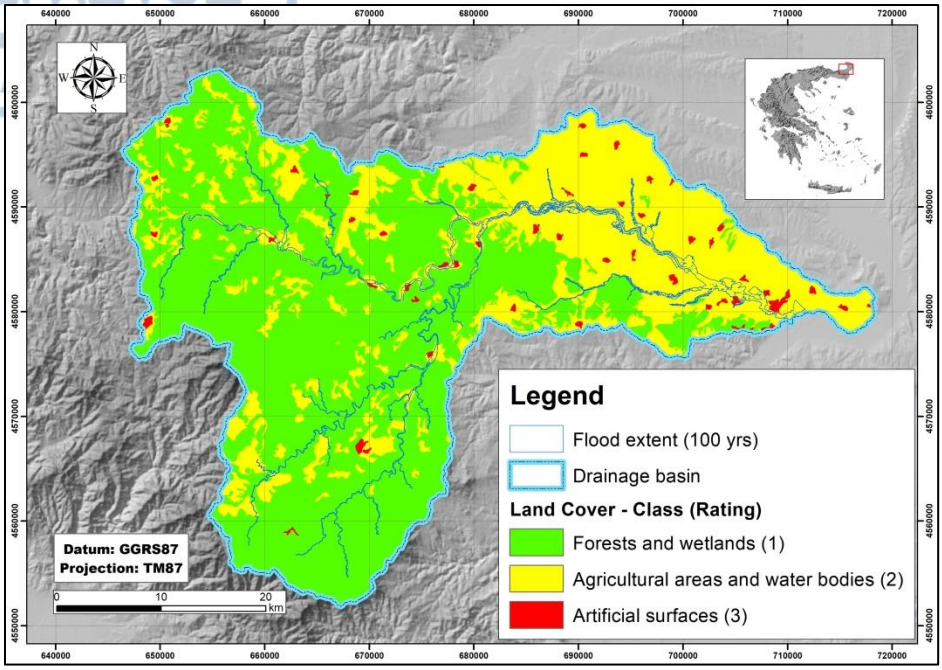

Figure 67: The data layer of the inundated areas that were predicted by flood hazard mapping (100-year return period scenario) has been superimposed upon the flood susceptibility classes of the land cover data layer.

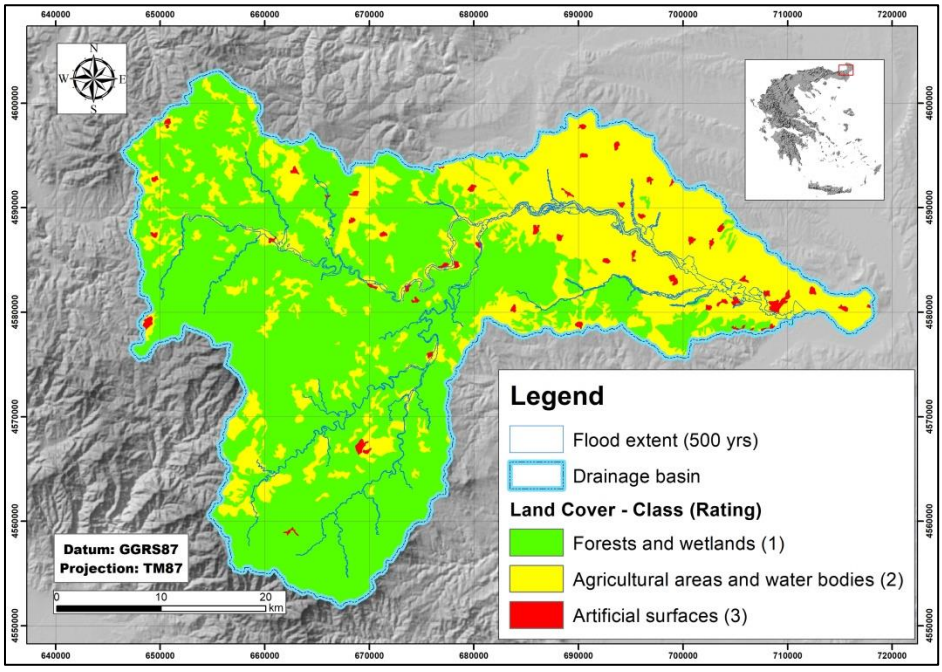

Figure 68: The data layer of the inundated areas that were predicted by flood hazard mapping (500-year return period scenario) has been superimposed upon the flood susceptibility classes of the land cover data layer.

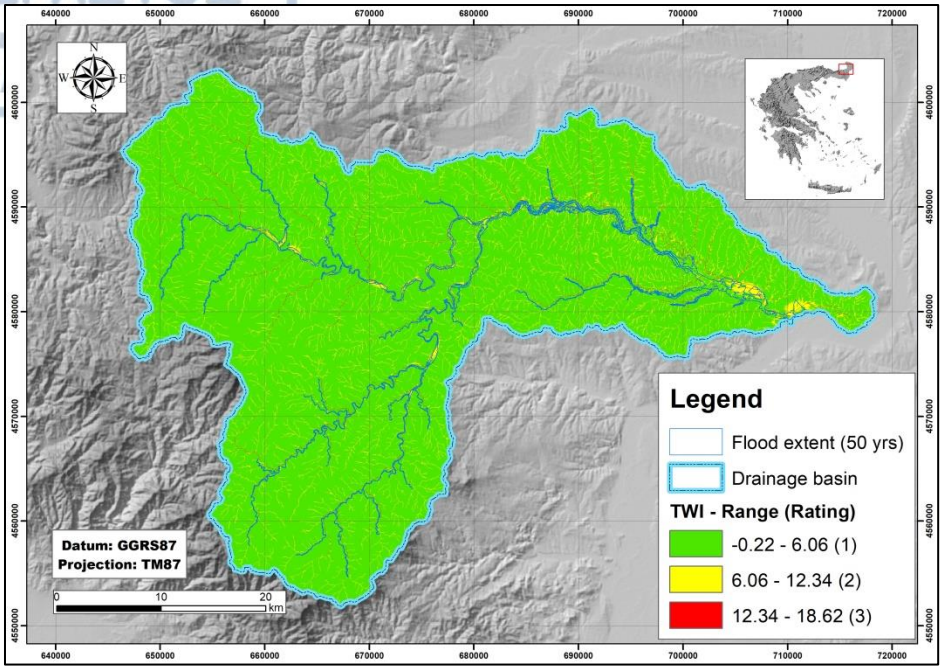

Figure 69: The data layer of the inundated areas that were predicted by flood hazard mapping (50-year return period scenario) has been superimposed upon the flood susceptibility classes of the TWI data layer.

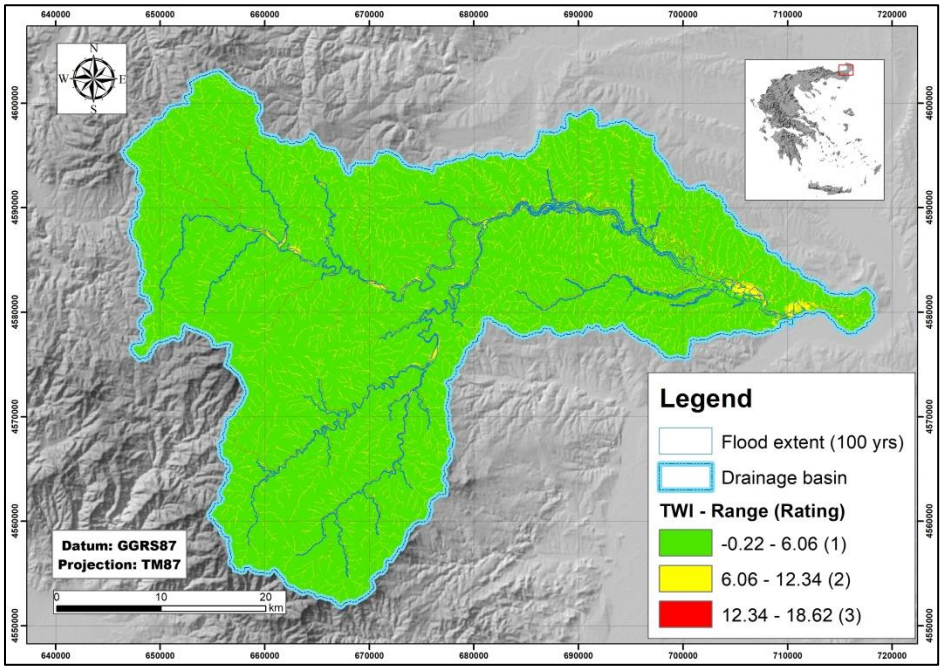

Figure 70: The data layer of the inundated areas that were predicted by flood hazard mapping (100-year return period scenario) has been superimposed upon the flood susceptibility classes of the TWI data layer.

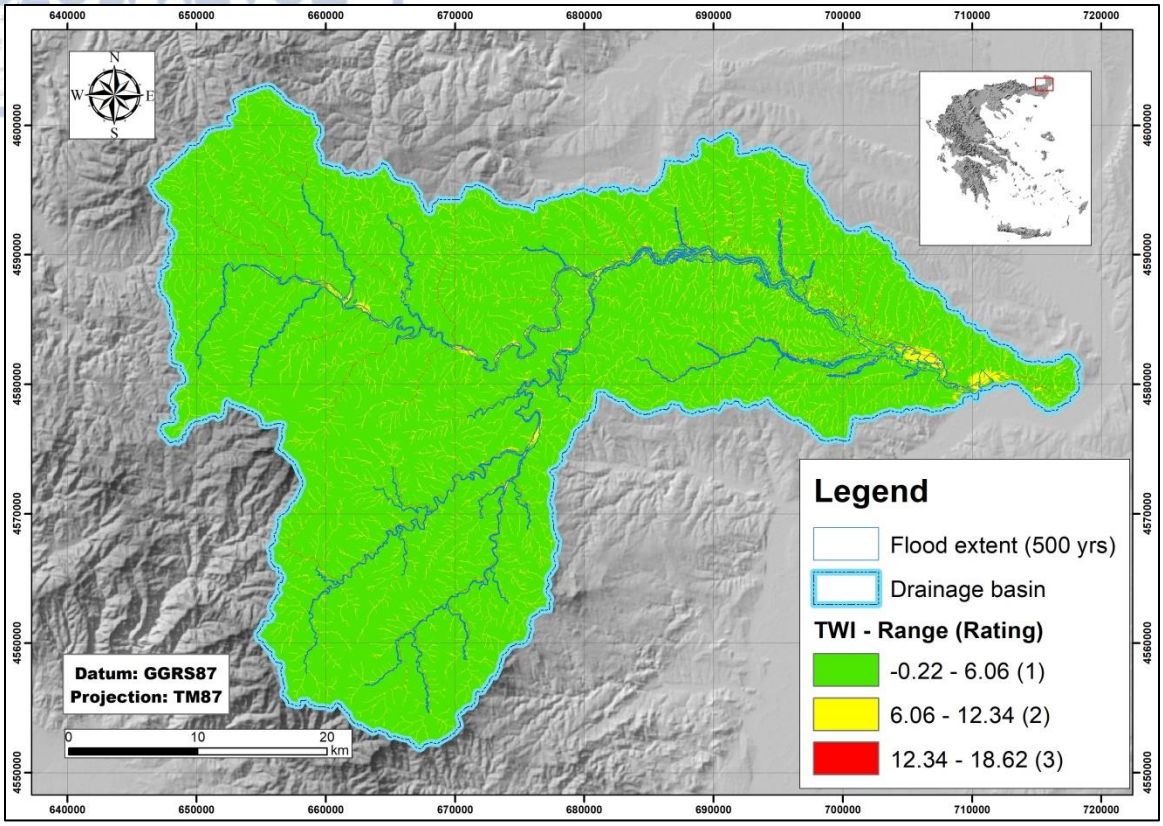

Figure 71: The data layer of the inundated areas that were predicted by flood hazard mapping (500-year return period scenario) has been superimposed upon the flood susceptibility classes of the TWI data layer.

With the completion of the hierarchy of factors, the pairwise comparison of the factors that affect flood susceptibility was carried out. The factors were paired with each other, in agreement with table 24, forming the pairwise comparison table 25 and then, by applying the arithmetic mean method on its results, table 26 was produced.

Moreover, table 27 sums up the factors, the classes of flood susceptibility into which they were classified, the rating that was assigned for each class and the weight that was calculated for each factor via the application of AHP methodology (Kazakis et al. 2015).

Table 25: Pairwise comparison of the factors that affect flood susceptibility.

	Elevation	**Distance from streams**	**Drainage Density**	**Slope angle**	**Geology**	**TWI**	**Land Use/ Cover**	**Rainfall**
Elevation	1	2	3	4	5	6	7	8
Distance from streams	1/2	1	2	3	4	5	6	7
Drainage Density	1/3	1/2	1	2	3	4	5	6
Slope angle	1/4	1/3	1/2	1	2	3	4	5
Geology	1/5	1/4	1/3	1/2	1	2	3	4
TWI	1/6	1/5	1/4	1/3	1/2	1	2	3
Land Use / Cover	1/7	1/6	1/5	1/4	1/3	1/2	1	2
Rainfall	1/8	1/7	1/6	1/5	1/4	1/3	1/2	1
Total	2.718	4.593	7.5	11.28	16.08	21.83	28.5	36

According to equations (18), (19) and table 23, because they still refer to an 8 by 8 matrix, consistency ratio (CR) maintains its calculated value of 0.042. Since this value is less than 0.1, then the weights' consistency is still considered as affirmed.

Finally, the resulting susceptibility map was compiled by adding each factor's data layer in accordance with formula (20). Furthermore, its validation was performed by calculating, with the aid of ArcGIS's geoprocessing routines, the proportion of the inundated areas of the February 2010, April 2017 and March 2018 flood events that intersected with its high susceptibility areas.

Table 26: Calculation of the factor weights with the use of the arithmetic mean method.

	Elevation	**Distance from streams**	**Drainage Density**	**Slope angle**	**Geology**	**TWI**	**Land Use/Cover**	**Rainfall**	**Mean**
Elevation	0.368	0.435	0.403	0.355	0.311	0.275	0.246	0.222	0.327 (32.7%)
Distance from streams	0.184	0.218	0.268	0.266	0.249	0.229	0.211	0.194	0.227 (22.7 %)
Drainage Density	0.123	0.109	0.134	0.177	0.187	0.183	0.175	0.167	0.157 (15.7 %)
Slope angle	0.092	0.073	0.067	0.089	0.124	0.137	0.14	0.139	0.108 (10.8 %)
Geology	0.074	0.054	0.045	0.044	0.062	0.092	0.105	0.111	0.073 (7.3 %)
TWI	0.061	0.044	0.034	0.03	0.031	0.046	0.07	0.083	0.05 (5 %)
Land Use/Cover	0.053	0.036	0.027	0.022	0.021	0.023	0.035	0.056	0.034 (3.4 %)
Rainfall	0.046	0.031	0.022	0.018	0.016	0.015	0.018	0.028	0.024 (2.4 %)
Total									1 (100%)

Table 27: Synoptic table presenting the factors, their flood susceptibility classes, the rating that was assigned for each class and the weight for each factor that was assigned through AHP methodology.

Factor	Class	Rating	Weight
Elevation (m)	> 600	1	0.327
	150 - 600	2	
	0 - 150	3	
Distance from streams (m)	> 500	1	0.227
	200 - 500	2	
	0 - 200	3	
Drainage density (m/m^2)	2.15 - 9.68	1	0.157
	9.68 - 17.21	2	
	17.21 - 24.74	3	
Slope angle (°)	> 15	1	0.108
	2 - 5	2	
	0 - 2	3	
Geology	Permeable formations	1	0.073
	Semi - permeable formations	2	
	Impermeable formations	3	
TWI	-0.22 - 6.06	1	0.05
	6.06 - 12.34	2	
	12.34 - 18.62	3	
Land Cover	Forests and wetlands	1	0.034
	Agricultural areas and water bodies	2	
	Artificial surfaces	3	
Rainfall (mm)	579.34 - 623.25	1	0.024
	623.25 - 667.18	2	
	667.18 - 711.10	3	

3.5 Comparison between the zone of potential high flood risk that is suggested by the Ministry of Environment and Energy and the results of inundation, flood hazard and susceptibility mapping

In 2014 the Ministry of Environment and Energy compiled preliminary flood hazard and risk maps for the drainage basin of Evros River (Ministry of Environment and Energy 2014) in accordance with the 2007/60/EC Directive. The part of the zone of potential high flood risk that is included in these maps and intersected with the drainage basin of Erythropotamos River was compared with the results of inundation, flood hazard and susceptibility mapping, with the use of ArcGIS™ software, in order to examine whether there is spatial correlation between the aforementioned data layers.

3.6 Comparison between inundation mapping and flood hazard mapping

The results of flood hazard mapping, concerning the 0,5-year and 50,6-year return period scenarios, were tested for their accuracy against the results of inundation mapping of the 2010 flood event that were produced by utilizing the methodology established by Cian et al. (2018). To this end, the geometric data of the part of the drainage network that were used for each scenario' s hydraulic analysis lead to the examination of two cases: 1) hydraulic analysis that involved solely the thalweg and 2) hydraulic analysis that involved the river reaches of the 5^{th} order and higher. The selection of the return periods was based on the gauges of Didymoteicho's station, which indicated that the 0.5-year return period scenario corresponded with the flood discharge value that was gauged by Didymoteicho's station during the time that the ENVISAT/ASAR image was taken on 16/2/2010. Likewise, the 50.6-year return period scenario was selected on the grounds of corresponding to the return period of the maximum flood discharge that was gauged by Didymoteicho's station during the flood event, which was observed almost 24 hours before the time that the ENVISAT/ASAR "crisis image" was taken.

3.7 Comparison between flood susceptibility mapping and flood hazard mapping

The flood extent areas that were produced, with the aid of HEC-RAS and ArcGIS's extension Hec-GeoRAS, for the 50-year (high probability), 100-year (high probability) and 500-year (high probability) scenarios were compared with the areas of high flood susceptibility. To this end, the geometric data of the part of the drainage network that were used for each scenario's hydraulic analysis involved the river reaches of the 5th order and higher. This procedure was carried out in order to discern the spatial correlation between the aforementioned data layers.

3.8 Comparison between inundation mapping and the combination of flood susceptibility and hazard mapping

This procedure involved the union of the data layers of high flood susceptibility with each of the predicted inundated areas of the 50-year (high probability), 100-year (high probability) and 500-year (high probability) scenarios, with the use of ArcGIS's Geoprocessing tools. Moreover, the geometric data of the part of the drainage network that were used for each scenario's hydraulic analysis involved the river reaches of the 5th order and higher. Each of the resulting unified data layers was then compared with the data layer that unified all inundation mapping results (2010, 2017 and 2018 floods) that were produced by applying the methodology by Cian et al. (2018). This test was performed in order to discern whether the combination of flood susceptibility and hazard mapping can be used to improve their individual predictions of inundated areas at drainage basin scale.

4. Results

4.1 Inundation mapping results

According to the results that were produced by flood extent mapping, the inundated areas within Erytropotamos' drainage basin, regarding the 2010 flood event, covered a total of 15.75 km^2, regarding the application of ESA's (2008) suggested methodology (Figures 72 and 73).

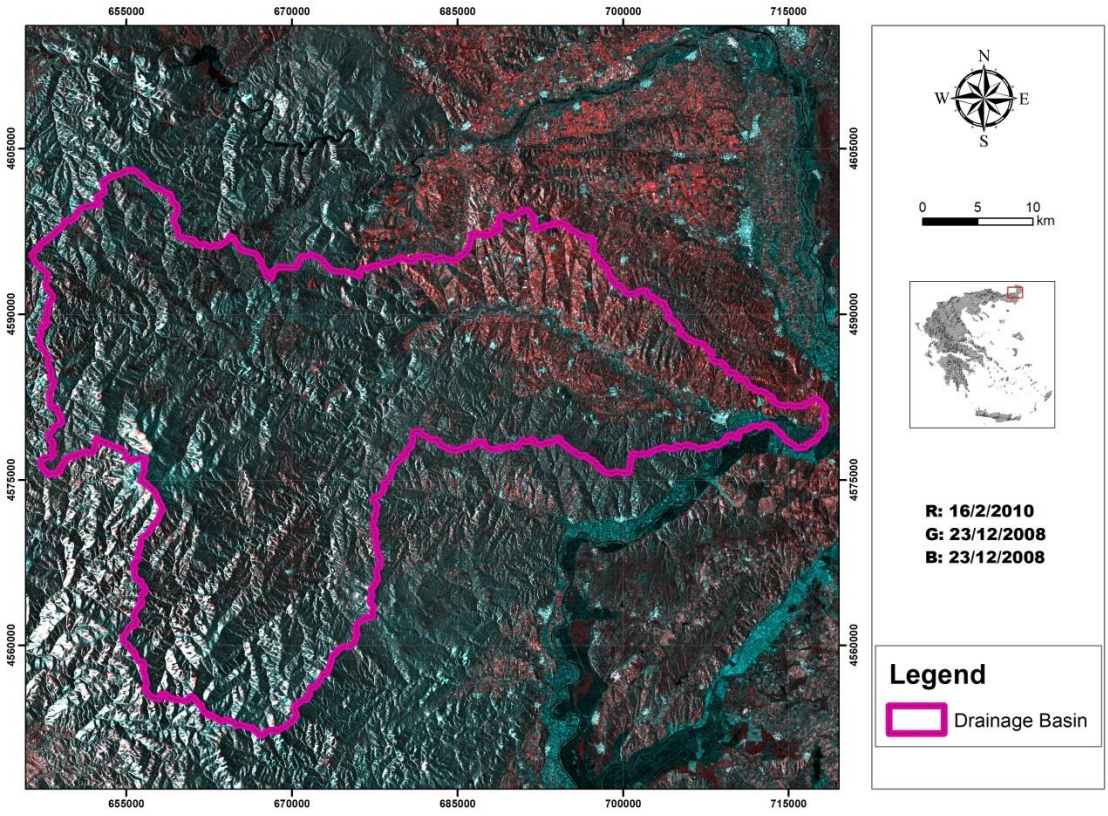

Figure 72: RGB: (16/2/2010, 23/12/2008, 23/12/2008) false color multitemporal radar image. In areas that are flooded, pixels appear bright cyan, while permanent water bodies appear in dark tones.

On the other hand, the results of flood extent mapping for the 2010 flood event, that were produced with the application of the Cian et al. (2018) methodology, indicate that the inundated areas covered a total of 6.84 km^2 (Figures 74 and 75). Moreover, the inundated areas of the flood events that occurred on April 2017 and March 2018 covered a total extent of 18.23 km^2 (Figures 76 and 77) and 20.60 km^2 (Figures 78 and 79)

respectively. The proportions of the inundated areas that were detected in open-land flooded areas and as shallow water in short vegetation areas are presented in more detail on Table 28.

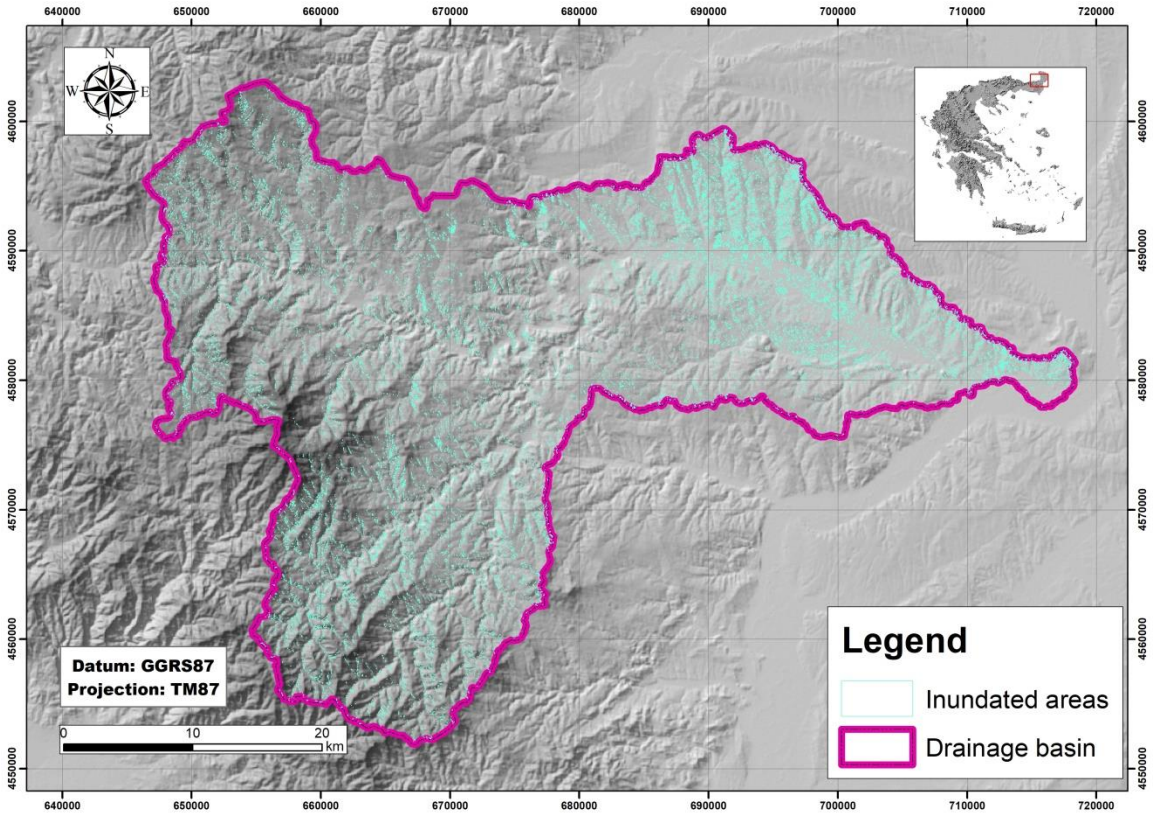

Figure 73: The 2010 inundated areas data layer that was produced via the application of ESA's (2008) suggested methodology.

The inundated areas between the 2017 and 2018 floods cover a common area of 18.06 km^2, while the common area between all the inundated areas that were produced by Cian et al. (2018) methodology covers an extent of 1.39 km^2. Additionally, the total inundated area that is covered by the combination of all flood events that were employed by Cian et al. (2018) methodology is 25.16 km^2.

Table 28: Flood extents of the inundated areas for February 2010, April 2017 and March 2018 flood events.

Flood event	NDFI based inundated area (km^2)	NDFVI based inundated area (km^2)	Total inundated area (km^2)
2010 February	6.49	0.35	6.84
2017 April	17.52	0.71	18.23
2018 March	19.28	1.32	20.60

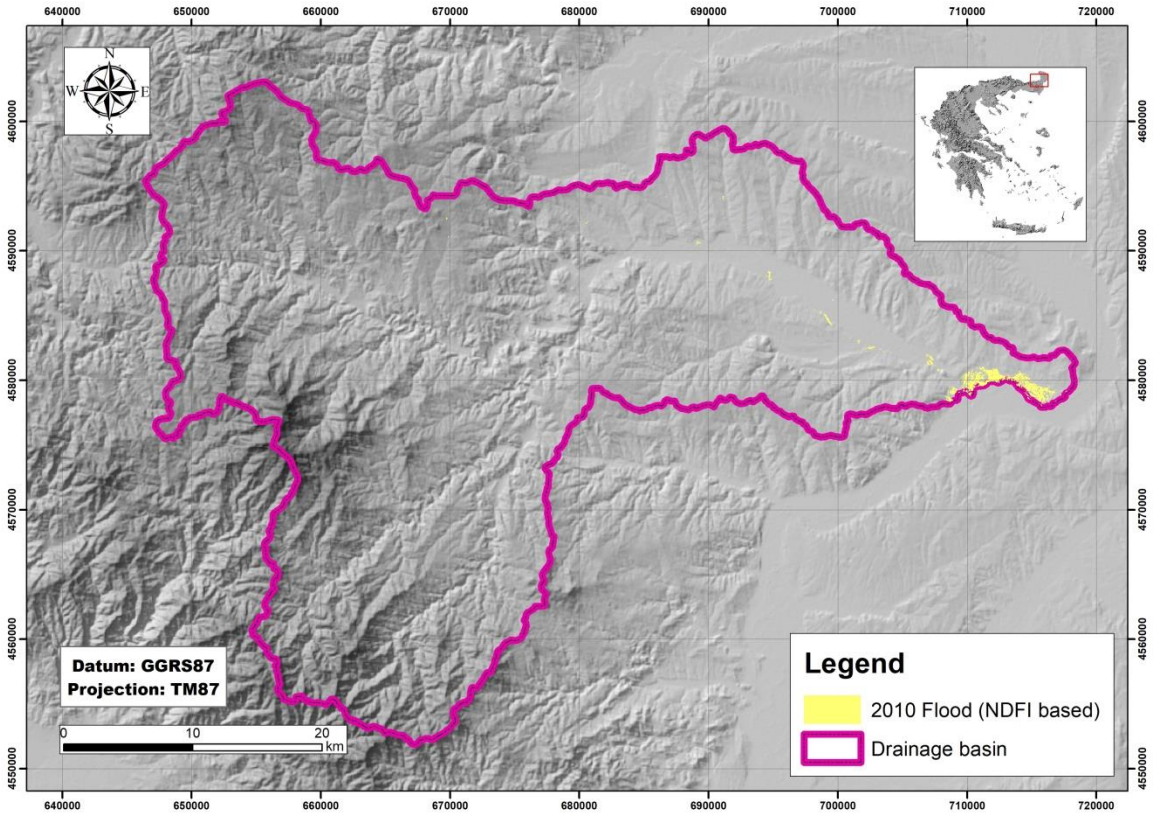

Figure 74: The NDFI based inundated areas of the 2010 flood.

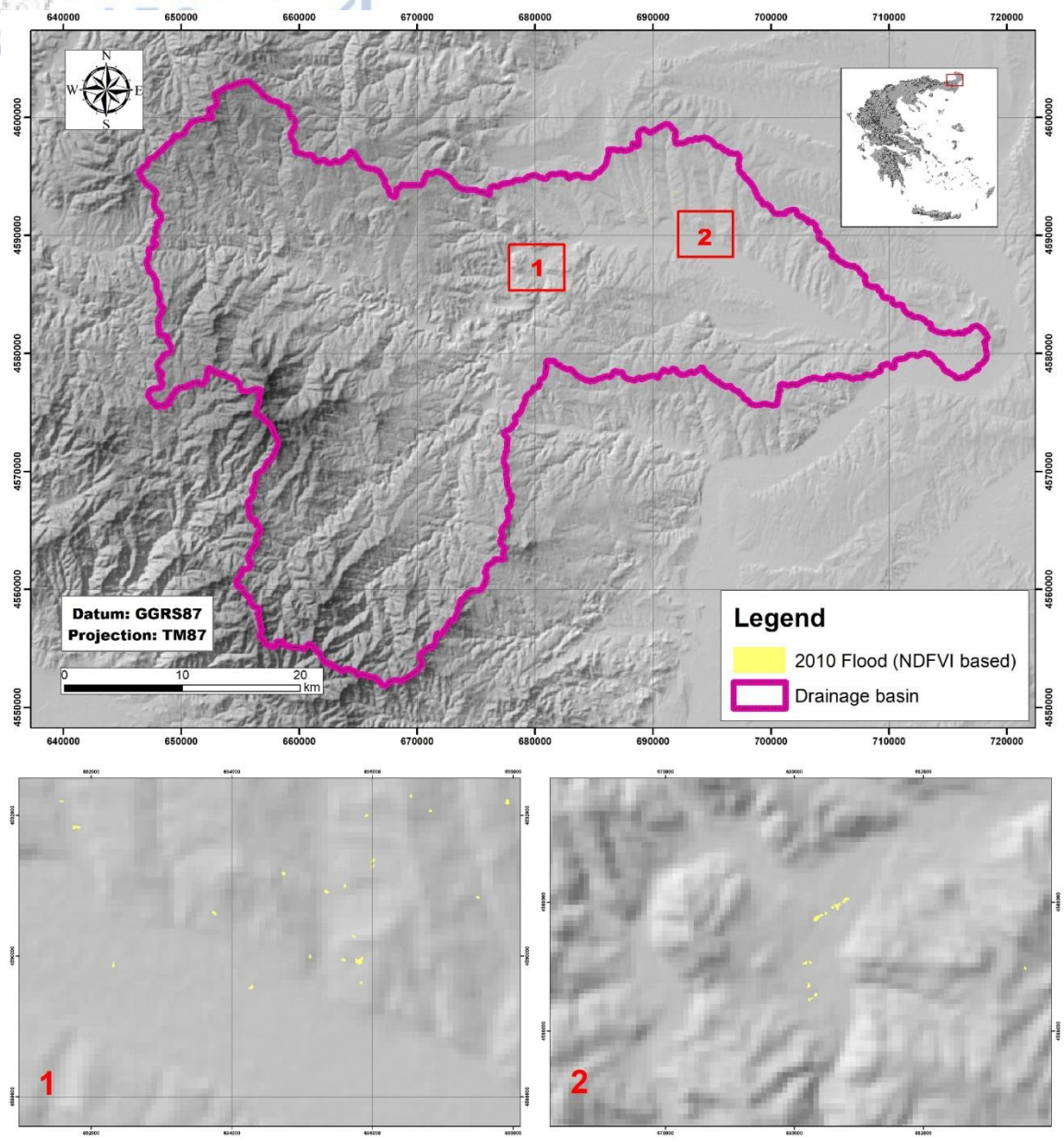

Figure 75: The NDFVI based inundated areas of the 2010 flood.

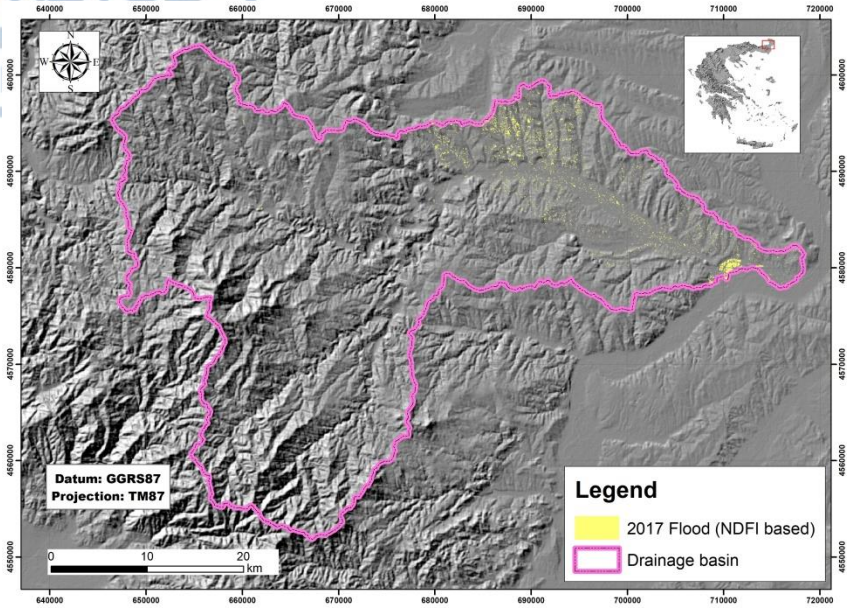

Figure 76: The NDFI based inundated areas of the 2017 flood.

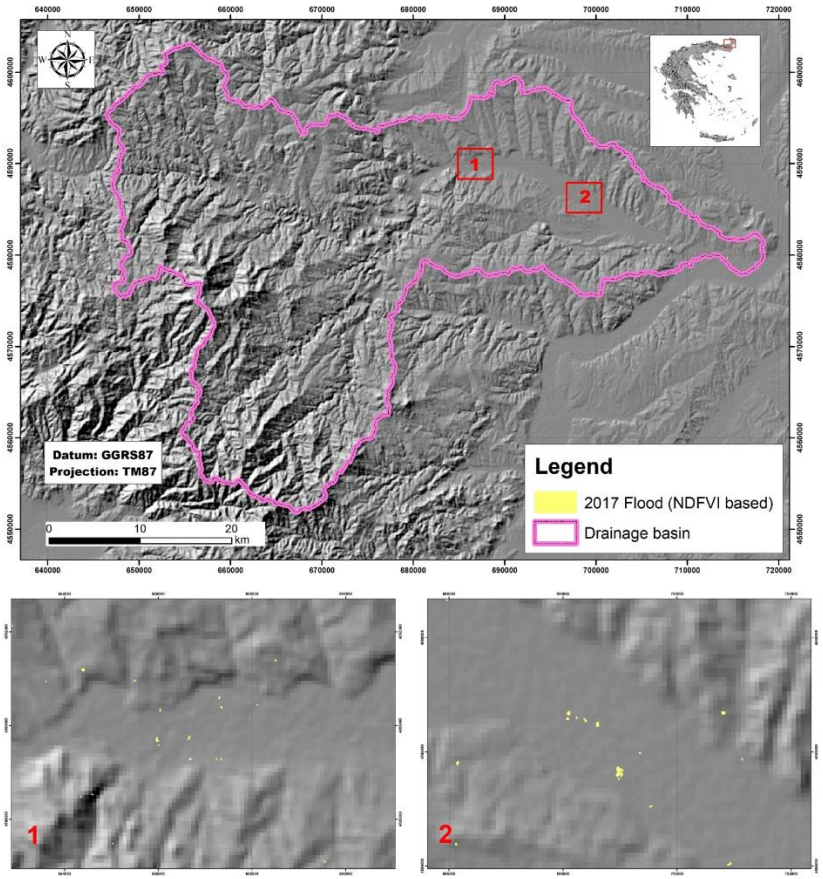

Figure 77: The NDFVI based inundated areas of the 2017 flood.

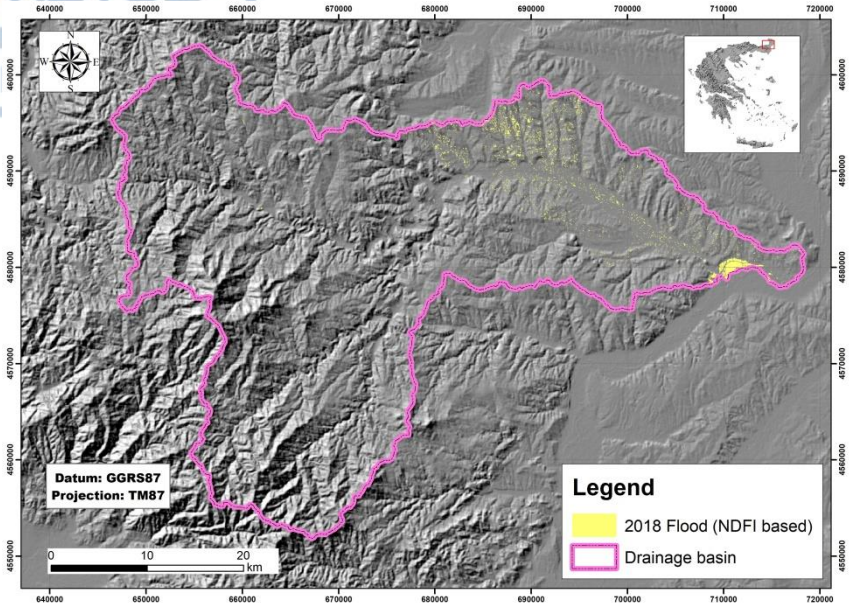

Figure 78: The NDFI based inundated areas of the 2018 flood.

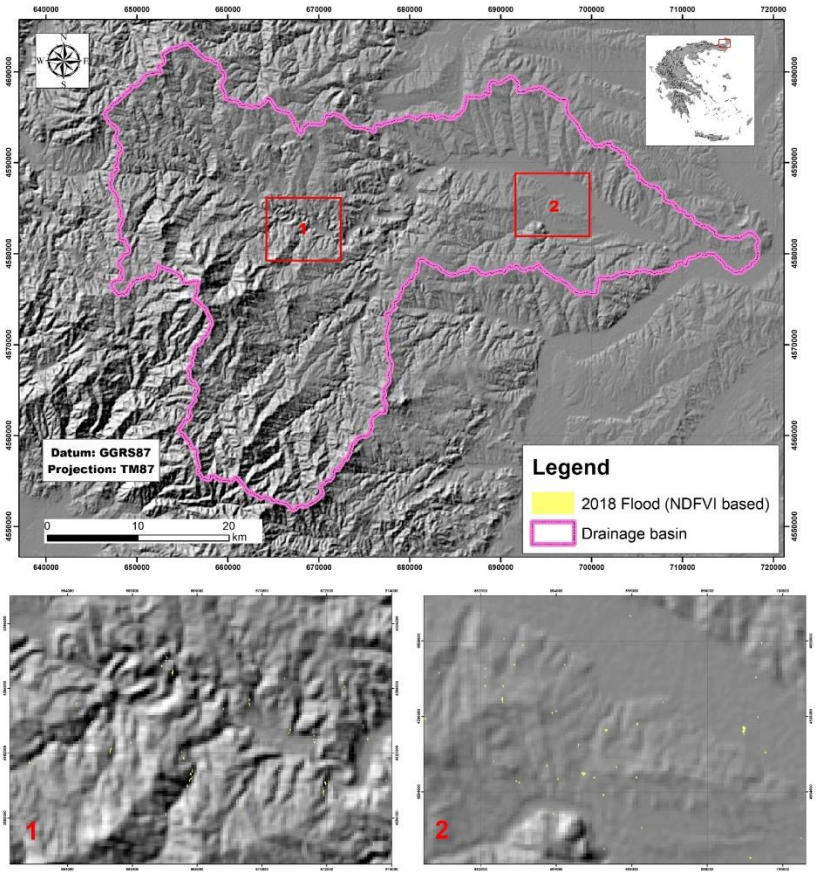

Figure 79: The NDFVI based inundated areas of the 2018 flood.

4.2 Flood hazard and risk mapping results

The flood hazard maps that were compiled for the return periods of: 1) 0.5 years, 2) 50 years, 3) 50.6 years, 4) 100 years and 5) 500 years depicted the spatial extent of the inundated areas and the spatial distribution of water depth for each scenario. Thalweg's geometry was used only in the 0.5 and 50.6 years scenarios, since its main purpose was to be compared with the 2010 flooded areas of inundation mapping. The inundated areas predicted by the 0.5-year return period scenario reach a total of 32.03 km^2 with a maximum water depth of 62.86m (Figures 80 and 81). Likewise, the 50-year, 100-year and 500-year return period scenarios predicted 44.27km^2, 45.16 km^2 and 46.46 km^2 of inundated areas respectively, with corresponding maximum water depths of 65.9 m, 66.41 m and 67.18 m (Figures 82 - 87). Furthermore, the 50.6-year return period scenario predicted inundated areas of 44.53 km^2 with a maximum water depth of 66.04 m (Figures 88 and 89). Finally, regarding the scenarios that involved solely the thalweg's geometry, the 5-year return period scenario predicted inundated areas of 23.05 km^2 with a maximum water depth of 46.76 m (Figures 90 and 91), while the 20,000-year return period scenario predicted inundated areas of 34.15 km^2 with a maximum water depth of 49.19 m (Figures 92 and 93). The results are presented synoptically in Table 29.

Table 29: Inundated areas extent and maximum water depths according to the scenarios that were used to perform flood hazard mapping in the drainage basin of Erythropotamos.

Return Period	Inundated area (km^2)	Maximum water depth (m)
0.5 year	32.03	62.86
0.5 year (thalweg)	23.05	46.76
50 year	44.27	65.9
100 year	45.16	66.41
500 year	46.46	67.18
50.6 year	44.53	66.04
50.6 year (thalweg)	34.15	49.19

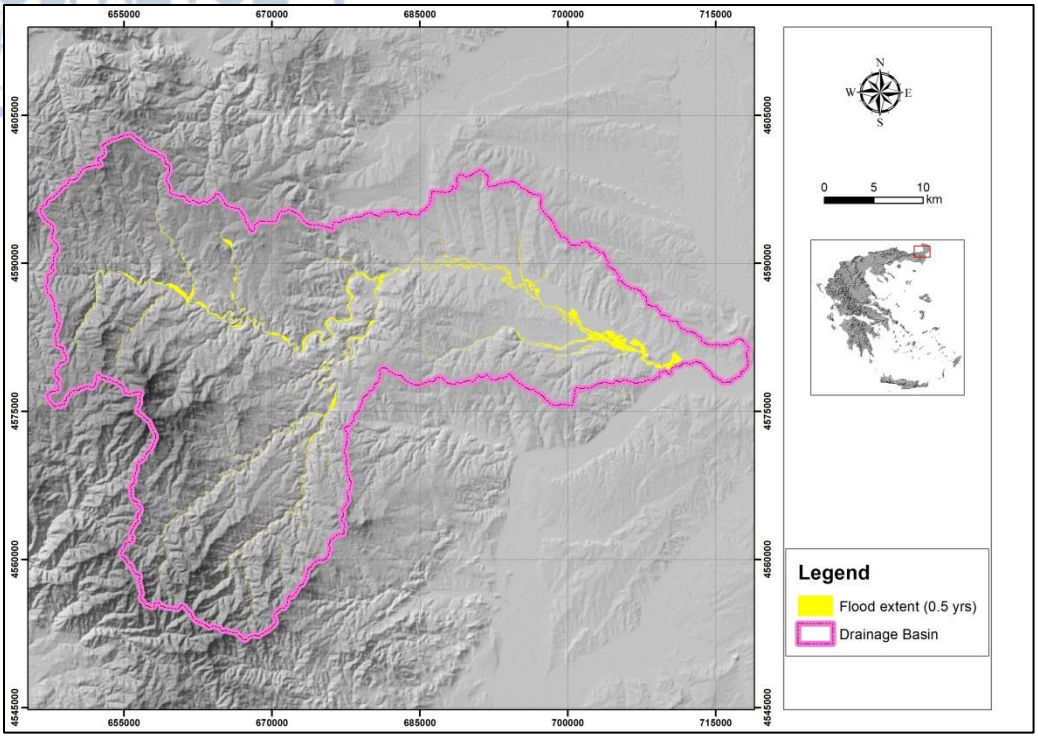

Figure 80: Inundated areas extent flood hazard mapping for the 0.5-year return period scenario.

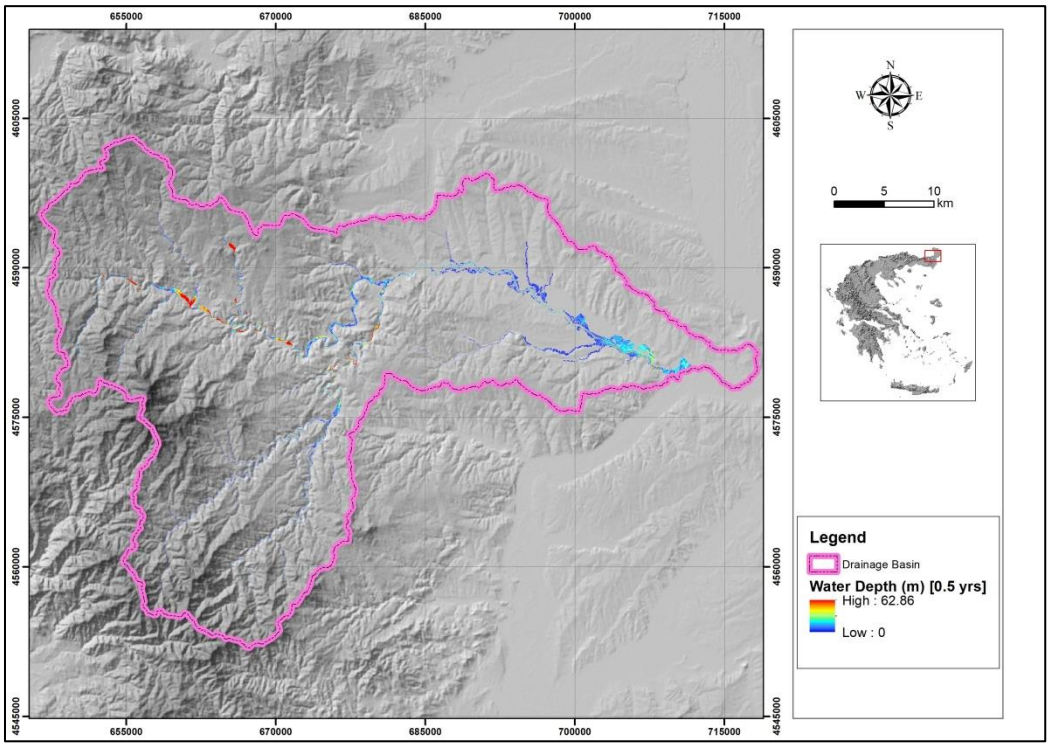

Figure 81: Water depth flood hazard mapping for the 0.5-year return period scenario.

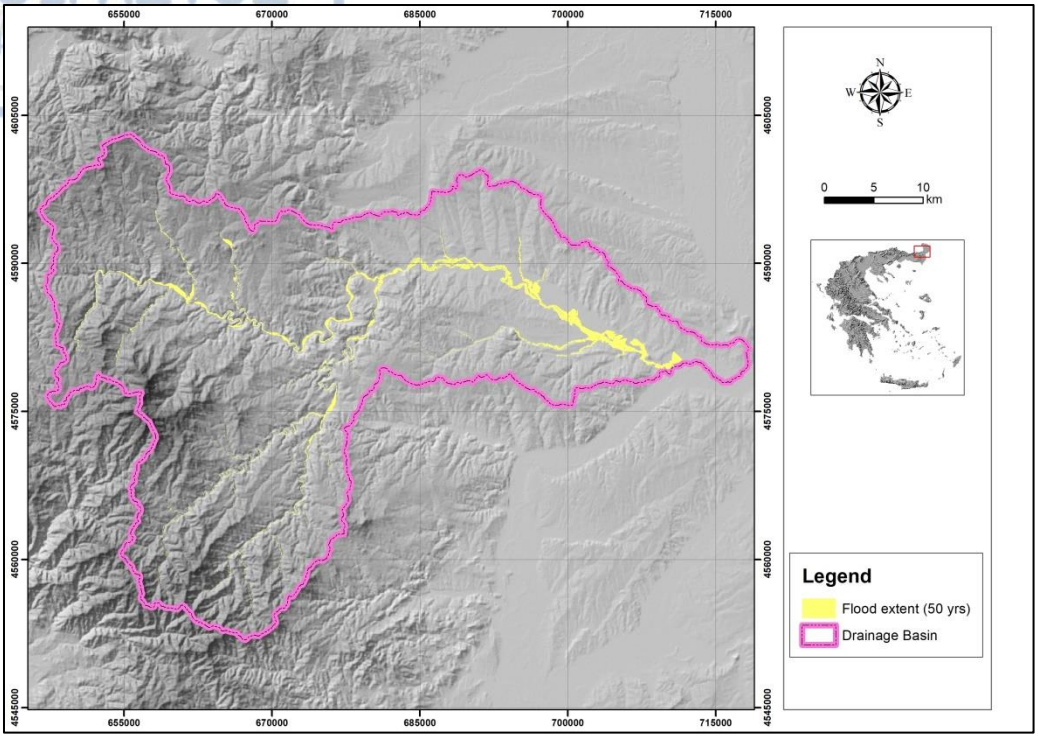

Figure 82: Inundated areas extent flood hazard mapping for the 50-year return period scenario.

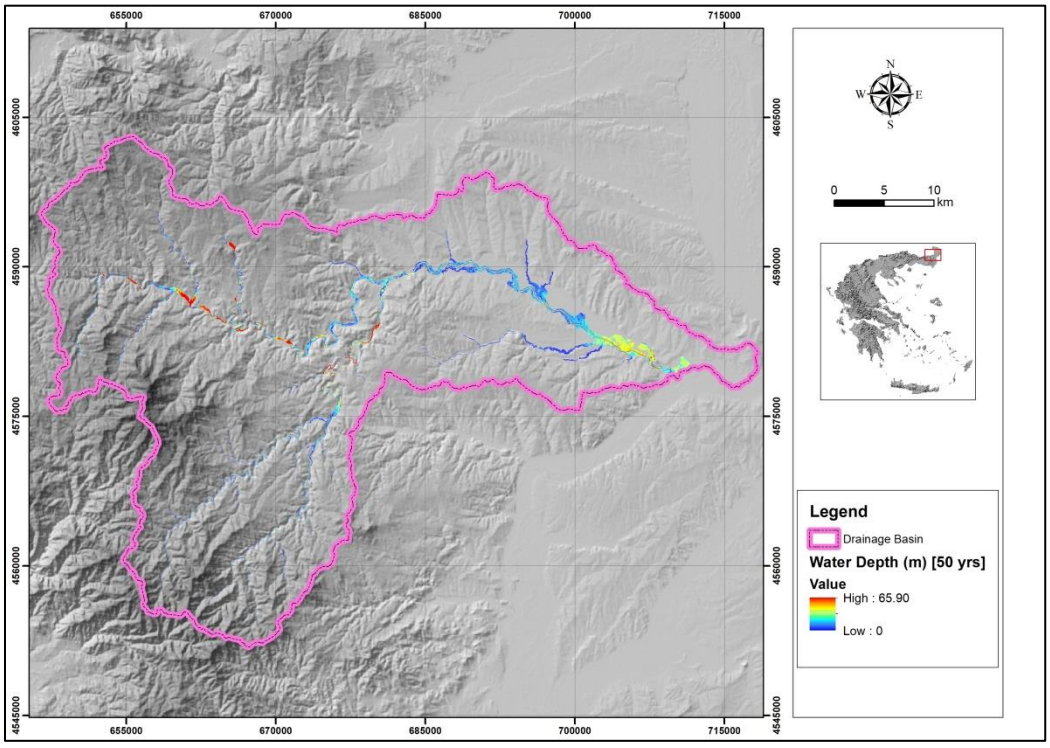

Figure 83: Water depth flood hazard mapping for the 50-year return period scenario.

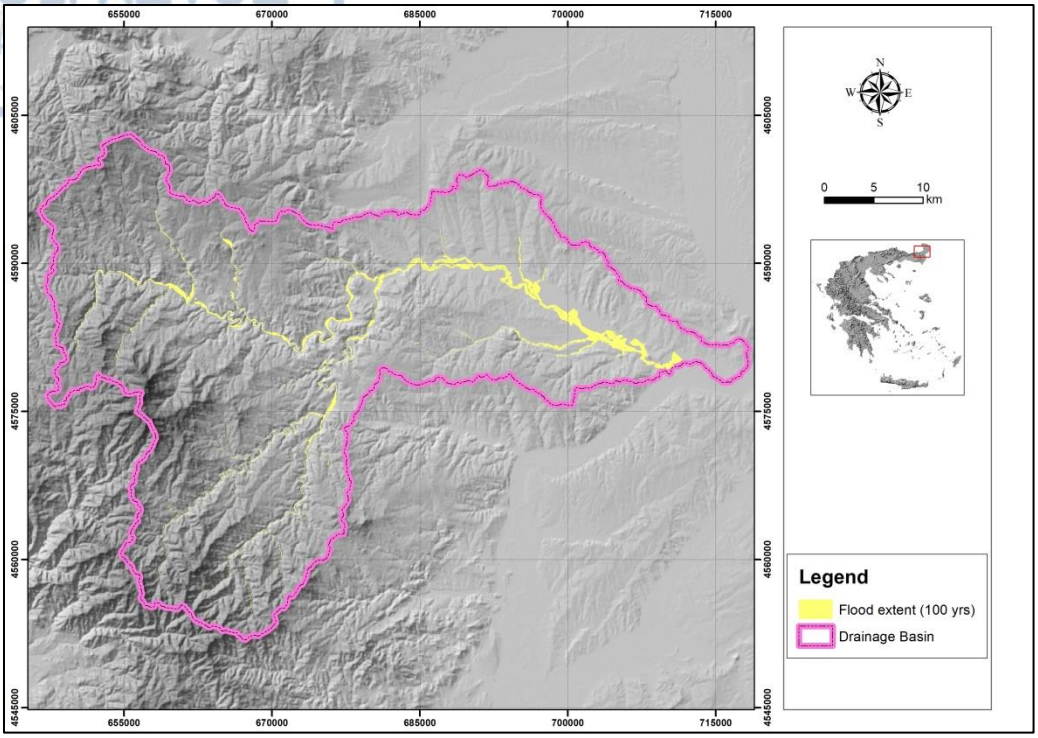

Figure 84: Inundated areas extent flood hazard mapping for the 100-year return period scenario.

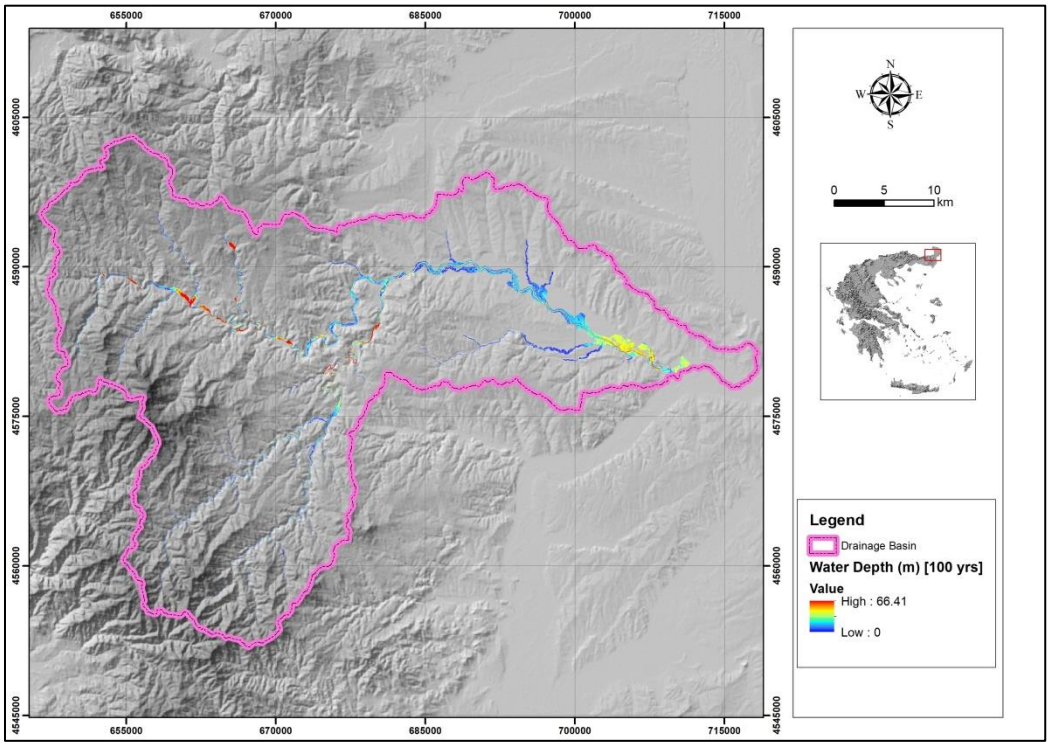

Figure 85: Water depth flood hazard mapping for the 100-year return period scenario.

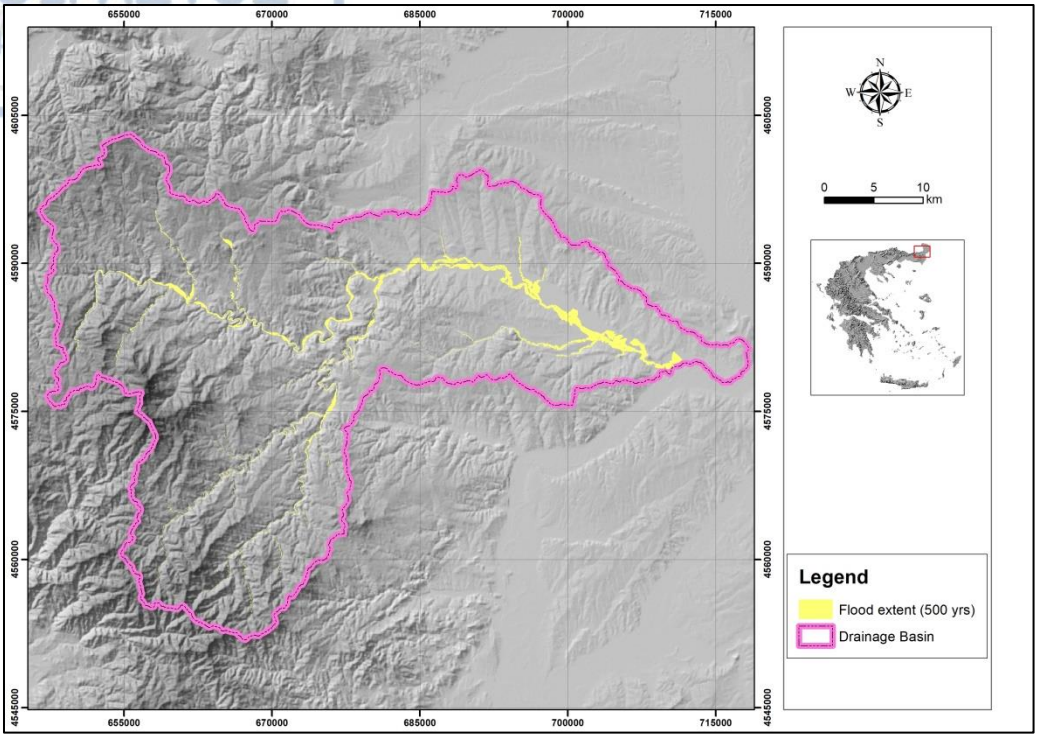

Figure 86: Inundated areas extent flood hazard mapping for the 500-year return period scenario.

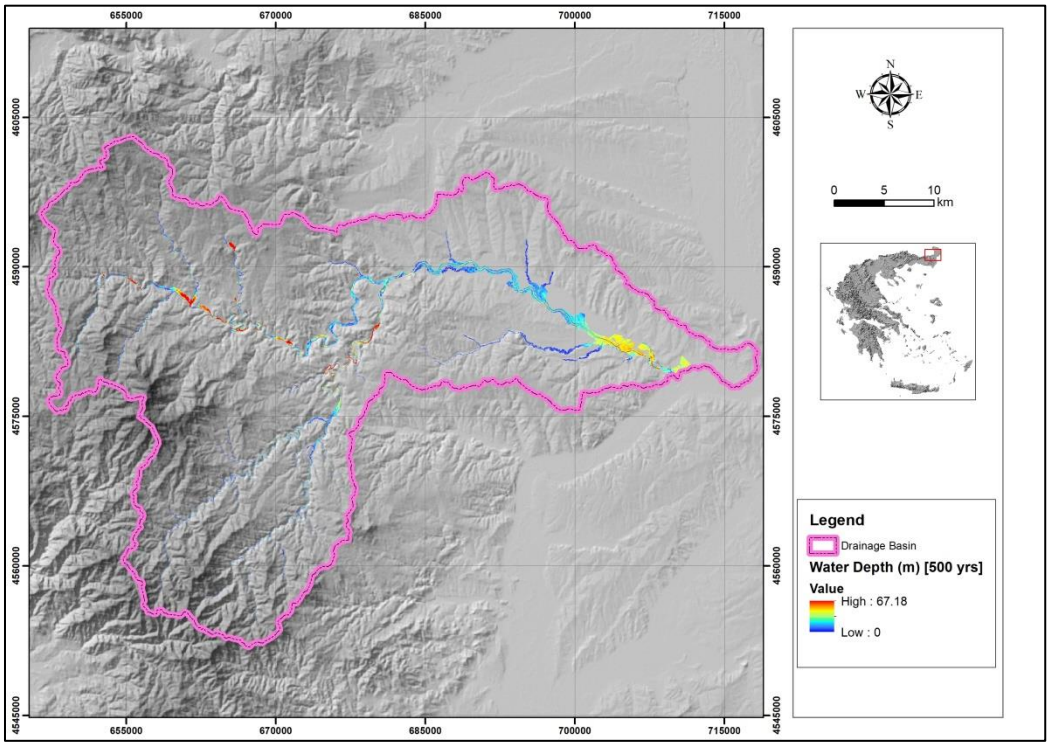

Figure 87: Water depth flood hazard mapping for the 500-year return period scenario.

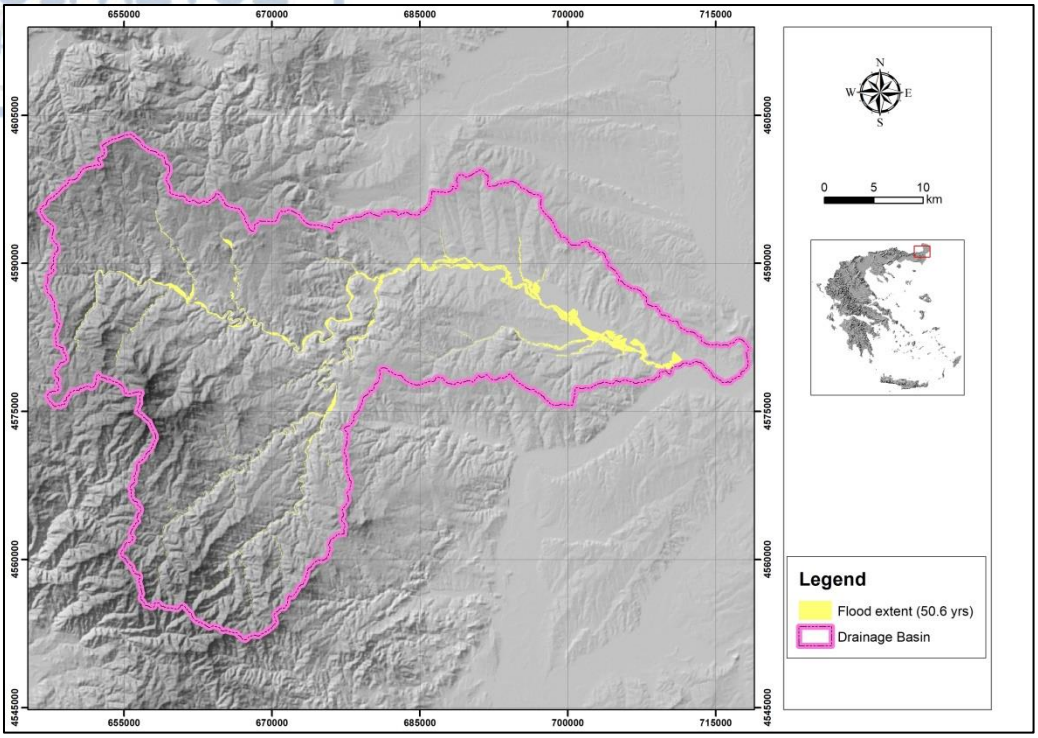

Figure 88: Inundated areas extent flood hazard mapping for the 50.6-year return period scenario.

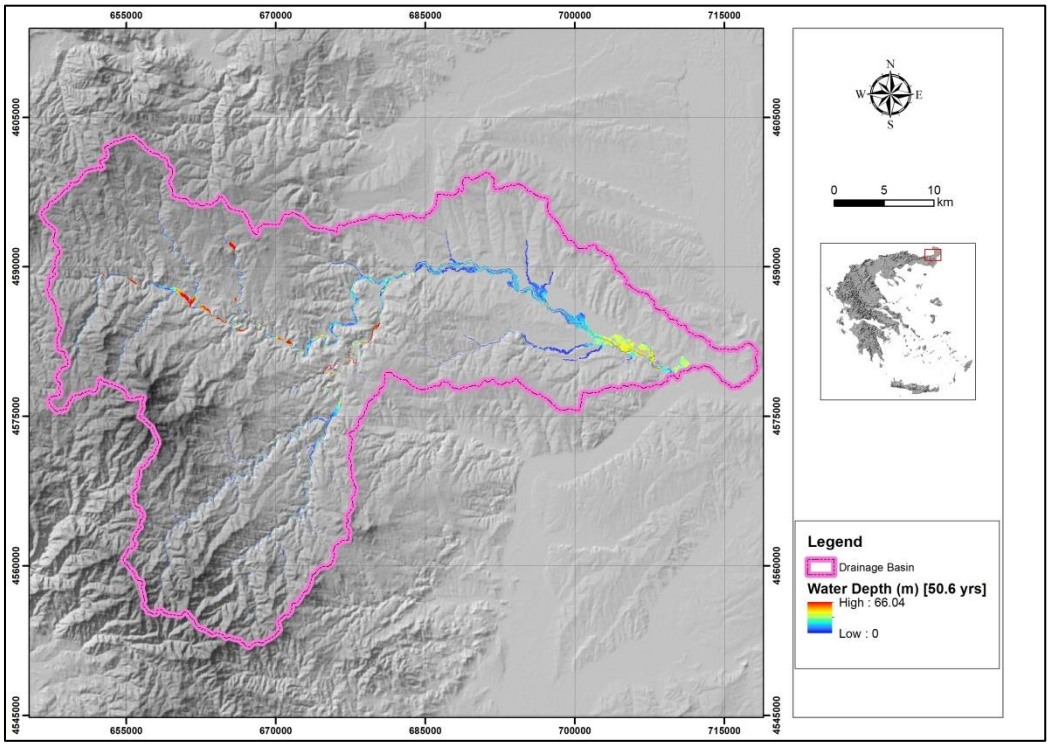

Figure 89: Water depth flood hazard mapping for the 50.6-year return period scenario.

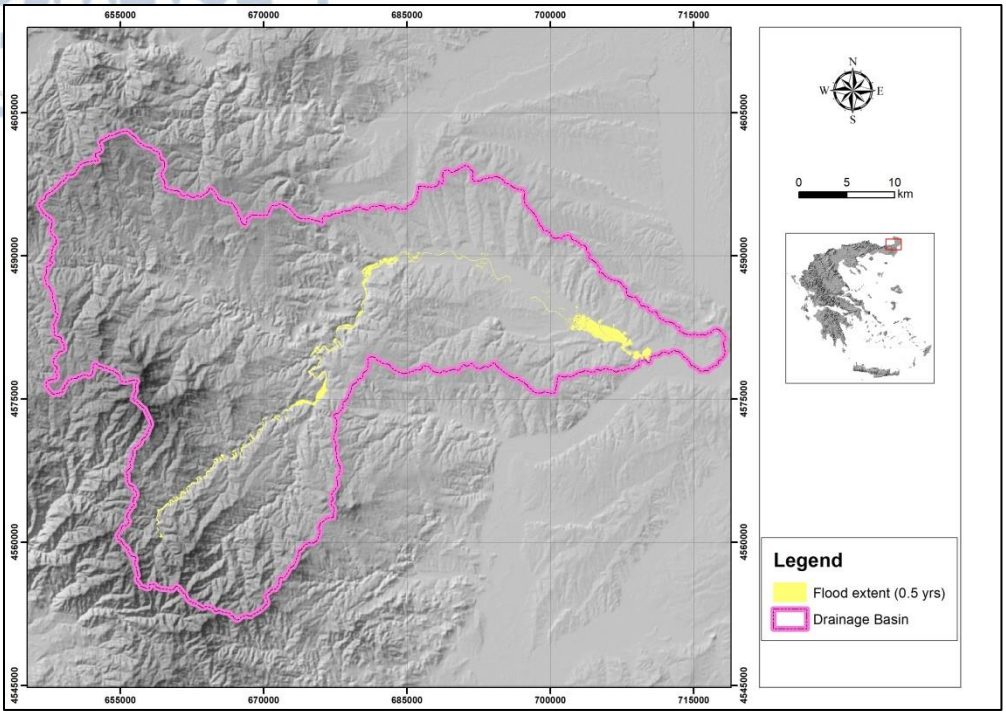

Figure 90: Inundated areas extent flood hazard mapping for the 0.5-year return period scenario involving only the thalweg of the drainage basin of Erythropotamos River.

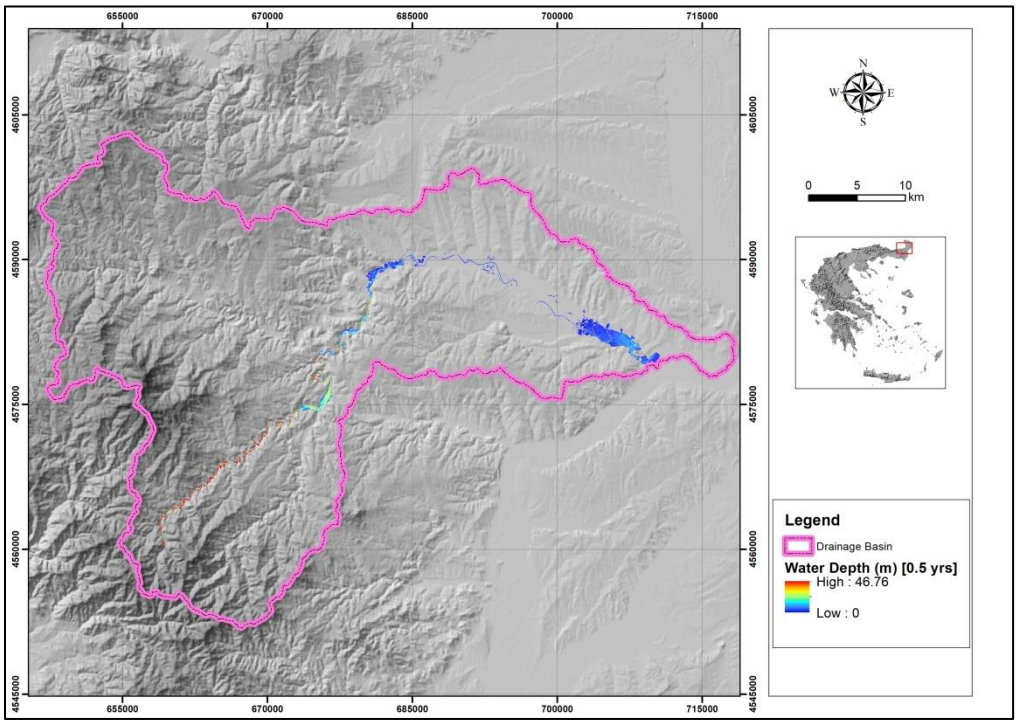

Figure 91: Water depth flood hazard mapping for the 0.5-year return period scenario involving only the thalweg of the drainage basin of Erythropotamos River.

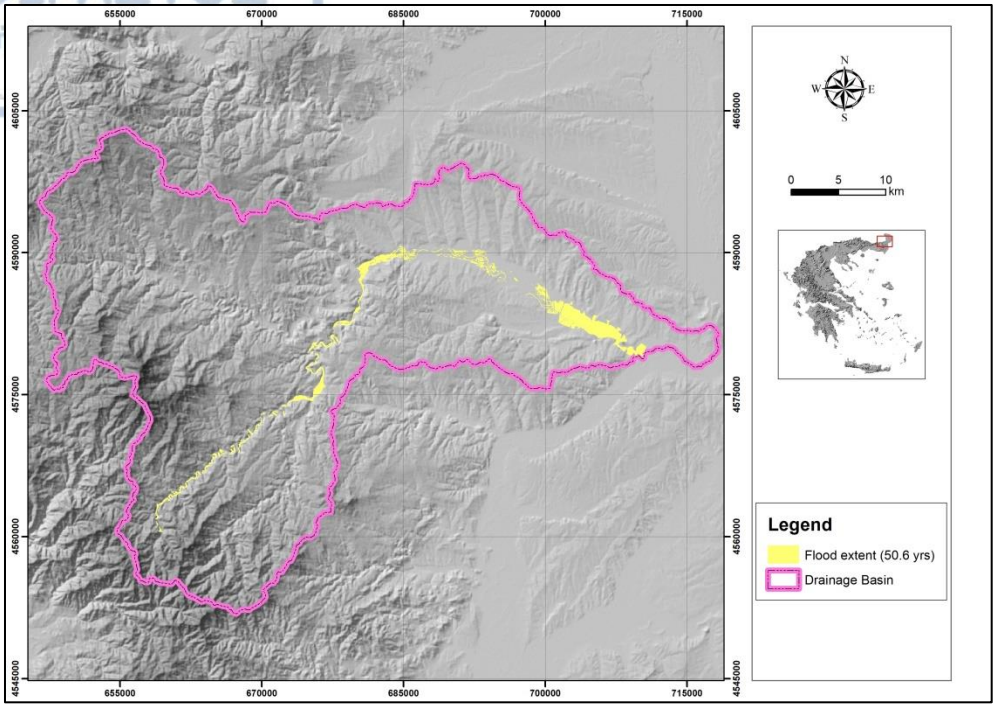

Figure 92: Inundated areas extent flood hazard mapping for the 50.6-year return period scenario involving only the thalweg of the drainage basin of Erythropotamos River.

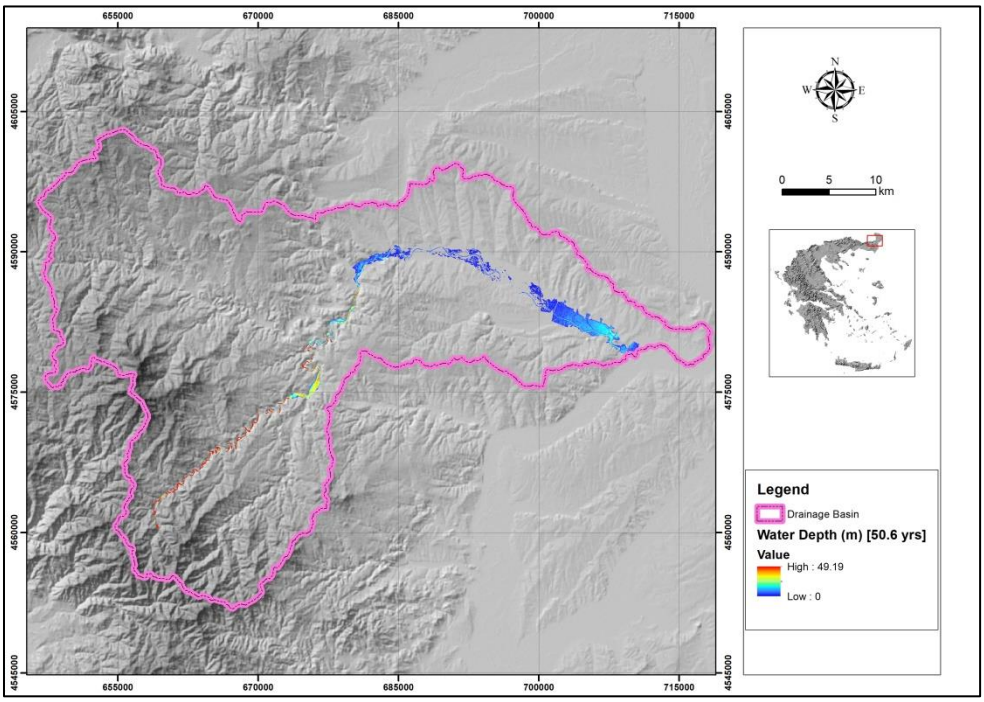

Figure 93: Water depth flood hazard mapping for the 50.6-year return period scenario involving only the thalweg of the drainage basin of Erythropotamos River.

Concerning the flood risk maps that were compiled according to the aforementioned scenarios, the extents of the predicted inundated areas were superimposed over the data layers of the protected areas of Filiouri Valley (GR1130011) and Oreinos Evros – Dereio Valley (GR1110010) and the areas that are categorized as artificial surfaces according to Corine Land Cover 2012 (Copernicus 2017) classification types (Figures 94 – 98). Specifically, this Corine Land Cover 2012 category includes areas of discontinuous urban fabric, industrial or commercial units, construction sites and sports or leisure facilities.

Furthermore, with the aid of ArcGIS Geoprocessing tools, it was calculated that for the 0.5-year return period scenario the predicted inundated areas intersected with 4.29 km^2 of protected zones and 0.39 km^2 of artificial surfaces. Likewise, the 50-year, 100-year and 500-year return period scenarios predicted an intersection of 5.81 km^2, 6 km^2 and 6.27 km^2 with the protected areas respectively, along with corresponding predicted intersections of 0.49 km^2, 0.51 km^2 and 0.54 km^2 with artificial surfaces. Finally, the 50.6-year scenario predicted an intersected area of 5.83 km^2 with the protected zones and an intersection of 0.5 km^2 with artificial surfaces. These results are summed up in Table 30.

Table 30: The areas of protected zones and artificial surfaces that are threatened by inundation according to each scenario.

Return Period	Protected areas (km^2)	Artificial surfaces (km^2)
5 year	4.29	0.39
50 year	5.81	0.49
50.6 year	5.83	0.5
100 year	6.00	0.51
500 year	6.27	0.54

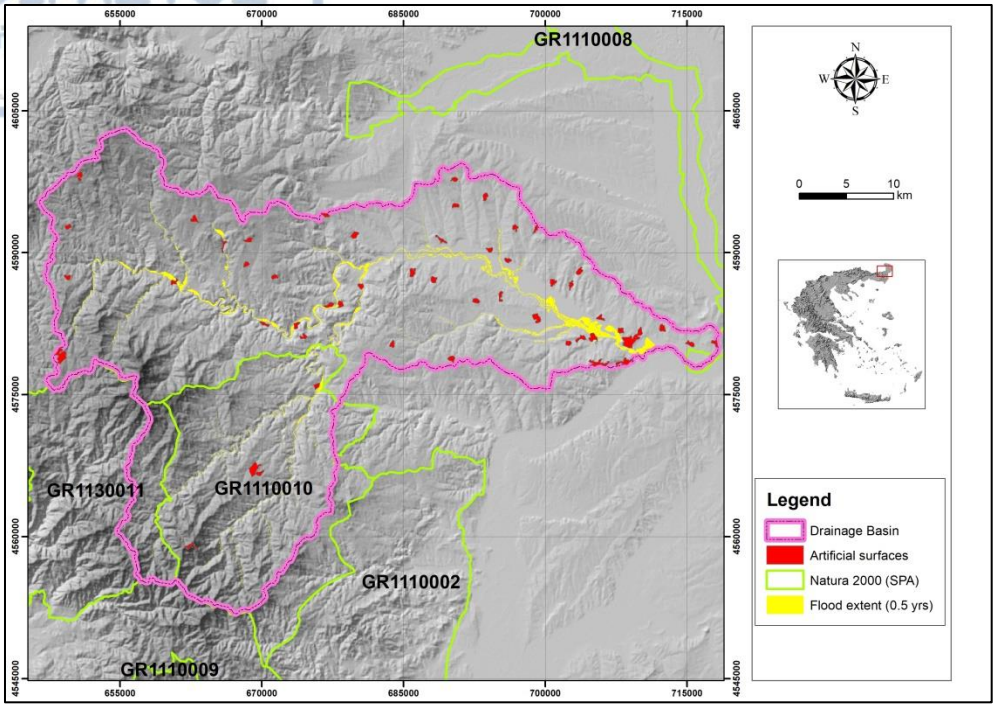

Figure 94: Superimposition of the predicted inundated areas of the 0.5-year scenario over the Natura 2000 zones and artificial surfaces.

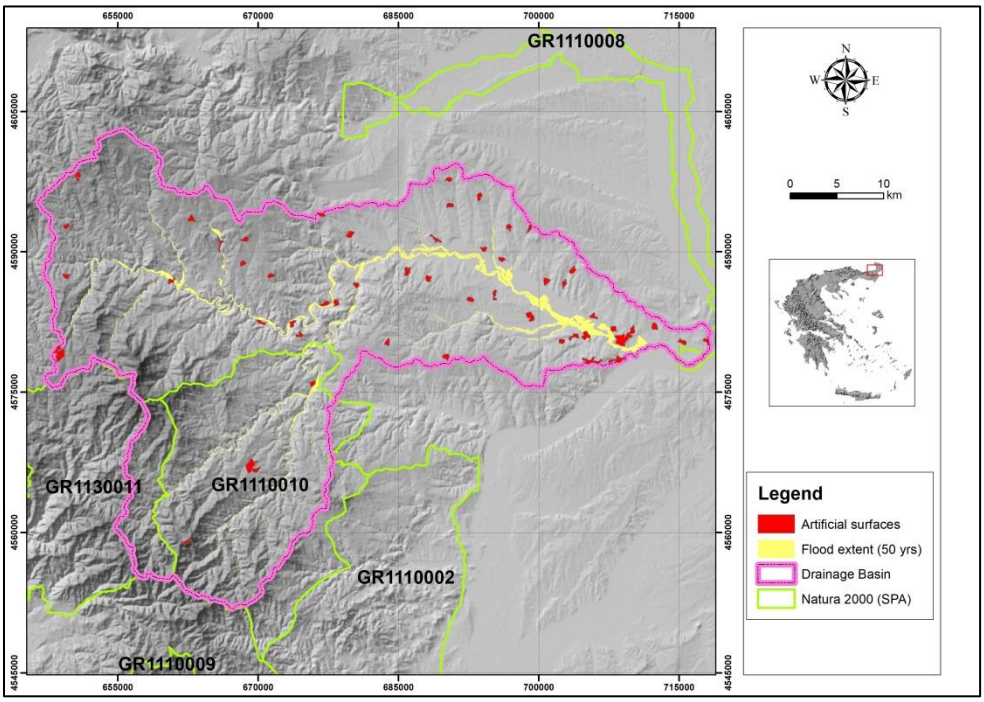

Figure 95: Superimposition of the predicted inundated areas of the 50-year scenario over the Natura 2000 zones and artificial surfaces.

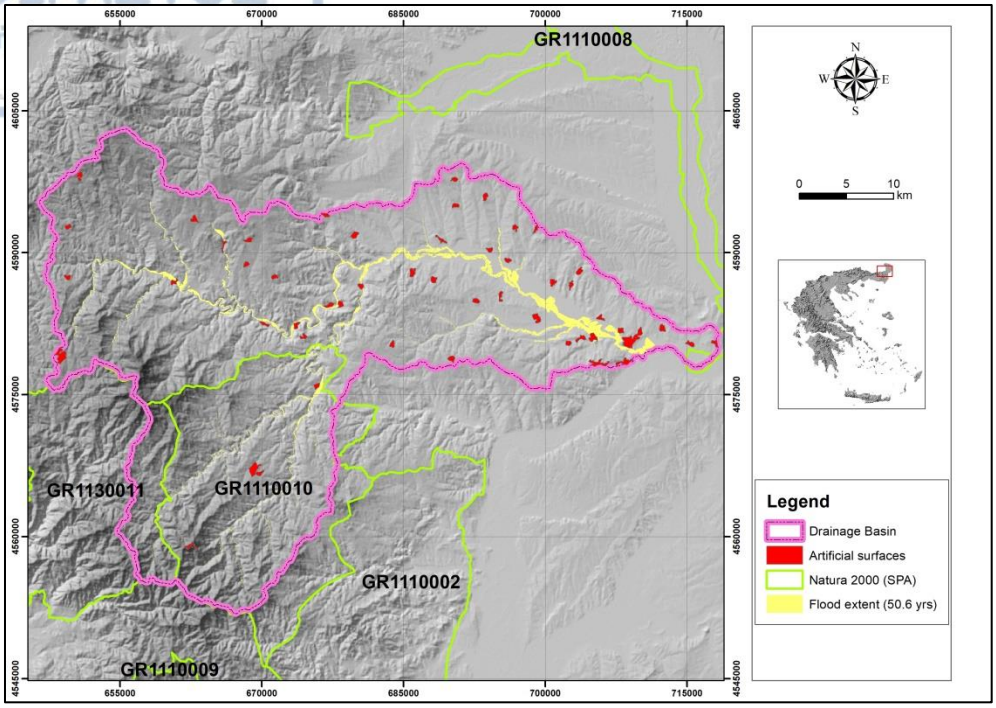

Figure 96: Superimposition of the predicted inundated areas of the 50.6-year scenario over the Natura 2000 zones and artificial surfaces.

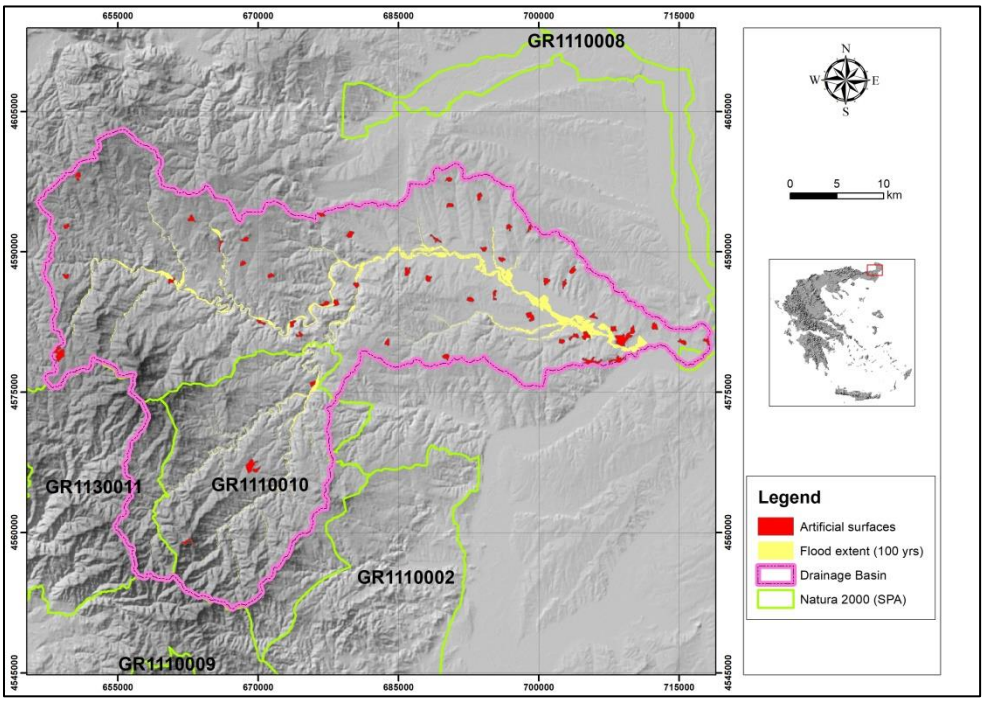

Figure 97: Superimposition of the predicted inundated areas of the 100-year scenario over the Natura 2000 zones and artificial surfaces.

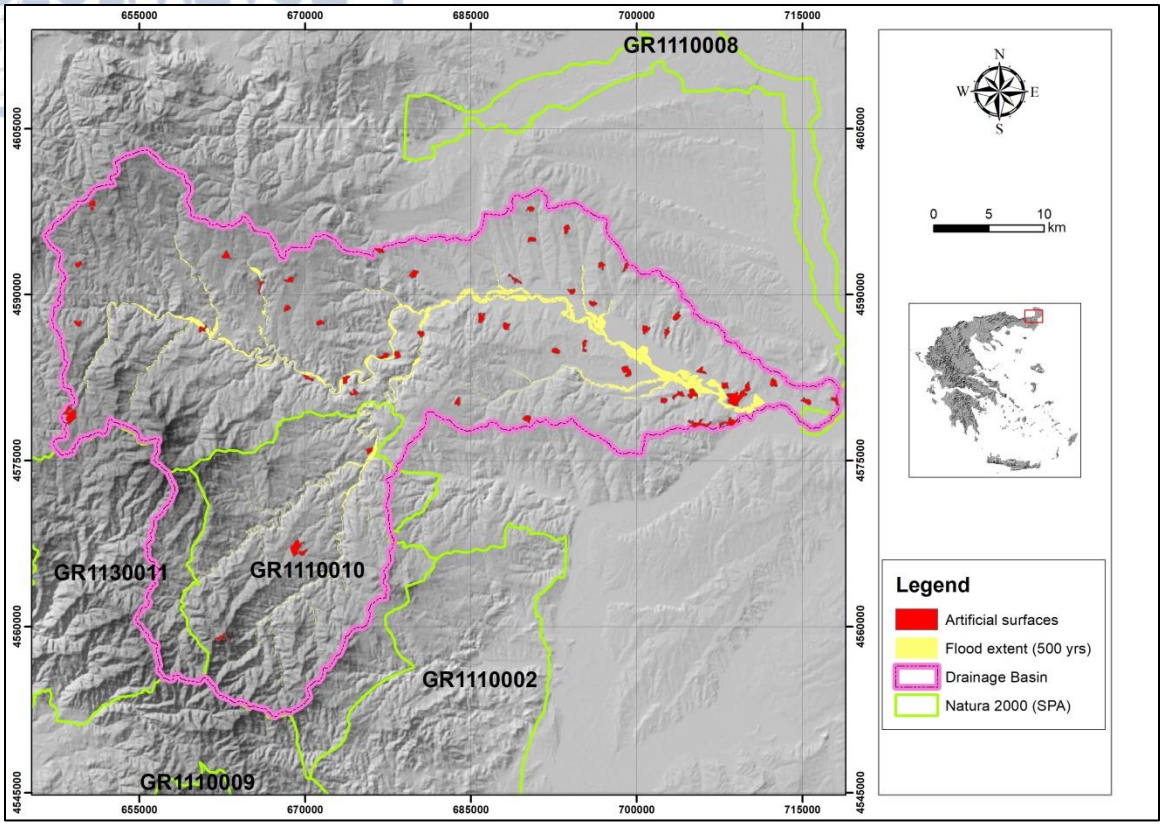

Figure 98: Superimposition of the predicted inundated areas of the 500-year scenario over the Natura 2000 zones and artificial surfaces.

4.3 Flood susceptibility mapping results

Regarding susceptibility mapping, the resulting maps were classified into three categories, which contained areas of high, medium, and low susceptibility (Figures 99 - 103). Areas of high flood susceptibility were coloured red, while areas of moderate and low flood susceptibility were coloured yellow and green respectively. Moreover, the application of AHP methodology produced the criteria weight for each indicator. According to these results, in the case where the hierarchy of factors was determined with the aid of inundation mapping, elevation was considered as the most important indicator with the weight value of 0.327, followed by the slope angle with the weight value of 0.227. Distance from stream and drainage density were respectively considered as the third and fourth most important criteria, and their weight values are 0.157 and 0.108, respectively. The weights of the remaining indicators were below 0.1, which indicated

that they present less important than aforementioned four indicators. The criteria weight value of geology, land use, TWI and rainfall are 0.073, 0.05, 0.034 and 0.024, respectively (Table 22). Likewise, in in the case where the hierarchy of factors was determined with the aid of flood hazard mapping, elevation was again the most important indicator with the weight value of 0.327, this time followed by the distance from streams with the weight value of 0.227. Drainage density and slope angle were respectively considered as the third and fourth most important criteria with weight values of 0.157 and 0.108, respectively. The less important indicators were those of geology, TWI, land use and rainfall, with criteria weight values of 0.073, 0.05, 0.034 and 0.024, respectively (Table 27).

Regarding validation, in the case where the hierarchy of factors was determined with the aid of inundation mapping, by superimposing the delineated areas of the April 2017 and March 2018 inundation mapping onto the resulting susceptibility map, with the aid of ArcGIS, calculations indicated that the largest part of the aforementioned estimated flood extents coincided with the areas of high and medium susceptibility of the resulting map (Figures 99 and 100). Regarding the April 2017 flood, from the total of 18.23 km^2 of the total inundated area in both open-land and in short vegetation, 10.6 km^2 (58.17%) intersected with the high flood susceptibility class. Additionally, high and medium susceptibility classes intersected with 17.54 km^2 (96.22 %) of the resulting flood extent. Correspondingly, from the total of 20.60 km^2 of the March 2018 inundated area, 12.22 km^2 (59.33%) were included within the high flood susceptibility class, while high and medium susceptibility classes intersected with 19.73 km^2 (95.8 %) of the resulting flood extent (Table 31).

Similarly, in the case where the hierarchy of factors was determined with the aid of flood hazard mapping, by superimposing the delineated areas of the February 2010, April 2017 and March 2018 inundation mapping onto the resulting susceptibility map, with the aid of ArcGIS, calculations indicated that the largest part of the aforementioned estimated flood extents coincided with the areas of high and medium susceptibility of the resulting map (Figures 101 - 103). Regarding the February 2010 flood, from the total of 6.84 km^2 of the total inundated area in both open-land and in short vegetation, 4.2 km^2 (61.4%)

intersected with the high flood susceptibility class. Additionally, high and medium susceptibility classes intersected with 6.74 km^2 (98.54 %) of the resulting flood extent. Correspondingly, from the total of 18.23 km^2 of the April 2017 inundated area, 10.04 km^2 (55.05%) were included within the high flood susceptibility class, while high and medium susceptibility classes intersected with 17.25 km^2 (94.62 %) of the resulting flood extent. Finally, from the total of 20.60 km^2 of the March 2018 inundated area, 11.29 km^2 (54.83%) were included within the high flood susceptibility class, while high and medium susceptibility classes intersected with 19.49 km^2 (94.61 %) of the resulting flood extent (Table 32).

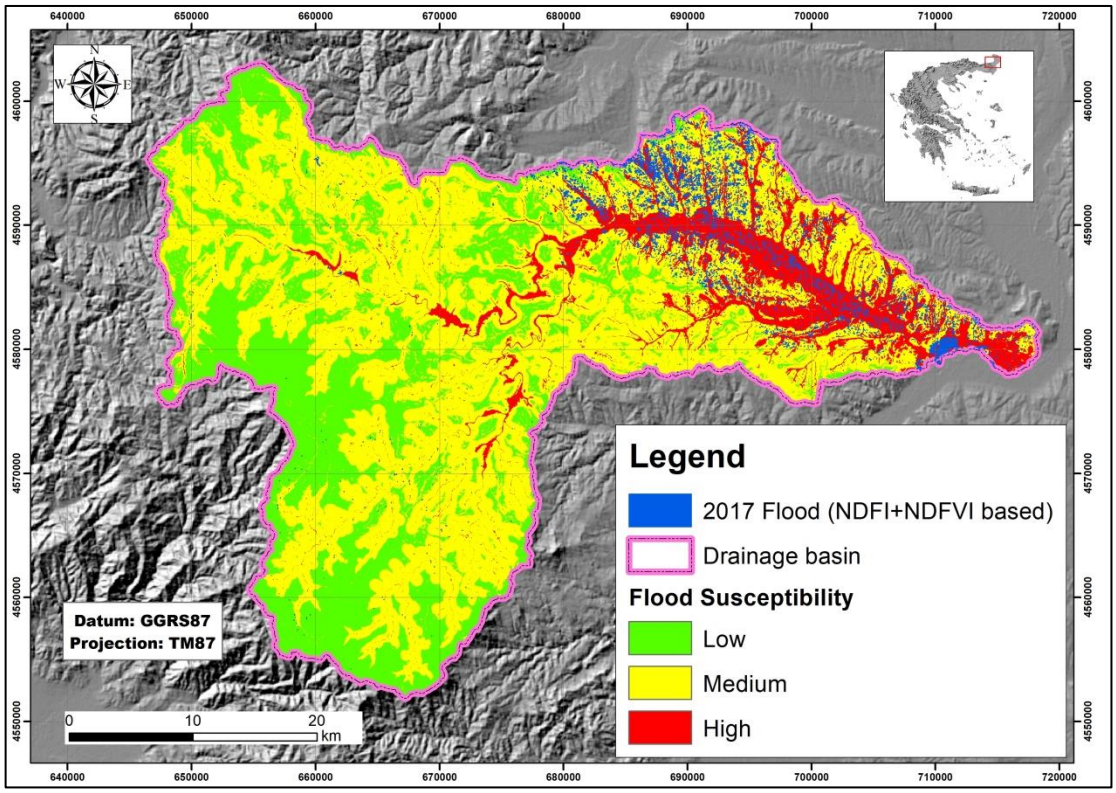

Figure 99: Superimposion of the April 2017 inundated areas (both NDFI and NDFVI based) over the flood susceptibility map.

Table 31: Area extent and percentage of the part of the March 2018 and April 2017 inundated areas, which intersect with high to medium classes of the susceptibility map.

Flood susceptibility classes	Inundated area (km^2)	Percentage (%)
2018 March flood		
High	12.22	59.33
High and medium	19.73	95.8
2017 April flood		
High	10.6	58.17
High and medium	17.54	96.22

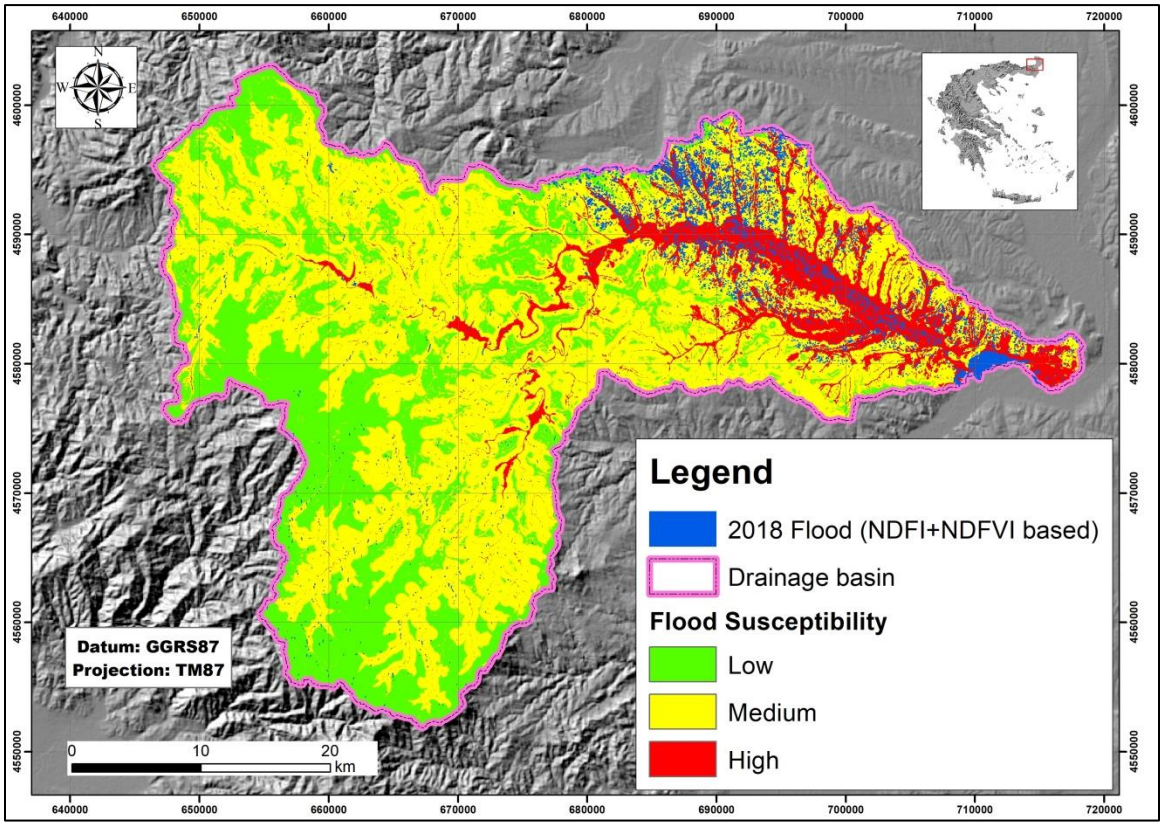

Figure 100: Superimposion of the April 2018 inundated areas (both NDFI and NDFVI based) over the flood susceptibility map.

Table 32: Area extent and percentage of the part of the March 2018, April 2017 and February 2010 inundated areas, which intersect with high to medium classes of the susceptibility map.

Flood susceptibility classes	Inundated area (km^2)	Percentage (%)
2018 March flood		
High	11.29	54.83
High and medium	19.49	94.61
2017 April flood		
High	10.4	55.05
High and medium	17.25	94.62
2010 February flood		
High	4.2	61.4
High and medium	6.74	98.54

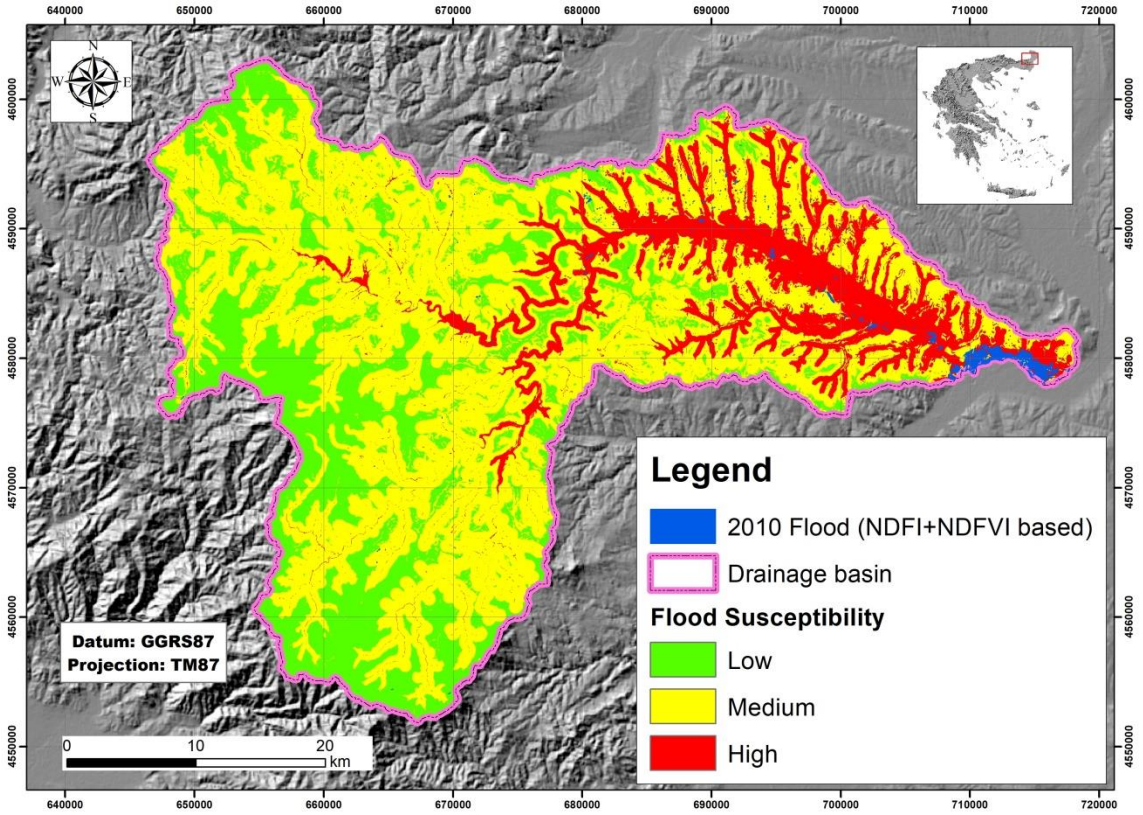

Figure 101: Superimposion of the February 2010 inundated areas (both NDFI and NDFVI based) over the flood susceptibility map.

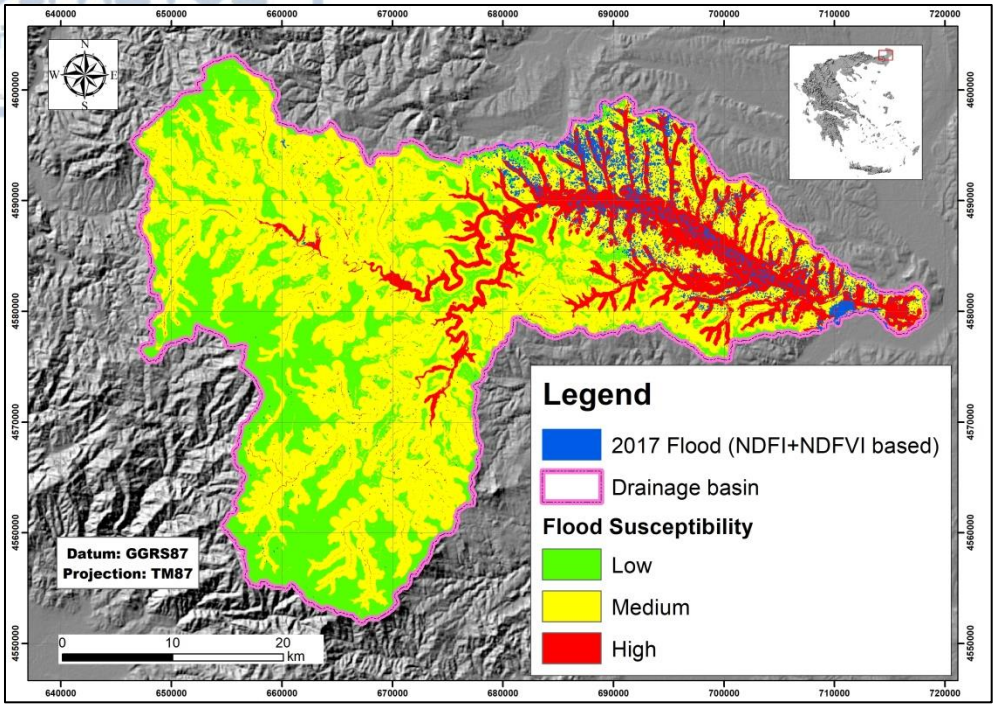

Figure 102: Superimposion of the April 2017 inundated areas (both NDFI and NDFVI based) over the flood susceptibility map.

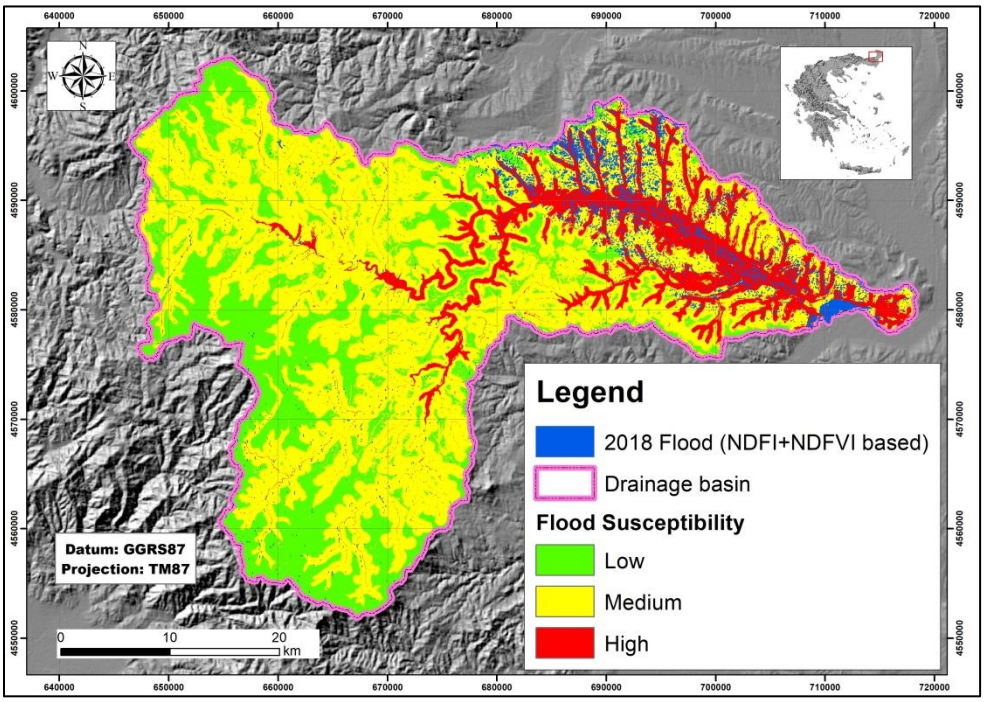

Figure 103: Superimposion of the April 2018 inundated areas (both NDFI and NDFVI based) over the flood susceptibility map.

4.4 Results of the comparison between the zone of potential high flood risk that is suggested by the Ministry of Environment and Energy and the results of inundation, flood hazard and susceptibility mapping

The zone of potential high flood risk that is included in the flood hazard and risk maps for the drainage basin of Evros River (Ministry of Environment and Energy 2014) covers an extent of 18.38 km^2, within the drainage basin of Erythropotamos. The comparison between this zone and the results of inundation mapping regarding the February 2010 flood event indicated that the common area between these data layers covered an extent of 5.26 km^2. Likewise, the intersected areas between the zone of potential high flood risk and the inundated areas of the April 2017and March 2018 floods covered an extent of 2.08 km^2 and 3.54 km^2 respectively (Figures 104-106 and Table 33).

Regarding the spatial correlation between the zone of potential high flood risk and the results of flood hazard mapping of the present dissertation thesis, the common area between the aforementioned zone and the predicted inundated areas of the 0.5 and 50.6 return period scenarios, concerning solely the thalweg geometry, covered an extent of 2.85 km^2 and 4.94 km^2 respectively. Likewise, the intersection between the zone of potential high flood risk and the results of flood hazard mapping, which involved the river reaches of 5^{th} order and higher, for the of 0.5, 50, 50.6, 100 and 500 years return period scenarios produced areas of 3.27, 3.44, 3.56, 3.56, 3.58 and 3.6 km^2 respectively (Figures 107-113 and Table 33).

Finally, the comparison between the zone of potential high flood risk and the resulting high flood susceptibility classes produced common areas of 16.12 km^2 and 13.2 km^2. The former value refers to the high flood susceptibility class of the resulting map that was compiled by determining the hierarchy of factors with the aid of inundation mapping, while the latter value corresponds to the high flood susceptibility class of the resulting map that was compiled by determining the hierarchy of factors with the aid of flood hazard mapping (Figures 114 and 115 and Table 33).

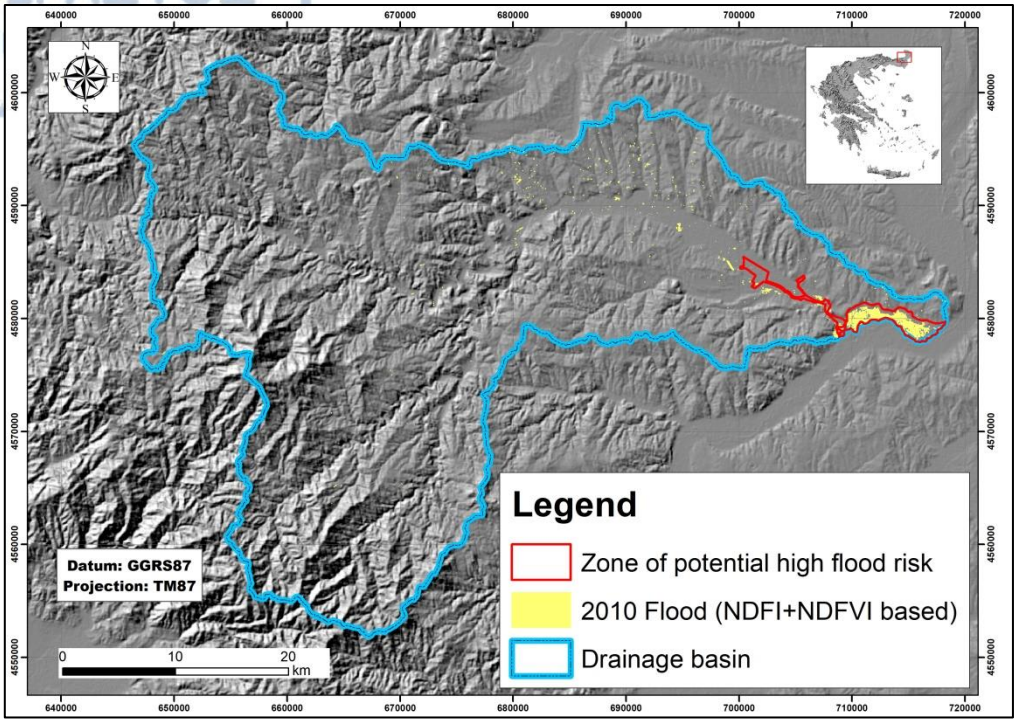

Figure 104: Comparison between the zone of potential high flood risk and the inundated areas of the February 2010 flood event.

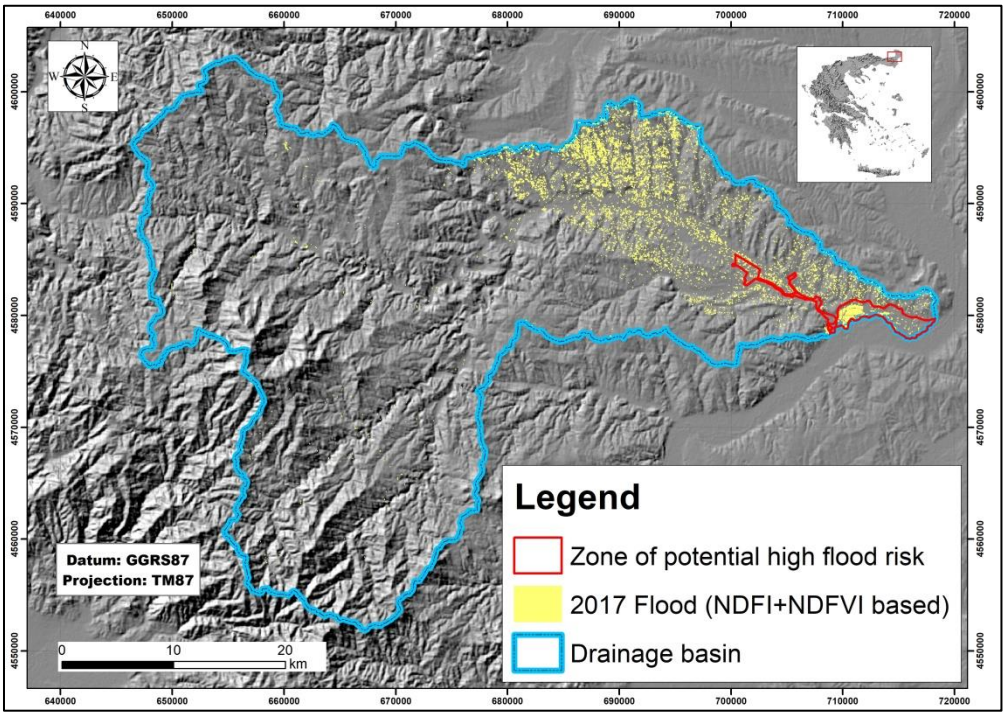

Figure 105: Comparison between the zone of potential high flood risk and the inundated areas of the April 2017 flood event.

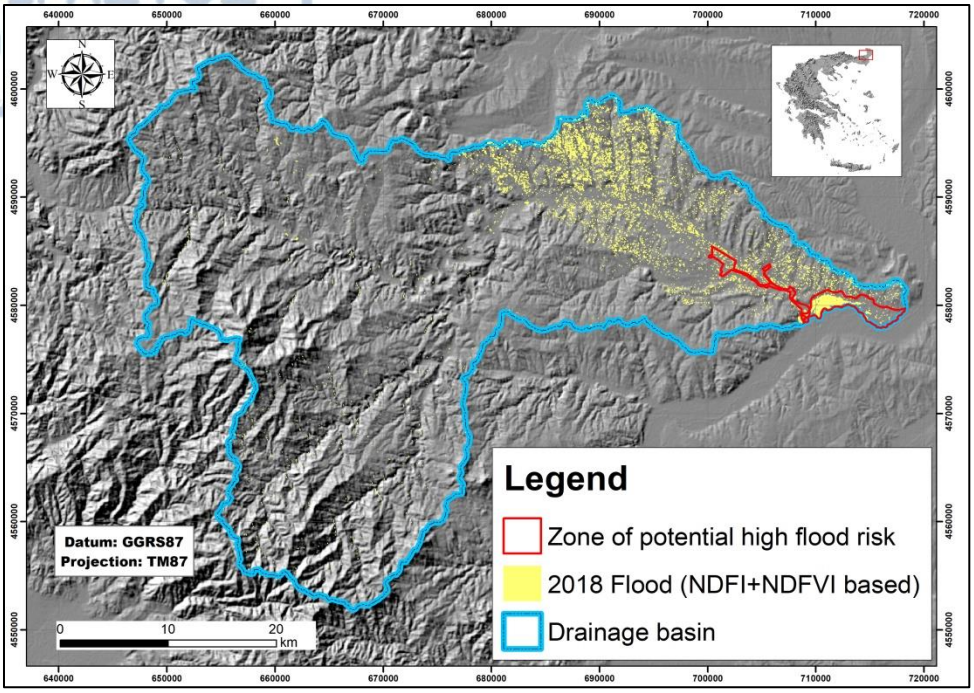

Figure 106: Comparison between the zone of potential high flood risk and the inundated areas of the March 2018 flood event.

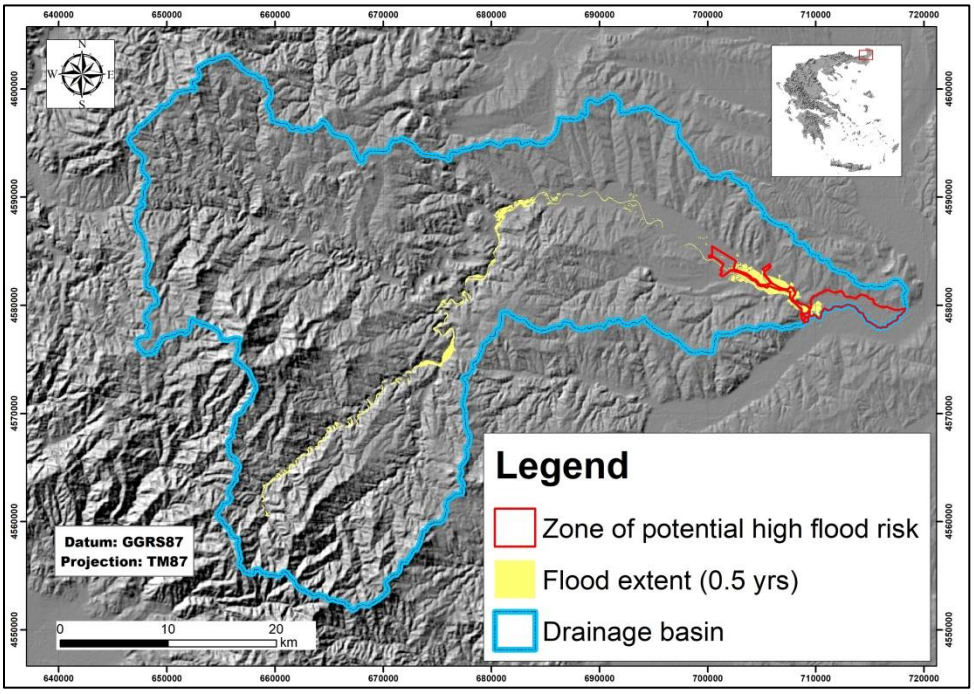

Figure 107: Comparison between the zone of potential high flood risk and the predicted inundated areas of the 0.5-year return period scenario which involved the thalweg geometry.

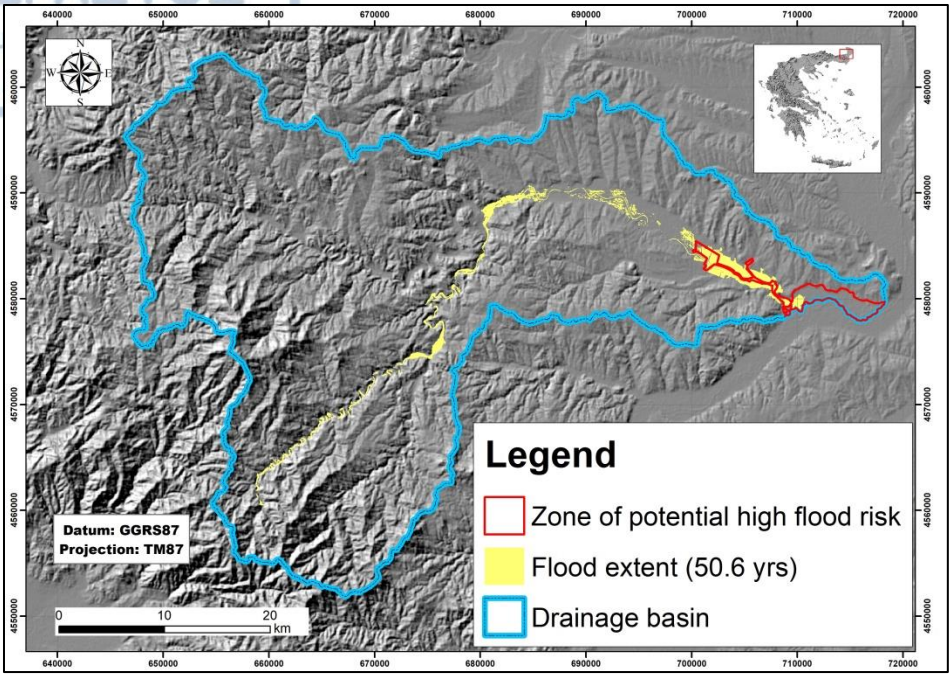

Figure 108: Comparison between the zone of potential high flood risk and the predicted inundated areas of the 50.6-year return period scenario which involved the thalweg geometry.

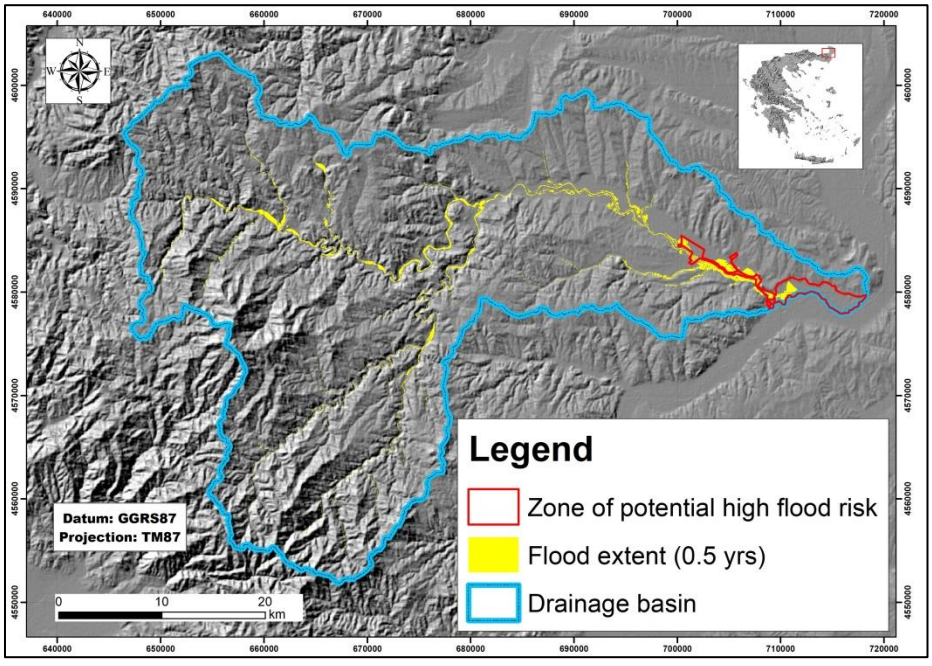

Figure 109: Comparison between the zone of potential high flood risk and the predicted inundated areas of the 0.5-year return period scenario which involved the river reaches of 5th order and higher

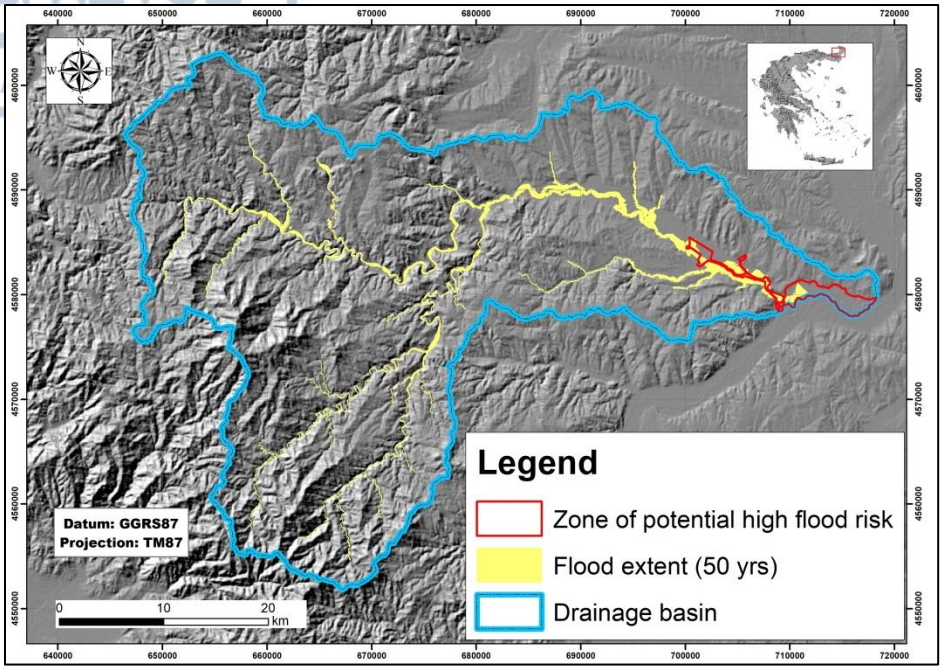

Figure 110: Comparison between the zone of potential high flood risk and the predicted inundated areas of the 50-year return period scenario which involved the river reaches of 5th order and higher

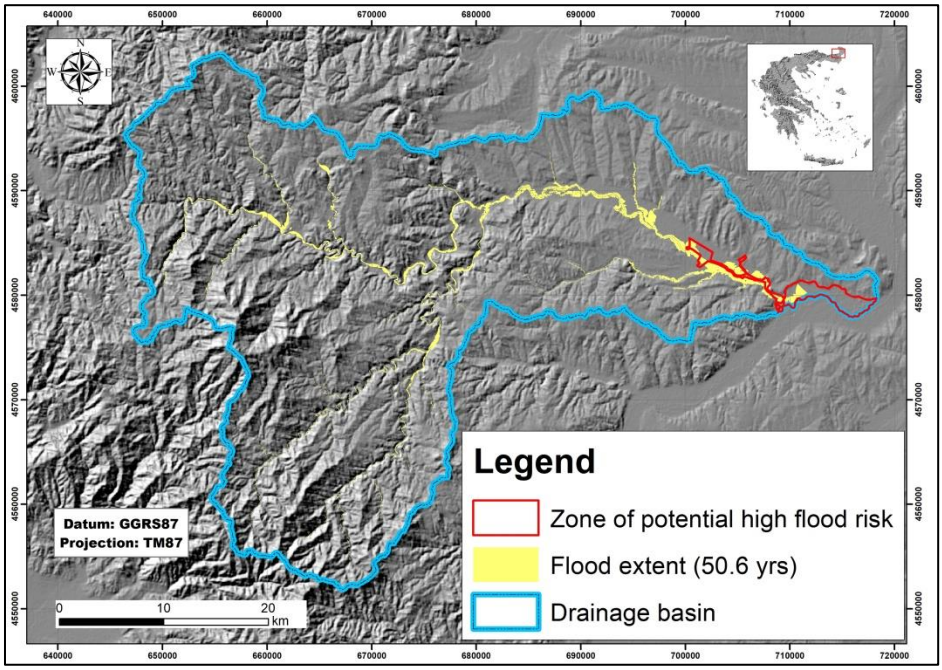

Figure 111: Comparison between the zone of potential high flood risk and the predicted inundated areas of the 50.6-year return period scenario which involved the river reaches of 5th order and higher

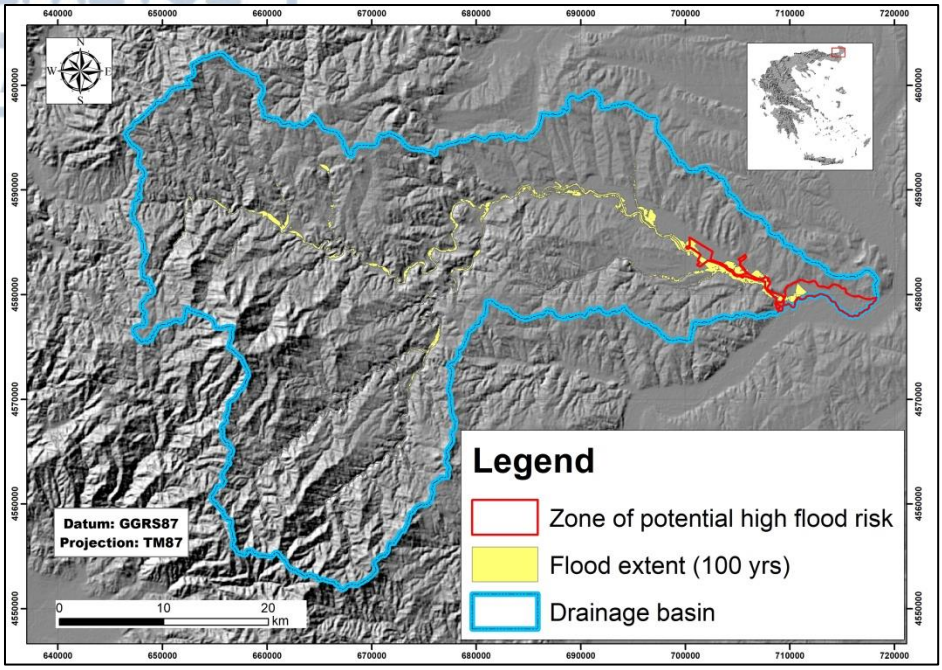

Figure 112: Comparison between the zone of potential high flood risk and the predicted inundated areas of the 100-year return period scenario which involved the river reaches of 5th order and higher

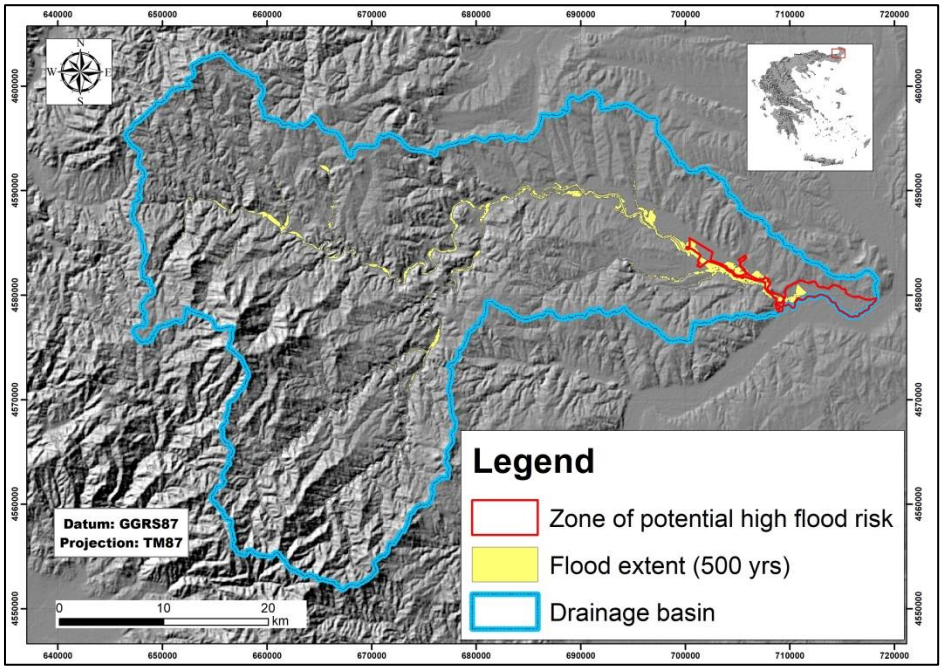

Figure 113: Comparison between the zone of potential high flood risk and the predicted inundated areas of the 500-year return period scenario which involved the river reaches of 5th order and higher

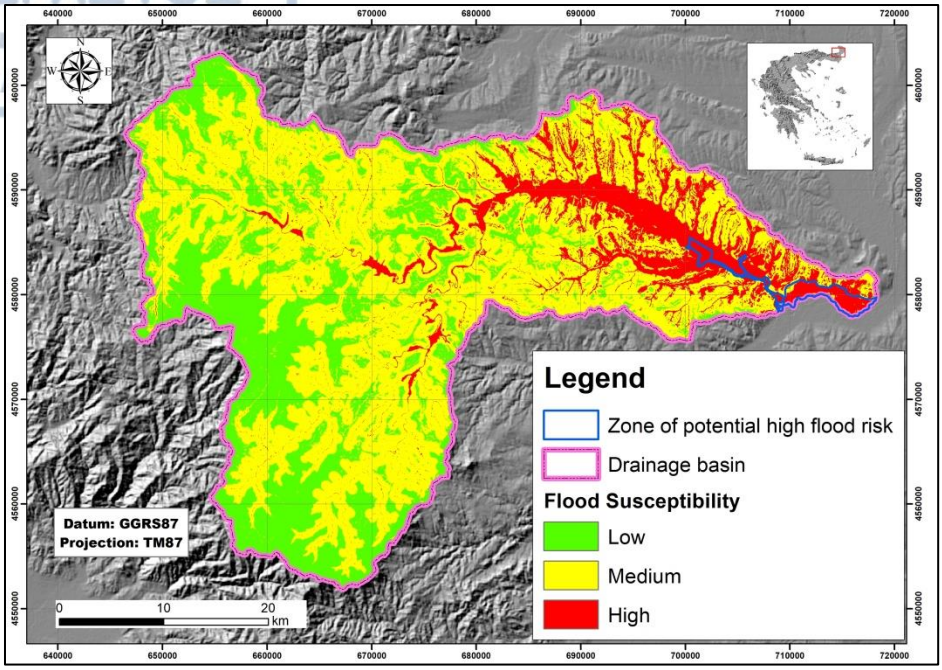

Figure 114: Superimposition of the zone of potential high flood risk upon the susceptibility map that was compiled by determining the hierarchy of factors with the aid of inundation mapping.

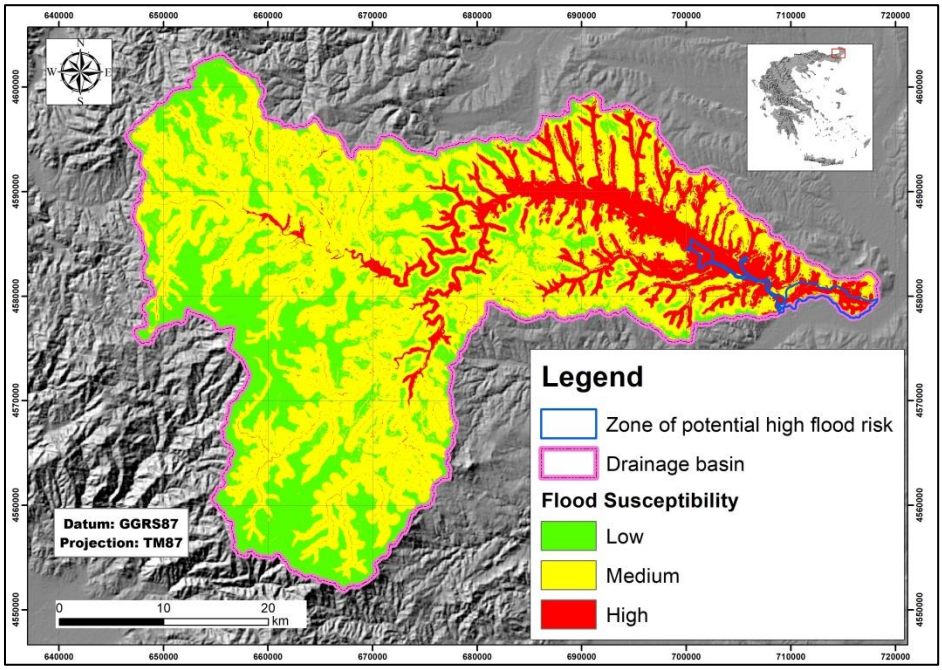

Figure 115: Superimposition of the zone of potential high flood risk upon the susceptibility map that was compiled by determining the hierarchy of factors with the aid of flood hazard mapping.

Table 33: Synoptic table indicating the extents of the intersected areas between the zone of potential high flood risk and the various results of flood hazard assessment.

Data layer	Common area (km^2)	Percentage (%)
2010 February flood	5.26	28.62
2017 April flood	2.08	11.32
2018 March flood	3.54	19.26
0.5-year flood hazard scenario (thalweg)	2.85	15.51
0.5-year flood hazard scenario	3.27	17.79
50-year flood hazard scenario	3.56	19.37
50.6-year flood hazard scenario (thalweg)	4.94	26.88
50.6-year flood hazard scenario	3.56	19.37
50-year flood hazard scenario	3.56	19.37
100-year flood hazard scenario	3.58	19.48
500-year flood hazard scenario	3.6	19.59
Susceptibility mapping (inundation mapping)	16.12	87.7
Susceptibility mapping (flood hazard mapping)	13.20	71.82

4.5 Results of the comparison between inundation mapping and flood hazard mapping

Regarding the portion of the area of the predicted flood extent for the 0.5-year return period scenario, which involved only the thalweg, that intersected with the inundated areas of the 2010 flood event that were detected with the use of the methodology developed by Cian et al. (2018), it covered an extent of 0.95 km^2. In the same manner, 1.15 km^2 of the area of the 50.6-year return period scenario that involved only the thalweg, coincided with the inundated areas of the 2010 flood.

Likewise, 1.05 km^2 and 1.21 km^2 of the areas of the 0.5-year and 50.6-year return period scenarios respectively, which concerned only the river reaches of the 5^{th} order and

higher, intersected with the inundated areas of the 2010 flood. These results are presented synoptically on Table 34.

Table 34: Area extents and percentage of the intersections between the inundated areas of the 2010 flood and the predicted flood extents of the 5-year and 20,000-year return period flood hazard mapping scenarios.

Flood Hazard Scenario	Inundated area intersection (km^2)	Percentage (%)
0.5-year (thalweg)	0.95	13.89
50.6-year (thalweg)	1.15	16.81
0.5-year	1.05	15.35
50.6-year	1.21	17.69

4.6 Results of the comparison between flood susceptibility mapping and flood hazard mapping

The portion of the high flood susceptibility class of the resulting map, which was compiled by determining the hierarchy of factors with the aid of inundation mapping that coincided with the areas of predicted flood extent for the 50-year scenario regarding the river reaches of 5th order and higher, reached a total of 29.39 km^2. Correspondingly, the rest of the intersected areas that involved the predicted flood extents of the 100-year and 500-year scenarios were 29.88 km^2 and 30.55 km^2 respectively (Table 35).

In a similar manner, the intersection of the high flood susceptibility class of the resulting map, which was compiled by determining the hierarchy of factors with the aid of flood hazard mapping, with the areas of predicted flood extent for the 50-year scenario regarding the river reaches of 5th order and higher, reached a total of 32.06 km^2. Accordingly, the rest of the intersected areas that involved the predicted flood extents of the 100-year and 500-year scenarios were 32.66 km^2 and 33.49 km^2 respectively (Table 36).

Table 35: Area extents and percentage of the intersections between the high flood susceptibility class of the resulting map, which was compiled by determining the hierarchy of factors with the aid of inundation mapping, and the predicted flood extents of the 50-year, 100-year and 500-year return period flood hazard mapping scenarios.

Flood Hazard Scenario	Predicted flood extent (km^2)	Intersected area (km^2)	Percentage (%)
50-year	44.27	29.39	77.53
100-year	45.16	29.88	76.36
500-year	46.46	30.55	73.97

Table 36: Area extents and percentage of the intersections between the high flood susceptibility class of the resulting map, which was compiled by determining the hierarchy of factors with the aid of flood hazard mapping, and the predicted flood extents of the 50-year, 100-year and 500-year return period flood hazard mapping scenarios.

Flood Hazard Scenario	Predicted flood extent (km^2)	Intersected area (km^2)	Percentage (%)
50-year	44.27	32.06	84.57
100-year	45.16	32.66	83.47
500-year	46.46	33.49	81.09

4.7 Results from the comparison between inundation mapping and the combination of flood susceptibility and hazard mapping

The common area between the unified inundation mapping results (25.16 km^2) of the 2010, 2017 and 2018 floods and the union of the data layers of high flood susceptibility, in the case of the corresponding map that was compiled by determining the hierarchy of factors with the aid of inundation mapping, with the predicted inundated areas of the 50-year (high probability) return period scenario covered an extent of 13.28 km^2. Likewise, the areas of the unified inundation mapping results that were intersected by the union of high flood susceptibility's data layer with the predicted flooded areas of the 100-year (high probability) and 500-year (high probability) scenarios reached a total of 13.29 km^2 and 13.30 km^2 respectively (Table 37).

Likewise, the intersected area between the unified inundation mapping results and the union of the data layers of high flood susceptibility, in the case of the corresponding map that was compiled by determining the hierarchy of factors with the aid of flood hazrd mapping, with the predicted inundated areas of the 50-year (high probability) return

period scenario covered an extent of 12.5 km^2. Likewise, the areas of the unified inundation mapping results that were intersected by the union of high flood susceptibility's data layer with the predicted flooded areas of the 100-year (high probability) and 500-year (high probability) scenarios reached a total of 12.51 km^2 and 12.52 km^2 respectively (Table 38).

Table 37: Area extents and percentage of the intersections between the unified inundation mapping results (2010, 2017 and 2018 floods) and the union of the data layers of high flood susceptibility of the resulting map, which was compiled by determining the hierarchy of factors with the aid of inundation mapping, with the predicted inundated areas of the 50-year, 100-year and 500-year return period flood hazard mapping scenarios.

Data Layers	Intersected area (km^2)	Percentage (%)
50-year flood hazard + high flood susceptibility areas	13.28	52.78
100-year flood hazard + high flood susceptibility areas	13.29	52.82
500-year flood hazard + high flood susceptibility areas	13.30	52.86

Table 38: Area extents and percentage of the intersections between the unified inundation mapping results (2010, 2017 and 2018 floods) and the union of the data layers of high flood susceptibility of the resulting map, which was compiled by determining the hierarchy of factors with the aid of flood hazard mapping, with the predicted inundated areas of the 50-year, 100-year and 500-year return period flood hazard mapping scenarios.

Data Layers	Intersected area (km^2)	Percentage (%)
50-year flood hazard + high flood susceptibility areas	12.50	49.68
100-year flood hazard + high flood susceptibility areas	12.51	49.72
500-year flood hazard + high flood susceptibility areas	12.52	49.76

5. Discussion

5.1 Discussion on the results of inundation mapping

Concerning the inundated areas of the 2010 flood (Figures 74 and 75) that were detected via the methodology developed by Cian et al. (2018), it can be observed that their major part is concentrated near the basin mouth of the catchment. On the other hand, the inundated areas of the 2010 flood that were detected by using ESA's (2008) methodology (Figures 72 and 73), appeared to be scattered all over the drainage basin and mostly concentrated on the E and NE parts of the drainage basin. Additionally, there is noticeable difference between the flood extents that were produced by the two methodologies, with ESA's (2008) methodology providing 15.75 km^2 of inundated areas in comparison with the 6.84 km^2 of inundated areas that were detected with the aid of the methodology by Cian et al. (2018). In ESA (2008) methodology the threshold that is applied on the change detection image is based on amplitude DN values, making it difficult to be applied on other radar sensors. It is also empirical and is supposed to detect inundation in open land only, which may explain why some inundated areas, might have been misclassified.

Regarding the results that were produced by the application of the methodology developed by Cian et al. (2018), it appeared that the inundated areas of the 2017 and 2018 floods are strongly correlated, since an area of 18.06 km^2 is common between them. On the contrary, the common inundated area between the results of the ENVISAT/ASAR and SENTINEL-1 A/B imagery is only 1.39 km^2. Furthermore, by comparing the flood extents of the flood events, it appeared that the inundated areas of 2010 are considerably smaller than the inundated areas of 2018 and 2017. The 2010 flood covered an extent of 6.84 km^2, in comparison with the inundated areas of the 2017 and 2018 flood events, which covered areas of 18.23 km^2 and 20.60 km^2 respectively. In the first place, the aforementioned observations on spatial correlation and size difference, between the inundated areas that were delineated by ENVISAT/ASAR and SENTINEL-1 A/B imagery, might indicate that the 2010 flood had probably a lower return period than the other two flood events. However, according to the river gauges provided by the station on Didymoteicho's bridge, it has to be taken under consideration that the date on which the

ENVISAT/ASAR image was taken (16/2/2010) was after the peak discharge of the flood event, which took place on the 15/2/2010. Since the station went out of order in 2012, and there are no such measurements available for the floods that occurred in April 2017 and March 2018, there might be a possibility that the inundated areas of these events appear to cover a comparatively larger extent either because their respective flood events had a higher return period or because there is a possibility that the SENTINEL-1 A/B flood images were most likely taken near the peak discharge of their respective flood events. Also, another factor that may partly contribute to the size difference between the aforementioned inundated areas might be attributed to the difference of spatial resolutions between ENVISAT/ASAR and SENTINEL-1 A/B imagery. Since SENTINEL-1 A/B imagery has greater spatial resolution than ENVISAT/ASAR imagery then it is possible that the former has the capability to detect small inundated areas that cannot be scanned by the sensor of the latter.

Finally, regarding the uncertainties that exist in flood inundation mapping with the use of Remote Sensing and especially SAR, it has to be mentioned that such techniques and methodologies suffer mostly from speckle and from under or over-detection of flood extents especially in urban and vegetated areas. Currently there is no methodology that can entirely overcome these difficulties. However, flood inundation mapping is still considered appropriate for validation in cases of flood susceptibility and flood hazard mapping. Moreover, flood hazard mapping in combination with SAR inundation mapping appear to produce some promising results. (Giustarini et al. 2013, Giustarini et al. 2015a, Giustarini et al. 2015b, Schumann and Moller 2015, Refice et al. 2018)

5.2 Discussion on the results of flood hazard and risk mapping

First of all, the resulting values of rainfall intensity that were derived from equation (12) were much higher in comparison with the corresponding values that were produced by equation (13). Concerning the results that were derived from the application of formula (13), the lowest values were observed in the case of Mikro Dereio, while, on the other hand, the highest values of rainfall intensity were observed in the case of Mega Dereio (Table16).

Moreover, by examining the results of flood hazard mapping, it can be observed that the main portion of the predicted flood extents, for all the scenarios that referred both to the thalweg and the river reaches of the 5th stream order and higher, is mostly concentrated on the eastern half of the main watercourse and towards the basin mouth (Figures 80, 82, 84, 86, 88, 90 and 92). Regarding the spatial distribution of water depth, high values appear on the W and NW parts of the drainage basin in the case of the scenarios that utilized the river reaches of 5th order and higher (Figures 81, 83, 85, 87 and 89), while the scenarios that employed only the thalweg indicated high values of water depth on the SW part of the catchment (Figures 91 and 93). Moreover, the predicted flood extent areas of the scenarios that involved the river reaches of 5th order and higher occupy areas that are approximately 10 km^2 larger than the corresponding predicted flood extent areas of the scenarios that involved solely the thalweg (Table 29). In the case of maximum water depth values, the scenarios that involved the river reaches of 5th order and higher presented maximum values that were approximately 16-17m higher than those that were observed by the corresponding scenarios that involved only the thalweg (Table 29). Finally, concerning the scenarios that employed the river reaches of 5th order and higher, it can be observed, that both the extents of the predicted flooded areas and the maximum values of water depth increase proportionately with the return period (Table 29). However, the rate, with which the predicted flooded areas and the maximum values of water depth increased their values for each higher return period scenario, kept decreasing (Table 29).

Regarding the flood hazard mapping results, it can be observed that the areas that are mostly affected by floods are the protected areas of Filiouri Valley (GR1130011) and Oreinos Evros – Dereio Valley (GR1110010), rather than the areas that are categorized as artificial surfaces according to Corine Land Cover 2012 (Copernicus 2017) classification types (Table 30). Specifically, the protected area of Oreinos Evros – Dereio Valley (GR1110010) appeared to be more affected by floods than the protected area of Filiouri Valley (GR1130011) (Figures 94-98).

5.3 Discussion on the results of flood susceptibility mapping

The present dissertation thesis tried to overcome the subjectivity of AHP by introducing the determination of the importance of the factors with the aid of either inundation mapping or flood hazard mapping. In both cases, according to the resulting criteria weights for each indicator (Tables 22 & 27), the most important factor regarding flood susceptibility in Erythropotamos' drainage basin was elevation, while rainfall, was the least important. Furthermore, topographical factors seemed to dominate over hydrological and meteorological factors, since in each case they were included in the top four most important factors of the resulting hierararchy. Regarding the spatial distribution of the areas of high flood susceptibility (Figures 99 – 103), in both cases, they are located on the eastern part of the study area. Specifically in the first half of the main stream and appear increased toward the basin mouth.

Concerning validation, in the case where the hierarchy of factors was determined with the use of the results of inundation mapping, the scores that were achieved by the validation of the susceptibility map were quite high. In particular, approximately 60% of the inundated areas from the April 2017 and March 2018 floods intersected with the high susceptibility zones of the map. The percentage rose to approximately 96% in the case that the aforementioned inundated areas intersect with the map's high to moderate susceptibility zones. Likewise, in the case where the hierarchy of factors was determined with via of the results of flood hazard mapping, the scores that were also satisfactory. Specifically, approximately 55% of the inundated areas from the April 2017 and March 2018 floods intersected with the high susceptibility zones of the map. The percentage rose to approximately 95% in the case that the aforementioned inundated areas intersect with the map's high to moderate susceptibility zones. Additionally, approximately 61% of the inundated areas from the February 2010 floods intersected with the high susceptibility zones of the map and that percentage rose to approximately 98% in the case where the aforementioned inundated areas intersect with the map's high to moderate susceptibility zones.

5.4 Discussion on the results of the comparison between the zone of potential high flood risk that is suggested by the Ministry of Environment and Energy and the results of inundation, flood hazard and susceptibility mapping

Initially, it worths mentioning that the zone of potential high flood risk that is suggested by Ministry of Environment and Energy is located on the easternmost part of the drainage basin of Erythropotamos River and towards the river mouth. It also occupies solely the Greek part of the studied catchment and does not cover any areas that are located on the Bulgarian part of the watershed.

Regarding the areas that were classified as inundated by the results of inundation mapping through the application of the methodology that has been introduced by Cian et al. (2018), they appeared, for the most of their part, to be poorly spatially correlated with the aforementioned zone (Table 33). Similarly, the common areas between the zone of potential high flood risk and the results of each scenario of flood hazard mapping that involved the river reaches of 5^{th} order or higher were also very small in size (Table 33). On the contrary, there appeared to be high spatial correlation between the results of susceptibility mapping and the zone of potential high flood risk. Especially in the case of the resulting susceptibility map that was compiled with the aid of inundation mapping, approximately 88% of the extent of the zone of potential high flood risk coincided with the high flood susceptibility area or the corresponding map (Table 33).

5.5 Discussion on the results that were produced by the comparison between inundation mapping and flood hazard mapping

The results of the comparison between inundation mapping and flood hazard mapping indicated that the areas that were produced by the two flood hazard assessment procedures were poorly spatially correlated, since none of the cases that were examined presented results above 18% (Table 34). The common areas in each examined case appeared to be mainly concentrated on the eastern half of the main watercourse and near the basin mouth.

5.6 Discussion on the results that were produced by the comparison between flood susceptibility mapping and flood hazard mapping

The results of the comparison between susceptibility mapping and flood hazard mapping indicated that the areas that were produced by the two flood hazard assessment procedures were strongly spatially correlated, since all of the cases that were examined presented results that exceeded 76% (Tables 35 & 36). Once again, the common areas in each examined case appeared to be mainly concentrated on the eastern half of the main watercourse and near the basin mouth. Moreover, it was observed that the highest results were produced by the correlation between the high flood susceptibility areas and the predicted flooded areas of the 50-year return period scenario. Finally, it can be noted that the spatial correlation was highest in the case of the high flood susceptibility areas of the map that was compiled with the aid of flood hazard mapping rather than with the map that was compiled with the use of inundation mapping.

5.7 Discussion on the results that were produced by the comparison between inundation mapping and the combination of flood susceptibility and hazard mapping

The results of the comparison between inundation mapping and the unified susceptibility mapping and flood hazard mapping results indicated that the areas that were produced by these flood hazard assessment procedures were moderately spatially correlated, since all of the cases that were examined did not managed to exceed 53% (Tables 37 & 38). The common areas in each examined case appeared to be mainly concentrated on the eastern and northeastern half of the main watercourse, as well as near the basin mouth.

6. Conclusions

This dissertation thesis contributes to the fields of Hydrology and Physical & Environmental Geography by initially assessing flood hazard in the drainage basin of Erythropotamos River, for which, although it is the recipient of frequent flood occurrences, so far no flood hazard assessment studies have been carried out. Even though the Ministry of Environment and Energy has conducted Flood Hazard Management Plans for the drainage basin of Evros River (Ministry of Environment and Energy 2014), it did not include the part of the catchment of Erythropotamos River that lies outside of the Greek borderline. Furthermore, this work applies various methodologies of flood hazard assessment to the watershed of Erythropotamos River and also compares and combines their results. This approach does not follow the current trend of the vast majority of the literature that covers flood hazard assessment, which tends to focus on developing or improving a single methodology of flood hazard assessment. Finally, regarding flood susceptibility mapping, this research introduces a concept that helps in dealing with the subjectivity that involves the determination of the importance of factors with the use of AHP. Specifically, the aforementioned hierarchy is determined according to the proportion of either the inundated area that is delineated by radar imagery or the inundated area that is predicted by hydraulic modelling that intersects with the factor's high susceptibility zone.

Therefore, having examined how Remote Sensing and GIS techniques contribute to flood hazard assessment in the drainage basin of Erythropotamos River, a number of conclusions could be drawn from the methodologies that were employed and the results that they produced.

6.1 Features of the study area

The drainage basin of Erythropotamos River covers an area of 1,618.5 km^2 and its elevation values range from 16m to 1,285m, while mean elevation is 328.22m. The greatest proportion of the study area is hilly (150m – 600m) and strongly inclined (5° – 15°). Furthermore, the geologic formations that dominate Erythropotamos' watershed are metamorphic and the prevalent land cover type is "forests and semi-natural areas".

Regarding the drainage network of the study area, it is of the dendritic type and the highest order of its reaches is the 7th order. Additionally, the catchment's drainage density is low, while the drainage basin belongs to the "old age" stage of the Erosion Cycle. Concerning the climate characteristics that are encountered within the drainage basin, the climate type is characterized as Sub-Mediterranean, sub-humid with severe winter, with the dry season lasting from mid-April until mid-August. Finally, within the watershed of Erythropotamos River lie parts of Filiouri Valley (GR1130011) and Oreinos Evros – Dereio Valley (GR1110010), which are Special Protection Areas (SPA) that belong to the Natura 2000 network.

6.2 Flood inundation mapping

Regarding flood inundation mapping with the aid of SAR imagery, the methodology suggested by ESA (2008) did not produce satisfactory results and proved to be difficult to apply to sensors other than ENVISAT/ASAR. On the other hand, the methodology developed by Cian et al. (2018) proved to be very reliable and versatile, because it can be applied successfully on both ENVISAT/ASAR and SENTINEL-1 A/B imagery. Although this procedure suffers from uncertainties such as the over and under-detection of floods in urban areas, which present varying degrees of difficulties, until today, in all SAR-based inundation mapping methodologies, this was not a major hurdle for applying it to the study area, because artificial surfaces covered only 1.1% of Eythropotamos' watershed.

Concerning the methodology developed by Cian et al. (2018), except from the observed size difference between the delineated ENVISAT/ASAR and SENTINEL-1 A/B inundated areas, there appeared to be strong spatial correlation between the inundated areas that were captured by SENTINEL-1 A/B imagery. On the other hand, there appeared to be weak spatial correlation between the delineated inundated areas between SENTINEL-1 A/B and ENVISAT/ASAR imagery. All of the aforementioned observations can be potentially attributed either to the different return periods of the flood phenomena that were captured by SAR imagery or the time during which the imagery was taken in relation with the peak of the flood. However, the difference in spatial

resolution between SENTINEL-1 A/B and ENVISAT/ASAR imagery might also partly explain the spatial differences that appear in their respective resulting inundated areas, since high spatial resolution can reveal inundated areas that cannot be captured by low spatial resolution imagery.

6.3 Flood hazard and risk mapping

The flood hazard mapping and subsequently the flood risk mapping procedures had to be applied to the whole of the drainage basin, which raised the question of which part of the drainage network would be involved in this task since involving the entire drainage network would increase the input of data volume to such a degree that it would be extremely difficult for HEC-RAS and HEC-GeoRAS to handle the calculations. For this reason, except from carrying out the flood hazard mapping procedure with the use of only the thalweg, this dissertation thesis suggested the use of bifurcation values in order to determine by geomorphological criteria which part of the drainage network is more prone to flooding (Das 2016). Although this methodology produced some promising results, it needs to be tested more thoroughly in order to become established.

Regarding the calculation of rainfall intensity, through which flood discharge, which is the input of steady flow hydraulic analysis that is performed by HEC-RAS, the universal equation (12) (Giandotti 1934 and Soulios 1996) produced higher values in comparison with equation (13) (Koutsogiannis et al. 2010, Ministry of Environment and Energy 2016). Additionally, the resulting predicted inundated areas covered a greater area and presented higher water depth values in the case where the geometry of the river reaches of 5^{th} order and higher were employed.

Finally, flood risk mapping indicated that the protected areas of Filiouri Valley (GR1130011) and Oreinos Evros – Dereio Valley (GR1110010) are threatened even by floods of high probability, with the former having to deal with the brunt of the threat rather than the latter.

6.4 Flood susceptibility mapping

Concerning the AHP, this research introduced the idea to use either inundation or flood hazard mapping in order to amend for its subjectivity when determining the importance between flood susceptibility factors. The larger the part of the inundated area delineated by radar imagery or predicted by hydraulic modelling that intersects with the factor's high susceptibility zone, the more important the factor is over the others.

Furthermore, the resulting susceptibility maps appeared to be in consistency with the, April 2017, March 2018 and, in the case where the hierarchy of factors was determined by the results of flood hazard mapping, February 2010 flood extents. The aforementioned inundated areas, which, according to each case, were not involved in the determination of the importance of the flood susceptibility factors, so that no bias could be assumed, coincided mostly with the high flood susceptibility class of the resulting maps.

According to the results of AHP, elevation was found in both cases to be the most dominant flood susceptibility factor in the catchment of Erythropotamos. This can be further ascertained by considering more future flood events in the same area and by taking advantage of the current and prospective availability of SENTINEL-1 imagery data. Furthermore, in the case where the hierarchy of factors was determined with the aid of flood hazard mapping, the aforementioned hierarchy did not appear to be affected by the various return period scenarios that were tested.

It also remains to be seen if the application of the presented methodologies on other drainage basins shall indicate each time another factor as more prevalent in flood susceptibility, thus maintaining the argument that the conditions that affect flood susceptibility are unique for each catchment.

6.5 The zone of potential high flood risk that is suggested by the Ministry of Environment and Energy

First of all, it is important to mention that the zone of potential high flood risk that is suggested by Ministry of Environment and Energy does not involve areas that are located on the Bulgarian part of Erythropotamos' catchment. This zone presented poor spatial correlation with either the areas that were delineated by inundation mapping or the

predicted flooded extents of the various return period scenarios that were employed by flood hazard mapping. On the contrary, high spatial correlation was observed between the aforementioned zone and the results of susceptibility mapping. Especially in the case of the resulting susceptibility map that was compiled with the aid of inundation mapping.

6.6 Combinations between the results of flood hazard assessment methodologies

Regarding the various combinations that were tested between the results of each flood hazard assessment procedure that was carried out in this dissertation, it was observed that the various scenarios of flood hazard mapping, regardless of the part of the drainage network that was involved into the analysis, did not produce flood extents that were strongly correlated with the inundated areas produced by SAR imagery. Furthermore, the areas of high flood susceptibility, regardless of what methodology was followed to determine the hierarchy of factors, appeared to be strongly correlated with the predicted flood extents of the of the various flood hazard mapping probability scenarios, especially when these employed the river reaches of the 5^{th} stream order or higher. Additionally, the unified flood extent areas of high flood susceptibility mapping with each of the predicted flood extent areas that were produced by the various scenarios of flood hazard mapping appeared in general moderately correlated with the unified inundation mapping results.

6.7 Overall conclusions

Having examined how the flood hazard assessment procedures of inundation mapping, flood hazard and susceptibility mapping operate within a drainage basin, it has been observed that each methodology, when used individually, produces satisfactory results but struggles to overcome its limitations. Inundation mapping with the use of SAR imagery suffers from under or over-detection of flood extents in urban and vegetated areas, whereas flood susceptibility mapping strives to overcome subjectivity in the determination of the hierarchy of the weighted factors and flood hazard mapping depends heavily on the precision of the DTM and the geometry that will be utilized. These flaws

are further exacerbated when the aforementioned methodologies are applied in drainage basins of large extent.

Inundation mapping and flood hazard mapping produced results that were poorly spatially correlated, even when each one of them was tested against the zone of potential high flood risk that is suggested by Ministry of Environment and Energy. However when flood hazard mapping was combined with the results of flood susceptibility mapping, the spatial correlation of their unified data layers with the unified resulting data layers of inundation mapping presented a significant increase. In the case of flood susceptibility mapping there is strong spatial correlation between its high susceptibility zone, the inundated areas that were delineated with SAR imagery, the predicted areas that were produced via HEC-GeoRAS and the zone of potential high flood risk that is suggested by Ministry of Environment and Energy. This might be attributed to the indirect inclusion of inundation and flood hazard mapping results into the flood susceptibility results via the AHP.

When it comes to flood hazard assessment in drainage basins, perhaps the more appropriate way to produce effective results might be to combine the aforementioned procedures rather than employ them individually. Flood susceptibility mapping can indirectly incorporate flood inundation and hazard mapping results, with the aid of AHP, within its own results and thus provide a vehicle for the combination of flood hazard assessment procedures. Of course this hypothesis ought to be further examined by being applied to other drainage basins in order to test its validity.

References

Aissia, M.A.B., Chebana, F., Ouarda, T.B.M.J., Roy, L., Desrochers, G., Chartier, I. and Robichaud, E., 2012. Multivariate analysis of flood characteristics in a climate change context of the watershed of the Baskatong reservoir, province of Québec, Canada. *Hydrological Processes*, 26, 130–142. DOI: https://doi.org/10.1002/hyp.8117.

Astaras, T., Oikonomidis, D. and Mouratidis, A., 2011. *Digital Cartography and GIS*. Disigma Publishing Group, Thessaloniki.

Bagnouls F., and Gaussen H., 1957. Les climats biologiques et leur classification. *Annales De Geographie*, 355, 193-220.

Bahremand, A., De Smedt, F., Corluy, J., Liu, Y.B, Poorova, J., Velcicka, L. and Kunikova, L., 2007. WetSpa model application for assessing reforestation impacts on floods in Margecany – Hornad watershed, Slovakia. Water Resourcess Management, 21, 1373–1391. DOI: https://doi.org/10.1007/s11269-006-9089-0.

Baky, A. A., Zaman, A. M. and Khan, A. U., 2012. Managing Flood Flows for Crop Production Risk Management with Hydraulic and GIS Modeling: Case study of Agricultural Areas in Shariatpur. *APCBEE Procedia*, 1, 318 – 324. DOI: https://doi.org/10.1016/j.apcbee.2012.03.052

Barkau, R. L., 1992. UNET, One-Dimensional Unsteady Flow Through a Full Network od Open Channels. *Computer Program*, St. Louis, MO.

Bates, P.D., 2004. Remote sensing and flood inundation modeling. *Hydrological Processes*, 18, 2593–2597. DOI: https://doi.org/10.1002/hyp.5649.

Bates, P.D., Horritt, M.S. and Fewtrell, T.J., 2010. A simple inertial formulation of the shallow water equations for efficient two-dimensional flood inundation

modelling. Journal of Hydrology, 387 (1-2), 33-45. DOI: https://doi.org/10.1016/j.jhydrol.2010.03.027

Bates, P.D., Horritt, M.S., Smith, C.N. and Mason, D., 1997. Integrating remote sensing observations of flood hydrology and hydraulic modelling. Hydrological Processes 11 (14), 1777-1795. DOI: https://doi.org/10.1002/(SICI)1099-1085(199711)11:14<1777::AID-HYP543> 3.0.CO;2-E

Bates, P.D. and De Roo, A.P.J., 2000. A simple raster based model for flood inundation simulation. *Journal of Hydrology*, 236, pp. 54–77. DOI: https://doi.org/10.1016/S0022-1694(00)00278-X

Bell, F.G., 1999. *Geological Hazards. Their assessment, avoidance and mitigation*. E and FN SPON, London.

Benito, G., and Hudson, P., 2010. Flood hazards: The context of fluvial geomorphology. In: I. Alcántara-Ayala & A. Goudie (eds) *Geomorphological Hazards and Disaster Prevention*. Cambridge, Cambridge University Press, pp. 111-128. DOI:10.1017/CBO9780511807527.010

Beven, K. and Kirkby, M., 1979. A Physically Based, Variable Contributing Area Model of Basin Hydrology. *Hydrological Science Bulletin*, 24, pp 43-69.

Bezes K. A., 1994. Interaction between surface water and groundwater in the valley of Evros' tributary Erythropotamos. Application of the mathematical model BEMERMHN. *Proceedings of the 2nd Hydrogeological congress*, Patras, 749-767.

Birkholz, S., Muro, M., Jeffrey, P. and Smith, H.M., 2014. Rethinking the relationship between flood risk perception and flood management. *Science of the Total Environment*, 478, pp. 12–20. DOI: https://doi.org/10.1016/J.SCITOTENV. 2014. 01 .061

Bridge, J.S., 2003. *River and Floodplains: Forms, Processes and Sedimentary Record*. Oxford: Blackwell.

Brivio, P.A., Colombo R., Maggi M. and Tomasoni R.. 2002. Integration of remote sensing data and GIS for accurate mapping of flooded areas. *International Journal of Remote Sensing*, 23 (3), 429–441. DOI: https://doi.org/10.1080/01431160010014729.

Brown, K.M., Hambridge, C.H. and Brownett, J.M., 2016 Progress in operational flood mapping using satellite synthetic aperture radar (SAR) and airborne light detection and ranging (LiDAR) data. *Progress in Physical Geography*, 40 (2), 196–214. DOI: https://doi.org/10.1177/0309133316633570.

Chapman, B., McDonald, K., Shimada, M., Rosenqvist, A., Schroeder, R. and Hess, L., 2015. Mapping Regional Inundation with Spaceborne L-Band SAR. *Remote Sensing*, 7, pp. 5440-5470. DOI: https://doi.org/10.3390/rs70505440.

Chen, Y., Liu, R., Barrett, D., Gao, L., Mingwei, Z., Renchullo, L. and Emelyanova, I., 2015. A spatial assessment framework for evaluating flood risk under extreme climates. Science of the Total Enviromnent. 538, 512–523. DOI: http://dx.doi.org/10.1016/j.scitotenv.2015.08.094

Chen, Y., Yu, J. and Khan, S., 2010. Spatial sensitivity analysis of multi-criteria weights in GIS-based land suitability evaluation. *Environmental Modelling and Software*, 25, 1582–1591. DOI: https://doi.org/10.1016/j.envsoft.2010.06. 001.

Chen, Y., Yu, J. and Khan, S., 2013. The spatial framework for weight sensitivity analysis in AHP-based multi-criteria decision making. Environmental *Modelling and Software*, 48, 129–140. DOI: https://doi.org/10.1016/j.envsoft.2013.06.010

Cian, F., Marconcini, M. and Ceccato, P., 2018. Normalized Difference Flood Index for rapid flood mapping: Taking advantage of EO big data. *Remote Sensing of Environment*. 209, 712-730. DOI: https://doi.org/10.1016/j.rse.2018.03.006.

Clement, M. A., Kilsby, C.G. and Moore, P., 2018. Multi-temporal synthetic aperture radar flood mapping using change detection. *Journal of Flood Risk Management*, 11, 152–168. DOI: 10.1111/jfr3.12303.

CoG (Committee of Geology), 1989. *Geologic map of P.R. Bulgaria*, Scale 1:50 000.

Colby J. D., Mulcahy, K. A. and Wang, Y., 2000. Modelling flooding extent from Hurricane Floyd in the coastal plains of North Carolina. *Environmental Hazards*, 2, 157–168. DOI: https://doi.org/10.1016/S1464-2867(01)00012-2

Cook, A., and Merwade, V., 2009. Effect of topographic data, geometric configuration and modeling approach on flood inundation mapping. *Journal of Hydrology*, 377, 131–142. DOI: https://doi.org/10.1016/j.jhydrol.2009.08.015

Costa J. E., 1988. Floods from Dam Failures. In: V. Baker, C. Kochel and P. Patton (eds) *Flood Geomorphology*. New York, Wiley Interscience, pp. 439-463.

CRED (Centre for Research on the Epidemiology of Disasters), UNISDR (UN Office for Disaster Risk Reduction), 2018. *UNISDR and CRED report: Economic Losses, Poverty & Disasters (1998 - 2017)*. CRED.

Crozier, M., and Glade, T., 2010. Hazard assessment for risk analysis and risk management. In: I. Alcántara-Ayala & A. Goudie (eds) *Geomorphological Hazards and Disaster Prevention*. Cambridge, Cambridge University Press, pp. 111-128. DOI:10.1017/CBO9780511807527.010

Das, L.M., 2016. Morphometric Analysis of Jiya Dhol River Basin. *International Journal of Science and Research*, 5 (3), 1482-1486.

Demek, J., 1972. *Manual of detailed geomorphological mapping*. Academia, Prague, 344 p.

Dewan, A.M., Islam, M.M., Kumamoto, T. and Nishigaki, M., 2007. Evaluating flood hazard for land-use planning in Greater Dhaka of Bangladesh using remote sensing and GIS techniques. *Water Resources Management*, 21, 1601–1612. DOI: https://doi.org/10.1007/s11269-006-9116-1.

Dikau R., 1989. The application of a digital relief model to landform analysis. In: J.F. Raper, (eds) *Three Dimensional Application in Geographical Information Systems*. London: Taylor and Francis, 51-77.

Domakinis, C., Mouratidis, A., Voudouris, K., Astaras, T., and Karypidou, M.C. Flood susceptibility mapping in Erythropotamos river basin with the aid of Remote Sensing and GIS [In press].

Domakinis, C., Oikonomidis, D., Voudouris, K. and Astaras, T., 2015. Using Geographic Information Systems (GIS) and Remote Sensing to map flood extent and to assess flood hazard in Erythropotamos river basin (Evros, Greece). *10th International Congress of the Hellenic Geographical Society, 22-24 October 2014, Thessaloniki*.

E.C. (European Council), 2007. Directive 2007/60/EC of the European Parliament and of the Council of 23 October 2007 on the assessment and management of flood risks. *Official Journal of the European Union*, L228, 6.11.2007.

Ettinger, S., Mounaud, L., Magill, C., Yao-Lafourcade, A.-F., Thouret, J.-C., Manville, V., Negulescu, C., Zuccaro, G., De Gregorio, D., Nardone, S., Uchuchoque, J.A.L., Arguedas, A., Macedo, L. and Llerena, N.M., 2016. Building vulnerability to hydro-geomorphic hazards: estimating damage probability from

qualitative vulnerability assessment using logistic regression. *Journal of Hydrology*, 541, 563–581. DOI: https://doi.org/10.1016/j.jhydrol. 2015.04.017.

Fick, S.E., and Hijmans R.J.,2017. Worldclim 2: New 1-km spatial resolution climate surfaces for global land areas. *International Journal of Climatology*, 37 (12), 4302 – 4315. DOI: https://doi.org/10.1002/joc.5086

Gan, T. Y., Zunic, F., Kuo, C.-C. and Strobl, T., 2012. Flood Mapping of Danube River a Romania using single and multi-date ERS2-SAR images. *International Journal of Applied Earth Observation and Geoinformation*, 18, 69-81. DOI: 10.1016/j.jag.2012.01.012.

Giandotti, M. 1934. *Previsione delle piene e delle magre dei corsi d'acqua*. Istituto Poligrafico dello Stato, 8, 107–117.

Giustarini, L., Hostache, R., Matgen, P. and Schumann, G.J.P., 2013. A change detection approach to flood mapping in urban areas using TerraSAR-X. *IEEE Transactions on Geoscience and Remote Sensing*, 51, (4), 2417–2430. DOI: https://doi.org/10.1109/TGRS.2012.2210901.

Giustarini, L., Chini, M., Hostache, R., Pappenberger, F. and Matgen, P.., 2015a. Flood hazard mapping combining hydrodynamic modeling and multi annual remote sensing data. *Remote Sensing*, 7 (10), 14200–14226. DOI: https://doi.org/10.3390/rs71014200

Giustarini, L., Vernieuwe, H., Verwaeren, J., Chini, M., Hostache, R., Matgen, P., Verhoest, N.E.C. and De Baets, B., 2015b. Accounting for image uncertainty in SAR-based flood mapping. *International Journal of Applied Earth Observation and Geoinformation*, 34, 70–77. DOI: https://doi.org/10.1016/ j.jag.2014.06.017.

Greek Ministry of Agriculture, 1978. *Bioclimatic Map of Greece*, Scale: 1: 1,000,000.

H.M.G.S. (HELLENIC MILITARY GEOGRAPHICAL SERVICE), 1970a. *Topographic map of Aisymi sheet*, Scale 1:50 000, Athens.

H.M.G.S. (HELLENIC MILITARY GEOGRAPHICAL SERVICE), 1970b. *Topographic map of Khardhamos sheet*, Scale 1:50 000, Athens.

H.M.G.S. (HELLENIC MILITARY GEOGRAPHICAL SERVICE), 1970c. *Topographic map of Sapai sheet*, Scale 1:50 000, Athens.

H.M.G.S. (HELLENIC MILITARY GEOGRAPHICAL SERVICE), 1970d. *Topographic map of Mega Dherion sheet*, Scale 1:50 000, Athens.

H.M.G.S. (HELLENIC MILITARY GEOGRAPHICAL SERVICE), 1970e. *Topographic map of Souflion sheet*, Scale 1:50 000, Athens.

H.M.G.S. (HELLENIC MILITARY GEOGRAPHICAL SERVICE), 1970f. *Topographic map of Ormenion sheet*, Scale 1:50 000, Athens.

H.M.G.S. (HELLENIC MILITARY GEOGRAPHICAL SERVICE), 1970g. *Topographic map of Rizia sheet*, Scale 1:50 000, Athens.

H.M.G.S. (HELLENIC MILITARY GEOGRAPHICAL SERVICE), 1970h. *Topographic map of Didymoteichon sheet*, Scale 1:50 000, Athens.

H.M.G.S. (HELLENIC MILITARY GEOGRAPHICAL SERVICE), 1970i. *Topographic map of Vyrsini sheet*, Scale 1:50 000, Athens.

H.M.G.S. (HELLENIC MILITARY GEOGRAPHICAL SERVICE), 1970j. *Topographic map of Metaxades sheet*, Scale 1:50 000, Athens.

H.M.G.S. (HELLENIC MILITARY GEOGRAPHICAL SERVICE), 1969a. *Topographic map of Pythion sheet*, Scale 1:50 000, Athens.

H.M.G.S. (HELLENIC MILITARY GEOGRAPHICAL SERVICE), 1969b. *Topographic map of Orestias sheet*, Scale 1:50 000, Athens.

Hardesty, S., Shen, X., Nikolopoulos, E., and Anagnostou, E., 2018. A Numerical Framework for Evaluating Flood Inundation Risk under Different Dam Operation Scenarios. *Water*, 10, 1798. DOI:10.3390/w10121798.

Han, Z.J., Wu, L., Ran, Y. and Ye, Y., 2003. The concealed active tectonics and their characteristics as revealed by drainage density in the North China plain (NCP). *Journal of Asian Earth Sciences*, 21, 989–998. DOI: https://doi.org/10.1016/S1367-9120(02)00175-X

Henry, J.B., Chastanet, P., Fellah, K. and Desnos, Y.L., 2006. Envisat multipolarized ASAR data for flood mapping. *International Journal of Remote Sensing*, 27, (9–10), 1921–1929. DOI: https://doi.org/10.1080/01431160500486724.

Hess, L. L., Melack, J. M., Solange, F. and Wang, Y., 1995. Delineation of Inundated area and vegetation along the Amazon floodplain with the SIR-C Synthetic Aperture Radar. *IEEE Transactions on Geoscience and Remote Sensing*, 33 (4), 896–905. DOI: 10.1109/36.406675

Hong, H., Panahi, M., Shirzadi, A., Ma, T., Liu, J., Zhu, A-X., Chen, W., Kougias, I. and Kazakis, N., 2018. Flood susceptibility assessment in Hengfeng area coupling adaptive neuro-fuzzy inference system with genetic algorithm and differential evolution. *Science of the total Environment*, 621, pp. 1124-1141. DOI: https://doi.org/10.1016/j.scitotenv.2017.10.114.

Horritt, M.S., 1999. A statistical active contour model for SAR image segmentation. *Image and Vision Computing*, 17 (3–4), 213–224. DOI: https://doi.org/10.1016/S0262-8856(98)00101-2

Horritt, M.S., 2006. A methodology for the validation of uncertain flood inundation models. *Journal of Hydrology*, 326, 153–165. DOI: https://doi.org/10.1016/j.jhydrol.2005.10.027

Horritt, M.S. and Bates, P. D., 2002. Evaluation of 1D and 2D numerical models for predicting river flood inundation. *Journal of Hydrology*, 268, 87–99. DOI: https://doi.org/10.1016/S0022-1694(02)00121-X

Horritt, M.S., Mason, D.C. and Luckman, A. J., 2001. Flood boundary delineation from synthetic aperture radar imagery using a statistical active contour model. *International Journal of Remote Sensing*, 22 (October 2014), 2489–2507. DOI: http://dx.doi.org/10.1080/01431160152497691.

Horton, R.E., 1932. Drainage basin characteristics. *Transactions*, American Geophysical Union, 13, 350-61.

Horton, R.E., 1945. Erosional development of streams and their drainage basins. *Bulletin of the Geological Society of America*, 56, 275-370.

Hupp, C. R., 1988. Plant ecological aspects of flood geomorphology and paleoflood history. In: V. Baker, C. Kochel and P. Patton (eds) *Flood Geomorphology*. New York, Wiley Interscience, pp. 335-356.

Hydrologic Engineer Center (H.E.C.), 1993. UNET, One-Dimensional Unsteady Flow Through a Full Network od Open Channels: User's Manual. U.S. Army Corps of Engineers, Davis, CA.

Hydrologic Engineer Center (H.E.C.), 2010. HEC-RAS River Analysis System: User's Manual. U.S. Army Corps of Engineers, Davis, CA.

Hydrologic Engineer Center (H.E.C.), 2011. HEC-GeoRAS GIS Tools for Support of HEC-RAS using ArcGIS: User's Manual. U.S. Army Corps of Engineers, Davis, CA.

I.G.M.E. (Institute of Geology and Mineral Exploration), 2002. *Synoptic geologic map of SE Rhodope – Thrace*, Scale 1:200 000, Xanthi.

Jodouin, S., Bentabeta, L., Zioua, D., Vaillancourta, J. and Armenakis C., 2003. Spatial database updating using active contours for multispectral images: application with Landsat 7. *ISPRS Journal of Photogrammetry and Remote Sensing*, 57, 346–355.

Junk, W. J., Baylay, P. B. and Sparks, R. E., 1989. The flood pulse concept in river-floodplain systems. In: D. P. Dodge (eds) *Proceedings of the International Large River Symposium (LARS)*. Canadian Special Publication in Fisheries and Aquatic Science, 106, 110 – 127.

Keller, E. A., Pinter, N., 2002. *Active tectonics: Earthquakes, Uplift, and Landscape*. Prentice Hall, New Jersey, U.S.A.

Kazakis, N., Kougias, I. and Patsialis, T., 2015. Assessment of flood hazard areas at a regional scale using an index-based approach and Analytical Hierarchy Process: application in Rhodope–Evros region, Greece. Science of the Total Environment, 538, 555–563. DOI: https://doi.org/10.1016/j.scitotenv.2015.08. 055.

Khalfallah, C. B. and Saidi, S., 2018. Spatiotemporal floodplain mapping and prediction using HEC-RAS – GIS tools: Case of the Mejerda river, Tunisia. *Journal of African Earth Sciences*, 142, 44-51. DOI: https://doi.org/10.1016/j.jafrearsci.2018.03.004

Kia, M.B., Pirasteh, S., Pradhan, B., Mahmud, A.R., Sulaiman, W.N.A. and Moradi, A., 2012. An artificial neural network model for flood simulation using GIS: Johor River Basin, Malaysia. Environmental Earth Sciences, 67, 251–264. DOI: https://doi.org/10.1007/s12665-011-1504-z.

Knighton. A. D., 1998. *Fluvial Forms and Processes*. Baltimore, MD: Edward Arnold.

Koutsogiannis, D., Markonis, I., Koukouvinos, A., Papalexiou, S.M., Mamasis, N. and Dimitriadis P., 2010. Hydrological survey of intense rainfalls in the drainage basin of Kifisos. Athens, 2010, pp. 31-42.

Leopold, L.B., Wolman M. G. and Miller J.P., 1964. Fluvial Processes. In: W. H. Freeman and Co (eds) *Geomorphology*. New York.

Li, J. and Heap A., 2014. Spatial interpolation methods applied in the environmental sciences: A review. *Environmental Modelling & Software*, 53, 173-189. DOI: https://doi.org/10.1016/j.envsoft.2013.12.008

Li, Y., Martinis, S., Plank, S. and Ludwig, R., 2018. An automatic change detection approach for rapid flood mapping in Sentinel-1 SAR data. *International Journal of Applied Earth Observation and Geoinformation*, 73, 123-135. DOI: https://doi.org/10.1016/j.jag.2018.05.023

Liu, K., Li, Z., Yao, C., Chen, J., Zhang, K. and Saifullah, M., 2016. Coupling the k-nearest neighbour procedure with the Kalman filter for real-time updating of the hydraulic model in flood forecasting. *International Journal of Sediment Research*, 31, 149–158. DOI: https://doi.org/10.1016/j.ijsrc.2016.02.002.

Long S., Fatoyinbo, T.E. and Policelli, F., 2014. Flood extent mapping for Namibia using change detection and thresholding with SAR. *Environmental Research Letters*, 9, 35002–35009. DOI: https://doi.org/10.1088/1748-9326/9/3/035002.

Lowry, R. T., Langham, E. J. and Mudry, N., 1981. A preliminary analysis of SAR mapping of the Manitoba Flood, May 1979. In: *American Water Resource Association, Satellite Hydrology*, 316−323.

Lyu, H. M., Sun, W. J., Shen, S. L. and Arulrajah, A., 2018. Flood risk assessment in metro systems of mega-cities using a GIS-based modeling approach. *Science of the Total Environment*, 626, 1012–1025. DOI: https://doi.org/10.1016/ j.scitotenv.2018.01.138.

Marti-Cardona B., Lopez-Martines C., Dolz-Ripolles J.and Blade-Castellet E., 2010. ASAR polarimetric, multi-incidence angle and multitemporal characterization of

Donana Wetlands for flood extent monitoring. *Remote Sensing of Environment* 114, 2802-2815. DOI: https://doi.org/10.1016/j.rse.2010.06.015

Martinis, S., Kersten, J. and Twele, A., 2015. A fully automated TerraSAR-X based flood service. *ISPRS Journal of Photogrammetry and Remote Sensing*, 104, 203–212. DOI: https://doi.org/10.1016/j.isprsjprs.2014.07.014.

Mason, D.C., Davenport I.J., Neal J., Schumann G.J.P. and Bates P.D., 2012. Near real-time flood detection in urban and rural areas using high resolution Synthetic Aperture Radar images. *IEEE Transactions on Geoscience and Remote Sensing*, 50, (8), 3041–3052. DOI: https://doi.org/10.1109/TGRS. 2011.2178030.

Matgen, P., Hostache, R., Schumann G.J.P., Pfister L., Hoffmann L. and Savenije H.H.G., 2011. Towards an automated SAR-based flood monitoring system: lessons learned from two case studies. *Physics and Chemistry of the Earth*, 36, (7–8), 241–252. DOI: https://doi.org/10.1016/j.pce.2010.12.009.

Mavromatis G., 1980. *The bioclimate of Greece*. Dassiki Erevna supp. 1-63 + annexe. Athens [in Greek].

Mayer, L., 1990. *Introduction to Quantitative Geomorphology: An Exercise Manual*. Englewood Cliffs, Prentice Hall, New Jersey, U.S.A.

Melton, M.A., 1958. Geometric properties of mature drainage systems and their representation in E4 Phase Space. *Journal of Geology*, 66, 35-54

Miliaresis A., 2006. *Specialized applications in ArcGIS*. ION Publishing Group, Athens, 34-38

Ministry of Environment and Energy, 2002. *Instructions for surveys on road construction works. Issue No 8: Sewerage – Drainage – Hydraulics works concerning road construction*. Ministry of Environment and Energy, General Secretariat of Public Works, Athens 2002. [in Greek]

Ministry of Environment and Energy, 2016. *Application of the 2007/60/EU Directive. Compilation of rainfall intensity-duration-frequency curves for Greece*. Ministry of Environment and Energy, Special Secretariat for water, Athens 2016. [in Greek]

Mouratidis A., 2011. *Contribution of Earth Observation data and GIS to mapping and managing flood evens in Greece*. Final Report of "GEOGIS floods" research project funded by the John S. Latsis Public Benefit Foundation.

Mouratidis, A. and Ampatzidis, D., 2019. European Digital Elevation Model (EU-DEM) validation against extensive Global Navigation Satellite Systems data and comparison with SRTM and ASTER-GDEM in Central Macedonia (Greece). ISPRS, *International Journal of Geo-Information*, 8(3), 108. DOI: https://doi.org/10.3390/ijgi8030108

Mouratidis, A., Nikolaidou, M., Doxani, G., Lampiri, M., Sarti, F. and Tsakiri-Strati, M., 2011. Flood studies in Greece using Earth Observation data and Geographical Information Systems. *Geological Remote Sensing Group (GRSG) Annual General Meeting*, 7-9 December 2011, ESA/ESRIN, Frascati, Italy.

Mouratidis, A. and Sarti, F., 2013. Flash-Flood Monitoring and Damage Assessment with SAR Data: Issues and Future Challenges for Earth Observation from Space Sustained by Case Studies from the Balkans and Eastern Europe. In: Krisp J., Meng L., Pail R., Stilla U., (eds) *Earth Observation of Global Changes (EOGC). Lecture Notes in Geoinformation and Cartography*. Springer, Berlin, Heidelberg, pp. 125-136. DOI https://doi.org/10.1007/978-3-642-32714-8_8.

Nandi, A., Mandal, A., Wilson, M. and Smith, D., 2016. Flood hazard mapping in Jamaica using principal component analysis and logistic regression.

Environmental Earth Sciences, 75, 465. DOI: https://doi.org/10.1007/s12665-016-5323-0.

Nanson G. C. and Croke J. C., 1992. A genetic classification of floodplains. *Geomorphology*, 4, 459 – 486.

Nico, G., Pappalepore, M., Pasquariello, G., Refice, A. and Samarelli, S., 2000. Comparison of SAR amplitude vs. coherence flood detection methods - a GIS application. *International Journal of Remote Sensing*, 21 (8), 1619–1631. DOI: http://dx.doi.org/10.1080/014311600209931.

Nikolaidou, M., Mouratidis, A., Doxani, G., Oikonomidis, D., Tsakiri-Strati, M. and Sarti, F., 2015. An on-line flood database for Greece supported by Earth Observation data and GIS. *Proceedings of the 10th International Congress of the Hellenic Geographical Society*, 22-24 October 2014, Thessaloniki, Greece, pp. 671-688.

Oeurng, C., Sauvage, S. and Sánchez-Pérez, J.-M., 2011. Assessment of hydrology, sediment and particulate organic carbon yield in a large agricultural catchment using the SWAT model. *Journal of Hydrology*, 401, 145–153. DOI: https://doi.org/10.1016/j.jhydrol.2011.02.017.

Papaioannou, G., Vasiliades, L. and Loukas, A., 2015. Multi-criteria analysis framework for potential flood prone areas mapping. *Water Resoures Management*, 29, 399–418. DOI: http://dx.doi.org/10.1007/s11269-014-0817-6.

Pike, R. J., and Wilson, S. E., 1971. Elevation relief ratio, hypsometric integral and geomorphic area-altitude analysis. *Geological Society of America Bulletin*, 82, 1079-1083.

Psomiadis, E., 2016. Flash flood area mapping utilising SENTINEL-1 radar data. *Proceedings of SPIE*, 10005. DOI: 10.1117/12.2241055.

Observator Instruments B.V., 2008. *Rain Gauge Transmitter OMC-210/212: User's Manual Version 1.02*. Ridderkerk, Netherlands.

Pappenberger, F., Beven K., Frodsham, K., Romanowicz, R. and Matgen, P., 2007. Grasping the unavoidable subjectivity in calibration of flood inundation models: A vulnerability weighted approach. *Journal of Hydrology*, 333, 275– 287. DOI: https://doi.org/10.1016/j.jhydrol.2006.08.017

Patrikaki, O., Kazakis, N., Kougias, I., Patsialis, Th., Theodosiou, N. and Voudouris, K., 2018. Assessing flood hazard at river basin scale with an index-based approach: The case of Mouriki, Greece. *Geosciences* 8 (50), 1-13. DOI: 10.3390/geosciences8020050

Pierdicca, N., Pulvirenti, L., Chini, M., Guerriero, L. and Candela, L., 2013. Observing floods from space: Experience gained from COSMO-SkyMed observations. *Acta Astronautica* 84, 122-133. DOI: http://dx.doi.org/10.1016 /j.actaastro.2012.10.034.

Pradhan, B., Hagemann, U., Tehrany, M.S. and Prechtel, N., 2014. An easy to use ArcMap based texture analysis program for extraction of flooded areas from TerraSAR-X satellite image. *Computers and Geosciences*, 63, 34–43. DOI: https://doi.org/10.1016/j.cageo.2013.10.011.

Prigent, C., Papa, F., Aires, F., Rossow, W. B. and Matthews, E., 2007. Global inundation dynamics from multiple satellite observations, 1993–2000. *Journal of Geophysical Research (Atmospheres)*, 112, D12107. DOI: https://doi.org/10.1029/2006JD007847.

Pulvirenti L., Pierdicca, N., Chini, M. and Guerriero, L., 2011a. Flood monitoring using multi-temporal COSMO-SkyMed data: Image segmentation and signature

interpretation. *Remote Sensing of Environment* (115), 990–1002. DOI: https://doi.org/10.1016/j.rse.2010.12.002.

Pulvirenti, L., Pierdicca, N., Chini, M., and Guerriero, L., 2011b. An algorithm for operational flood mapping from Synthetic Aperture Radar (SAR) data using fuzzy logic. *Natural Hazards and Earth System Sciences*, 11, 529–540. DOI: 10.5194/nhess-11-529-2011

Refice, A., D'Addabbo, A. and Capolongo, D. (Eds) 2018. *Flood Monitoring through Remote Sensing*. Springer Remote Sensing/Photogrammetry, Springer International Publishing. DOI: https://doi.org/10.1007/978-3-319-63959-8

Saaty, T.L., 1980. *The Analytic Hierarchy Process*. McGraw-Hill, New York.

Schlaffer, S., Matgen, P., Hollaus, M. and Wagner, W., 2015. Flood detection from multi-temporal SAR data using harmonic analysis and change detection. *International Journal of Applied Earth Observation and Geoinformation*. 38, 15–24. DOI: http://dx.doi.org/10.1016/j.jag.2014.12.001.

Schlaffer, S., Chini, M., Giustarini, L. and Matgen, P., 2017. Probabilistic mapping of floodinduced backscatter changes in SAR time series. *International Journal of Applied Earth Observation and Geoinformation*, 56, 77–87. DOI: http://dx.doi.org/10.1016/j.jag.2016.12.003.

Schumann, G., Di Baldassarre, G. and Bates, P., 2009. The utility of spaceborne radar to render flood inundation maps based on multialgorithm ensembles. *IEEE Transactions in Geoscience and Remote Sensing*, 47, 2801–2807 DOI: http://ieeexplore.ieee.org/lpdocs/epic03/wrapper.htm?arnumber=4907026

Schumann, G. J. – P., Bates P. D., Neal J. C and Andreadis, K. M., 2015. Chapter 2 - Measuring and Mapping Flood Processes In: John F. Shroder, Paolo Paron and

Giuliano Di Baldassarre (eds) *Hydro-Meteorological Hazards, Risks and Disasters*, Elsevier, 35-64.

Schumann, G.J.P. and Moller, D. K., 2015. Microwave remote sensing in flood inundation. *Physics and Chemistry of the Earth*, 83-84, 84-95. DOI: http://dx.doi.org/10.1016/j.pce.2015.05.002.

Schumm, S. A. (1956). Evolution of Drainage and slopes in Badlands of Perth Ambay, New Jersey. *Bulletin of Geological Society of America*, 67, 567- 646.

Seejata, K., Yodying, A., Wongthadam, T., Mahavik, N. and Tantanee, S.., 2018. Assessment of flood hazard areas using Analytical Hierarchy Process over the Lower Yom Basin, Sukhothai Province. *Procedia Engineering*, 212, 340–347. DOI: https://doi.org/10.1016/j.proeng.2018.01.044

Slade, R. M., and Patton, J., 2002. Major and Catastrophic Storms and floods In Texas: 215 Major and 41 Catastrophic Events From 1853 To September 1, 2002. *U.S. Geological Survey Open-File Report 03-193*.

Smith, K. and Petley, D., 2009. *Environmental hazards: Assessing risk and reducing disaster*. Routledge, New York, USA, 233-261.

Smith, K. and Ward, R., 1998. Floods: *Physical Processes and Human Impacts*. Chichester, John Wiley.

Son Tek / YSI (Yellow Springs Instrument Company), 2006. *Argonaut – SL System Manual Firmware version 11.3*. San Diego, USA

Soulios G., 1996. *General Hydrogeology*. University Studio Press, Thessaloniki, 50-75 [in Greek].

Stefanidis, S. and Stathis, D., 2013. Assessment of flood hazard based on natural and anthropogenic factors using analytic hierarchy process (AHP). *Natural Hazards: Journal of the International Society for the Prevention and Mitigation of Natural*

Hazards, Springer;International Society for the Prevention and Mitigation of Natural Hazards, 68, 569–585. DOI: https://doi.org/10.1007/s11069-013-0639-5.

Strahler, A. N., 1952. Hypsometric (area-altitude) analysis of erosional topology. *Geological Society of America Bulletin*, 63 (11): 1117–1142. DOI:10.1130/0016-7606(1952)63[1117:HAAOET]2.0.CO;2.

Strahler, A. N., 1957. Quantitative analysis of watershed geomorphology. *Transactions of the American Geophysical Union*, 38 (6), 913–920. DOI:10.1029/tr038i006p00913.

Tang, Z., Zhang, H., Yi, S. and Xiao, Y., 2018. Assessment of flood susceptible areas using spatially explicit, probabilistic multi-criteria decision analysis. *Journal of Hydrology* 558 (2018) 144–158. DOI: https://doi.org/10.1016/j.jhydrol. 2018.01.033

Tehrany, M.S., Pradhan, B. and Jebur, M.N., 2013. Spatial prediction of flood susceptible areas using rule based decision tree (DT) and a novel ensemble bivariate and multivariate statistical models in GIS. *Journal of Hydrology*, 504, 69–79. DOI: https://doi.org/10.1016/j.jhydrol.2013.09.034.

Tehrany, M.S., Pradhan, B. and Jebur, M.N., 2014. Flood susceptibility mapping using a novel ensemble weights-of-evidence and support vector machine models in GIS. *Journal of Hydrology*, 512, 332–343. DOI: https://doi.org/10.1016/j.jhydrol.2014.03.008.

Tehrany, M. S., Pradhan, B. and Jebur, M.N., 2015a. Flood susceptibility analysis and its verification using a novel ensemble support vector machine and frequency ratio method. *Stochastic Environmental Research and Risk Assessment*, 29, 1149–1165. DOI: https://doi.org/10.1007/s00477-015-1021-9.

Tehrany, M.S., Pradhan, B., Mansor, S. and Ahmad, N., 2015b. *Flood susceptibility assessment using GIS-based support vector machine model with different kernel types*. Catena 125, 91–101. DOI: https://doi.org/10.1016/j.catena.2014.10.017.

Thoms, M. C., 2003. Floodplain-river ecosystems: lateral connections and the implications of human interference. *Geomorphology*, 56, 335 – 350.

Tsyganskaya, V., Martinis, S., Marzahn, P. and Ludwig, R., 2018. Detection of Temporary Flooded Vegetation Using Sentinel-1 Time Series Data. *Remote Sensing*, 10, 1286. DOI: https://doi.org/10.3390/rs10081286.

Twele, A., Cao, W.X., Plank, S. and Martinis, S., 2016. Sentinel-1-based flood mapping: a fully automated processing chain. *International Journal of Remote Sensing*, 37, (13), 2990–3004. DOI: https://doi.org/10.1080/01431161.2016. 1192304.

Vieux, B.E., 2004. *Distributed Hydrologic Modelling using GIS*. Kluwer Academic Publishers, Netherlands, pp 123-124.

Voudouris, K., 2013. *Technical Hydrogeology – Groundwater*. Tziolas Publications, Thessaloniki, 140-141 [in Greek].

Voudouris, K., Mavrommatis, T. and Antonakos, A., 2007. Hydrologic balance estimation using GIS in Korinthia prefecture, Greece. *Advances in Science and Research* 1, 1-8. DOI: https://doi.org/10.5194/asr-1-1-2007

Wang, Y., Koopmans, B.N. and Pohl, C., 1995. The 1995 flood in the Netherlands monitored from space – a multi-sensor approach. *International Journal of Remote Sensing*, 16 (15), pp 2735–2739. DOI: https://doi.org/10.1080/0143116950895 6399

Wang, Y., Li, Z. and Tang, Z., 2011. A GIS-based spatial multi-criteria approach for flood risk assessment in the Dongting Lake Region, Hunan, Central China. *Water Resources Management*, 25, 3465–3484. DOI: https://doi.org/10.1007/s11269-011-9866-2.

Wang, Z., Lai, C., Chen, X., Yang, B., Zhao, S. and Bai, X., 2015. Flood hazard risk assessment model based on random forest. *Journal of Hydrology*, 527, 1130–1141. DOI: https://doi.org/10.1016/j.jhydrol.2015.06.008.

Ward, P.J., Jongman, B., Salamon, P., Simpson, A., Bates, P., De Groeve, T., Muis, S., De Perez, E.C., Rudari, R., Trigg, M.A. and Winsemius, H.C., 2015. Usefulness and limitations of global flood risk models. *Nature Climate Change*, 5, 712–715. DOI: doi:10.1038/nclimate2742.

Wolman, M.G. and Leopold, L. B., 1957. River Flood Plains: Some Observations of their formation. *U.S. Geological Survey Professional Paper*, 282C, 87 – 109.

Xiao, Y., Yi, S. and Tang, Z., 2018. Integrated flood hazard assessment based on spatial ordered weighted averaging method considering spatial heterogeneity of risk preference. *Science of the Total Environment*, 599-600, 1034–1046. DOI: https://doi.org/10.1016/j.scitotenv.2017.04.218

Y.S.I. (Yellow Springs Instrument Company) Inc., 2006. *6-Series Multiparameter Water Quality Sondes: User Manual*. San Diego, USA

Yésou, H., Sarti, F., Tholey, N., Mouratidis, A., Clandillon, S., Huber, C., Studer, M. and De Fraipont, P., 2013. Addressing emergency flood mapping and monitoring of inland water bodies with sentinel 1-2. Expectations and perspectives. *Living Planet Symposium*, 9-13 September 2013, Edinburgh, UK, ESA SP-722.

Zhao, G., Pang, B., Xu, Z., Yue, J. and Tu, T., 2018. Mapping flood susceptibility in mountainous areas on a national scale in China. *Science of the Total Environment*, 615, 1133–1142. DOI: https://doi.org/10.1016/j.scitotenv.2017.10.037

Zhong, S., Yang, L., Toloo, S., Wang, Z., Tong, S., Sun, X., Crompton, D., FitzGerald, G. and Huang, C., 2018. The long-term physical and psychological health impacts of flooding: A systematic mapping. *Science of the Total Environment*, 626, 165–194. DOI: https://doi.org/10.1016/J. SCITOTENV.2018.01.041.

Zhou, Z., Stefanon, L., Olabarrieta, M., D'Alpaos, A., Carniello, L. and Coco, G., 2014. Analysis of the drainage density of experimental and modelled tidal networks. *Earth Surface Dynamics*, 2, 105–116. DOI: https://doi.org/10.5194/esurf-2-105-2014

Zoka, M., Psomiadis, E. and Dercas, N., 2018. The Complementary Use of Optical and SAR Data in Monitoring Flood Events and Their Effects. *Proceedings*, 2, 644. DOI: https://doi.org/10.3390/proceedings2110644.

Internet sources

Copernicus, 2017. *Europe's eyes on Earth – Land Monitoring Service*. https://land.copernicus.eu/pan-european/corine-land-cover/clc-2012?tab=download (accessed on 25/11/2017)

E-evros.gr, 2018. https://www.e-evros.gr/gr/eidhseis/3/sto-idio-ergo-8eates-3ana-plhmmyres-sto-didymoteixo/post34667

European Environment Agency (E.E.A.), 2017. *Copernicus Land Monitoring Service - EU-DEM*. Published 7/12/2017 from: https://www.eea.europa.eu/data-and-maps/data/copernicus-land-monitoring-service-eu-dem.

E.S.A. NEST (Next ESA SAR Toolbox), 2014. https://earth.esa.int/web/nest/home/

E.S.A. Sentinel Online, 2019a. *Overview*. https://earth.esa.int/web/guest/missions/esa-operational-eo-missions/sentinel-1

E.S.A. Sentinel Online, 2019b. *Instrument Payload*. https://sentinel.esa.int/web/sentinel/missions/sentinel-1/instrument-payload

E.S.A. STEP (Science toolbox Exploitation Platform) 2018. *SNAP*. https://step.esa.int/main/toolboxes/snap/

European Space Agency (E.S.A.), 2008. *Radar Flood Mapping*. http://earth.eo.esa.int/download/eoedu/Earthnet-website-material/toaccessfrom-Earthnet/2010_AndeSAT-practicalsessions_Bolivia/NESTprocessing_floodmapping.pdf

European Space Agency (E.S.A.), 2019a. Envisat. https://earth.esa.int/web/guest/missions/esa-operational-eo-missions/envisat

European Space Agency (E.S.A.), 2019b. ASAR. https://earth.esa.int/web/guest/missions/esa-operational-eo-missions/envisat/instruments/asar

Filotis, 2019. *Database for the Natural Environment of Greece*. https://filotis.itia.ntua.gr/

Inevros.gr, 2017. http://www.inevros.gr/2017/04/21/didimoteixo-plimmires-vroxi/

Ministry of Environment and Energy, 2014. https://floods.ypeka.gr/index.php?option=com_content&view=article&id =1108& Itemid =1150

R.E.M.TH. (Region of Eastern Macedonia and Thrace), 2018. https://www.google.com/maps/d/viewer?hl=el&ie=UTF8&msa=0&ll=41.30237845280439%2C26.5457875805688&spn=1.601924%2C3.304138&t=h&z=12&mid=1T1BniXw4NgQEw9klL_uNqOCcXKM

UN-ISDR 2004. Terminology for disaster risk reduction. UN-International strategy for Disaster Reduction, available at: www.unisdr.org/eng/library/lib-terminology-eng%20home.htm

Appendices

Appendix A - Didymoteicho's gauging station

The gauging station that is located on Didymoteicho's bridge, on the northern part of the city, has been installed by the Department of Civil Protection of the region of Evros and is comprised of three measurement instruments: 1) the Argonaut – Side Looking (SL) system, which is an acoustic Doppler current meter, 2) the Rain Gauge Transmitter OMC-210 and 3) the Y.S.I. (Yellow Springs Instrument Company) 6600 V2 multiparameter water quality sonde.

A1. Argonaut – SL

The Argonaut – SL (Figure 116) is an acoustic Doppler current meter with the ability to scan horizontally across water bodies such as channels, harbors and rivers. It is not only used in measurements of total water flow, water levels and velocity, but it can also be easily installed on all kinds of vertical structures such as bridge abutments, river banks etc. (Son Tek / YSI Inc. 2006)

Figure 116: The Argonaut –SL acoustic Doppler current meter. . (Son Tek / YSI Inc. 2006)

Specifically, Argonaut – SL enables velocity measurements in a user-programmable cell that extents horizontally up to 120m from the instrument. The maximum gauging distance depends on the operational frequency and the system also includes a vertical acoustic beam for water level measurements, which can be used in order to compute total flow when combined with channel geometry (supplied by the used) and velocity. Moreover, this instrument employs user – friendly Windows – based software along with a contemporary acoustic Doppler instrumentation. Also, with the use of a single mode of operation, the aforementioned instrument provides confident measurements of water flow and current velocities that can easily achieve high levels of accuracy. (Son Tek / YSI Inc. 2006)

Additionally, Argonaut – SL can operate in a wide range of sites and can be useful in lots of water resource applications such as water supply, velocity indexing, river discharge monitoring, irrigation channels, flood alert systems, offshore platforms, vessel traffic/ship berthing and pollution monitoring.

Finally, it is worth mentioning that, for many years, it has been established that the acoustic Doppler current meters, are among the most reliable ways to effectively gauge water velocity. Furthermore, Argonaut – SL measurements are carried out with the aid of a remote sampling volume that can filter flow distortion, while Doppler technology can deal with extremely low velocity values, thus allowing for accurate calculations in the case of low flows. Additionally, the computational algorithms are the same for velocity values that range from1 cm/s to 6 m/s, meanwhile the gauging system has no moving parts and is not only resistant to biofouling contamination, but also allow for the use of anti-fouling paint in order to cover growth. Finally, Argonaut – SL does not require calibration since velocity data are free from drift. (Son Tek / YSI Inc. 2006)

A2. Rain Gauge Transmitter OMC-210

The Rain Gauge Transmitter OMC-210 (Figure 117) is used in rainfall measurements. This instrument has been devised in order to perform with high precision under the most adverse conditions. OMC-210 collects rainfall with the use of a funnel whose inside diameter is 22.57 cm and its circular area covers an extent of 400cm^2. The construction of

the funnel has been performed in such a way so that, through the application of the proper area and shape, the prevention of raindrop loss can be achieved. Regarding the funnel's operation, it concentrates rainfall water to a gold plated double bucket that automatically empties when it becomes full. The proper emptying of the bucket is achieved via the shape and the gold plating of the bucket. The tipping of the bucket, which occurs when the later empties its contents, causes a reed contact that has been placed beside the bucket to become activated and generate a signal. The bucket empties when its contents reach 4, 8 or 20 cm^3 of rain water and then they are lead through stainless steel pipes to the system's outlets that have been placed in its base plate. Moreover, the outlets are encased in stainless steel mash which prevents animal interference. (Observator Instruments B.V. 2008)

Figure 117: The Rain Gauge Transmitter OMC-210. (Observator Instruments B.V. 2008)

When needed, rain measurements can be produced via a film heater that is placed inside the housing. A switch that is affected by temperature, which operates on temperatures of ± 2 °C, controls the heater whose consumption is approximately 2A. (Observator Instruments B.V. 2008)

A3. YSI 6600 V2 multiparameter water quality sonde.

The YSI 6600 V2 sonde (Figure 118) is a multi-parameter, water quality measurement, and data collection system, which is widely used in assessments, research

and the checking of compliance according to certain environmental regulations. Furthermore, a sonde, which might involve multiple probes that may in turn contain more than one sensor to monitor water quality data, is an instrument that is shaped like a torpedo and can be immersed in water in order to collect water quality data. (Y.S.I. Inc. 2006)

Figure 118: The YSI 6600 V2 sonde. (Y.S.I. Inc. 2006)

The aforementioned monitoring system is made of PVC and stainless steel, it can operate in fresh, sea or polluted water at temperatures ranging from -5 to +50°C and at depths ranging from 0 to 200m. The sensors that are available for the YSI 6600 V2 sonde can measure: temperature, conductivity, rapid pulse dissolved oxygen, pH, ORP (Oxidation Reduction Potential), ammonium, nitrate, chloride, depth. There is also the option of two total optical sensors that can measure turbidity, chlorophyll, rhodamine WT, Phycocyanin-Containing Blue-Green Algae (BGA-PC) and Phycoerythrnin-Containing Blue-Green Algae (BGA-PE). (Y.S.I. Inc. 2006)

Appendix B – ENVISAT and ASAR (Advanced Synthetic Aperture Radar)

ENVISAT (Environmental Satellite) (Figure 119) succeeded ESA's ERS (European Remote Sensing) satellite series. It launched successfully in 1/3/2002 carrying 10 instruments in its payload and, by weighting 8t, it had been registered as the largest civilian Earth observation mission. ENVISAT instruments enhanced ERS data sets, not

only with the aid of radiometers that are capable to measure temperature, radar altimeters and state-of-the-art imaging radars, but also with the use of newly introduced instruments such as the medium-resolution spectrometer that is able to discern with equal ease ocean color and land features. Moreover, trace gases could be monitored via the two atmospheric sensors on board the ENVISAT satellite. On 8/4/2012, the sudden loss of contact with the ENVISAT satellite marked the end of the mission. (E.S.A. 2019a)

The continuity between the ERS-1/2 AMI (Active Microwave Instrument) and the image mode (SAR) was achieved through the Advanced Synthetic Aperture Radar (ASAR) that was operating at C-band. Additionally, the instrument presented a wider variety in terms of modes of operation and improved performance concerning polarization, coverage and range of incidence angles. The instrument improvements that contributed in the successful performance of ASAR comprised of: 1) a digital waveform generation for pulse "chirp" generation, 2) a ScanSAR mode of operation by beam scanning in elevation, 3) a full active array antenna equipped with distributed transmit/receive modules which provided distinct transmit and receive beams and 4) a block adaptive quantisation scheme. The detailed technical characteristics of ASAR are presented in Table a. (ESA 2019b)

Figure 119: Model of Envisat. (E.S.A. 2019a)

Table 39: Characteristics of ENVISAT's ASAR instrument. (E.S.A. 2019b)

Type	Imaging microwave radars
Technical Characteristics	
Spatial Resolution	Global Monitoring mode: approximately 1000m x 1000m Wide Swath mode: approximately 150m x 150m. Image, Wave and Alternating Polarisation modes: approximately 30m x 30m.
Accuracy	Radiometric accuracy: 0.65 dB, Radiometric resolution in range: 1.5-3.5 dB
Waveband	Microwave: C-band, with choice of 5 polarisation modes (VV, HH,VV/HH, HV/HH, or VH/VV)
Swath Width:	Wide swath and global monitoring modes: 400km or more, Wave mode:5km, Image and alternating polarisation modes: up to 100km

Appendix C – NEST software

The Next ESA SAR Toolbox (NEST) is an open source toolbox that was created by ESA. The GPL (General Public License) license allow the software to visualize, analyze, process and read not only ESA (SENTINEL-1, ENVISAT, ERS-1/2) but also other spaceborne (ALOS PALSAR, COSMO-SkyMed, TerraSAR-X, JERS-1, RADARSAT 1-2) SAR data processed to Level-1 or higher. (E.S.A. NEST 2014)

NEST has been replaced by ESA's SNAP (Sentinel Application Platform) software.

Appendix D – SENTINEL-1 A/B

The Copernicus, which was previously known as GMES (Global Monitoring for Environment and Seurity), is a joint initiative between the European Space Agency (ESA) and the European Commission (EC) produced the SENTINEL-1 (Figure 120) mission to be used as the European Radar Observatory. The aforementioned European

initiative aims for the implementation of information services that deal with security and environment. Its research field relies not only on ground-based information but also on the collection of observation data from Earth Observation satellites. (E.S.A. Sentinel Online 2019a)

Figure 120: Sentinel-1 satellite. (E.S.A. Sentinel Online 2019a)

Additionally, the radar on board the SENTINEL-1 mission operates at C-band using four exclusive imaging modes with different coverage (up to 400 km) and resolution (down to 5 m), enabling prompt product delivery, very short revisit times and dual polarisation capability. Furthermore, accurate measurements of spacecraft attitude and position are available for each observation. (E.S.A. Sentinel Online 2019a)

The mission is comprised of two satellites, namely SENTINEL-1A and SENTINEL-1B, which were launched at 3/4/2014 and 25/4/2016 respectively, sharing the same orbital plane. (E.S.A. Sentinel Online 2019a)

The SENTINEL-1 mission is functioning in a conflict-free, pre-programmed operation mode, providing high resolution imagery of shipping routes, coastal zones and even global landmasses, while it is also covering the global ocean by providing vignettes. This not only guarantees the compilation of a long term data archive that is invaluable for applications that require such long time series, but also ensures the provision of high quality services that are required by operational services. (E.S.A. Sentinel Online 2019a)

Concerning the instruments that can be found on board onboard SENTINEL-1 mission there is a single C-band synthetic aperture radar that functions at the 5.405 GHz

frequency. This instrument includes a right-looking active phased array antenna that allows for fast scanning in both azimuth and elevation, whereas enabling 520 Mbit/s X-band downlink capacity and data storage capacity of 1 410 Gb. (E.S.A. Sentinel Online 2019b)

Two parallel receive chains for H and V polarisation and a transmit chain, which can switch between V and H, support C-SAR instrument's function in dual polarisation (VV+VH and HH+HV). (E.S.A. Sentinel Online 2019b)

The acquisition modes that operate for the SENTINEL-1 mission are the following: 1) Extra-Wide swath (EW), 2) Wave mode (WV) 3) Stripmap (SM) and 4) Interferometric Wide swath (IW). From the aforementioned modes, the IW mode over land and the WV over open oceans are the primary conflict-free ones.

The continuity with ENVISAT and ERS missions is achieved through the ***Stripmap*** (SM) imaging mode, which allows coverage with a 5 m by 5 m resolution over a narrow swath width of 80 km. Furthermore, by changing the elevation beamwidth and the beam incidence angle, the selection of one out of six imaging swaths can be achieved.

The combination between a moderate geometric resolution (5 m by 20 m) and a large swath width (250 km) can be enabled through the ***Interferometric Wide swath*** (IW) imaging mode, which, with the use of Terrain Observation with Progressive Scans SAR (TOPSAR), captures images from three sub-swaths. High quality images can be produced and scalloping can be prevented via the TOPSAR technique, which not only can allow the electronical steering of the beam from backward to forward in the azimuth direction for each burst, but also allows the steering of the beam in range such as in SCANSAR. Adequate overlapping between the wave number spectrum (in the elevation domain) and the Doppler spectrum (in the azimuth domain) can enable the conduction of Interferometry. Moreover, homogeneous image quality for the whole of the swath can be achieved by the application of the TOPSAR technique.

The need for short revisit times and wide coverage that are of paramount importance in cases that concern maritime, ice and polar zone operational services is being covered with the aid of the ***Extra Wide swath*** (EW) imaging mode. The latter operates like the IW mode, the only difference being the use of a TOPSAR technique that employs five

sub-swaths, which provide a better resolution (20 m by 40 m). Likewise the IW mode the EW mode can also be used for interferometry.

Ocean wave models, when combined with SENTINEL-1 ***Wave mode*** (WM), can provide information regarding the heights, wavelength and direction of waves on open oceans. Moreover, the stripmap imagettes of 20 km by 20 km, which cover wave mode acquisitions, are produced on two different incidence angles. Wave imagettes are acquired on 100 km intervals, while imagettes of the same incidence angle have a distance of 200 km between them.

Appendix E – SNAP (Sentinel Application Platform) software

This software, developed by C-S, Array Systems Computing and Brockmann Consult, has been created in order to unify all Sentinel Toolboxes. (E.S.A. STEP 2018)

Generic EO Data Abstraction, Portability, Extensibility, Graph Processing Framework, and Modular Rich Client Platform Tiled Memory Management are the technological innovations that enable SNAP architecture for effective Earth Observation analysis and processing. (E.S.A. STEP 2018)

Appendix F – HEC-RAS (Hydrologic Engineering Center – River Analysis System) software

Sediment transport-mobile bed modelling, water temperature analysis and one dimensional steady and unsteady flow river hydraulics calculations can be carried oiut via the U.S. Army Corps of Engineers' River Analysis System (HEC-RAS) software. It was developed at the Hydraulic Engineering Center (HEC), which is a division of the Institute for Water Resources (IWR), U.S. Army Corps of Engineers.

Interactive use with the aid of a multi-tasking environment is a major characteristic of the HEC-RAS software. The software architecture includes data storage and management capabilities, a graphical user interface (GUI), graphics and reporting facilities and separate analysis components.

The one-dimensional river analysis components that are utilized by HEC-RAS are the following: 1) water quality analysis, 2) movable boundary sediment transport computations, 3) unsteady flow simulation and 4) steady water flow water surface profile computations. It is noteworthy that all the aforementioned components utilize common geometric and hydraulic computation routines, along with common geometric data representation. Additionally, HEC-RAS includes several hydraulic design features that can be used as long as the computation of the basic water surface profiles has been completed. (HEC 2010)

River Analysis Components

Steady flow water surface profiles. The calculation of water surface profiles by conducting steady flow analysis can be achieved by carrying out this component of the hydraulic modelling system. Drainage networks that range from a single reach to a complete dendritic system can be handled by HEC-RAS, while the aforementioned component enables dealing with the modelling of supercritical, subcritical and mixed flow regimes of water surface profiles.

The one-dimensional energy equation forms the foundation of HEC-RAS main computational procedures, while energy losses can be computed by contraction/expansion (coefficient multiplied by the change in velocity head) and by friction (Manning's equation). Moreover, rapid variations of the water surface profile are handled by the momentum equation in situations that might involve hydraulics of bridges, profiles at river confluences (stream junctions) and mixed flow regime calculations (i.e. hydraulic jumps).

The aforementioned computations include cases such as structures in the floodplain, culverts, dams, bridges and weirs. Flood insurance studies and floodplain management evaluate floodway encroachments by employing the steady flow system. Furthermore, levees and channel modifications can be incorporated in the calculations in order to cater for the changes that they cause in water surface profiles.

Steady flow components in HEC-RAS contain special features such as: 1) stable channel design and analysis 2) culvert opening analysis 3) multiple plan analyses 4)

multiple bridge and/or, split flow optimization and 5) multiple profile computations. (HEC 2010)

Unsteady flow simulation. This component is utilized in the simulation of one-dimensional unsteady flow via a network that is comprised of open channels. An adapted form of the UNET model that was conceived by Dr. Robert L. Barkau provides the unsteady flow equation solver (Barkau 1992 and HEC 1993). This component initially created for calculations that concerned subcritical flow regime, but the release of version 3.1, enabled mixed flow regime (drawdowns, supercritical subcritical and hydraulic jumps,) calculations in the unsteady flow calculations module.

The unsteady flow model also contained hydraulic structures that were initially used in the steady flow component such as hydraulic calculations for culverts, bridges, cross-sections etc.

Also, the unsteady flow component involves the following special features: 1) pumping stations, 2) levee breaching and overtopping, 3) pressurized pipe systems, 4) dam break analysis and 5) navigation dam operations. (HEC 2010)

Sediment transport/movable boundary conditions. This HEC-RAS component aims in carrying out simulations of one-dimensional sediment transport/movable boundary calculations, which are produced by deposition and scouring over various time intervals that typically involve years, while applications to single flood events are still feasible.

This mode uses the grain size fraction in its computations, thus enabling the simulation of hydraulic armoring and sorting. The main features of this component enable the following: 1) hydraulic modeling of channel dredging, 2) hydraulic modelling of complete drainage networks, 3) the employment of a plethora of equations regarding the sediment transport computation and 4) inclusion of encroachment and levee alternatives.

Additionally, the main goal of this component is the simulation of long-term trends in a stream channel concerning deposition and scour that might be caused by changes in channel geometry or the duration and frequency in water stage and discharge. The application of the aforementioned component concerns: 1) prediction of the influence of dredging on the rate of deposition, 2) evaluation of deposition in reservoirs, 3) designing

of channel contractions required to maintain navigation depths, 4) evaluation of sedimentation in fixed channels and 5) the estimation of maximum possible scour during large flood. (HEC 2010)

Water quality analysis. This function of HEC-RAS enables the conducting of riverine water quality analyses. The current HEC-RAS version can carry out detailed temperature analysis and gauges concerning a limited number of water quality constituents such as: Dissolved Organic Phosphorous, Dissolved Nitrite Nitrogen, Dissolved Organic Nitrogen, Algae, Carbonaceous Biological Oxygen Demand, Dissolved Nitrate Nitrogen, Dissolved Ammonium Nitrate, Dissolved Orthophosphate and Dissolved Oxygen. (HEC 2010)

Appendix G – HEC-GeoRAS software

HEC-GeoRAS is an extension of the Geographic Information System software program ArcGIS™, which was copyrighted and developed by the Environmental Systems Research Institute Inc. (E.S.R.I.) in Redlands at California.

The initial compilation of the extension was carried out by ESRI and the Hydrologic Engineering Center (HEC) via a Cooperative Research and Development Agreement that ensures the constant development of HEC-GeoRAS with the aid of Research and Development funds.

Geospatial data employed by Hydrologic Engineering Center's River Analysis System (HEC-RAS) can be processed and analyzed through the HEC-GeoRAS set of ArcGIS tools. Digital Terrain Models (DTM) and complementary data sets can be used in order to produce the geometric data HEC-RAS import file with the use of the aforementioned extension and its interface enables the procedure to be carried out by even amateur users. Likewise, the results of hydraulic analysis exported from HEC-RAS can also be processed by HEC-GeoRAS.

The viewing of files that are exported from HEC-RAS, along with files of geometric data that are imported into it, are compiled by HEC-GeoRAS. A Digital Terrain Model (DTM), which can be represented by a Triangulated Irregular Network (TIN) or a GRID, and data extracted from data sets (ArcGIS Layers) are used in order to produce the import

file. The RAS Layers employed by the extension include the DTM and the data layers, while the intersection of the RAS Layers forms the basis under which the geometric data are compiled.

The completion of the geometric data is necessary in order to be imported in HEC-RAS for hydraulic computations that require flow data as input. HEC-GeoRAS spatial analysis can be carried out on the exported water surface and velocity results derived from hydraulic computations that were conducted in HEC-RAS and were imported back to ArcGIS™. The data exchange file (*.sdf) is used in order to transfer GIS data between HEC-RAS and ArcGIS™. (HEC 2011)

Photos

Photo 1: The bridge of Didymoteicho, upon which the gauging station has been placed.

Photo 2: The gauging station on Didymoteicho.

Photo 3: Erythropotamos' main watercourse near the basin mouth.

Photo 4: Aspect of the upstream part of Erythropotamos River taken from the bridge of Didymoteicho.

Photo 5: Aspect of the downstream part of Erythropotamos River taken from the bridge of Didymoteicho.

Photo 6: Erythropotamos' left part of the floodplain, near Didymoteicho.

Photo 7: Boats that are used for fishing have been chained on trees on Erythropotamos' floodplain in order not to be carried away by floods.

Photo 8: The old brigde of Didymoteicho crossing over Erythropotamos' main watercourse.

Photo 9: Weir on one of Erythrpotmos' main tributaries.

Photo 10: A tributary of Erythropotamos River.

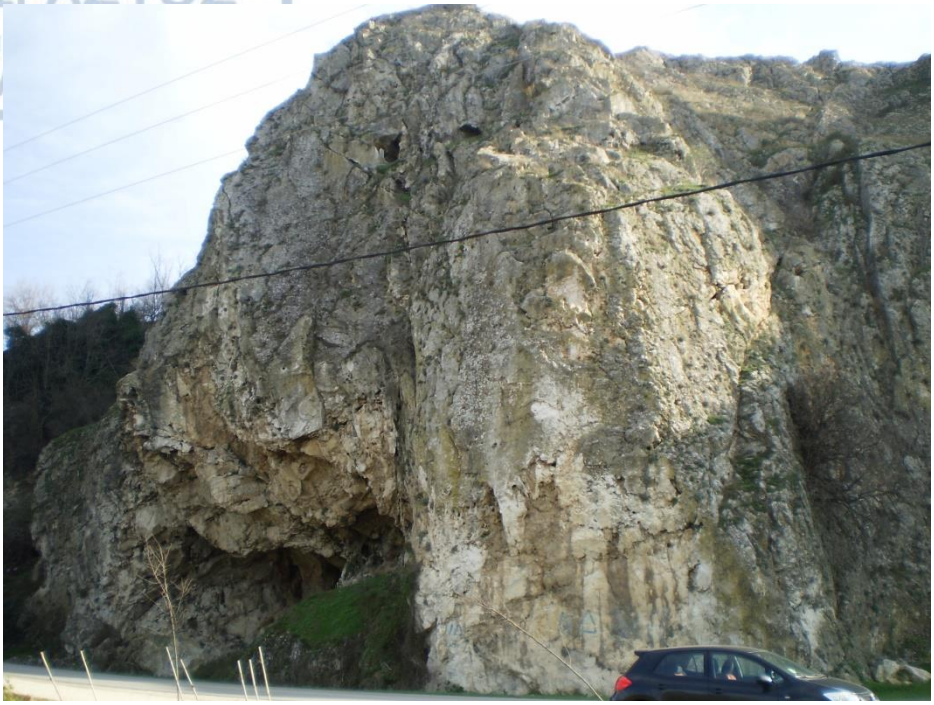

Photo 11: Mafic rocks (O2) formation comprised of gabbros, gabbrodiorite, diabase and pillow lavas located approximately 1 km NW of Didymoteicho.

Photo 12: Mafic rocks (O2) formation comprised of gabbros, gabbrodiorite, diabase and pillow lavas located approximately 1 km NW of Didymoteicho.